Using Hyperspectral Images to Map Moisture Content and Basic Density of Boards and Frozen and Thawed Logs

By

Ataollah Haddadi Goyaghaj

Civil Engineer, Faculty of Geodesy and Gematics, K.N.Toosi University of Technology, Tehran, Iran, 2009

A Dissertation Submitted in Partial Fulfillment of the Requirements for the Degree of

Doctor of Philosophy

in the Graduate Academic Unit of Forestry and Environmental Management

Supervisor: Brigitte Leblon, Ph.D. University of New Brunswick

Advisory Committee: James Burger, Ph.D. BurgerMetrics
Zarin Pirouz, M.Sc. FPInnovations
Kevin Groves, M.Sc. FPInnovations
Joseph Nader, Ph.D. FPInnovations

Examining Board: Yonghao Ni, Ph.D. Department of Chemistry, Chairperson
Rod Stirling, Ph.D. HRA/Forestry & Environmental Management
Maurice Defo, Ph.D. HRA/Forestry & Environmental Management

External Examiner: Stephen Kelley, Ph.D. Professor and Department Head, Department of Forest Biomaterials, North Carolina State University, Raleigh, NC, USA

This dissertation is accepted by the Dean of Graduate Studies
THE UNIVERSITY OF NEW BRUNSWICK
January, 2016

© Ataollah Haddadi (2016)

Abstract

The purpose of this research was to investigate the use of near infrared hyperspectral imaging (NIR-HSI) for in-line moisture content (MC) and basic specific gravity (BSG) estimation of thawed and frozen logs as well as of boards. We also developed a method to classify the logs according to their MC, BSG, species, and log state (frozen and thawed). Samples from three different species (black spruce, quaking aspen, balsam poplar) for logs and one species (subalpine fir) for board were collected and dried in different steps. We also considered frozen samples for logs. For each step hyperspectral NIR images and weight measurements were acquired.

The images were subjected to the following processing. They were first calibrated into reflectance. Then, bad pixels were found and replaced by a corrected value using a median filter. A new method was developed to find and remove abnormal spectra. It consisted of a combination of the *boxplot* method and principle component analysis (PCA). The remaining spectra were converted into absorbance spectra. The raw absorbance spectra were subjected to several spectral transformations, such as the multiplicative scatter correction (MSC), as well as the first, and second derivatives.

For the board, the best PLS model was found in using raw spectra for both MC and BSG estimation and had an $RMSE_V$ of 10.8% and 0.007, respectively. For the log samples, PLS models were calibrated by considering two factors: log state (thawed and frozen conditions) and species, and their combination. Then the models were applied to the whole board images in order to produce 2D images of MC and BSG.

Models were better with thawed logs than with frozen logs. The models estimated MC with an RMSE that varies between 2.94% in the case of black spruce to 15.49% in the case of balsam poplar. The model's accuracy for BSG estimation was the best when all the three species were used together ($RMSE_V$=0.036). PLS discriminant analysis (PLS-DA) was also applied to sort log samples into three MC or BSG classes, species, or the log state (frozen and thawed). The overall accuracy of PLS-DA models were above 72% for both MC and BSG sorting and above 85% for the species and log state sorting.

Finally, the Kubelka-Munk theory equations were employed to calculate several wood optical properties from visible-near-infrared reflectance spectra acquired over thin samples of quaking aspen and black spruce. The properties included absorption and scattering coefficients, transport absorption, reduced scattering, and penetration depth. The sample MC was then estimated using PLS regression method from the absorption and scattering coefficient spectra. Absorption coefficient spectra between 800 and 1800 nm can provide PLS models having an acceptable accuracy for MC estimation (R^2_{CV}=0.83 and $RMSE_{CV}$=2.32%), regardless of the species.

Acknowledgments

I would like to express my deep appreciation to my supervisor, Prof. Brigitte Leblon, for her support and guidance throughout the research. Her continued support led me to the right way. I would also like to extend my appreciation to my advisory committee members: Dr. James Burger, *BurgerMetrics Co*, Dr. Joseph Nader, Ms. Zarin Pirouz, and Mr. Kevin Groves, *FPInnovations,* for their insightful comments and encouragement and their careful review of my manuscripts and the thesis itself. Dr. James Burger suddenly passed away on 6 September 2014. He was one of the smartest and the most energetic people I know. I will be forever be thankful to him. My thesis and my manuscripts were written in memoriam of him. I would also like to express my gratitude to Dr. Satoru Tsuchikawa, *Nagoya University*, who helped me for the last manuscript.

My sincere appreciation is extended to Gorden Chow and Dr. Hui Wan from FPInnovations, to my student fellows Dr. Guillaume Hans and Clevan Lamason from UNB; to Dr. Armand LaRocque, Dean McCarthy from UNB and Kathie Phung who helped me to collect the data and finish the experiments. Without their help, I was not being able to finish my experiment at the right time. Dr. Guillaume Hans also helped me for the last manuscript.

The financial support for this research was provided through a Natural Science and Engineering Research Council of Canada (NSERC) Strategic Grant awarded to Prof. B. Leblon et al., through the New Brunswick Innovation Foundation (NBIF)

Research Assistantship Initiative Program grant awarded to Prof. B. Leblon, and through FPInnovations . I also got a scholarship from the Forest Products Society in 2014.

Last but not least, I would like to give my special thanks to my parents and siblings who always supported me spiritually throughout these years in Canada despite the distance and throughout my life in general. This thesis is dedicated to them.

Table of contents

List of tables

List of figures

List of acronyms

Acronyms	Description
2D	Two-Dimensional
ANN	Artificial Neural Network
AOTF	Acoustic Optical Tunable Filters
ASD	Analytical Spectral Devices
BD	Basic Density
BSG	Basic Specific Gravity
CCD	Charge-Coupled Device
CS	Cross Section
CV	Cross Validation
DA	Discriminant Analysis
DN	Digital Numbers
EM	Electromagnetic
EMC	Equilibrium Moisture Content
FPS	Frame Per Second
FSP	Fiber Saturation Point
H	Hydrogen
HSI	Hyperspectral Images
K-M	Kubelka-Munk
LCTF	Liquid Crystal Tunable Filters
LV	Latent Variable
MC	Moisture Content
MLR	Multiple Linear Regression
MOE	Module of Elasticity
MOR	Module of Rupture
MSC	Multiplicative Scatter Correction
NDTE	Non-Destructive Testing and Evaluation
NDT	Non-Destructive Testing
NIR	Near Infrared
NIRS	Near Infrared Spectroscopy
OLS	Ordinary Least Squares
OSB	Oriented Strand Board
PCA	Principal Component Analysis
PCR	Principal Component Regression
PLS	Partial Least Squares
R^2	Coefficient of Determination
RDP	Ratio of Performance to Deviation
RH	Relative Humidity
RMSEC	Root Mean Square Error of Calibration
RMSECV	Root Mean Square Error of Cross Validation
RMSEV	Root Mean Square Error of Validation
ROI	Region of Interest

Acronyms	Description
SNR	Signal to Noise Ratio
SNV	Standard Normal Variate
SVD	Singular Value Decomposition
T	Temperature
VIS	Visible

"We may use wood with intelligence only if we understand wood." Frank Lloyd Wright

Chapter 1. Introduction

1.1. General context

The forest products industry plays an important role in the Canada's economy. Canada has 348 million hectares of forest land, which is equal to 38% of the total land area of Canada and 9% of the world's total forests. 44% of Canada's forests are certified as sustainable forests. Canada is the second largest exporter of forest products in the world, after the USA. In 2013, Canada reached the first place in forest products trade balance with a value of C$ 19.3 billion, which is approximately C$5 billion more than the second place, Sweden. The same year, Canada's forest industries added $19.8 billion to the country's GDP. Moreover, the forest industry in Canada has contributed extensively to employment and creating jobs. More than 216,500 people were directly involved in this industry in 2013. In 2013, the Canadian forest industry achieved a profit of C$2.7 billion, which is 152% of 2012 and it was the highest obtained profit over the past eight years (Natural Resources Canada, 2015).

Softwood lumber, structural panels, newsprint, and pulp and paper products are the main wood products of the forest industry in Canada. In Canada 47% of the wood products are softwood lumber and paper-related materials. In the case of newsprint, demand has dropped by 65% since 2000 due to electronic documents being preferred to paper documents. Softwood lumber makes up 20% of Canada's forest product exports (Natural Resources Canada, 2015). The market for lumber during the last few years

slightly declined; however, it has restarted to increase because of the US market recovery (Natural Resources Canada, 2015) and it has received more attention, due to problems related to oil or other non-renewable resources.

Mechanization of the wood products processing directly affects the final product quality. It also decreases the cost of the production chain and environmental impacts by decreasing the waste and optimization in drying process. These processes require inexpensive, fast, and reliable techniques to estimate diverse wood properties. Non-destructive testing (NDT) systems have been applied extensively to achieve this objective. They allow measuring wood properties without destruction of the samples (Bucur, 2003b, Trung and Leblon, 2011). NDT systems also help mechanization process in the wood industries by providing information that may not be provided by human inspection, because they use other wavelengths than the human eyes.

1.2. Wood properties

Understanding of wood microstructure is important because it plays a major role in the wood properties estimation. Indeed, the characterization of the wood microstructure can help users to quantify the chemical, mechanical, and physical properties of wood. Wood properties have a direct relationship with the quality of final products. Thus, it is important to measure or estimate wood properties. For example, with information on the wood properties, a sophisticated grading system could be developed that would guarantee that products meet standards for an optimum cost. Estimation of wood properties would also help finding the right material to make the

right products. For example, structural lumber requires a high density and pulp and paper products require low density raw materials (Saranpaa 2003).

Depending on the scale, the sample properties can be considered homogeneous or not. The scale starts from submicroscopic scale dealing with cellulosic crystals to megascopic scale dealing with a group of trees (Bucur, 2003b). This thesis focused on the scale between microscopic and mesoscopic dealing with cells and annual rings (mm) and tree sections (10 cm), respectively.

1.2.1. Chemistry

Water, organic, and mineral constituents form wood. A small amount of extractives and inorganics can also be found in trees. In a living tree, water is the dominant component, but in dry wood, the main elements in cell walls are sugar-based polymers or carbohydrates (65-75%) such as cellulose, hemicellulose, and pectin.

A summary of wood chemical composition is presented in Table 1-1 for both hardwood and softwood species. Softwood species contain generally more lignin than hardwood species. However, it is the opposite for the amount of holocellulose, cellulose, extractive, and ash (Pereira et al., 2003, Bowyer et al., 2007, Rowell, 2013).

Table 1-1: Main wood components (in %) for hardwood and softwood (Pereira et al., 2003, Walker, 2006, Rowell, 2013).

Species	Holocellulose	Cellulose	Lignin	Extractive	Ash
Hardwood	71.7 ± 5.7	45.4 ± 3.5	23.0 ± 3.0	4 ± 3	0.5 ± 0.3
Softwood	64.5 ± 4.6	43.7 ± 2.6	28.8 ± 2.6	3 ± 2	0.3 ± 0.1

Holocellulose is the major chemical component in wood cell walls, which is the combination of cellulose (40–45%) and hemicelluloses (15-25%). These polymers contain a substantial number of hydroxyl groups that can absorb or desorb water (Pereira et al., 2003, Rowell, 2013). Lignin exists mainly in the secondary cell wall and the spaces between the cell walls, which are middle lamella. Lignin has a complex structure compared to cellulose because there is no single repeating unit in its molecular structure. It is composed of aromatic polymers of phenyl-propane units. It contains 15-20% of methoxyl (Pereira et al., 2003, Rowell, 2013). Extractives are the minor constituents of the wood cell walls. Typically, they contain organic compounds such as fatty acids, fatty alcohol, resin, terpenes, and waxes. The variations in color, smell, and durability of wood are due to extractives. Generally, heartwood has more extractives than sapwood (Pereira et al., 2003, Bowyer et al., 2007, Rowell, 2013).

In addition to all organic compounds in wood, there are some inorganic compounds also called ashes. Their contribution to forming wood is less than 0.5%. Ashes contain different elements; however, more than 80% of them consist of Ca, K, and Mg. Ashes exist in the form of oxalates, carbonates, and sulfates, or part of a carboxyl group.

1.2.2. Heterogeneity

Wood compared to other construction materials is created by nature, so there is heterogeneity in the wood chemical and physical properties from the bottom to the top of a tree, and from the bark to the pith. Furthermore, wood is vulnerable to climate, weathering, and humidity (Panshin and De Zeeuw, 1980). Species have a strong effect

on chemical and physical wood properties as well as the structure and types of cells. In this section, the main contributors to the wood heterogeneity are explained.

1.2.2.1. Cell wall

At the microscopic scale, wood is not homogeneous because of cell characteristics. Wood is a composite of different cells and each cell has two different regions: the cell wall and lumen. The lumen is void and has no structure, but the cell wall is structured in three main regions, which include: the middle lamella, the primary wall, and the secondary wall. The main components of the primary and secondary walls are pectin and lignin, respectively. The middle lamella is the space between two adjacent cells, which is lignified (Panshin and De Zeeuw, 1980, Walker, 2006, Rowell, 2013). The primary cell wall is characterized by the random orientation of the cellulose micro-fibrils. The rest of the wall, which is the secondary cell wall, is composed of three layers: S1, S2, and S3 (Barnett and Jeronimidis, 2003, Rowell, 2013).

S1 is a thin layer and has a large micro-fibril angle (50-70°). The next layer, S2, is the most important layer in the cell wall. The overall properties of wood are determined by this layer. It has lower lignin content with lower micro-fibril angles (5-30°). S3 is between S2 and lumen. It is thin, but has high micro-fibril angles (>70°), and low lignin content, which makes it suitable for water transpiration (Barnett and Jeronimidis, 2003, Rowell, 2013).

1.2.2.2. Hardwood vs. softwood

The main factor responsible for the wood heterogeneity is species. Wood species are classified as hardwood (angiosperms) and softwood (gymnosperms). Most of softwood species have needle-leaves and are evergreen, and hardwood species are usually broad-leaved and deciduous. According to the wood structure, the main difference between hardwood and softwood is the existence of vessel elements in hardwood, whereas softwoods lack these cells and have a simpler structure. Hardwoods also contain a greater degree of variability in cell types (Walker, 2006, Rowell, 2013).

Tracheids are the main cells in softwood species. Their contribution to the wood volume is more than 90%. Typically, they are 2-5 mm long, 50-60 µm wide, and have a thickness of 2-8 µm (Bowyer et al., 2007, Tsuchikawa, 2007). Tracheids are responsible for water conductivity and the mechanical properties of softwood species. They are connected together through circular board pits and they have a longitudinal overlap of 20-30% with their adjacent cells. The other type of cells in softwood are axial parenchyma, resin canal complexes, and rays (Barnett and Jeronimidis, 2003, Rowell, 2013).

Hardwood species have fibrous elements, vessel elements, axial parenchyma cells, and rays. Compared to softwood, the variation of each cell in terms of size and pattern are greater for hardwood species. Vessel elements or pores exist only in hardwood for water conduction. They have different sizes, but are much shorter than tracheids. Different patterns of pores appear in diffuse porous and ring porous species. Fibers' function in hardwood is the same as for the tracheid in softwood. They have a

shorter length and their thickness is directly related to wood density and strength, which lead to as low density such as for cottonwood or as high density such as for bulletwood (Rowell, 2013).

1.2.2.3. Stem, length, and wood age

Wood properties also change from the bark to the pith or from the bottom to the top of a tree. Juvenile wood is the region, where wood is formed at an early stage, which is closer to the pith. From the bottom to the top of the tree, the percentage of juvenile wood gradually increases. (Walker, 2006, Bowyer et al., 2007, Rowell, 2013). Juvenile wood has a high micro-fibril angle in S2 layer; thus juvenile wood has a tendency to have a high longitudinal shrinkage (Bowyer et al., 2007, Rowell, 2013). The percentage of juvenile wood is linked to the quality of wood because in juvenile wood, the cell length is 20-30% shorter than in mature wood and cell walls are thinner, as shown by the tracheid dimensions for both juvenile and mature wood of Norway spruce (*Picea abies*) of Table 1-2 (Brandstrom, 2001). Short cells and thin cell walls are associated with a lower density and a lower strength.

Table 1-2: Tracheid dimensions for both juvenile and mature wood of Norway spruce (Brandstrom, 2001).

Tracheid dimension	**Juvenile wood**	**Mature wood**
Tracheid length (mm)	1.28–2.70	2.80–4.29
Cell wall thickness (μm)	0.80–4.60	2.10–7.53

Annual rings also generate wood properties variations and mainly trigger density variations. They are built as a function of the temperature and water availability. In

summer, when water is abundant, earlywood is built, but in the winter season, latewood is formed, which is thicker and denser (Table 1-3). Each spring, the new ring forms, but sometimes, false growth rings are built depending on the temperature (Bowyer et al., 2007). The seasonal effect makes the transition from earlywood to latewood being generally sharp for non-tropical species. By contrast, this transition is gradual in tropical species because there is no sharp differences between seasons. The size of cell walls in growth rings is generally constant, but the lamella from earlywood to latewood gradually decrease, and sudden and distinct changes in lamella across the rings can be seen (Rowell, 2013).

Table 1-3: Tracheid wall thickness of Norway spruce latewood and earlywood (Brandstrom, 2001).

	Earlywood (µm)	**Latewood (µm)**
Radial	3.52	6.23
Tangential	2.9	4.69

Wood properties are also different in the heartwood and sapwood regions, which have different functions. As trees grow up, some parts of the tree gradually become non-functional in conducting food and water. This region is the heartwood, which typically has a darker color, close to pith, and is surrounded by sapwood. Sapwood is conducting water with biochemicals, which are mainly starch and lipids. Heartwood also acts as storage of some biochemicals such as the extractives. Most of the sapwood cells are alive, but the only alive cells in heartwood are parenchyma that are used to store or to produce extractives (Rowell, 2013). During the maturation process, the transformation of sapwood to heartwood occurs. It has been shown that the formation of heartwood is

independent of growth rate and tree size (Bowyer et al., 2007). The heartwood can often be detected visually by its dark color because of the presence of extractives and/or by measuring chemical components such as, for example, pinosylvin content in Scots pine (Bergstrom, 2003).

1.2.2.4. Compression Wood and Knots

Variations in wood properties also occur because of wind and gravity, which lead to compression in softwood or tension in hardwood. Compression or tension wood has a density up to 40% greater than a normal wood and is not desirable. The cell structures in compression or tension wood have just S1 and S2 layers with a higher micro-fibril angle than the normal wood (Walker, 2006, Bowyer et al., 2007). It is important to avoid compression wood in lumber products because it causes longitudinal shrinkage and decreases the strength of the products.

Knots also increase the heterogeneity in wood. They are an imperfection in wood products, which appears as a circular dark shape. In softwood, the acceptable average volume of knots is 0.5-2.0%. However, this small amount has a drastic impact on wood properties and downgrades the quality of lumber. Knot density is more than 1000 kg/m^3, which can be 2-3 times of the normal wood's density. Knot chemical properties are also different. The amount of resin in knots increases by 30% (Walker, 2006, Bowyer et al., 2007).

1.2.3. Anisotropy

Wood is an anisotropic material. Indeed, each wood direction has different properties, while other materials such as metal, plastic, and glass can be isotropic. In a tree, three sections can therefore be defined: cross section or transversal, tangential, and radial. In the transversal or cross section, the cell walls, the annual rings, heartwood, and sapwood zones are appearing. This surface is perpendicular to the fiber orientation. By contrast, radial or tangential sections are characterized by surfaces parallel to the grain orientation. The radial direction is from pith to bark and the tangential direction is from the bottom to the top of a tree (Bowyer et al., 2007, Rowell, 2013).

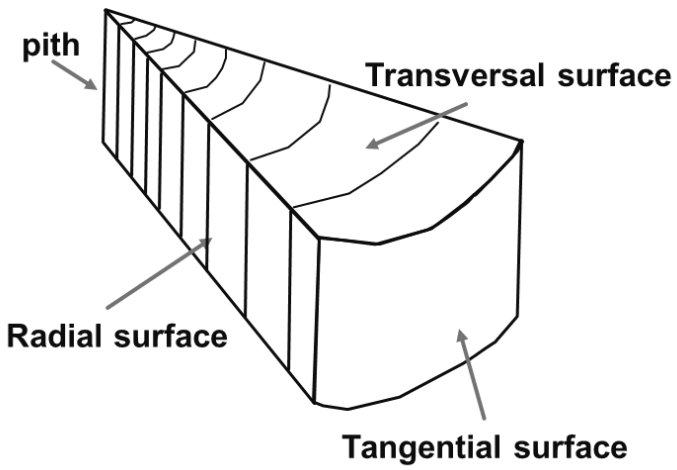

Figure 1-1: Cross section or transversal, tangential, and radial sections of a tree trunk.

These sections differ by both their physical properties, which include morphology and surface roughness and their chemical properties, which include their permeability and molecular composition (Rowell, 2013). The surface roughness of radial and tangential sections are similar, but are different than those of cross sections because of cell orientation. Wood anisotropy is also responsible for mechanical

properties (Forest Products Laboratory, 2010) and light absorption variations. In transversal sections, light can penetrate more deeply and absorbed more accordingly because this section contains the tracheid cross section (Fujimoto et al., 2008). In Figure 1-2, the mean and standard deviations of 1000 absorption spectra between 950 and 1650 nm for a black spruce sample having a moisture content of 11.5% and a basic specific gravity of 0.427 are shown as a function of the sections. The spectra were collected by a hyperspectral imaging system. This figure shows that the absorbance spectrum of the radial and tangential sections has a lower level and variation than the absorbance spectrum of the transversal section. The same pattern was observed with other species for instance quaking aspen and balsam poplar.

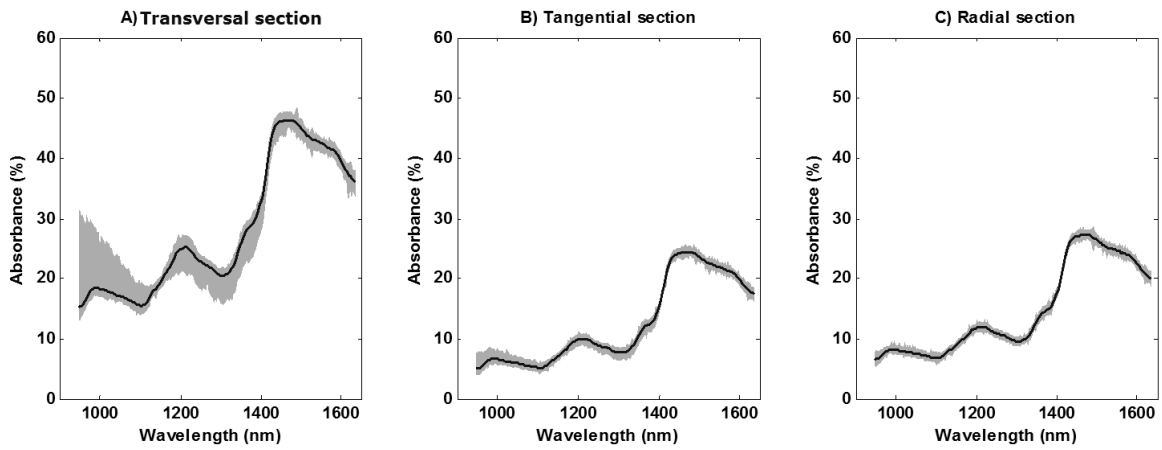

Figure 1-2: Mean and two standard deviations of absorbance spectra for (A) the transversal section (B) the tangential section, and (C) the radial section in the case of a black spruce sample (MC= 11.5%, BSG= 0.427)

1.2.4. Hygroscopicity

Wood is a hygroscopic material, because it has an ability to absorb or desorb water from the environment. Wood can exchange water with its environment until an

equilibrium moisture content (EMC) is reached. There is a non-linear relationship between EMC and the relative humidity (RH) and temperature (T). This relationship is represented by a function called *sorption isotherm function* (Bowyer et al., 2007, Forest Products Laboratory, 2010). Wood EMC decreases when the temperature increases or when the relative humidity decreases. First, the water inside the lumen, called free water, is lost following by the cell wall water, called bound water. Fiber saturation point (FSP) is reached when there is no more free water in wood. For most species, FSP is around 30%. Below this point, more energy is required to dry wood because adsorption forces (hydrogen bonding) hold water molecules. Wood starts to shrink when bound water is lost. Conversely, when cell walls absorb water, wood starts to swell. Shrinkage and swelling can be defined for each direction of wood as well as according to the wood volume. The longitudinal shrinkage is negligible, which makes wood a suitable material for construction projects. The radial shrinkage is between 2% and 6%, while the tangential shrinkage is 1.5-2 times greater than the radial shrinkage. Generally, the shrinkage varies according to the sample size, wood density, and the rate of drying (Bowyer et al., 2007, Forest Products Laboratory, 2010).

1.2.5. Moisture content

Water in wood has significant effects on all wood properties including its physical and mechanical properties. Thus, interactions between wood and water influence all steps of the production chain and the final product quality. For example, moisture content (MC) variations in wood cause vicissitude and unequal shrinkage. It also increases the cost of transportation and decreases the amount of thermal energy by

not allowing hydrocarbons to burn (Denig et al., 2000, Bowyer et al., 2007, Forest Products Laboratory, 2010). Thus, it is important to estimate MC in all steps of the production chain.

In the wood products industry, the amount of water is expressed as the percentage of the oven-dry weight by:

$$MC\ (\%) = \frac{M_g - M_{od}}{M_{od}} \times 100$$

Equation 1.1

where M_g (kg) is the mass of the moist (green) wood sample and M_{od} (kg) is the mass of the oven-dry wood. The most accurate, reliable method to measure MC is to weight the wet sample and then dry it in an oven at 103 ± 2ºC to remove all water. The oven-dried sample is then re-weighted. More information about this process can be found in *method A* of ASTM-D4442–07 (2009). However, this approach is destructive and it takes time. Moreover, volatile constituents are removed during the drying process, which causes small errors in MC calculation (Skaar, 1988). Some other spot measurement tools such as electric moisture meters provide a quick estimation of MC, but their accuracy is low for samples with MC above 25%. They mainly include resistance (pin type) or dielectric (flat plate) meters (Skaar, 1988).

In some applications, the wood MC is defined based on the percentage of total weight, which is the weight of green or wet wood (Equation 1.2). This definition is suitable for the fuel and the pulp and paper industries (Bowyer et al., 2007):

$$MC_w\ (\%) = \frac{M_g - M_{od}}{M_g} \times 100$$

Equation 1.2

There are many factors contributing to MC variations. In a living tree, the water weight can be equal or greater than the dry wood substance weight. Moreover, the water distribution is not homogeneous in tree trunks. The green MC of sapwood is higher in hardwood than in softwood species (Panshin and De Zeeuw, 1980, Bowyer et al., 2007, Forest Products Laboratory, 2010). When a tree is harvested, wood MC gradually starts to decrease. During the drying process, regardless of the species, the water moves from a high concentration zone to a lower concentration by diffusion. Such diffusion produces an increase in the MC variation in the sample. Impermeable regions also generate MC variations. For most species, the sapwood is permeable, so its drying rate is higher than impermeable regions such as heartwood. Also, some species, such as fir and aspen, contain wet-wood or wet pockets. These impermeable zones decrease the drying rate and require careful attention during the drying process (Kroll et al., 1992, Cai, 2006, Bowyer et al., 2007, Watanabe et al., 2012b).

1.2.6. Density and Basic specific gravity

Density or specific gravity is one of the most important wood physical properties. Many of wood mechanical properties, heat transmission, diffusion coefficient, and pulp yield properties are directly related to the density. Other properties such as the wood anatomy, shrinkage, and swelling are also a function of the density. Wood with higher density has more cell walls and/or has a higher proportion of

latewood. The density of cell walls is 1520 kg/m^3 (Walker, 2006, Bowyer et al., 2007), so in a piece of quaking aspen with a density of 399 kg/m^3, approximately 74% of the volume is void or lumen. Knowledge of density is also required to estimate the modulus of rupture (MOR) (Wang et al., 2000, Yin et al., 2010) and the modulus of elasticity (MOE) (Barnett and Jeronimidis, 2003, Mora et al., 2009) from ultrasonic or acoustics measurements. Density monitoring can also be used for early detection of wood decay. Indeed, decayed wood is less dense than sound wood because cellulose and lignin in the cell walls are consumed or modified by fungal activities (Kelley et al., 2002, Stirling et al., 2007). Wood density can help to detect compression wood, which is denser than the normal wood (Diaz-Vaz et al., 2009).

Wood density can be represented using three variables. The first one is the density (*sensu stricto*) at a specific MC (ρ_{MC}), which is the ratio between the mass and the volume of the sample at a given moisture content (Forest Products Laboratory, 2010, Williamson and Wiemann, 2010):

$$\rho_{MC} = \frac{W_{MC}}{V_{MC}}$$

Equation 1.3

where:

- ρ_{MC} is the density of the sample at a given moisture content (kg/m^3)
- W_{MC} is the mass of the sample at a given MC (kg)
- V_{MC} is the volume of the sample at a given MC (m^3)

Usually, ρ_{MC} is expressed either for air-dry, oven-dry, or green conditions. The oven-dry wood density is mainly related to cellulose, hemicellulose, lignin, and the proportion of void space in the wood.

Another variable to express the wood density is the basic density (*BD*), which is defined as the ratio between the mass of an oven-dry sample to the volume of the same sample when it is green (Walker, 2006, Williamson and Wiemann, 2010, Watanabe et al., 2012a)

$$BD = \frac{W_{OD}}{V_{Green}}$$

Equation 1.4

where:

- W_{OD} is the weight of the oven-dry sample (kg)
- V_{Green} is the volume of the sample when it is green (m^3)

According to Williamson and Wiemann (2010), the wood volume does not change above the fiber saturation point (FSP) (MC_{FSP} around 30%). V_{Green} can thus be considered to be equivalent to the saturation volume that is measured following *Method B* of ASTM-D2395–07a (2009) after completely soaking the sample in water.

The third variable is the basic specific gravity (*BSG*), which is the ratio between the basic density (BD) and the water density (Forest Products Laboratory, 2010, Williamson and Wiemann, 2010).

$$BSG = \frac{BD}{\rho_{water}}$$

Equation 1.5

where:

- BD = basic density of the sample (kg/m^3)
- ρ_{water} = water density (kg/m^3) which is equal to 1000 kg/m^3 or to 1 g/cm^3 at 4°C and under normal atmospheric pressure

BD or BSG is the most useful description of wood density, because W_{OD} does not depend on the sample MC and because V_{Green} is constant. BSG was shown to be related to cell diameters, cell lengths, cell wall thickness, the proportion of the different cell types within the tree, and the presence of extractives (Panshin and De Zeeuw, 1980, Barnett and Jeronimidis, 2003).

It is important to know the wood density variability since it contains information about strength variability. Wood density varies according to many factors such as species, geographic location, site conditions, location in the trunk of a tree, and genetic sources. In many species, the basis of the tree tends to have a higher density than the high part of the tree. Generally, in softwood, the density decreases with increasing tree height and increases with increasing distance from the pith (Barnett and Jeronimidis, 2003, Bowyer et al., 2007). In fast growing species, the proportion of cell walls and lumen changes and thus affects the density. In severe conditions, compression or tension wood, which has a higher density, may occur (Barnett and Jeronimidis, 2003, Hein et al., 2009).

1.3. Non-destructive testing of wood properties

Non-destructive testing (NDT) is a science to identify physical, mechanical, and/or chemical properties of materials without changing their end-use application and retaining sample for further analysis (Bucur, 2003a). Most NDT techniques do not need sample preparation or do not require dangerous chemicals. Moreover, they can be fast and repeatable over a sample. The NDT techniques have been employed in the wood product industry such as for sorting and grading lumber (Ross and Pellerin, 1994).

NDT applied to wood are very different than those applied to homogeneous isotropic materials (Ross and Pellerin, 1994), because of the heterogeneous nature of the material. Wood property estimation uncertainties are triggered by wood's biological nature or degradation because of the environment (Bucur, 2003b).

In wood NDT applications, the radiation storage or attenuation due to the wood properties is measured. Therefore, mathematical and/or statistical methods have to be employed to relate the measured properties of wood to the recorded radiation. NDT techniques used for wood characterization are classified according to the properties investigated or to the wavelength of irradiation used by the sensor (Bucur, 2003a, Hans, 2015). They can also be classified as non-imaging systems, which just provide one measurement, or as imaging systems, which give spatial information about the properties. In this thesis, we tested a hyperspectral near-infrared (NIR) imaging system to produce 2D images of MC and density and a visible-NIR spot spectrometer to measure optical properties of wood.

In physics, radiation propagation is described in terms of waves or particles. From the wave point of view, radiation is an oscillating electromagnetic (EM) field with a continuous range of energies or frequencies. An EM wave consists of two mutually perpendicular electric and magnetic fields, which are perpendicular to the propagation direction. From the particle point of view, radiation consists of packets of energy called photons (Stuart, 2004). The range of frequencies starts from radio waves (10^4 Hz) to gamma ray (10^{20} Hz).

The energy of each region of the EM spectrum is related to the wavelength or frequency of the EM radiation and has been parametrized by the Maxwell's theory of electro- and magneto-dynamics. The energy can be calculated by the following equation (Stuart, 2004):

$$E_q = hf = hc/\lambda$$

Equation 1.6

where c is the speed of light (3×10^8 m/s), λ is the wavelength (m) of the electromagnetic radiation, f is the frequency of the electromagnetic radiation (Hz), and h is Planck's constant (6.626×10^{-34} J.s or 4.135×10^{-15} eV.s).

The most common ranges of EM radiation used in NDT sensors that are commercially available for industrial applications are X-rays, visible, infrared, thermal infrared, and microwave. The infrared range (0.7 – 1000 µm) is divided into several parts: near-infrared (NIR) (700 – 2500 nm), mid infrared (MIR) (3 – 30 µm), and far

infrared (FIR) (30 – 1000 µm). In this thesis, the NIR wavelengths were used to estimate MC, BSG, and optical properties of various wood samples.

1.3.1. X-ray

X-ray-based methods measure the attenuation coefficient of the corresponding EM radiation. This parameter can be related to wood chemical and physical properties. Indeed, X-ray radiations penetrate through the wood and X-ray sensors measure the corresponding attenuation coefficient that can be related to wood chemistry, moisture content or density (Bucur, 2003a). Bucur (2003a 2003b) and Wei et al. (2011) reviewed studies that uses X-ray images acquired over wood samples to measure density variations, MC variations for example in wood drying processes, for inspecting logs and lumber defects, for determining stability of wooden building elements, in preservation of wood monuments and fine arts, for growth rate assessment, for pollution effects on trees, and in dendrochronology sudies.

The first studies of testing X-ray sensors over wood, used systems that were designed for medical or airport applications and were not suitable for the wood industry (Wei et al. 2011). More recently, commercial X-ray systems were developed for the wood industry (Table 1-4). They are mainly multiple view scanners. Only one is a true computer tomography (CT) scanner. Images acquired with these scanners allow the 3D reconstruction of the wood sample, such as it is shown in Wei et al. (2009), because they provide information on the wood sample from a multiple view angle.

Table 1-4: Commercial X-ray sensor applied to wood products.

Wood product	Type of X-ray scanner	Scanner name	Conveyor speed (m/min)	Company	Website
Log	Multiple views	Wood-X	N/A	Bintec Oy	http://www.bintec.fi
		OPMES AX1	200	Inray Oy Ltd	http://www.inray.fi
		Logeye300	300	MiCROTEC GmbH	http://microtec.eu
		RS-XRay	200(*)	Rema Control AB	http://www.remasawco.se
	Computer tomography (CT)	CT Log	180	MiCROTEC GmbH	http://microtec.eu
Lumber	Multiple views	X-Scan	210	Luxscan	http://www.luxscan.com
		Goldeneye 300/500/600/900	100	MiCROTEC GmbH	http://microtec.eu

(*) pieces/min

All the devices listed in Table 1-4 are X-ray systems that can measure wood properties at a large scale (timber) (Bucur, 2003a, Wei et al., 2011). However, there is one high resolution X-ray scanner that is embedded in the SilviScan system that was designed to measure several wood properties at a micro scale (cell size) including, density, stiffness, micro-fibril angle, and tracheid diameter (Evans, 1994, Shelbourne et al., 1997, Evans and Ilic, 2001). For all the X-ray systems, there are some issues in using them operationally, because of health and safety concerns and costs (Wei et al., 2011).

1.3.2. Visible and NIR spectroscopy

Visible light (450-750 nm) and NIR (750-2500 nm) sensors provide a wide range of superficial information about the wood sample. Conventional visible color cameras are already used for grading and sorting, and for defect detection (Brunner et al., 1990), classification of wood surface features (Butler et al., 2002), species identification (Gigac and Fiserova, 2010), and wood quality assessment of the wood surface features (Ruz et

al., 2005). However, visible cameras show limitations as the result depends on the surface wetness as well as on sample aging. Indeed, weathering, aging, and changes in MC alter the wood surface color (Gigac and Fiserova, 2010).

Also visible cameras have a limited used for measuring some wood chemical and physical properties, as the main absorption bands of some major wood chemicals are located in the near-infrared region. These bands are related to overtones and combinations of molecular vibrations as described in Schwanninger et al. (2011) and in Leblon et al. (2013). Among all bonds, NIR spectra are more sensitive to hydrogen bonding such as CH, NH, and OH. This fact makes NIR spectra suitable for determining water content using quantitative or discriminant analysis. However, combinations of fundamental overtones are not very strong and in most cases, they are overlapped. These issues make the NIR spectra very complex to analyze, but NIR tools have a great potential as a versatile and attractive technique for in-line, on-line, or off-line process monitoring because they are fast and do not need sample preparation as much as other systems (So et al., 2004, Burns and Ciurczak, 2007).

1.3.3. Thermal infrared (TIR)

Thermal infrared systems operate in the 3 to 12 µm wavelength range and measure the surface temperature image of the sample. They are two kinds of TIR systems: active and passive sensors. Active sensors have their own heating source, while passive sensors use an external source of heating. The main disadvantage of active thermal infrared thermal sensors is that they can induce damage in the sample and the main disadvantage of passive sensors is the difficulty of capturing thermal images of

wood when the temperature contrast is too low. Both systems also need a fast recording system to capture the image (Bucur, 2003a).

TIR systems were employed for the detection of singularities and defects in wood (Lopez et al., 2014). Passive infrared techniques were used for detecting cavities (Catena et al., 1990), detection of knots and voids in lumber, because internal defects change the thermodynamic behavior of the wood and surface temperature (Burcham et al., 2012, Lopez et al., 2014).

1.3.4. Microwave and radio frequency (RF)

Microwave techniques are based on the determination of the dielectric properties of the material. Wood dielectric properties are directly related to its MC, density, and fiber direction (Ramasamy and Moghtaderi, 2010). Microwave signals can penetrate through the wood and can provide in-depth information, which may not be seen with other systems. However, such sensors are sensitive to vibrations which disturb the polarization of the microwave signal (Bucur, 2003a). Microwave systems have been used for internal defects and grain direction as well as to assess structural discontinuities of logs (Bucur, 2003a). It also has been tested to estimate MC and BSG of different wood species (Moschler and Hanson, 2008, Hans, 2015, 2015c, 2015d, Hans et al., 2015b) and knot detection (Baradit et al., 2009).

1.3.5. Acoustic

Ultrasonic techniques record ultrasonic waves reflected or transmitted from the sample. As in the case of X-rays, ultrasonic images can be acquired by translation of

detectors around the sample at different angles and by measuring the intensity of reflected or transmitted waves. However, unlike X-ray, ultrasonic rays do not travel in a straight line in heterogeneous samples. Due to this reason, ultrasonic systems require an accurate, fast reconstruction algorithm to achieve useful signal from a sample. These systems are capable of delivering high resolution images for small samples, standing trees, and wood-base composites. Ultrasonic techniques have been used extensively for decay detection in both sample and standing trees as well as detection of knots, defect, and compression wood (Bucur, 2003a). They were also employed to estimate modulus of rupture (MOR) and modulus of elasticity (MOE) of wood samples. However, wood density at specific MC is required to find the relationship between acoustic measurements and wood mechanical properties (Wang et al., 2000, Yin et al., 2010).

1.4. NIR spectroscopy

1.4.1. Principle

When an EM radiation interacts with a molecule, a quantum of energy is emitted or absorbed. The energy of the quantum is equal to the energy between two adjacent energy levels of the molecule. However, illuminating a sample with near infrared radiations (750-2500 nm) induce vibrational and rotational movements of its molecules. For example, for a water molecule (H_2O), there are 3 translational, 2 rotational, and 3 vibrational degrees of freedom associated to fundamental vibrational frequencies (Stuart, 2004).

In a normal mode, all atoms move in a phase with the same frequency, but with different amplitudes. In addition to the fundamental vibration mode, there are first, second, and so on overtones and combinations of different vibrational transitions. The NIR region have absorption bands that are related to overtones and combination vibrations. The intensity of overtone absorption bands is a function of the anharmonicity constant (Stuart, 2004, Burns and Ciurczak, 2007). For example, H-based stretching has the largest anharmonicity constant and therefore high intensity of overtone absorption bands can be seen. As a result, it dominates the NIR region (Burns and Ciurczak, 2007).

Reflectance is the most common method for capturing NIR spectra. In the reflectance mode, diffuse and specular reflection happen (Figure 1-3). Almost 10-15% of the reflected light is made of specular reflectance. This reflectance may not be really useful because specular photons have not penetrated enough, and they do not carry chemical information of the sample (Boldrini et al., 2012). Diffuse reflectances (85-90% of the reflected light) contain the signature of the absorption bands. For example, in the NIR range, water OH bands exhibit five absorption bands (760, 970, 1190, 1450, 1940 nm) (Burns and Ciurczak, 2007, Schwanninger et al., 2011), which make NIR spectroscopy a promising technique to determine and/or quantify moisture content.

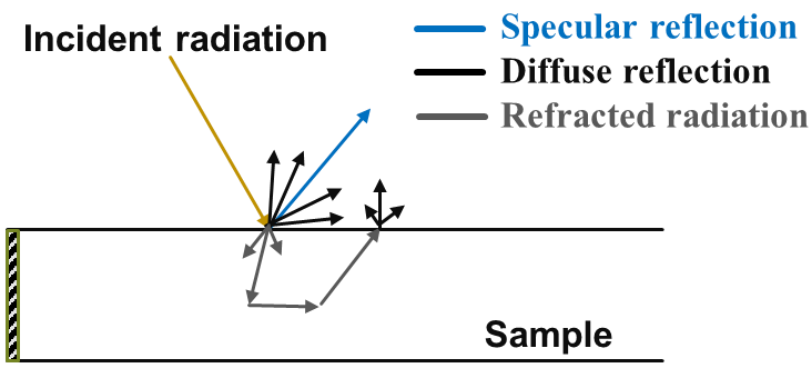

Figure 1-3: Specular and diffuse reflection mode

By defining the ratio of the reflected radiation from the sample to the total incident radiation the reflectance (R_λ) can be calculated by:

$$R_\lambda = I/I_0$$

Equation 1.7

where I is the reflected light from the sample and I_0 is the total incident radiation.

The absorbance (A_λ) is then given by:

$$A_\lambda = \mathrm{Log}(1/R_\lambda)$$

Equation 1.8

The amount of a substance can be quantified using the absorbance because A_λ has a relationship to its concentration (c), the molar absorption coefficient (ε), and path length of the radiation (δ) (Danson et al., 1992, Stuart, 2004, Burger, 2006)

$$A_{\lambda} = c.\varepsilon.\delta$$

Equation 1.9

The interpretation of NIR spectra is challenging, because absorption bands can be broad and occurrence of overlapping between the absorption bands can occur. In the NIR region, there are only first and second overtones (and combination of them) whatever the compound. The intensity for the overtones is quite weak, as it is about 0.01 and 0.001 of the fundamental absorption intensity (Stuart, 2004, Workman and Weyer, 2012). In addition, the NIR spectra are affected by the sample temperature. For example, an increasing temperature will lead to a lower degree of hydrogen bonding in the compounds that make the sample and the related absorption bands will shift toward lower wavelengths (Stuart, 2004, Burns and Ciurczak, 2007, Workman and Weyer, 2012). Despite these complexities in analyzing NIR spectra, chemometric techniques can be employed to extract useful information from the NIR spectra (Burns and Ciurczak, 2007).

1.4.2. Chemometrics

Chemometrics can be defined as the application of statistical methods to the analysis of experimental data in chemistry. It can be used for qualitative, quantitative, and discriminant analyses of NIR spectra (Burns and Ciurczak, 2007). For quantitative analysis, Equation 1.9 can be simplified as:

$$c = A*b$$

Equation 1.10

where $b = (\varepsilon\delta)^{-1}$. This equation can also be extended to:

$$\mathbf{Y} = \mathbf{Xb} + \mathbf{e}$$

Equation 1.11

where **Y** is the concentration or response variable, **X** is the absorbance or explanatory variable, **b** is the coefficient which contains the information about the concentration and path length of the radiation, and **e** represents the error. There are several methods to find **b** of Equation 1.11, such as ordinary least squares (OLS), artificial neural network, principal component regression (PCR), and partial least squares (PLS) regression. In this thesis, we employed PLS and PLS discriminant analysis (PLS-DA) to quantify MC and BSG of wood and to discriminate wood species as a function of these wood properties. We also used principal component analysis (PCA) to find outliers and abnormal spectra in the image analysis steps.

PLS regression uses two matrices, predictor or explanatory (**X**) and response (**Y**) variables, to build a model. The PLS algorithm is mainly employed for quantitative analysis, as the range of **Y** is continuous. PLS can be applied to collinear and noisy data. It is also useful, when the number of predictive variables is tremendous. Moreover, both **X** and **Y** variables do not have to follow a specific distribution function. These characteristics make the PLS algorithm the best approach to analyze NIR spectra (Martens and Naes, 1989, Wold et al., 2001).

In PLS, a new set of variables, called X-scores (**T**), is defined and is used for the modeling of both, **X** and **Y**. This variable is a good summary of **X** and can be multiplied by the loading matrix, **P**, to form **X**. Compared to multiple linear regression (MLR) or PCR, PLS finds the best part of **X** correlated to **Y**. The rest of **X** may contain noises and/or variations non-related to **Y**. This ability of PLS provides a better accuracy than other methods (Martens and Naes, 1989, Wold et al., 2001).

In PLS modeling, it is essential to determine the optimal number of latent variables (LV). Using a high number or a low number of LV increases the risk of over-fitting or under-fitting and decrease the predicting power of the model (Gowen et al., 2011). The most reliable approach to define the optimum number of LV is the cross-validation (CV) method. In this approach, the data are divided into different groups. A PLS model is calibrated using all groups with the exception of one. The latter group is used for prediction purposes and calculate the RMSE (root mean square differences between actual and predicted **Y**) of the cross validation. This process is repeated for different number of LV. The optimal number of LV is associated to the first local minimum RMSE (Wold et al., 2001). For example, in Figure 1-4, the root mean square error of cross validation ($RMSE_{cv}$) for different LV is presented for a PLS model that estimates subalpine fir moisture content. The optimal number of latent variables is 6.

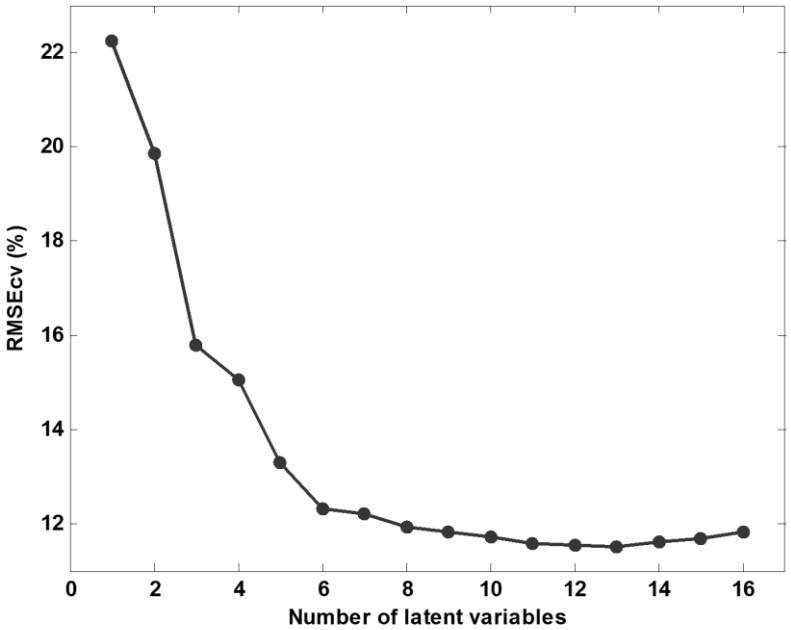

Figure 1-4: Determination of the optimal number of PLS latent variables (LV) as a function of the RMSECV. The optimal number of PLS latent variables is 6.

PLS-DA is a special case of PLS in which the **Y** variable is discrete or can be presented in a discrete format so that each class is represented by a number (dummy variable). This method is suitable for classification and qualification purposes as well as for grouping samples with similar characteristics (Szymanska et al., 2012). As in PLS, the optimal number of LV can be defined by using a cross-validation method.

1.4.3. Spectrum transformation

Before using NIR spectra for quantitative (PLS) or discriminant analysis (PLS-DA), unwanted effects have to be removed from the spectra because they are not related to the response variable (**Y**). For solid samples like wood, undesirable effects can be caused by inhomogeneity in path lengths, radiation scattering, and random or

instrumental noise (Wold et al., 1998). Spectra preprocessing can help to improve the robustness and accuracy of the models.

Many transformations for preprocessing spectra have been proposed for example: multiplicative scatter correction (MSC) (Isaksson and Naes, 1988, Heigl et al., 2007), extended multiplicative scatter correction (EMSC) (Martens and Stark, 1991), standard normal variate (SNV) (Barnes et al., 1989), and 1st and 2nd derivative transformations (Demetriades-Shah et al., 1990). These techniques can reduce physical interferences in NIR spectra, while maintaining the chemical information.

MSC assumes that the scattering coefficients are independent from the wavelengths and can be separated from the chemical information (Burger et al., 1997, Buddenbaum and Steffens, 2012). This transformation removes both additive and multiplicative correction effects by fitting each spectrum to an ideal spectrum that is the average of all sample spectra through a least squares calculation. In SNV, spectra are first centered and then scaled according to their mean and standard deviation, respectively. It was showed, that SNV has a linear relationship to MSC and both transformations provide a similar accuracy in quantification analysis (Dhanoa et al., 1994). In 1st and 2nd derivative spectra, it is assumed that the scattering will be removed by subtracting the reflectance from neighbors' wavelength reflectance. Derivative analysis of spectra has been proposed mainly in analytical chemistry to suppress background signals and to resolve overlapping spectral absorption bands (Demetriades-Shah et al., 1990, Danson et al., 1992). With derivative analysis, the amount of noise in the spectra also increases, which is the main disadvantage of this method. In all of these

transformations, a constant scattering coefficient over all wavelengths has been expected (Burger et al., 1997). It was also shown that these transformations may remove a small portion of chemical information from NIR spectra (Martens et al., 2003).

1.4.4. Wood properties prediction

NIR spectroscopy has been used in food and agricultural industry since the 1950's (Workman and Weyer, 2007). This technique has been quickly extended to other products, such as forest products. Compared to the traditional method such as oven-dry method, spectroscopy has the following advantages (Salzer and Siesler, 2009):

- It is quick and reliable
- It does not need sample preparation
- It extracts more information from single recorded spectra
- It is a non-destructive technique
- It can be used by unskilled personnel

The most useful wavelength NIR range for quantitative and discriminant analysis is 900-2500 nm, because below 900 nm the absorption bands are weak. NIR spectroscopy has been developed for non-destructive measurements of wood physical properties, including estimation of moisture content and basic specific gravity (Thygesen, 1994, Thygesen and Lundqvist, 2000b, Defo et al., 2007, Mora et al., 2008, Russ et al., 2009, Cooper et al., 2011, Mora et al., 2011a, Xu et al., 2011, Inagaki et al., 2012, Abasolo et al., 2013, Hans et al., 2013, Haddadi et al., 2015a, 2015b, 2015c, Hans et al., 2015a), stiffness and strength (Fujimoto et al., 2007), modulus of elasticity (MOE)

and modulus of rupture (MOR) (Gindl et al., 2001, Fujimoto et al., 2008, Xu et al., 2011), fiber length (Inagaki et al., 2012), shrinkage (Hein, 2012), micro-fibril angle (Meder et al., 2010, Hein, 2012), compression strength (Hoffmeyer and Pedersen, 1995), species identification (Tsuchikawa et al., 2003, Adedipe et al., 2008, Haartveit and Flæte, 2008, Russ et al., 2009, Cooper et al., 2011, Hans et al., 2015a), heartwood and sapwood segregation (Bergstrom, 2003, Hans et al., 2015a), juvenile and mature wood classification (Lestander et al., 2008) as well as estimation of chemical properties (So et al., 2004, Alves et al., 2006, Poke and Raymond, 2006, Sandberg and Sterley, 2009, Meder et al., 2010, Downes et al., 2011, Sheng et al., 2011).

In NIR spectroscopy studies for wood MC or BSG estimation, different factors which generate variations of these properties have been taken into account in the modeling approach such as temperature (Thygesen and Lundqvist, 2000b, Hans et al., 2013, 2015a), wood type (heartwood or sapwood) (Karttunen et al., 2008, Hans et al., 2015a), wood anisotropy (Schimleck et al., 2005, Defo et al., 2007, Fujimoto et al., 2008), and wavelength range effect (Adedipe and Dawson-Andoh, 2008). In the BSG modeling, the effect of MC has also been considered because it influences the spectra (Via et al., 2003, Hans et al., 2013, Haddadi et al., 2015c, Hans et al., 2015a).

Most of the aforementioned NIR spectroscopy studies used single spot measurement systems. The spectra obtained from these single spot measurements are then related to bulk MC or BSG. This approach does not represent well the spatial variability of the wood properties in the sample because biological materials like wood

are heterogeneous. However, it is important to monitor such variability in several wood manufacturing processes (Olson and Arganbright, 1977, Panshin and De Zeeuw, 1980).

By contrast, imaging systems can provide spatial information about the entire surface of the sample, which make them useful sensors for at-line or on-line process monitoring (Lindstrom et al., 2014). Combining imaging systems with NIR spectroscopy allows benefiting from both technologies at the same time. It will provide a distribution map of the wood properties of a sample, which would allow better process optimization along the production chain. More explanation about NIR imaging systems will be provided in Section 1.5.

1.4.5. Kubelka-Munk theory and optical properties

All the aforementioned studies used statistical analysis to relate the wood properties to the NIR measurements. An alternative would be to use a more deterministic approach based on physical principles. Tsuchikawa et al. (1996) developed an optical model, which explicitly describes the physical interactions between wood properties and NIR spectra. Wood is modeled as an aggregate of semi-infinite inclined square tubes representing the tracheids with a membrane having a certain thickness. The model also assumes that the incident radiation is made of parallel beams.

For each wavelength λ, the diffuse reflectance $R_\lambda(d)$ and transmittance $T_\lambda(d)$ can be computed by the Kubelka-Munk (K-M) theory equations. In the K-M theory, the propagation of radiation in a medium that absorbs, emits, and scatters is described in two-fluxes approach (Kortum, 1969). The theory has the following assumptions

(Olinger and Griffiths, 1988, Cheong et al., 1990): (i) the radiation propagates in the sample in a two flux which are opposite to each other; (ii) the illumination over the sample is monochromatic, (iii) the scattered radiation distribution is isotropic or is specular; (iv) the sample is made of particles that are randomly distributed in the different sample layers and that have a size much smaller than the layer thickness and the wavelength of the incident radiation; and (v) the surface of the sample is much greater than its thickness.

According to this theory, when the thickness of a sample (*d*) increases, its reflectance increases, but its transmittance decreases. Thereby, for each wavelength λ, $R_\lambda(d)$ and $T_\lambda(d)$ are expressed as a function of the sample thickness *d*, the scattering (S_λ), and absorption (K_λ) coefficients by the following equations (Kortum, 1969):

$$T_\lambda(d) = \frac{\beta}{\alpha \sinh X + \beta \cosh X}$$

$$R_\lambda(d) = \frac{\sinh X}{\alpha \sinh X + \beta \cosh X}$$

Equation 1.12

where

$$X = \beta . S_{\lambda} . d$$

$$\alpha = \frac{K_{\lambda}}{S_{\lambda}} + 1$$

$$\beta = \sqrt{\alpha^2 - 1}$$

Equation 1.13

where d is the sample thickness (mm), $T_{\lambda}(d)$ is the transmittance of the sample having a thickness d, $R_{\lambda}(d)$ is the reflectance of the sample having a thickness d, K_{λ} is the absorption coefficient (mm^{-1}), and S_{λ} is the scattering coefficient (mm^{-1}). $T_{\lambda}(d)$, $R_{\lambda}(d)$, K_{λ}, and S_{λ} depend on the wavelength (λ).

Because wood does not easily transmit radiations, only the diffuse reflectance can be used to easily derive the scattering (S_{λ}), and absorption (K_{λ}) coefficients. In order to estimate both S_{λ} and K_{λ} from $R_{\lambda}(d)$ using Equations (1.12 – 1.13), there is the need to have at least two reflectance measurements from a sample in two different thicknesses. It is important to understand that S_{λ} and K_{λ} of the K-M theory are only approximation of the true scattering coefficient (μ_s) and absorption coefficient (μ_k). True absorption and scattering coefficients represent the probability of absorption and scattering per unit path length (Shi and Anderson, 2009) and they are about half of S_{λ} and K_{λ}, respectively (Olinger and Griffiths, 1988, Hapke, 1993). However, K_{λ} and S_{λ} allow deriving other optical parameters of the scanned samples, such as the transport

absorption ($\sigma_{\lambda a}$) and the reduced scattering coefficient ($\sigma_{\lambda s}(1\text{-}g)$) (van Gemert and Star, 1987, Sterenborg et al., 1989, Shi and Anderson, 2010, Roy et al., 2012) by:

$$K_{\lambda} = \frac{2\sigma_{\lambda a}}{1+\sigma_{\lambda a}/\left(2\left[\sigma_{\lambda a}+\sigma_{\lambda s}(1-g)\right]\right)}$$

Equation 1.14

$$S_{\lambda} = \frac{\frac{3}{4}\sigma_{\lambda s}(1-g)}{1+19\sigma_{\lambda a}/\left(30\left[\sigma_{\lambda a}+\sigma_{\lambda s}(1-g)\right]\right)}$$

Equation 1.15

where $\sigma_{\lambda a}$ is transport absorption (mm^{-1}), $\sigma_{\lambda s}(1\text{-}g)$ is reduced scattering coefficient (mm^{-1}), g is the anisotropy factor (dimensionless) which is computed as the mean cosine scattering angle. It equals to zero in the case of isotropic scattering.

Both $\sigma_{\lambda a}$ and $\sigma_{\lambda s}(1\text{-}g)$ allow defining another optical parameter, which is the penetration depth (δ_{λ}) by (Sterenborg et al., 1989):

$$\delta_{\lambda} = \left(3\sigma_{\lambda a}\left[\sigma_{\lambda a}+\sigma_{\lambda s}(1-g)\right]\right)^{-0.5}$$

Equation 1.16

δ_{λ} is a good indicator of the radiation penetration in the sample, although that is not the effective penetration depth, which is the depth where the amount of radiation energy or intensity is reduced to 37% (Welch and van Gemert, 2011). Note that, Equations (1.14 – 1.16) are only valid when the scattering dominates the absorption.

While Tsuchikawa et al. (1996)'s model is quite complex to use for estimating MC or BSG from hyperspectral images, the K-M theory equations (Equations 1.12 and 1.13) have been employed in this thesis to derive the scattering (S_λ), and absorption (K_λ) coefficients from hemispherical diffuse reflectance spectra recorded between 400 and 2500 nm on thin wood samples extracted from log disks of a hardwood species (quaking aspen (*Populus tremuloides* Michx.)) and a softwood species (black spruce (*Picea mariana* Mill.)). These coefficients were then related to the sample MC using the partial least squares (PLS) regression method.

1.4.6. Factors influencing the NIR spectra and resulting estimation

1.4.6.1. Species

Wood properties change from one species to another and these changes affect the reflected radiation and, in turn, quantitative or discriminant analysis. This is particularly important for the estimation of the density, which is a species-dependent property. Figure 1-5 shows the influence of the species on the mean MSC spectra collected by an NIR hyperspectral imaging system over the transversal section of thawed samples of quaking aspen, balsam poplar, and black spruce that have an MC between 8 and 12%. The mean BSG is 0.44 for quaking aspen, 0.43 for balsam poplar, and 0.46 for black spruce. There is a turning point in the spectra at 1130 nm. Black spruce absorbance is lower than the one of quaking aspen and balsam poplar for wavelengths below 1130 nm, but is higher for wavelengths above 1130 nm. The same pattern was also observed with frozen samples. Combining species in a single PLS model will therefore be beneficial. Schimleck et al. (2001) showed that the combination of *Eucalyptus delegatensis* and

Pinus radiata improved the estimation of density by NIR spectroscopy. Hans et al. (2015a) found that the best BSG estimation accuracy was obtained by combining quaking aspen (*Populus tremuloides Michx.*) and balsam poplar (*Populus balsamifera* L.) in a same model.

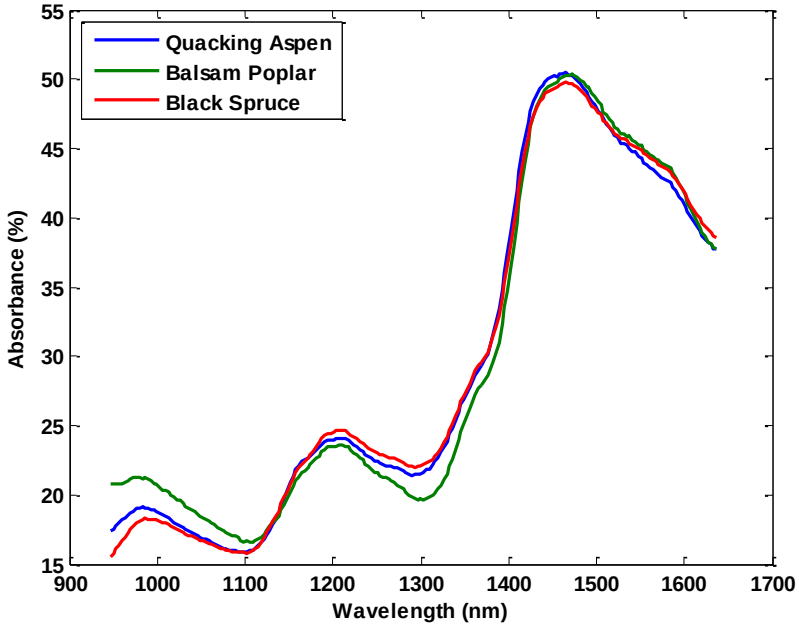

Figure 1-5: Influence of the species on the MS-corrected spectra acquired over the transversal section of thawed samples. All the samples have an MC of 12% and have similar BSG (BSG_{aspen} = 0.44, BSG_{poplar} = 0.43, BSG_{spruce} = 0.46).

1.4.6.2. Anisotropy

The MC prediction accuracy using NIR spectroscopy was much better when measurements were performed on the transversal section than on other sections as shown on red oak (*Quercus spp.*) (Defo et al., 2007) as well as on quaking aspen, balsam poplar, and black spruce samples (Hans et al., 2013, Hans 2015, Hans et al., 2015a). These results could be explained by the fact that the incident radiation over the

transversal section directly interacts with free water in lumens and therefore carries more information about water. Moreover, radiation can penetrate more deeply through the transversal section. On the two other sections (radial and tangential section), radiation interacts first with the cell walls and then with the lumen water (Tsuchikawa et al., 1996).

Anisotropy also contributes to surface roughness differences, which affects the radiation reflectance. The transversal section contains the tracheid cross section, which generates more variations in the spectra than the radial and tangential sections (Figure 1-2). NIR spectra having lower absorbance in the radial and tangential section than in the transversal section were already reported from thawed Sitka spruce (*Picea sitchensis*) samples (Tsuchikawa et al., 1996) and green red oak lumber (Defo et al., 2007). Both authors explained that the transversal section is rougher than the radial and tangential sections because of fiber orientation. When the sample surface becomes rough, the scattering from the surface becomes uneven and influences the reflectance measurements. Similar results were also reported from frozen and thawed black spruce samples (Hans et al., 2013).

1.4.6.3. Hygroscopicity

NIR spectra from hypersepctral camera cannot well distinguish bound water from free water in wood, by contrast to the magnetic resonance imaging technology (Lamason et al. 2014). However, free water and bond water have a different spectral influence on the NIR absorbance spectra. Above the fiber saturation (30% MC), the MC variations on the NIR absorbance spectra are mainly around 1460-1470 nm, because of

the absorption band of the free water. Below the fiber saturation (30%MC) where there is only bound water in the wood, drying the wood to 10% MC leads to a small shift in other wavelengths which are related to lignin (1410 and 1440 nm) and cellulose absorption bands (1490 and 1510 nm), because of the hydrogen bonding between water and cell wall compounds (Figure 1-6).

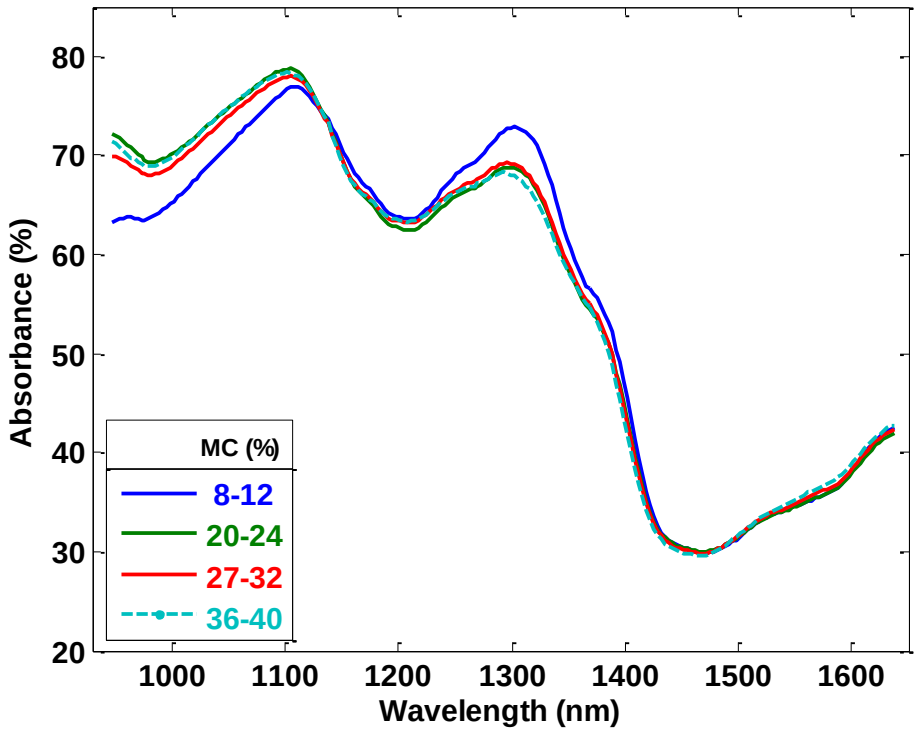

Figure 1-6: Absorbance spectra as a function of MC for selected thawed balsam poplar samples.

Wood density and MC are directly related to each other. Indeed, the density is the proportion of cell walls to voids, and water exists in cell walls and voids. In a specific species, when MC decreases, the density decreases because the wood weight declines, while the volume does not change. However, when MC is below the fiber saturation point, wood starts to shrink and its volume decreases. Consequently, the

density has to be defined in relation to a specific MC. An alternative is to employ BSG, which is independent of MC.

For estimating BSG from NIR spectra acquired over wood samples subjected to different drying steps, a weak BSG estimation will be produced because of the influence of MC over the spectra. As a result, NIR absorbance spectra will change as a function of BSG differently for samples with a wide range of MC (Figure 1-7(a)) and for samples with low MC (less than 12%) (in Figure 1-7(b)). In Figure 1-7(a), a distinct pattern cannot be seen because of the MC influence. By contrast, in Figure 1-7(b), the entire spectrum shifts upward when BSG increases. The shift in the spectra is more apparent in the spectral domain around 1500 nm than in the other parts of the spectrum. This spectral region corresponds to the first OH-bond overtone that is linked to cellulose (Schwanninger et al., 2011). PLS models for predicting BSG will therefore be different according to the MC level of the samples, as shown by several studies on black spruce, quaking aspen, and balsam poplar samples in both thawed and frozen conditions (Hans et al., 2013, Hans, 2015, Hans et al., 2015a).

(a)

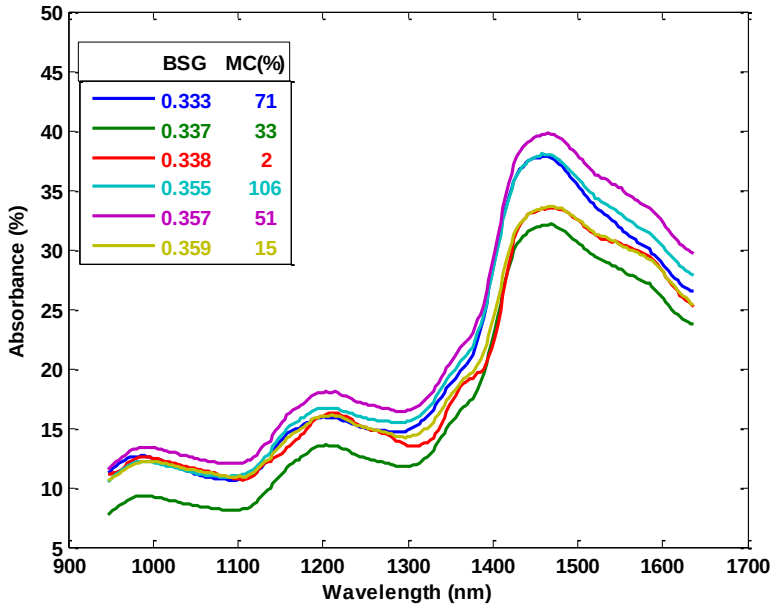

(b)

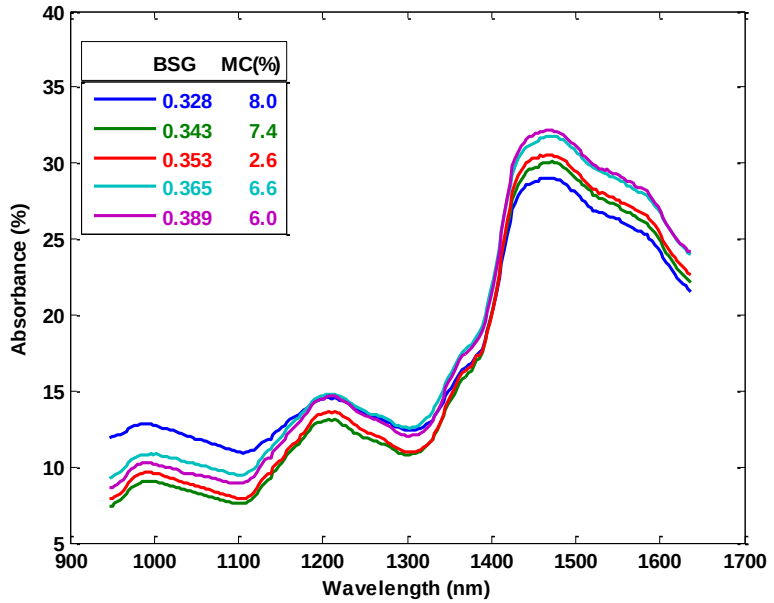

Figure 1-7: Absorbance spectra as a function of BSG for selected black spruce samples (a) covering the whole MC range (b) having low MC (<12%).

1.4.6.4. Frozen and thawed conditions

NIR spectrum carries information about the overtones and combination of fundamental bands. Rising temperatures cause changes in molecular vibrations and consequently in the absorption spectrum (Swierenga et al., 2000). Most studies collected spectra at normal temperatures, but the effect of temperature on proposed models to estimate wood properties is needed for northern countries such as Canada, where large temperature variations are common. Decreasing temperatures produce shifts towards high wavelengths, such as the one Haddadi et al. (2015c) observed over black spruce samples (Figure 1-8). However, the shift around 1450 nm was lower than those reported for spectra acquired over sapwood and heartwood of black spruce (17.2 nm and 8.6 nm, respectively) (Hans et al., 2013) and of Norway spruce (*Picea abies* L.) H. Karst (25 nm and 5 nm, respectively) (Thygesen and Lundqvist, 2000a). MC and frost can also influence the amplitude of the shift (Thygesen and Lundqvist, 2000a). Figure 1-8 also shows a sharp peak (with high absorbance) at 1445 nm caused by the frost over the surface of the frozen samples. Hans et al. (2013) also observed such a sharp peak and explained it by the presence of ice that produces scattering.

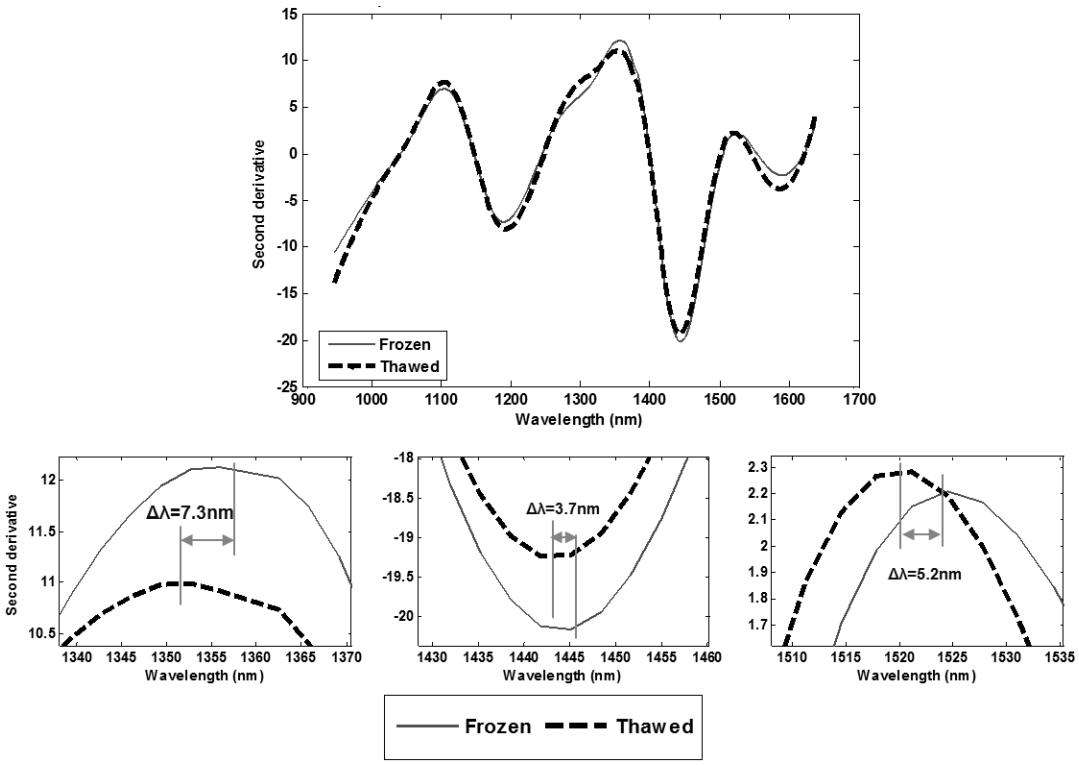

Figure 1-8: Second derivative corrected spectra for a frozen and thawed black spruce sample (MC= 18.1%, BSG= 0.422) and detailed snapshots of the spectra showing the spectral shift due to changes in log states. The spectra have been acquired on transversal sections.

1.5. VIS-NIR hyperspectral imaging

1.5.1. Hyperspectral Imaging Systems

As we already explained above, in order to reduce the waste, decrease the cost, and increase the productivity in the wood industry, wood properties should meet defined quality criteria. However, wood is highly variable, For example, the moisture content, the density, and other chemical properties can vary within annual rings because of the variable amount of latewood and earlywood. They can also vary between the sapwood

and heartwood regions. For example, the sapwood has usually a higher MC than the heartwood. Wood properties can also vary as a function of the height level in the trunk, because of different amounts of juvenile and mature wood (Panshin and De Zeeuw, 1980, Barnett and Jeronimidis, 2003). All this variability has an influence of the efficiency in the process chain and may influence the end-product quality. For example, low quality lumber is often associated with wood having heterogeneous density. There is therefore the need in sawmills to develop sensors for measuring the variation of MC and BSG across raw materials and products. Only sensors such as NIR hyperspectral imaging systems can provide 2D images of wood properties. In addition, these systems provide images with high spatial resolution (in the order of mm) and high spectral resolution (around 3 nm) that are suitable for accurate imaging of MC and BSG of wood samples.

Hyperspectral imaging systems may be a little more expensive in terms of hardware and more complex to use than the simple NIR spectrometer, but they have the enormous advantages of directly providing 2D information on the wood sample, while NIR spectrometers only provide spot measurements.

Hyperspectral images, also called hyper cubes (Figure 1-9), contain reflectance spectra for each point (around 1 mm) of the target surface over hundreds of wavelengths (Geladi et al., 2004, Salzer and Siesler, 2009, Li et al., 2013). The spectra have a narrow spectral (hyperspectral) sampling, e.g. less than 10 nm. Hyperspectral systems are better than multispectral broadband systems, because they capture more than 100 spectral bands continuously, without overlapping, and in a fine spectral resolution for each pixel,

while multispectral broadband systems capture limited spectral bands in a coarse spectral resolution (Chang, 2007, Li et al., 2013). The fine resolution of the hyperspectral data allows derivative analysis, which is useful to resolve overlapping absorption bands to better separate components of the global spectrum (Demetriades-Shah et al., 1990).

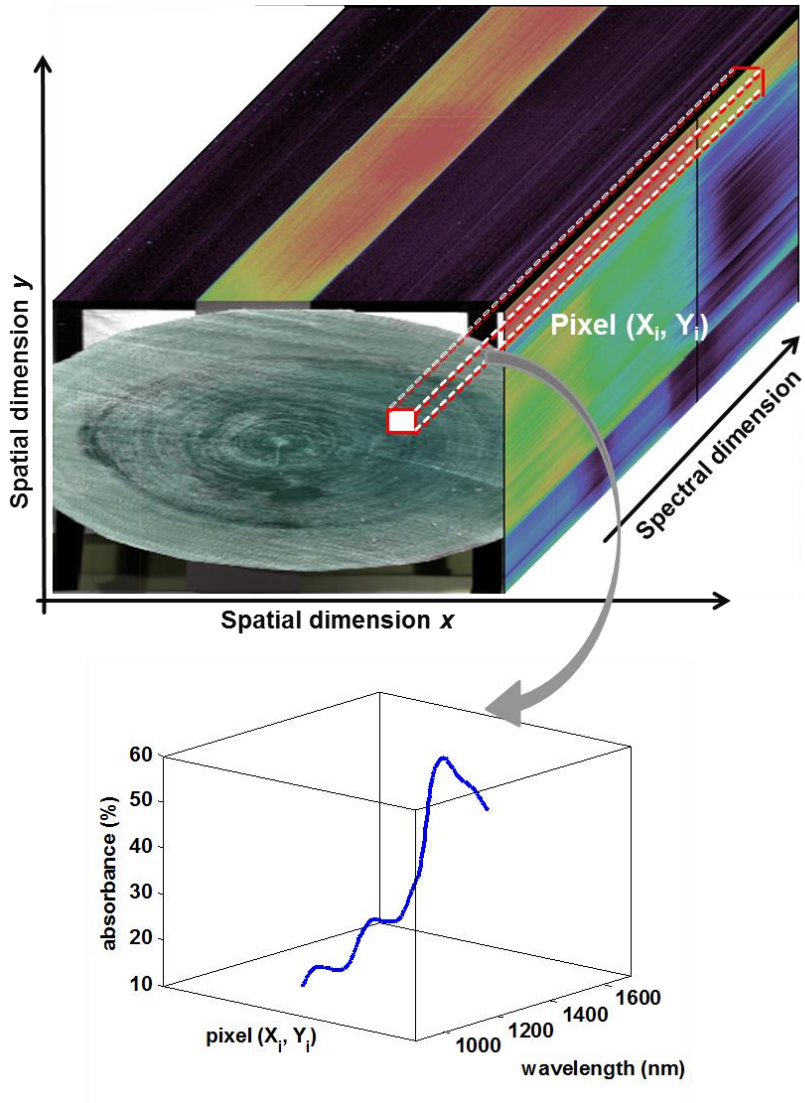

Figure 1-9: Hypercube data of a wood sample, and corresponding spectrum for a particular pixel.

There are four main techniques used to capture a hyperspectral image which differ according to the spectral recording method: point-scanning or whiskbroom imaging, pushbroom imaging, staring imaging, and snapshot imaging (Boldrini et al., 2012, Li et al., 2013).

In the point-scanning or whiskbroom imaging mode, the spectral information is captured through a rotating mirror. The mirror scans the sample from side to side of the conveyor, and the conveyor moves perpendicular to the direction of scan. Behind the mirror, there is a prism to disperse the reflected radiation from the sample and a single detector is used to record the spectra. By scanning the whole sample in both spatial dimensions, a hypercube image from the sample can be acquired. However, this system needs time to capture spectra for both dimensions since the recording process is repeated for each point. The short time period capturing for each point is also the reason that such systems are only able to acquire images at low spectral resolution and with a low signal to noise ratio (Boldrini et al., 2012, Li et al., 2013). Such system is useful for scanning small static objects.

With the pushbroom or line scan camera, all spectra for one spatial dimension are simultaneously acquired by an array detector. In order to get a hypercube image, either the camera or the target should move in the direction perpendicular to the array detector. The spectral resolution of this system can be higher than the whiskbroom one. The most common method for spectral dispersion in this system is a prism-grating-prism (PGP), which provides high spectral resolution (Boldrini et al., 2012, Li et al., 2013). This system is very useful for in-line or on-line applications, because the line

scan camera can scan the entire samples, regardless of their length. This system also is the most popular in commercial NIR hyperspectral systems. In this thesis, we will use a pushbroom (line scan) camera (*Specim*), which can provide hypercubes. This system is a combination of an imaging spectrograph, a temperature stabilized camera, an illumination unit, and a translation unit (Figure 1-10).

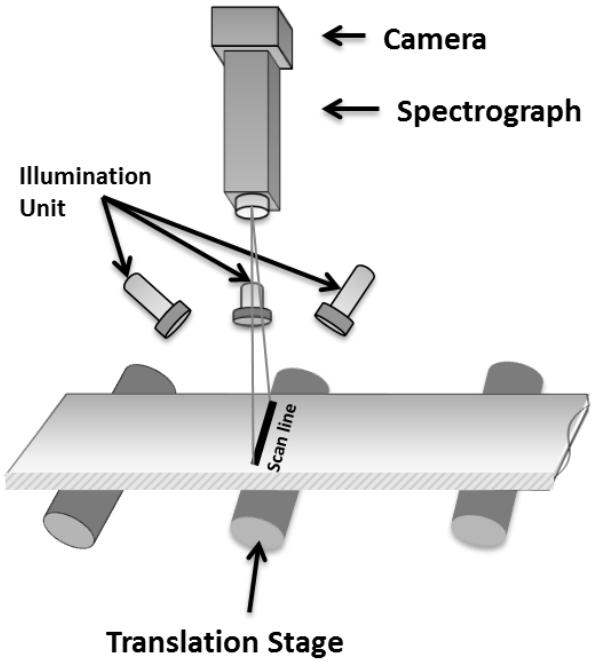

Figure 1-10: Main components of a line scan hyperspectral imaging system.

The illumination unit should provide homogeneous incident radiation over the imaged spot of the camera. High intensity radiation can cause detector saturation in some wavelengths, and low intensity radiation leads to low signal to noise ratios.

The staring imaging or frame type captures a single band/image in both spatial dimensions. In this system, different filters provide different wavelengths. A CCD matrix then records the 2D image in the predefined wavelengths. The number of

bands/images depends on the number of filters. The most common filters for this system are acoustic-optical-tunable filters (AOTF) or liquid crystal tunable filters (LCTF). Users can define the number of bands and modify the system by changing the filters. With this system, a high spatial resolution image can be acquired. However, the spectral resolution and SNR are lower than in the pushbroom imaging system, because the amount of the recorded radiation in each wavelength is low (Boldrini et al., 2012, Li et al., 2013).

The last type of imaging system is the snapshot or single shot system. It can record both spatial and spectral information over a sample without scanning. The spectral dispersion element in this system is a prism, and a CCD matrix captures the hypercube data. This system is based on a two-dimensional transmission dispersive element, which is between two lenses. The first lens collimates the light coming from the sample then dispersive element diffracts the radiation and the second lens projects the diffracted radiation onto the CCD matrix. The spectral resolution in this system is lower than in the staring mode system, but the time for data collection is shorter than the other systems (Li et al., 2013).

1.5.2. Image analysis methods

The main steps to process hypercube data for extracting spectra from the images are: 1) image calibration, 2) recovering bad pixels that produce extreme reflectance values at some wavelengths, 3) removing abnormal spectra.

1.5.2.1. Image calibration

The image calibration includes converting the digital numbers (DN) of the acquired images into true reflectance values by:

$$\boldsymbol{R} = (\boldsymbol{X} - \boldsymbol{B}) \,/\, (\mathbf{W} - \mathbf{B})$$

Equation 1.17

where $\boldsymbol{R}$ is the true reflectance vector of the sample, $\boldsymbol{X}$ is the raw DN vector of the sample, and $\boldsymbol{B}$ and $\boldsymbol{W}$ are the vectors representing the reflectance spectra of the black and white panels, respectively.

As shown in Equation 1-17, the calibration of the images into reflectance images requires at least one image over a white reference panel and one image over a black reference panel, which their reflectance is known. Both reference panels should be large enough to cover the whole sample imaged by the camera and should have a highly homogeneous reflectance. The images of the white and black reference panels should be acquired each time before acquiring the sample images. The black panel image can be produced simply by covering the input lens with a black cap, while the white panel image is usually acquired over a *Spectralon* panel (*Spectralon Co.*, www.labsphere.com).

In several studies on wood property estimation using NIR-HSI data, this step is the only preprocessing step, and spectra were used directly in the modeling (Agresti et al., 2013, Fernandes et al., 2013b, 2013a, Kobori et al., 2013).

1.5.2.2. Bad pixels

The NIR wood spectra can exhibit random reflectance maxima and minima at some wavelengths, called "*bad pixels*" as shown in Figure 1-11. They are due to the following causes: (i) the detector saturates, (ii) the detector does not measure any reflectance, (iii) the detector always measures the same reflectance value, and (iv) the detector measures only a proportion of the true reflectance (Grahn and Geladi, 2007). These extreme reflectance values can be replaced by the reflectance of neighbor wavelength channels (Burger, 2009). Since the position of the bad pixels is the same in all images, they can be found using the black and white panel images and their position can then be used to correct all the images acquired over the wood samples.

After finding the wavelengths corresponding to extreme reflectance values, the corresponding reflectance values need to be estimated. This can be done simply by replacing the average of reflectance value of their neighbors' wavelengths, such as it is done with mean or median filters.

In this thesis, we use a median filter because a median filter can work with non-linear data and does not consider the statistical data distribution (Richards and Jia, 2006). A median filter sorts the reflectance values within the bad pixel window in descending or ascending order, and the middle of the sorted data is selected as the filter output. The output excludes the values, which do not fit the pattern of the local neighborhood.

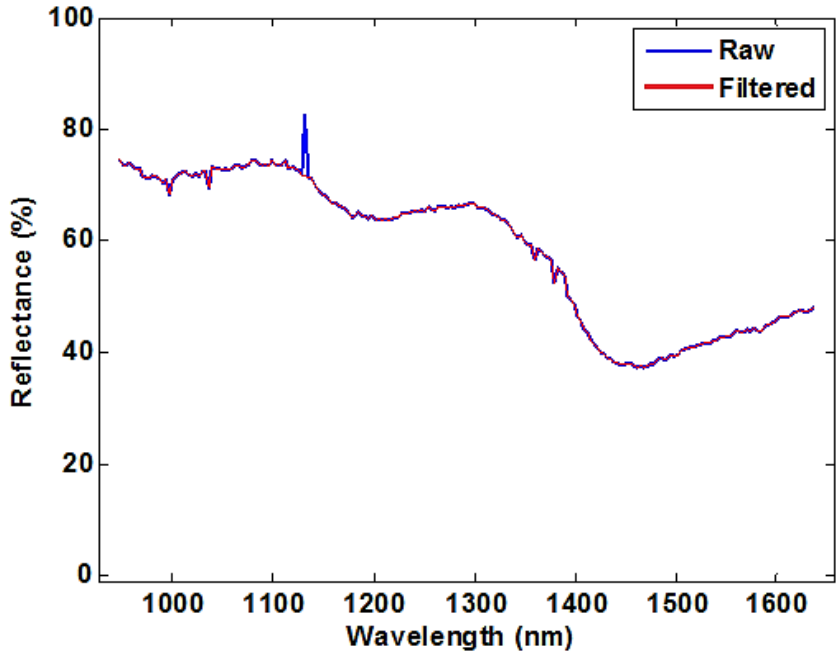

Figure 1-11: Raw spectra contains bad pixel, which can be recovered by a median filter

1.5.2.3. Abnormal spectra

Generally, images acquired with digital imaging sensor arrays have "dead" pixels, which produce abnormal spectra (Burger and Geladi, 2005). In Figure 1-12, all the spectra are associated with the same wood sample, but some of them are distinctively different than the majority of the spectra. These dead pixels correspond to the following cases: (1) the sensor is not measuring at the pixel location; (2) the sensor is producing an abnormal DN value at the pixel location; (3) there are bark, knots, and other defects in the imaged wood at the pixel location.

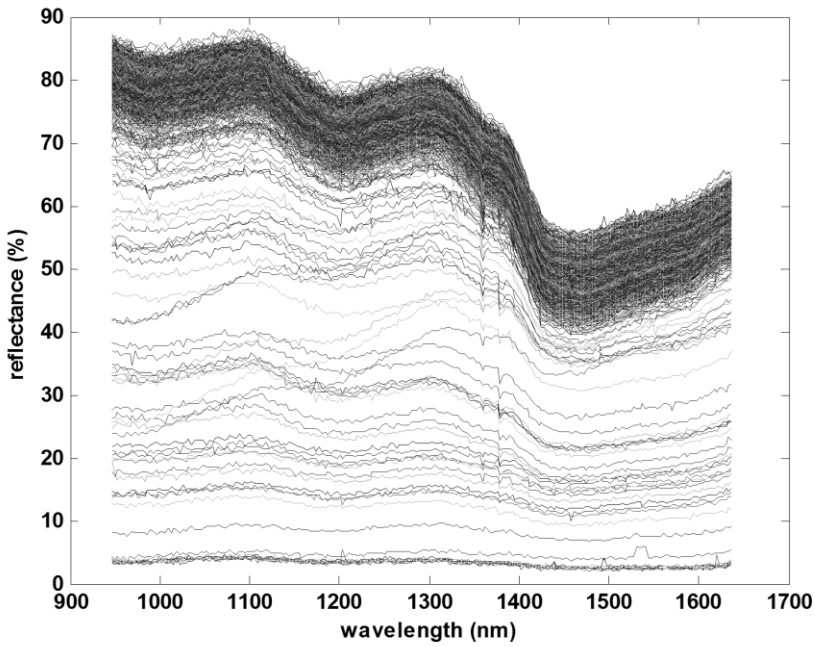

Figure 1-12: Reflectance spectra for a sample that also contain abnormal spectra.

Several methods have been proposed to identify these abnormal spectra. In a study using hyperspectral images over loblolly pine wood disks, pixels of the bark and knot region were visually delineated and masked out (Mora et al., 2011b), but such a method can be tedious and inaccurate. Thumm et al. (2010) removed non-wood spectra from the dataset by a simple threshold reflectance between 1260 and 1460 nm. Such method may not be accurate or extended to other species. In this thesis, we used a combination of the principal component analysis (PCA) and the *boxplot* method of Laurikkala et al. (2000). First, the spectra are projected using PCA into a new space that has uncorrelated axis. PCA projection allows us to easily identify abnormal spectra since they are located outside the cloud, which corresponds to the “good” spectra in the two-dimensional planes made by the first and second principal components.

The Mahalanobis distance between the cloud point median and the individual spectra can then be calculated by (Richards and Jia, 2006):

$$D = (\boldsymbol{X} - \boldsymbol{X_M})^T \Sigma^{-1} (\boldsymbol{X} - \boldsymbol{X_M})$$

Equation 1.18

where D is the Mahalanobis distance of a spectrum from the cloud point median, **X** is the PC_1 and PC_2 vectors for an individual spectrum, $\mathbf{X_M}$ is the median PC_1 and PC_2 vectors for all spectra, and Σ is the covariance matrix of PC_1 and PC_2. By contrast to the Euclidean distance, the Mahalanobis distance allows us to consider the weight of the PCs: PC_1 has a higher weight in the distance calculation than PC_2.

These distances are then used into the *boxplot* method of Laurikkala et al. (2000) as follows. The first (q_1) and third (q_3) quartiles of the distance distribution are computed as:

$$q_1 = 0.25 * (N - 1)$$

$$q_3 = 0.75 * (\mathrm{N} - 1)$$

Equation 1.19

where N is the number of spectra. These quartiles are then used to compute the maximum distance (MAX), which is the acceptable distance for an individual spectrum can present in order not to be considered as an abnormal spectrum, as:

$$\mathrm{MAX} = q_3 + 1.5 * (q_3 - q_1)$$

Equation 1.20

Every time, abnormal spectra are removed from the dataset, the median value of the cloud may change. Therefore, the *boxplot* method needs to be applied iteratively, which can be time consuming. In practice, since the median of the cloud changes very slightly, the number of iterations can be limited to two or three. Because each spectrum is associated with a particular pixel of the sample image, the position of the abnormal pixels in the image can also be found.

1.5.3. Wood properties prediction

Most of the studies using NIR spectra to predict wood properties are based on point-measurements. There are few studies that use hyperspectral images. Hyperspectral imaging systems have been tested to identify compression wood in Norway spruce (*Picea abies* L.) and in Scot pine (*Pinus sylvestris* L.) lumber (Nystrom and Hagman, 1999). The wavelength range of the system was between 400 and 710 nm with a spectral resolution of 1.2 nm. The camera was set at 70 cm from the wood surface and provided images with a spatial resolution of 0.45×2.5 mm in cross-section and along the lumber. Hyperspectral imaging was also used for detecting compression wood in Norway spruce stem cross-sections (Duncker and Spiecker, 2009). The range of wavelengths used was between 400 nm and 1000 nm with a spectral resolution of 5 nm. The spatial resolution of the images was less than 0.1 mm. More recently, these systems have been used to map the chemical composition of wood (Thumm et al., 2010). These authors collected spectra over the range of 900-1700 nm with a 3.6 nm spectral resolution to provide the

distribution of lignin, galactose, and glucose. The camera was set at 49.5 cm above the sample surface and provided images with a spatial resolution of 1.05 mm. Mora et al. (2011b) used a hyperspectral imaging system working in the 1000-1700 nm range with a spectral resolution of 5 nm to map the MC and density of loblolly pine (*Pinus Taeda* L.) disks. In order to get the spatial resolution of less than 1 mm, the camera was set at 1.5 m above the target. An imaging system that works in the 400-1000 nm spectral domain with a 3.7 nm spectral resolution was also employed to the map MC of European beech (*Fagus sylvatica* L.) and Scots pine (*Pinus sylvestris* L.) disk cross-sections (Kobori et al., 2013). The spatial resolution of the images was around 0.06×0.11 mm. Hyperspectral image in the range of 380-1028 nm with the spatial resolution of less than 0.1 mm was also used to predict the density of Stone pine (*Pinus pinea*) disks. They employed X-ray images to calculate the density and built models to estimate density through two different algorithms, PLS and ANN (Artificial Neural Network) (Fernandes et al., 2013b, 2013a). Wood color changes caused by photo degradation have also been examined by VIS-NIR hyperspectral images acquired over poplar (*Populus spp.*) board samples (which had an MC of 12%) in two different wavelength ranges: 400-1000 nm and 1000-2500 nm (Agresti et al., 2013).

The main difference between the modeling of wood properties in traditional NIR spectroscopy and in NIR hyperspectral imaging is that, in NIR spectroscopy, there is a reference value for each collected spectrum, whereas in NIR hyperspectral imaging, there is one image containing more than hundreds of spectra for each reference value. This issue makes hyperspectral image analyses more complex. One solution is to summarize the spectra of each image by considering the median or mean spectrum. An

alternative approach is to consider a region containing more than one spectrum for each image and repeating the reference value for all spectra in the region. In the estimation of MC for subalpine fir species, Haddadi et al. (2015a) considered both methods and found that the highest accuracy was obtained with the median spectra from each sample. Also the aforementioned studies of wood MC and BSG estimation using hyperspectral imaging systems did not consider the influence of species, anisotropy, log condition (frozen and thawed), and hygroscopicity in the modeling. In this thesis, the influence of some of these factors is examined.

1.6. Thesis goal, objectives, and hypotheses

The overall goal of this dissertation is to test and develop an NIR hyperspectral system that could be used as a fast non-destructive sensor for monitoring the spatial distribution of moisture content (MC) and basic specific gravity (BSG) of logs and boards. This system will help to characterize both wood properties and the distribution of wood properties. Such an optimization could lead to a decrease in energy consumption and manufacturing costs and to an improvement of the quality of the final products. Log sorting according to moisture content is important for the oriented strand board (OSB) industry for example because this property affects log shave size and glue bonding. It has been shown that the non-destructive estimation of wood MC in the OSB industry could save up to $300,000 annually (Knudson and Chen, 2001).

Monitoring log BSG is important for the pulp and paper industry, to replace the high BSG black spruce by low BSG aspen. Because low BSG equals to poor strength properties (Barnett and Jeronimidis, 2003). Lumber MC is important to be monitored in

the kiln drying process because of a huge energy consumption, which can be reduced using advanced control systems (Léger and Amazouz, 2003). Wood MC is finally an important element in wood transportation cost. Besides having a direct influence, MC and BSG are also related to other wood properties, such as physical and mechanical properties, resistance to biological deterioration and non-stability in dimension (Panshin and De Zeeuw, 1980, Barnett and Jeronimidis, 2003, Bowyer et al., 2007, Isaksson et al., 2013).

This thesis work is part of a research program to investigate several NDTE methods that perfectly meet the above mentioned requirements for characterizing wood moisture content and density. The other NDTE methods include near-infrared (NIR) spectroscopy, time-resolved NIR, GPR, and nuclear magnetic resonance (NMR) imaging were the subject of two other companion theses. However, except for the NMR imaging systems, these systems only provide spot measurements, which cannot reflect the spatial variability of the property in wood. Biological materials like wood are heterogeneous. Thus, only one measurement or even some measurements in different locations are not sufficient to show the distribution of wood properties across the product. Near infrared hyperspectral imaging (NIR-HSI) systems can provide such distribution of wood properties at a fine resolution by capturing thousands of spectra within a two-dimensional space in a short period of time (Geladi et al., 2004, Salzer and Siesler, 2009).

This dissertation is limited to the investigation of NIR hyperspectral images to estimate MC and BSG of logs and lumber related to several tree species (black spruce,

quaking aspen, balsam poplar, and subalpine fir) that have a major economic importance for the Canadian forest products sector. The imaging system that will be tested here is a line scanning system, as line scanning systems allow acquiring images of samples of any size at a high spatial and spectral resolution. In order to be used in the plant, the acquired images should be processed as fast as possible. The images should also be able to measure MC and BSG over frozen material that can occur in Canada during winter. Most of the previous NIR spectroscopy used an empirical statistical approach and it is necessary to test a more deterministic approach using physics-based theories such as the Kubelka-Munk theory.

Two major objectives were pursued:

- **To test the use of NIR-HSI images acquired over logs and lumbers to produce 2D images of MC and BSG through a combination of an image processing method and partial least squares model.**
- **To determine wood MC using a more deterministic approach based on the Kubelka-Munk theory and to derive related wood optical parameters.**

1.6.1. Image processing method

NIR hyperspectral imaging systems have been tested to identify compression wood (Nystrom and Hagman, 1999, Duncker and Spiecker, 2009) to map chemical composition of wood (Thumm et al., 2010), and to estimate MC and basic density of loblolly pine, European beech, Scots pine, and Stone pine (Mora et al., 2011b, Fernandes et al., 2013b, 2013a, Kobori et al., 2013). However, in all of these studies, the

image processing method involved several manual visual interpretations of the image, which can be tedious and produces inaccurate results.

A first specific objective of this thesis is to develop a fast image processing method that allows retrieving clean spectra from NIR-HSI images acquired over logs and lumber.

The following hypotheses were made:

- Recovering bad pixels that produce extreme reflectance values at some wavelengths can be done using a median filter
- Abnormal spectra can be removed using a combination of a principal component analysis (PCA) with the *boxplot* method of Laurikkala et al. (2000)
- The image processing method should be fast and reliable regardless of the wood properties.

1.6.2. MC and BSG 2D images

As reviewed in Haddadi et al. (2015a, 2015b) and Leblon et al. (2013), the majority of the studies employing NIR spectra for estimating wood MC or BSG use point measurements that are not able to give a spatial distribution of the property across the sample. A few studies estimated MC or BSG images from NIR-HSI images using partial least squares models (Mora et al., 2011b, Fernandes et al., 2013b, Kobori et al., 2013). However, all these studies were done over thawed wood and there is the need to test the models over frozen wood which occurs in Canada during winter.

A second objective is to develop partial least squares (PLS) regression models that allow producing 2D images of MC and BSG of the logs or boards. The models take into account the influence of the tree species for both the logs and the lumbers, and in the case of the log, of the log state (frozen/thawed). The species considered in the thesis were chosen for their economic importance in Canada: black spruce (*Picea mariana* Mill.), balsam poplar (*Populus balsamifera* L.), quaking aspen (*Populus tremuloides* Michx.), and subalpine fir (*Abies lasiocarpa* Hook.)

The following hypotheses were made:

- MC and BSG of boards and logs can be predicted non-destructively and in real-time directly using an NIR-HSI system using partial least squares models.
- Partial least squares models applied to NIR images acquired over subalpine fir boards can produce 2D images of MC and BSG
- Partial least squares models applied to NIR images acquired over frozen and thawed logs from three different species and collected on can produce 2D images of MC and BSG independently of the species and the log state
- Partial least squares models are effective to estimate MC images from NIR-HSI even if the MC values are large
- BSG images are better estimated, if the MC of the sample is low

1.6.3. Wood MC and other optical wood properties using the Kubelka-Munk theory

All the aforementioned studies that estimated MC or BSG from NIR spectra are based on partial least squares models that have an empirical nature, being a statistical multivariate analysis. An alternative would be to use a more deterministic approach that estimates wood optical parameters using a physics-based model. Only one optical model was developed so far, which explicitly describes the interaction between wood characteristics and NIR spectra using the Kubelka-Munk theory (Tsuchikawa et al., 1996). Wood is modeled as an aggregate of semi-infinite inclined square tubes representing the tracheids with a membrane having a certain thickness. The model assumes that the incident radiation is made of parallel beams. The model was developed for Sitka spruce and there is the need to test the method over other species of economic importance in Canada, such as black spruce and quaking aspen. Also, Tsuchikawa et al. (1996)'s model only estimates the absorption K_λ and scattering S_λ coefficient spectra from NIR reflectance spectra and there is the need to estimate MC from the K_λ or S_λ spectra. Also, the K_λ and S_λ spectra allow computing other wood optical parameters, such as the transport absorption coefficient ($\sigma_{\lambda a}$), the reduced scattering coefficient ($\sigma_{\lambda s}(1\text{-}g)$), and the penetration depth (δ_λ.). The effect of MC on these optical parameters is also analyzed.

A third specific objective of this thesis is to derive MC from absorption K_λ and scattering S_λ coefficient spectra that were derived from NIR reflectance spectra using the Kubelka-Munk theory. A fourth specific objective of this thesis is to investigate the

effect of species and wavelength ranges over the MC estimation using the Kubelka-Munk approach. Two species were considered here: a hardwood species (quaking aspen (*Populus tremuloides* Michx.)) and a softwood species (black spruce (*Picea mariana* Mill.)). A fifth specific objective of this thesis is to derive the transport absorption coefficient ($\sigma_{\lambda a}$) spectra, the reduced scattering coefficient ($\sigma_{\lambda s}(1\text{-}g)$) spectra, and the penetration depth (δ_λ) spectra from the K_λ and S_λ spectra and to investigate the effect of MC on these optical parameters.

The following hypotheses were made:

- The Kubelka-Munk theory equations applied to NIR reflectance spectra allow deriving the absorption K_λ and scattering S_λ coefficient spectra
- The absorption K_λ and scattering S_λ coefficient spectra should be similar between the black spruce and Sitka spruce species, but very different for the quaking aspen species
- MC is better related to the absorption K_λ spectra than to the scattering S_λ coefficient spectra
- The transport absorption coefficient ($\sigma_{\lambda a}$) spectra, the reduced scattering coefficient ($\sigma_{\lambda s}(1\text{-}g)$) spectra, and the penetration depth (δ_λ.) spectra can be derived from the absorption K_λ and scattering S_λ coefficient spectra
- MC has an influence over the transport absorption coefficient ($\sigma_{\lambda a}$) spectra, the reduced scattering coefficient ($\sigma_{\lambda s}(1\text{-}g)$) spectra, and the penetration depth (δ_λ.) spectra

1.7. Thesis organization

This thesis is organized into six chapters. The introduction (Chapter 1) reviews the principles of the NDT methods used to assess wood product properties. Among all types of NDT methods, we primarily focused on the NIR hyperspectral imaging system. Chapters 2 to 5 present the four manuscripts on which the thesis is based.

Chapter 2 is entitled "Using near infrared hyperspectral images on subalpine fir board – Part 1: Moisture content estimation" and was published in *Wood Material Science & Engineering* in 2015. This manuscript presents all the required preprocessing steps to achieve clean spectra from a hyperspectral imaging system. We also built a model to estimate MC of subalpine fir.

Chapter 3 is entitled "Using near infrared hyperspectral images on subalpine fir board – Part 2: Density and basic specific gravity estimation" and was published in *Wood Material Science & Engineering* in 2015. This manuscript presents the calculation of density and basic specific gravity of dried wood samples. A model used to estimate density and basic specific gravity of subalpine fir species is presented. The effect of MC variation on the estimation of BSG is also discussed.

Chapter 4 is entitled "Prediction of wood properties for thawed and frozen logs of quaking aspen, balsam poplar, and black spruce from near-infrared hyperspectral images" and was published in *Wood Science and Technology* in 2015. This manuscript presents the influence of species and log state (thawed and frozen) on the spectra collected from quaking aspen (*Populus tremuloides* (Michx.)), balsam poplar (*Populus*

balsamifera (L.)), and black spruce (*Picea mariana* Mill.)). Models were developed to estimate MC and BSG of these species according to several factors. We also built a general model in which several factors were taken into account. PLS-DA was also employed to sort the logs in different classes of MC and BSG, as well as to discriminate species and log state (thawed and frozen).

Chapter 5 is entitled "Optical properties of wood and their relationship to moisture content" and was published in *Journal of Near Infrared Spectroscopy*. This manuscript presents the calculation of wood optical properties of quaking aspen (*Populus tremuloides* Michx.)) and black spruce (*Picea mariana* Mill.)) based on the Kubelka-Munk theory. The MC and species effects on wood optical properties were discussed and models to estimate the sample MC from optical properties and raw or transformed spectra were provided.

Chapter 6 is the conclusion of the thesis and provides recommendations for future research. Finally, an appendix that delivers the supplementary information is provided.

For Chapters 2 through 5, the author designed the experimental procedure with the approval of his supervisors and advisory committee, designed the image processing method, performed the data analysis, wrote the first draft of each manuscript, and corrected each manuscript based on the inputs from the respective co-authors and referees.

For Chapters 2, 3, 4 and 5, the author conducted the experiments with the help of other UNB students (Guillaume Hans, Clevan Lamason, and Kathie Phung), and technicians from FPInnovations (Gordon Chow) and UNB (Dean McCarthy).

1.8. References

Abasolo M., Lee D.J., Raymond C., Meder R. & Shepherd M. (2013) Deviant near infrared spectra identifies *Corymbia hybrids*. *Forest Ecology and Management*, 304: 121-131. doi: 10.1016/j.foreco.2013.04.040

Adedipe O.E. & Dawson-Andoh B. (2008) Prediction of yellow-poplar (*Liriodendron tulipifera*) veneer stiffness and bulk density using near infrared spectroscopy and multivariate calibration. *Journal of Near Infrared Spectroscopy*, 16(5): 487-496. doi: 10.1255/jnirs.812

Adedipe O.E., Dawson-Andoh B., Slahor J. & Osborn L. (2008) Classification of red oak (*Quercus rubra*) and white oak (*Quercus alba*) wood using a near infrared spectrometer and soft independent modelling of class analogies. *Journal of Near Infrared Spectroscopy*, 16(1): 49-57. doi: 10.1255/Jnirs.760

Agresti G., Bonifazi G., Calienno L., Capobianco G., Lo Monaco A., Pelosi C., Picchio R. & Serranti S. (2013) Surface investigation of photo-degraded wood by colour monitoring, infrared spectroscopy, and hyperspectral imaging. *Journal of Spectroscopy*. doi: 10.1155/2013/380536

Alves A., Schwanninger M., Pereira H. & Rodrigues J. (2006) Calibration of NIR to assess lignin composition (h/g ratio) in maritime pine wood using analytical pyrolysis as the reference method. *Holzforschung*, 60(1): 29-31. doi: 10.1515/HF.2006.006

ASTM-D2395–07a (2009) *Standard test methods for specific gravity of wood and wood-based materials*, ASTM International, West Conshohocken, PA, doi: 10.1520/D2395-07A, www.astm.org.

ASTM-D4442–07 (2009) *Standard test methods for direct moisture content measurement of wood and wood-base materials*, ASTM International, West Conshohocken, PA, doi: 10.1520/D4442-07, www.astm.org.

Baradit E., Aedo R. & Aguilera C. (2009) Imaging processing for knot detection in wood using microwaves. *Wood Research*, 54(3): 55-60

Barnes R.J., Dhanoa M.S. & Lister S.J. (1989) Standard normal variate transformation and de-trending of near-infrared diffuse reflectance spectra. *Applied Spectroscopy*, 43(5): 772-777

Barnett J.R. & Jeronimidis G. (Eds) (2003) *Wood quality and its biological basis.* Oxford; Boca Raton, FL: CRC Press, 226 pages.

Bergstrom B. (2003) Chemical and structural changes during heartwood formation in *Pinus sylvestris*. *Forestry*, 76(1): 45-53. doi: 10.1093/forestry/76.1.45

Boldrini B., Kessler W., Rebner K. & Kessler R.W. (2012) Hyperspectral imaging: A review of best practice, performance and pitfalls for in-line and on-line applications. *Journal of Near Infrared Spectroscopy*, 20(5): 483-508. doi: 10.1255/1003

Bowyer J.L., Shmulsky R. & Haygreen J.G. (2007) *Forest products and wood science: An introduction.* Oxford, UK: John Wiley & Sons. 496 pages.

Brandstrom J. (2001) Micro- and ultrastructural aspects of Norway spruce tracheids: A review. *IAWA Journal*, 22(4): 333-353. doi: 10.1163/22941932-90000381

Brunner C.C., Shaw G.B., Butler D.A. & Funck J.W. (1990) Using color in machine vision systems for wood processing. *Wood and Fiber Science,* 22(4): 413-428

Bucur V. (2003a) *Nondestructive characterization and imaging of wood.* Berlin, Germany: Springer. 354 pages.

Bucur V. (2003b) Techniques for high resolution imaging of wood structure: A review. *Measurement Science & Technology,* 14(12): R91-R98. doi: 10.1088/0957-0233/14/12/R01

Buddenbaum H. & Steffens M. (2012) The effects of spectral pretreatments on chemometric analyses of soil profiles using laboratory imaging spectroscopy. *Applied and Environmental Soil Science,* 2012: 12. doi: 10.1155/2012/274903

Burcham D.C., Leong E.C. & Fong Y.K. (2012) Passive infrared camera measurements demonstrate modest effect of mechanically induced internal voids on *Dracaena fragrans* stem temperature. *Urban Forestry & Urban Greening,* 11(2): 169-178. doi: 10.1016/j.ufug.2012.01.001

Burger J. (2009) Replacement of hyperspectral image bad pixels. *NIR news,* 20(7): 25-27. doi: 10.1255/nirn.11xx

Burger J. & Geladi P. (2005) Hyperspectral NIR image regression. Part 1: Calibration and correction. *Journal of Chemometrics,* 19(5-7): 355-363. doi: 10.1002/Cem.938

Burger J.E. (2006) *Hyperspectral NIR image analysis, data exploration, correction, and regression*. Doctoral Thesis, Swedish University of Agricultural Sciences, Arkitektkopia, Umeå, Sweden, 131 pages.

Burger T., Kuhn J., Caps R. & Fricke J. (1997) Quantitative determination of the scattering and absorption coefficients from diffuse reflectance and transmittance measurements: Application to pharmaceutical powders. *Applied Spectroscopy,* 51(3): 309-317. doi: 10.1366/0003702971940404

Burns D.A. & Ciurczak E.W. (Eds) (2007) *Handbook of near-infrared analysis.* Boca Raton, FL, USA: CRC Press, 808 pages.

Butler D.A., Brunner C.C. & Funck J.W. (2002) Wood-surface feature classification via extended-color imagery. *Forest Products Journal,* 52(6): 80-84

Cai L.P. (2006) Using steam explosion to improve the dryability of wet pocket wood. *Forest Products Journal,* 56(7-8): 75-78

Catena G., Palla L. & Catalano M. (1990) Thermal infrared detection of cavities in trees. *European Journal of Forest Pathology,* 20(4): 201-210

Chang C.I. (2007) *Hyperspectral data exploitation: Theory and applications.* New Jersey, USA: John Wiley & Sons. 465 pages.

Cheong W.F., Prahl S.A. & Welch A.J. (1990) A review of the optical-properties of biological tissues. *IEEE Journal of Quantum Electronics,* 26(12): 2166-2185. doi: 10.1109/3.64354

Cooper P.A., Jeremic D., Radivojevic S., Ung Y.T. & Leblon B. (2011) Potential of near-infrared spectroscopy to characterize wood products. *Canadian Journal of Forest Research,* 41(11): 2150-2157. doi: 10.1139/X11-088

Danson F.M., Steven M.D., Malthus T.J. & Clark J.A. (1992) High-spectral resolution data for determining leaf water-content. *International Journal of Remote Sensing,* 13(3): 461-470. doi: 10.1080/01431169208904049

Defo M., Taylor A.M. & Bond B. (2007) Determination of moisture content and density of fresh-sawn red oak lumber by near infrared spectroscopy. *Forest Products Journal,* 57(5): 68-72

Demetriades-Shah T.H., Steven M.D. & Clark J.A. (1990) High-resolution derivative spectra in remote-sensing. *Remote Sensing of Environment,* 33(1): 55-64. doi: 10.1016/0034-4257(90)90055-Q

Denig J., Wengert E.M. & Simpson W.T. (2000) Drying hardwood lumber, U.S. Department of Agriculture, Forest Service, Forest Products Laboratory, Tech. Rep. FPL–GTR–118, Madison, WI, USA, 138 pages.

Dhanoa M., Lister S., Sanderson R. & Barnes R. (1994) The link between multiplicative scatter correction (MSC) and standard normal variate (SNV) transformations of NIR spectra. *Journal of Near Infrared Spectroscopy,* 2(1): 43-47. doi: 10.1255/jnirs.30

Diaz-Vaz J.E., Ananías R.A., Rodríguez S., Torres M., Fernández A. & Poblete H. (2009) Compression wood in *Pinus radiata* ii: Density and chemical composition. *Ciencia y tecnología,* 11(2): 139-151. doi: 10.4067/S0718-221X2009000200005

Downes G.M., Meder R., Bond H., Ebdon N., Hicks C. & Harwood C. (2011) Measurement of cellulose content, kraft pulp yield and basic density in eucalypt woodmeal using multisite and multispecies near infra-red spectroscopic calibrations. *Southern Forests,* 73(3-4): 181-186. doi: 10.2989/20702620.2011.639489

Duncker P. & Spiecker H. (2009) Detection and classification of Norway spruce compression wood in reflected light by means of hyperspectral image analysis. *IAWA Journal,* 30(1): 59-70. doi: 10.1163/22941932-90000203

Evans R. (1994) Rapid measurement of the transverse dimensions of tracheids in radial wood sections from Pinus-radiata. *Holzforschung,* 48(2): 168-172

Evans R. & Ilic J. (2001) Rapid prediction of wood stiffness from microfibril, angle and density. *Forest Products Journal,* 51(3): 53-57

Fernandes A., Lousada J., Morais J., Xavier J., Pereira J. & Melo-Pinto P. (2013a) Comparison between neural networks and partial least squares for intra-growth ring wood density measurement with hyperspectral imaging. *Computers and Electronics in Agriculture,* 94: 71-81. doi: 10.1016/j.compag.2013.03.010

Fernandes A., Lousada J., Morais J., Xavier J., Pereira J. & Melo-Pinto P. (2013b) Measurement of intra-ring wood density by means of imaging VIS/NIR spectroscopy (hyperspectral imaging). *Holzforschung,* 67(1): 59-65. doi: 10.1515/Hf-2011-0258

Forest Products Laboratory (2010) *Wood handbook: Wood as an engineering material.* Madison, WI, USA: U.S. Department of Agriculture, Forest Service, Forest Products Laboratory. 508 pages.

Fujimoto T., Kurata Y., Matsumoto K. & Tsuchikawa S. (2008) Application of near infrared spectroscopy for estimating wood mechanical properties of small clear and full length lumber specimens. *Journal of Near Infrared Spectroscopy,* 16(6): 529-537. doi: 10.1255/Jnirs.813

Fujimoto T., Yamamoto H. & Tsuchikawa S. (2007) Estimation of wood stiffness and strength properties of hybrid larch by near-infrared spectroscopy. *Applied Spectroscopy,* 61(8): 882-888. doi: 10.1366/000370207781540150

Geladi P., Burger J. & Lestander T. (2004) Hyperspectral imaging: Calibration problems and solutions. *Chemometrics and Intelligent Laboratory Systems,* 72(2): 209-217. doi: 10.1016/j.chemolab.2004.01.023

Gigac J. & Fiserova M. (2010) Identification of wood species by application of visible spectral reflectance. *Wood Research,* 55(1): 79-86

Gindl W., Teischinger A., Schwanninger M. & Hinterstoisser B. (2001) The relationship between near infrared spectra of radial wood surfaces and wood mechanical properties. *Journal of Near Infrared Spectroscopy,* 9(4): 255-261. doi: 10.1255/jnirs.311

Gowen A.A., Downey G., Esquerre C. & O'Donnell C.P. (2011) Preventing over-fitting in PLS calibration models of near-infrared (NIR) spectroscopy data using regression coefficients. *Journal of Chemometrics,* 25(7): 375-381. doi: 10.1002/Cem.1349

Grahn H. & Geladi P. (2007) *Techniques and applications of hyperspectral image analysis.* Chichester, UK: John Wiley & Sons. 390 pages.

Haartveit E.Y. & Flæte P.O. (2008) Near infrared spectroscopy (NIRS) as a tool for effective classification of wood In *51st International Convention of Society of Wood Science and Technology,* (Concepción, Chile), pp. 1-9

Haddadi A., Burger J., Leblon B., Pirouz Z., Groves K. & Nader J. (2015a) Using near infrared hyperspectral images on subalpine fir board - part 1: Moisture content estimation. *Wood Material Science & Engineering,* 10(1): 27-40. doi: 10.1080/17480272.2014.965743

Haddadi A., Burger J., Leblon B., Pirouz Z., Groves K. & Nader J. (2015b) Using near infrared hyperspectral images on subalpine fir board - part 2: Density and basic specific gravity estimation. *Wood Material Science & Engineering,* 10(1): 41-56. doi: 10.1080/17480272.2015.1011231

Haddadi A., Leblon B., Nader J., Pirouz Z. & Groves K. (2015c) Prediction of wood properties for thawed and frozen logs of quaking aspen, balsam poplar, and black spruce from near-infrared hyperspectral images. *Wood Science and Technology,* doi: 10.1007/s00226-015-0767-z

Hans G. (2015) *Real-time and non-destructive characterization of wood log properties using near-infrared and ground penetrating radar sensors*. Doctoral Thesis, University of New Brunswick, Fredericton, NB, Canada, 336 pages.

Hans G., Leblon B., Cooper P., LaRocque A., Nader J. & Stirling R. (2015a) Determination of moisture content and basic specific gravity of *Populus tremuloides* (Michx.) and *Populus balsamifera* (l.) logs using a portable near-infrared spectrometer. *Wood Material Science & Engineering,* 10(1): 3-16. doi: 10.1080/17480272.2014.916349

Hans G., Leblon B., Stirling R., Nader J., LaRocque A. & Cooper P. (2013) Monitoring of moisture content and basic specific gravity in black spruce logs using a handheld MEMS-based near-infrared spectrometer. *The Forestry Chronicle,* 89(5): 605-618. doi: 10.5558/tfc2013-112

Hans G., Redman D., Leblon B., Nader J. & LaRocque A. (2015b) Determination of log moisture content using early-time GPR signals. *Wood Material Science and Engineering*, 10(1): 112-129. doi: 10.1080/17480272.2014.939714

Hans G., Redman D., Leblon B., Nader J. & LaRocque A. (2015c) Determination of log moisture content using ground penetrating radar (GPR). Part 1. Partial least squares (PLS) method. In *Holzforschung*,0, doi: 10.1515/hf-2014-0286

Hans G., Redman D., Leblon B., Nader J. & LaRocque A. (2015d) Determination of log moisture content using ground penetrating radar (GPR). Part 2. Propagation velocity (PV) method. In *Holzforschung*,0, doi: 10.1515/hf-2014-0287

Hapke B. (1993) *Theory of reflectance and emittance spectroscopy.* Cambridge, England; New York, USA: Cambridge University Press. 455 pages.

Heigl N., Petter C.H., Rainer M., Najam-Ul-Haq M., Vallant R.M., Bakry R., Bonn G.K. & Huck C.W. (2007) Near infrared spectroscopy for polymer research, quality control and reaction monitoring. *Journal of Near Infrared Spectroscopy*, 15(5): 269-282

Hein P.R.G. (2012) Estimating shrinkage, microfibril angle and density of *eucalyptus* wood using near infrared spectroscopy. *Journal of Near Infrared Spectroscopy*, 20(4): 427-436. doi: 10.1255/jnirs. 1005

Hein P.R.G., Campos A.C.M., Trugilho P.F., Lima J.T. & Chaix G. (2009) Near infrared spectroscopy for estimating wood basic density in *eucalyptus urophylla* and *eucalyptus grandis*. *Cerne*, 15(2): 133-141. doi: abr./jun. 2009

Hoffmeyer P. & Pedersen J.G. (1995) Evaluation of density and strength of Norway spruce wood by near infrared reflectance spectroscopy. *Holz als Roh- und Werkstoff*, 53(3): 165-170. doi: 10.1007/BF02716418

Inagaki T., Schwanninger M., Kato R., Kurata Y., Thanapase W., Puthson P. & Tsuchikawa S. (2012) *Eucalyptus camaldulensis* density and fiber length estimated by near-infrared spectroscopy. *Wood Science and Technology*, 46(1-3): 143-155. doi: 10.1007/s00226-010-0379-6

Isaksson T., Brischke C. & Thelandersson S. (2013) Development of decay performance models for outdoor timber structures. *Materials and Structures*, 46(7): 1209-1225. doi: 10.1617/s11527-012-9965-4

Isaksson T. & Naes T. (1988) The effect of multiplicative scatter correction (msc) and linearity improvement in NIR spectroscopy. *Applied Spectroscopy*, 42(7): 1273-1284

Karttunen K., Leinonen A. & Sarén M.-P. (2008) A survey of moisture distribution in two sets of scots pine logs by NIR-spectroscopy. *Holzforschung*, 62(4): 435. doi: 10.1515/HF.2008.060

Kelley S.S., Jellison J. & Goodell B. (2002) Use of NIR and pyrolysis-mbms coupled with multivariate analysis for detecting the chemical changes associated with brown-rot biodegradation of spruce wood. *Fems Microbiology Letters*, 209(1): 107-111

Knudson R.M. & Chen L. (2001) Effect of aspen log moisture content on stranding, strand quality and properties of OSB, Forintek, Contract No. 2001-2322, Alberta Research Council, Edmonton, AB, Canada, 51 pages.

Kobori H., Gorretta N., Rabatel G., Bellon-Maurel V., Chaix G., Roger J.M. & Tsuchikawa S. (2013) Applicability of VIS-NIR hyperspectral imaging for

monitoring wood moisture content (MC). *Holzforschung,* 67(3): 307-314. doi: 10.1515/Hf-2012-0054

Kortum G. (1969) *Reflectance spectroscopy principles, methods, applications.* Berlin-Heidelberg, Germany: Springer-Verlag. 366 pages.

Kroll R.E., Ritter D.C., Gertjejansen R.O. & Au K.C. (1992) Anatomical and physical-properties of balsam poplar (*Populus-balsamifera* l) in minnesota. *Wood and Fiber Science,* 24(1): 13-24

Lamason, C., MacMillan, B., Balcom, B., Leblon, B., Pirouz, Z. 2014. Examination of water phase transitions in *Picea mariana* by magnetic resonance and magnetic resonance imaging, *Wood and Fiber Science*, 46: 1-14

Laurikkala J., Juhola M. & Kentala E. (2000) Informal identification of outliers in medical data, In *14th European Conference on Artificial Intelligence and 5th International Workshop on Intelligent Data Analysis in Medicine and Pharmacology IDAMAP-2000,* (Berlin, Germany), pp. 20-24

Leblon B., Adedipe O., Hans G., Haddadi A., Tsuchikawa S., Burger J., Stirling R., Pirouz Z., Groves K., Nader J. & LaRocque A. (2013) A review of near-infrared spectroscopy for monitoring moisture content and density of solid wood. *Forestry Chronicle,* 89(5): 595-606. doi: 10.5558/tfc2013-111

Léger F. & Amazouz M. (2003) An evaluation of wood kiln control practices, Natural Resources Canada, CANMET Energy Technology Center, 2003–047, Varennes, QC, Canada, 84 pages.

Lestander T.A., Lindeberg J., Eriksson D. & Bergsten U. (2008) Prediction of Pinus sylvestris clear-wood properties using NIR spectroscopy and biorthogonal partial least squares regression. *Canadian Journal of Forest Research,* 38(7): 2052-2062. doi: 10.1139/X08-047

Li Q.L., He X.F., Wang Y.T., Liu H.Y., Xu D.R. & Guo F.M. (2013) Review of spectral imaging technology in biomedical engineering: Achievements and challenges. *Journal of Biomedical Optics,* 18(10). doi: 10.1117/1.JBO.18.10.100901

Lindstrom S.W., Nilsson D., Nordin A., Nordwaeger M., Olofsson I., Pommer L. & Geladi P. (2014) Quality assurance of torrefied biomass using RGB, visual and near infrared (hyper) spectral image data. *Journal of Near Infrared Spectroscopy,* 22(2): 129-139. doi: 10.1255/jnirs.1100

Lopez G., Basterra L.A., Ramon-Cueto G. & de Diego A. (2014) Detection of singularities and subsurface defects in wood by infrared thermography. *International Journal of Architectural Heritage,* 8(4): 517-536

Martens H. & Naes T. (1989) *Multivariate calibration.* Chichester, UK: John Wiley & Sons. 438 pages.

Martens H., Nielsen J.P. & Engelsen S.B. (2003) Light scattering and light absorbance separated by extended multiplicative signal correction. Application to near-infrared transmission analysis of powder mixtures. *Analytical Chemistry,* 75(3): 394-404. doi: 10.1021/ac020194w

Martens H. & Stark E. (1991) Extended multiplicative signal correction and spectral interference subtraction - new preprocessing methods for near-infrared spectroscopy. *Journal of Pharmaceutical and Biomedical Analysis,* 9(8): 625-635

Meder R., Marston D., Ebdon N. & Evans R. (2010) Spatially-resolved radial scanning of tree increment cores for near infrared prediction of microfibril angle and chemical composition. *Journal of Near Infrared Spectroscopy,* 18(6): 499-505. doi: 10.1255/Jnirs.903

Mora C.R., Schimleck L.R., Clark A. & Daniels R.F. (2011a) Determination of basic density and moisture content of merchantable loblolly pine logs by near infrared spectroscopy. *Journal of Near Infrared Spectroscopy,* 19(5): 391-399. doi: 10.1255/Jnirs.947

Mora C.R., Schimleck L.R. & Isik F. (2008) Near infrared calibration models for the estimation of wood density in *Pinus taeda* using repeated sample measurements. *Journal of Near Infrared Spectroscopy,* 16(6): 517-528. doi: 10.1255/Jnirs.816

Mora C.R., Schimleck L.R., Isik F., Mahon J.M., Clark A. & Daniels R.F. (2009) Relationships between acoustic variables and different measures of stiffness in standing *Pinus taeda* trees. *Canadian Journal of Forest Research,* 39(8): 1421-1429. doi: 10.1139/X09-062

Mora C.R., Schimleck L.R., Yoon S.C. & Thai C.N. (2011b) Determination of basic density and moisture content of loblolly pine wood disks using a near infrared hyperspectral imaging system. *Journal of Near Infrared Spectroscopy,* 19(5): 401-409. doi: 10.1255/Jnirs.948

Moschler W.W. & Hanson G.R. (2008) Microwave moisture measurement system for hardwood lumber drying. *Drying Technology,* 26(9): 1155-1159. doi: 10.1080/07373930802266264

Natural Resources Canada (2015) The state of Canada's forests: Annual report 2014, Canadian Forest Service, G. o. Canada, Fo1-6/2014E, 63 pages.

Nystrom J. & Hagman O. (1999) Real-time spectral classification of compression wood in *Picea abies*. *Journal of Wood Science,* 45(1): 30-37. doi: 10.1007/Bf00579521

Olinger J.M. & Griffiths P.R. (1988) Quantitative effects of an absorbing matrix on near-infrared diffuse reflectance spectra. *Analytical Chemistry,* 60(21): 2427-2435

Olson J.R. & Arganbright D.G. (1977) Uniformity factor - proposed method for expressing variations in specific gravity. *Wood and Fiber,* 9(3): 202-210

Panshin A.J. & De Zeeuw C. (1980) *Textbook of wood technology: Structure, identification, uses, and properties of the commercial woods of the united states and Canada.* New York, USA: McGraw-Hill. 722 pages.

Pereira H., Graca J., & Rodrigues J.C., (2003) Wood chemistry in relation to quality,

Barnett J.R. and Jeronimidis G. (EDs.), *Wood quality and its biological basis* (53-86), Oxford; Boca Raton, FL, CRC Press.

Poke F.S. & Raymond C.A. (2006) Predicting extractives, lignin, and cellulose contents using near infrared spectroscopy on solid wood in *eucalyptus globulus*. *Journal of Wood Chemistry and Technology,* 26(2): 187-199. doi: 10.1080/02773810600732708

Ramasamy S. & Moghtaderi B. (2010) Dielectric properties of typical Australian wood-based biomass materials at microwave frequency. *Energy & Fuels,* 24: 4534-4548. doi: 10.1021/ef100623e

Richards J.A. & Jia X. (2006) *Remote sensing digital image analysis: An introduction.* Berlin, Germany: Springer. 420 pages.

Ross R.J. & Pellerin R.F. (1994) Nondestructive testing for assessing wood members in structures. A review, U.S. Department of Agriculture, Forest Service, Forest Products Laboratory, General Technical Report FPL-GTR-70, Madison, WI, USA, 42 pages.

Rowell R.M. (2013) *Handbook of wood chemistry and wood composites.* Boca Raton, USA: CRC Press. 687 pages.

Roy A., Ramasubramaniam R. & Gaonkar H.A. (2012) Empirical relationship between kubelka–munk and radiative transfer coefficients for extracting optical parameters of tissues in diffusive and nondiffusive regimes. *Journal of Biomedical Optics,* 17(11): 115006-115006. doi: 10.1117/1.JBO.17.11.115006

Russ A., Fiserova M. & Gigac J. (2009) Preliminary study of wood species identification by NIR spectroscopy. *Wood Research,* 54(4): 23-32

Ruz G.A., Estevez P.A. & Perez C.A. (2005) A neurofuzzy color image segmentation method for wood surface defect detection. *Forest Products Journal,* 55(4): 52-58

Salzer R. & Siesler H.W. (2009) *Infrared and Raman spectroscopic imaging.* Weinheim, Germany: John Wiley & Sons. 530 pages.

Sandberg K. & Sterley M. (2009) Separating Norway spruce heartwood and sapwood in dried condition with near-infrared spectroscopy and multivariate data analysis. *European Journal of Forest Research,* 128(5): 475-481. doi: 10.1007/s10342-009-0296-0

Saranpaa P. (2003) wood density and growth, Barnett J.R., and Jeronimidis G. (EDs.), *Wood quality and its biological basis* (87-117). Oxford; Boca Raton, FL: CRC Press.

Schimleck L.R., Evans R. & Ilic J. (2001) Application of near infrared spectroscopy to a diverse range of species demonstrating wide density and stiffness variation. *IAWA Journal,* 22(4): 415-429. doi: 10.1163/22941932-90000386

Schimleck L.R., Jones P.D., Clark A., Daniels R.F. & Peter G.F. (2005) Near infrared spectroscopy for the nondestructive estimation of clear wood properties of *Pinus taeda* l. From the southern united states. *Forest Products Journal,* 55(12): 21-28

Schwanninger M., Rodrigues J.C. & Fackler K. (2011) A review of band assignments in near infrared spectra of wood and wood components. *Journal of Near Infrared Spectroscopy,* 19(5): 287-308. doi: 10.1255/Jnirs.955

Shelbourne T., Evans R., Kibblewhite P. & Low C. (1997) Inheritance of tracheid transverse dimensions and wood density in radiata pine. *Appita Journal,* 50(1): 47-50

Sheng Y., Mian X., Yi-fei J., Guo-feng W. & Jun-wen P. (2011) Determination of holocellulose and alpha-cellulose contents in triploid clones of *Populus tomentosa*. Using NIRS. *Advanced Material Science and Technology, Pts 1 and 2,* 675-677: 329-332. doi: 10.4028/www.scientific.net/MSF.675-677.329

Shi Z.Q. & Anderson C.A. (2009) Scattering orthogonalization of near-infrared spectra for analysis of pharmaceutical tablets. *Analytical Chemistry,* 81(4): 1389-1396. doi: 10.1021/ac802105v

Shi Z.Q. & Anderson C.A. (2010) Pharmaceutical applications of separation of absorption and scattering in near-infrared spectroscopy (NIRS). *Journal of Pharmaceutical Sciences,* 99(12): 4766-4783. doi: 10.1002/Jps.22228

Skaar C. (1988) *Wood-water relations.* Berlin, Germany: Springer-Verlag. 283 pages.

So C.L., Via B.K., Groom L.H., Schimleck L.R., Shupe T.F., Kelley S.S. & Rials T.G. (2004) Near infrared spectroscopy in the forest products industry. *Forest Products Journal,* 54(3): 6-16

Sterenborg H.J.C.M., van Gemert M.J.C., Kamphorst W., Wolbers J.G. & Hogervorst W. (1989) The spectral dependence of the optical properties of human brain. *Lasers in Medical Science,* 4(4): 221-227. doi: 10.1007/BF02032451

Stirling R., Trung T., Breuil C. & Bicho P. (2007) Predicting wood decay and density using NIR spectroscopy. *Wood and Fiber Science,* 39(3): 414-423

Stuart B.H. (2004) *Infrared spectroscopy: Fundamentals and applications.* John Wiley & Sons. 203 pages.

Swierenga H., Wülfert F., de Noord O.E., de Weijer A.P., Smilde A.K. & Buydens L.M.C. (2000) Development of robust calibration models in near infra-red spectrometric applications. *Analytica Chimica Acta,* 411(1–2): 121-135. doi: 10.1016/S0003-2670(00)00718-2

Szymanska E., Saccenti E., Smilde A.K. & Westerhuis J.A. (2012) Double-check: Validation of diagnostic statistics for PLS-DA models in metabolomics studies. *Metabolomics,* 8(1): S3-S16. doi: 10.1007/s11306-011-0330-3

Thumm A., Riddell M., Nanayakkara B., Harrington J. & Meder R. (2010) Near infrared hyperspectral imaging applied to mapping chemical composition in wood samples. *Journal of Near Infrared Spectroscopy,* 18(6): 507-515. doi: 10.1255/Jnirs.909

Thygesen L.G. (1994) Determination of dry matter content and basic density of Norway spruce by near infrared reflectance and transmittance spectroscopy. *Journal of Near Infrared Spectroscopy,* 2: 127–135. doi: 10.1255/jnirs.39

Thygesen L.G. & Lundqvist S.O. (2000a) Nir measurement of moisture content in wood under unstable temperature conditions. Part 1. Thermal effects in near infrared spectra of wood. *Journal of Near Infrared Spectroscopy,* 8(3): 183-189. doi: 10.1255/jnirs.277

Thygesen L.G. & Lundqvist S.O. (2000b) Nir measurement of moisture content in wood under unstable temperature conditions. Part 2. Handling temperature fluctuations. *Journal of Near Infrared Spectroscopy,* 8(3): 191-199. doi: 10.1255/jnirs.278

Trung T. & Leblon B. (2011) The role of sensors in the new forest products industry and forest bioeconomy. *Canadian Journal of Forest Research-Revue Canadienne De Recherche Forestiere,* 41(11): 2097-2099

Tsuchikawa S. (2007) A review of recent near infrared research for wood and paper. *Applied Spectroscopy Reviews,* 42(1): 43-71. doi: 10.1080/05704920601036707

Tsuchikawa S., Hayashi K. & Tsutsumi S. (1996) Nondestructive measurement of the subsurface structure of biological material having cellular structure by using near-infrared spectroscopy. *Applied Spectroscopy,* 50(9): 1117-1124. doi: 10.1366/0003702963905114

Tsuchikawa S., Inoue K., Noma J. & Hayashi K. (2003) Application of near-infrared spectroscopy to wood discrimination. *Journal of Wood Science,* 49(1): 29-35. doi: 10.1007/s100860300005

van Gemert M.J.C. & Star W.M. (1987) Relations between the Kubelka-Munk and the transport equation models for anisotropic scattering. *Laser Life Sci,* 1: 287-298

Via B.K., Shupe T.F., Groom L.H., Stine M. & So C.L. (2003) Multivariate modelling of density, strength and stiffness from near infrared spectra for mature, juvenile and pith wood of Longleaf pine (*Pinus palustris*). *Journal of Near Infrared Spectroscopy,* 11(5): 365-378

Walker J.C.F. (2006) *Primary wood processing: Principles and practice.* Dordrecht, The Netherlands: Springer. 596 pages.

Wang X., Ross R.J., Erickson J.R., Forsman J.W., McGinnis G.D. & Groot R.C.D. (2000) Nondestructive methods of evaluating quality of wood in preservative-treated piles, U.S. Department of Agriculture, Forest Service, Forest Products Laboratory, F. Service, Research Note FPL-RN-0274, Madison, WI, USA, 11 pages.

Watanabe K., Kobayashi I., Kuroda N., Harada M. & Noshiro S. (2012a) Predicting oven-dry density of sugi (*Cryptomeria Japonica*) using near infrared (NIR) spectroscopy and its effect on performance of wood moisture meter. *Journal of Wood Science,* 58(5): 383-390. doi: 10.1007/s10086-012-1268-4

Watanabe K., Mansfield S.D. & Avramidis S. (2012b) Wet-pocket classification in *Abies lasiocarpa* using spectroscopy in the visible and near infrared range. *European Journal of Wood and Wood Products,* 70: 61-67. doi: 10.1007/s00107-010-0490-2

Wei Q., Leblon B. & LaRocque A. (2011) On the use of X-ray computed tomography for determining wood properties: A review. *Canadian Journal of Forest Research-Revue Canadienne De Recherche Forestiere,* 41(11): 2120-2140. doi: 10.1139/X11-111

Wei, Q., Zhang, S.Y., Chui, Y.H., and Leblon, B. (2009) Reconstruction of three-dimensional images of internal log characteristics by means of successive two-dimensional log computed tomography images. *Holzforschung,* 63(5): 575-580

Welch A.J. & van Gemert M.J.C. (2011) *Optical-thermal response of laser-irradiated tissue.* Dordrecht, Heidelberg, Germany; London, UK; New York, USA: Springer. 972 pages.

Williamson G.B. & Wiemann M.C. (2010) Measuring wood specific gravity ... Correctly. *American Journal of Botany,* 97(3): 519-524. doi: 10.3732/Ajb.0900243

Wold S., Antti H., Lindgren F. & Ohman J. (1998) Orthogonal signal correction of near-infrared spectra. *Chemometrics and Intelligent Laboratory Systems,* 44(1-2): 175-185. doi: 10.1016/S0169-7439(98)00109-9

Wold S., Sjostrom M. & Eriksson L. (2001) Pls-regression: A basic tool of chemometrics. *Chemometrics and Intelligent Laboratory Systems,* 58(2): 109-130. doi: 10.1016/S0169-7439(01)00155-1

Workman J. & Weyer L. (2007) *Practical guide to interpretive near-infrared spectroscopy.* CRC Press. p.

Workman J. & Weyer L. (2012) *Practical guide and spectral atlas for interpretive near-infrared spectroscopy*. Taylor & Francis. 326 pages.

Xu Q.H., Qin M.H., Ni Y.H., Defo M., Dalpke B. & Sherson G. (2011) Predictions of wood density and module of elasticity of balsam fir (*Abies balsamea*) and black spruce (*Picea mariana*) from near infrared spectral analyses. *Canadian Journal of Forest Research*, 41(2): 352-358. doi: 10.1139/X10-215

Yin Y., Nagao H., Liu X. & Nakai T. (2010) Mechanical properties assessment of *cunninghamia lanceolata* plantation wood with three acoustic-based nondestructive methods. *Journal of Wood Science*, 56(1): 33-40. doi: 10.1007/s10086-009-1067-8

Chapter 2. Using Near-Infrared Hyperspectral Images on Subalpine Fir Board – Part 1: Moisture Content Estimation[1]

2.1. Abstract

In this study, moisture content (MC) images of subalpine fir (*Abies lasiocarpa* Hook) boards were derived from near-infrared hyperspectral images (NIR-HSI) in the 947-1637 nm range. 107 cubic samples with the size of 4 cm were prepared from 14 boards. All samples were dried to various moisture contents during several steps until being completely dried. Hyperspectral images and weight measurements were acquired over each sample at each drying step. The samples have MC ranging from 1% to 137% (dry basis). The images were first calibrated into reflectance. Then, bad pixels were found and replaced by a corrected value using a median filter. A modified version of the *boxplot* method was used to find abnormal spectra that were then removed. The remaining spectra were converted into absorbance spectra. They were then split into a calibration and a validation data set according to the boards they were extracted from to build and validate a partial least squares (PLS) regression model between the near-infrared absorbance spectra and the measured MCs. The PLS model was applied first to the sample images, then to the whole board images in order to produce 2D images of MC.

---

[1] This chapter was published in *Wood Material Science & Engineering* (Vol 10, issue 1, page 27-40, 2015) under the following authorship: Ataollah Haddadi, James Burger, Brigitte Leblon, Zarin Pirouz, Kevin Groves, and Joseph Nader. doi: 10.1080/17480272.2014.965743. It is reproduced with the permission of the Taylor & Francis Group (see letter permission in Appendix D)

2.2. Introduction

Optimization of several manufacturing operations in the wood products industry, such as log sorting, pulp yield assessment, scaling, and grading of the wood products can be improved by getting information on wood physical and chemical properties. Among all the quality-related wood properties, moisture content (MC) is one of the most important properties since it affects several processes, such as transportation and drying (Denig et al., 2000). It has also an influence on the wood physical and mechanical properties, on the resistance to biological deterioration, and on the non-stability in dimension (Panshin and De Zeeuw, 1980, Bowyer et al., 2007, Isaksson et al., 2013).

Oven-drying of wood samples is the most universal method for estimating MC, but it is destructive and time-consuming (Skaar, 1988). Electrical moisture meters exist, but they cannot well estimate MC above the fiber saturation point (FSP). At FSP, there is no free water (liquid water in cell lumina or cavities), but cell walls are completely saturated. For most of the wood species, FSP is around 30% (Panshin and De Zeeuw, 1980, Forest Products Laboratory, 2010). An alternative method to predict MC above and below FSP is to use systems that are based on near-infrared spectroscopy (NIRS) protocols. NIRS systems have been already tested to estimate MC of black spruce (*Picea mariana* Mill.) disks (Hans et al., 2013) and loblolly pine (*Pinus taeda* L.) disks (Mora et al., 2008, Mora et al., 2011a), but they only provide spot measurements which cannot reflect the spatial variability of moisture content in the sample. Such variability is important to monitor for several wood manufacturing processes (Olson and Arganbright, 1977, Panshin and De Zeeuw, 1980). For example, in a single species, the sapwood

which is close to the bark of the tree has living cells with high amount of water and minerals, while the heartwood, which is the inactive part of the tree has low MC (Panshin and De Zeeuw, 1980).

Hyperspectral imaging systems allow measuring the spatial distribution of wood properties across the products through a non-destructive, contactless, and real-time method. Hyperspectral images (HSI), also called hyper cubes, record reflectance spectra for each pixel of the target surface over 100's of wavelengths (Geladi et al., 2004, Salzer and Siesler, 2009). The acquired spectra have a narrow spectral (hyperspectral) sampling, e.g. less than 10 nm. Hyperspectral systems are better than multispectral broadband systems, because they capture more than 100 spectral bands continuously in a fine resolution for each pixel, while multispectral broadband systems capture limited spectral bands in a coarse spectral resolution (Chang, 2007). The fine resolution of the hyperspectral data allows derivative analysis which is useful to resolve overlapping spectra to better separate components of the global spectrum (Demetriades-Shah et al., 1990).

Hyperspectral imaging systems have been tested to identify compression wood in Norway spruce (*Picea abies* L.) and in Scot pine (*Pinus sylvestris* L.) lumber (Nystrom and Hagman, 1999). The wavelength range of the system was between 400 and 710 nm with a spectral resolution of 1.2 nm. The camera was set at 70 cm from the wood surface and provided images with a spatial resolution of 0.45×2.5 mm in cross-section and along the lumber, respectively. Hyperspectral imaging was also used for detecting compression wood in Norway spruce stem cross-sections (Duncker and

Spiecker, 2009). The range of wavelengths was between 400 nm and 1000 nm with a spectral resolution of 5 nm. The spatial resolution of the images was less than 0.1 mm. More recently, these systems have been used to map the chemical composition of wood (Thumm et al., 2010). These authors collected spectra over the range of 900-1700 nm with a 3.6 nm spectral resolution to provide the distribution of lignin, galactose, and glucose. The camera was set at 49.5 cm above the sample surface and provided images with a spatial resolution of 1.05 mm. Mora et al. (2011b) used a hyperspectral imaging system working in the 1000-1700 nm range with a spectral resolution of 5 nm to map MC and density of loblolly pine (*Pinus Taeda* L.) disks. In order to get the spatial resolution of less than 1 mm, the camera was set at 1.5 m above the target. Kobori et al. (2013) mapped MC of European beech (*Fagus sylvatica* L.) and Scots pine (*Pinus sylvestris* L.) disk cross-sections with an imaging system that works in the 400-1000 nm spectral domain with a 3.7 nm spectral resolution. The spatial resolution of the images was around 0.06 x 0.11 mm.

This paper presents a method to estimate MC images from NIR-HSIs that were acquired by an imaging spectrometer in the 947-1637 nm wavelength range. The images were acquired over subalpine fir (*Abies lasiocarpa* Hook) board samples and entire boards and processed using a new method that includes the use of median filter to find and replace bad pixels and of a modified version of the *boxplot* method to find abnormal spectra. In addition, our study used samples that have MCs ranging from 1 to 137% (dry basis) while other studies on the use of NIR HSIs only used samples having a limited range of MCs (45-65% for (Mora et al., 2011b), 23-121% in Kobori et al. (2013)). Our

MC range is within literature ranges, as the maximum MC for subalpine fir varies from 98% (Watanabe et al., 2012) to 165% (Alkan et al., 2007).

Subalpine fir is native to western Canada and is gaining economic importance as the supply of lodgepole pine is reduced by the mountain pine beetle infestation. It is marketed as kiln-dried lumber and belongs to the group of spruce-pine-fir (SPF) species, which are used for structural components. Drying subalpine fir boards is difficult because they may contain wet-pockets. The drying rate of wet-pockets is relatively low and requires longer drying to reach desired moisture contents. Bacteria are suspected to be the main cause for wet-pockets which have higher MC compared to other board regions (Ward and Pong, 1980, Watanabe et al., 2012). Because they are located in some regions of the lumber or board, but not in the entire of the board, they produce an uneven MC distribution that leads to uneven drying rates and shrinkage within boards, which in turn leads to degradation and value loss. The only known method to avoid degradation is to separate boards with wet-pockets for drying at substantially lower rates. Therefore, a good estimation of the spatial variability of the lumber or board MC will allow better optimization of the kiln drying process. Such estimation requires the use of imaging systems as spot measurement systems cannot measure spatial variability.

2.3. Materials and methods

2.3.1. Sampling and moisture measurements

The samples used for this study were extracted from 14 subalpine fir *(Abies lasiocarpa* Hook) boards having a size of 12×4×275 cm^3 (Figure 2-1). All boards were

first planned and then cut in two or three samples at different locations by a handheld circular saw mounted with a laser that helped an accurate cutting of the samples. As shown in Figure 2-1, the samples were not extracted from the board ends as these often dry faster than the other parts of the board. Also samples with visual defects, such as decay and knots, were excluded from the experiment.

The samples have a too high MC variability and thus were recut in three smaller samples with the size of 4×4×4 cm^3 to obtain samples with homogeneous MC. Before cutting the boards, they were all imaged by an X-ray system in order to find homogeneous sections of the boards without any defect or abnormality in terms of wetness, knots or density. After cutting the samples, they were again visually checked to eliminate those with decay or knots. The boards were acquired once and samples were cut in 1 day. Each sample was then subjected to the drying cycle, which took about two weeks to complete.

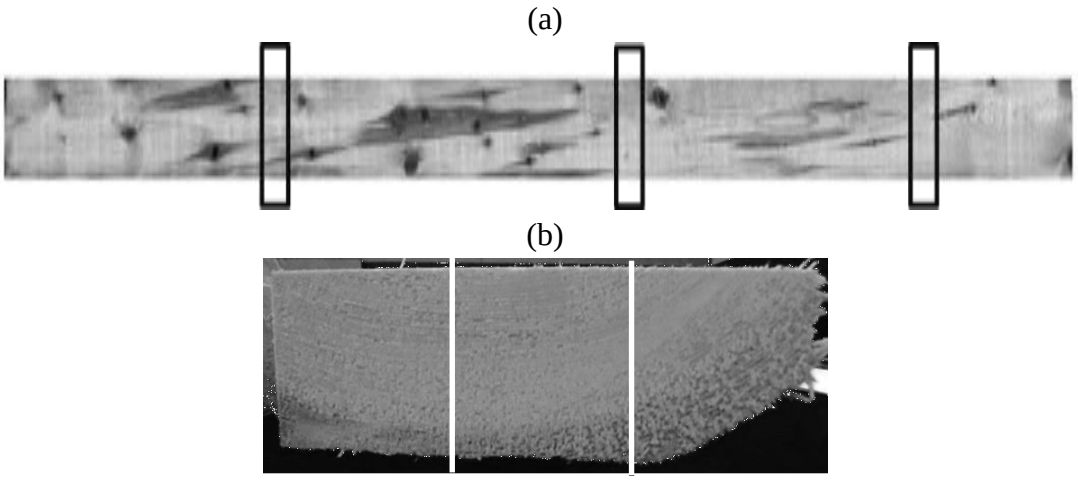

Figure 2-1: Location of the samples extracted from the whole board (a) tangential section view and (b) cross-section view.

In total, hundred and seven 4×4×4 cm^3 samples were extracted from the 14 boards. In order to get all ranges of MCs, these samples were dried in various steps to reach various MCs. There were 20h between two subsequent drying steps. We tested a shorter time of 5h as in Kobori et al. (2013), but the difference between two successive fresh weights was not significant. Indeed, our samples were larger than the Kobori et al. (2013) samples. For the first two steps, the samples were air-dried at 20°C and for the last steps, the samples were oven-dried at increasing temperatures from 25°C to 103°C.

Image acquisition was carried out at each drying step on the sample radial section. It was followed by measuring the sample fresh weight using an electronic scale with 0.01 g sensitivity. The samples were kept in a dry location during measurements to avoid absorbing moisture from the environment. Indeed, all the experiments were carried out at FPInnovations, Vancouver, BC in August 2012, when the relative humidity can be high enough (from 60 to 90%) to influence the sample moisture. Furthermore, after the oven-drying step, the samples were cooled down to room temperature. At the last drying step, the oven-dry weight and moisture content (in percentage of the dry weight) of each sample were determined following *Method A* of ASTM-D4442–07 (2009) by:

$$MC(\%\, dry\ basis) = \frac{M_{wet} - M_{dry}}{M_{dry}} * 100$$

Equation 2.1

Where M_{wet} is the wet weight (g) of the sample and M_{dry} is the weight (g) of the oven-dry sample.

The resulting moisture content (% dry basis) varied between 1.0 % and 137.0%, with a mean value of 44.03% and a standard deviation of 28.82%. Figure 2-2 presents the drying rate for three samples that were extracted from board 8 and 14, respectively. We can see that the initial MC of the two samples extracted from board 14 has a difference of 30% because they were not located on the same location in the board.

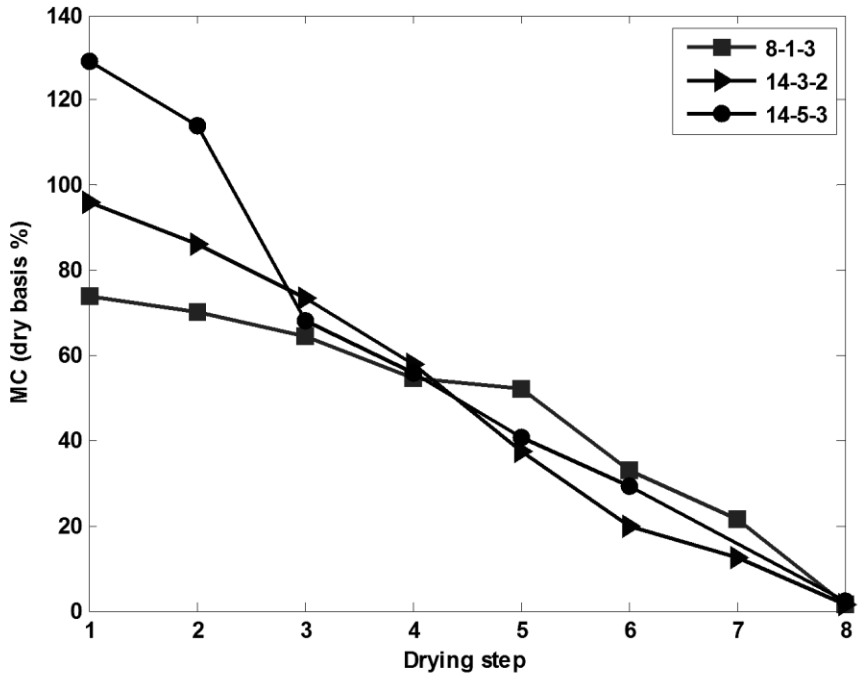

Figure 2-2: Drying curves of three small samples extracted from board 8 and 14, respectively.

After each image acquisition of small samples, the whole boards were also imaged with the same setting of the camera.

2.3.2. Image acquisition

Hyperspectral images of wood were acquired using the *HyperSee* software (*Burgermetrics, Latvia*, www.burgermetrics.com) working with an NIR hyperspectral system (*Spectral Imaging Ltd., FIN–90571 Oulu, Finland*). The system is a combination of a *N17E ImSpector* imaging spectrograph, and a temperature stabilized *InGaAs* camera (Figure 2-3).

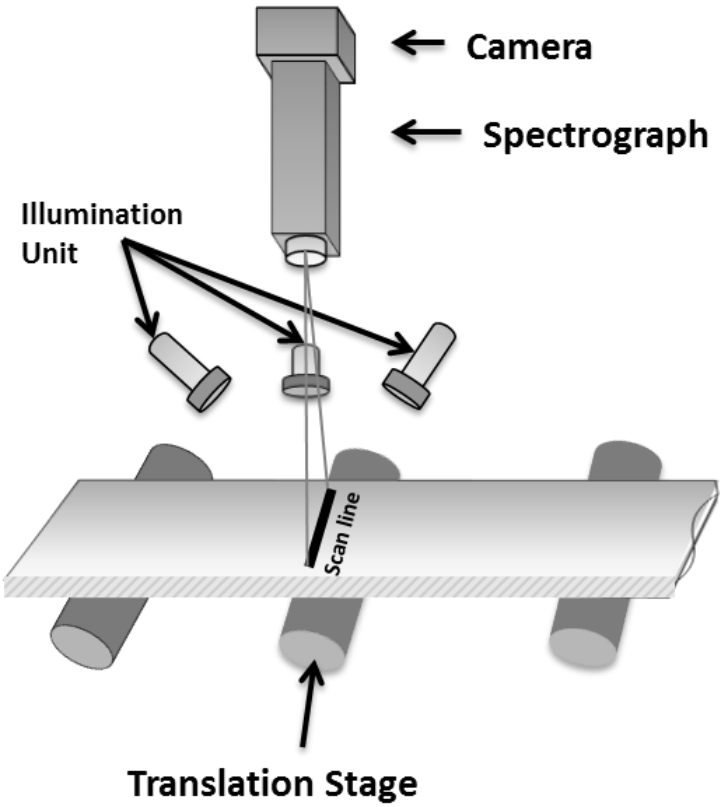

Figure 2-3: Main components of the hyperspectral imaging system.

The camera takes images by pushbroom type line scans in 320 pixels and 256 wavelength channels. The first four and the last 41 wavelength channels were too noisy.

The corresponding SNR was less than 10, while the signal to noise ratio (SNR) for the other wavelengths were higher than 200. The retained 210 channels are related to 138 wavelengths between 947nm and 1637 nm, since the instrument has a spectral interval of 3.3 nm. In addition to the camera and spectrograph, two more components should operate properly to get a high quality hyper cube image: the translation stage and the illumination unit. The line-scan camera measure spectral information in one spatial dimension. The second spatial dimension is acquired by moving the target by a linear translation stage, perpendicular to the camera imaging line. Therefore, the resolution in this direction depends on the speed on the translation stage. The height and focus of the camera were modified by trials and errors to get sharp and high quality images with a minimum of one mm pixel size over the entire wood sample. For both the small samples and the whole board, the camera was positioned at 48 cm height above the conveyor surface and has a fore lens having a focal length of 22.5 mm and a constant field of view of 17.5°. Such setting allows scanning 15 cm width objects. The pixel size in the direction of the scan line was 0.6 mm. By adjusting the speed of conveyor to almost 10 mm/s, the pixel size in this direction was set to 1.0 mm, with a number of frames per second for the camera of 5 frames/s. The 5 frames were averaged to improve the signal-to-noise ratio. The final pixel size was 1.0×0.6 mm, which allows observing the differences between latewood and earlywood on the imaged samples. Latewood and earlywood are formed during the winter and summer, respectively (Panshin and De Zeeuw, 1980). They produce tissues having a different size of cell walls and lumina because water availability and weather conditions are different in summer and winter.

The illumination unit should provide homogeneous light over the imaged spot of the camera. High intensity light can cause detector saturation in some wavelengths and low intensity light leads to low signal to noise ratios. A sufficient and homogeneous light over sample was provided by three *Analytical Spectral Devices* (ASD) (http://www.asdi.com/) *PRO LAMP* studio lights around the imaging spot of the camera. They are 70 W quartz-tungsten-halogen light sources with integrated reflector. The stability of the light source during image acquisition was controlled by acquiring images using the same setting over a white *Spectralon* panel (*Spectralon Co.*, www.labsphere.com). The images of the white and black panel were recorded after each sample image acquisition. The white panel has a reflectance of more than 99% in the near-infrared range. The stability of the detectors of the camera was analyzed by the white panel images at different times. We found that the sensitivity of the first detector was low and that this detector did not work very well. However, this detector had no effect on the quality of the images because it corresponds to the first mm from the edge of the image that do not image the wood sample.

Since acquiring individual sample images would be time consuming or leading to changes in sample MC at each drying step, these sample images were acquired over 15 to 21 samples at the same time (Figure 2-4). Some spaces were made between samples to prevent the influence of each sample on its neighbors and to distinguish them easily for further analysis. All the samples had a leveled horizontal surface to avoid any illumination effect on unlevelled surfaces.

Figure 2-4: Image of individual samples.

After 8 drying steps, 856 small images associated with their MC value were collected. We also acquired images of each whole board using the same camera setting.

2.3.3. Image processing

The flowchart of Figure 2-5 gave the main image processing steps that include: 1) image calibration, 2) recovering bad pixels that produce extreme reflectance values at some wavelengths, 3) delineating the small samples on each image; and 4) removing abnormal spectra. The whole image processing was performed in *MATLAB 7.12.0 (970 West 190th Street, Suite 530, Torrance, CA 90502, U.S.)* and *ENVI-IDL* image processing software (*Exelis Visual Information solution, Boulder, Colorado, USA*).

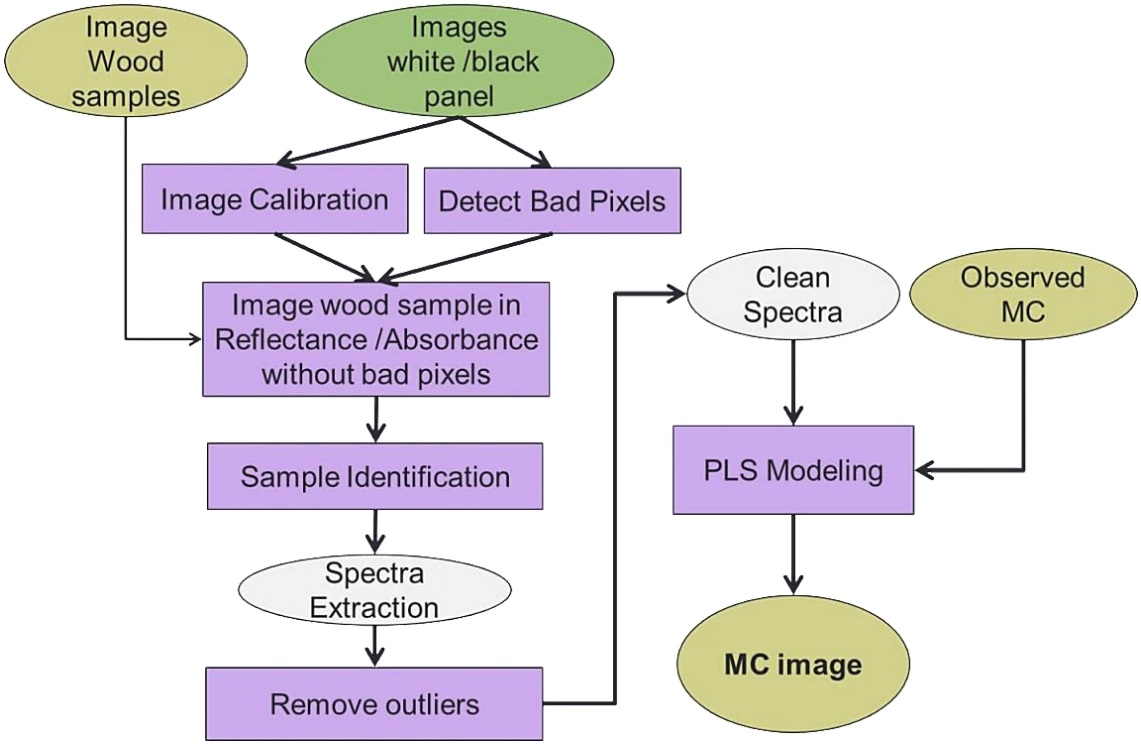

Figure 2-5: Flowchart of the image processing method used in the study.

2.3.3.1. Image calibration

The image calibration includes translating the digital numbers (DN) of the acquired images into reflectance and normalization of the detector response curve. The second operation is needed because of the non-uniformity of the light source and detector sensitivity. The calibration of the images into reflectance images requires at least one image over a white reference panel and one panel over a black reference panel, both having a known reflectance. Both reference panels should be large enough to cover the whole sample imaged by the camera and should have a highly homogeneous reflectance. The images of the white and black reference panels should be acquired each time before acquiring the sample images. The black panel image was produced by

covering the lens with a black cap, while the white panel image was acquired over the *Spectralon* panel. In both cases, 50 frames were acquired with the same setting as for the sample images. The conversion of the image DNs into reflectances was then computed by:

$$R = (X - B) / (\mathrm{W} - \mathrm{B})$$

Equation 2.2

where $\boldsymbol{R}$ is the true reflectance vector of the sample, $\boldsymbol{X}$ is the raw DN vector of the sample, and $\boldsymbol{B}$ and $\boldsymbol{W}$ are the vectors representing the reflectance spectra of the black and white panels, respectively.

2.3.3.2. Bad pixels

The near-infrared wood spectra exhibited random reflectance maxima and minima at some wavelengths, called here "*bad pixels*". They are due to the following causes: (i) the detector saturates, (ii) the detector does not measure any reflectance, (iii) the detector always measures the same reflectance value, and (iv) the detector measures only a proportion of the true reflectance (Grahn and Geladi, 2007). These extreme reflectance values can be replaced by the reflectance of neighbor wavelength channels (Burger, 2009). Since the position of the bad pixels is the same in all images, they can be found using the black and white panel images and their position can then be used for all the images acquired over the wood samples. To find the bad pixels, we considered the raw DN image of the black panel and the reflectance images of both the white and black panels. We did not use the raw image of the white panel because it is a measure of the illumination radiance which is not uniform across the wavelengths and is more

related to the illumination source than to the sensor. By contrast, the raw DN image of the black panel corresponds to the dark current of the sensor and thus well represents the instrumental noise. Also, the reflectance image of each panel is useful as it gives a uniform reflectance value across the wavelengths (0% for the black panel and 99% for the white panel). For all these three images, the local reflectance minima or maxima corresponding to the bad pixels were found by comparing the measured spectra to the median spectra. Wavelengths which do not satisfy the 95% confidence level of the measurements in each image were considered as bad wavelengths that are related to bad pixels. Based on this method, 2692 bad cases (wavelength*pixel), i.e., 4% of the total number of cases were found and considered for recovering (Figure 2-6). Figure 2-6 shows that the wavelength channels higher than #120, i.e., higher than 1350 nm, contain a higher proportion of bad pixels, and that the wavelength channels between #124 (1352.6 nm) and #128 (1365.85 nm) have extreme reflectance values for all the pixels.

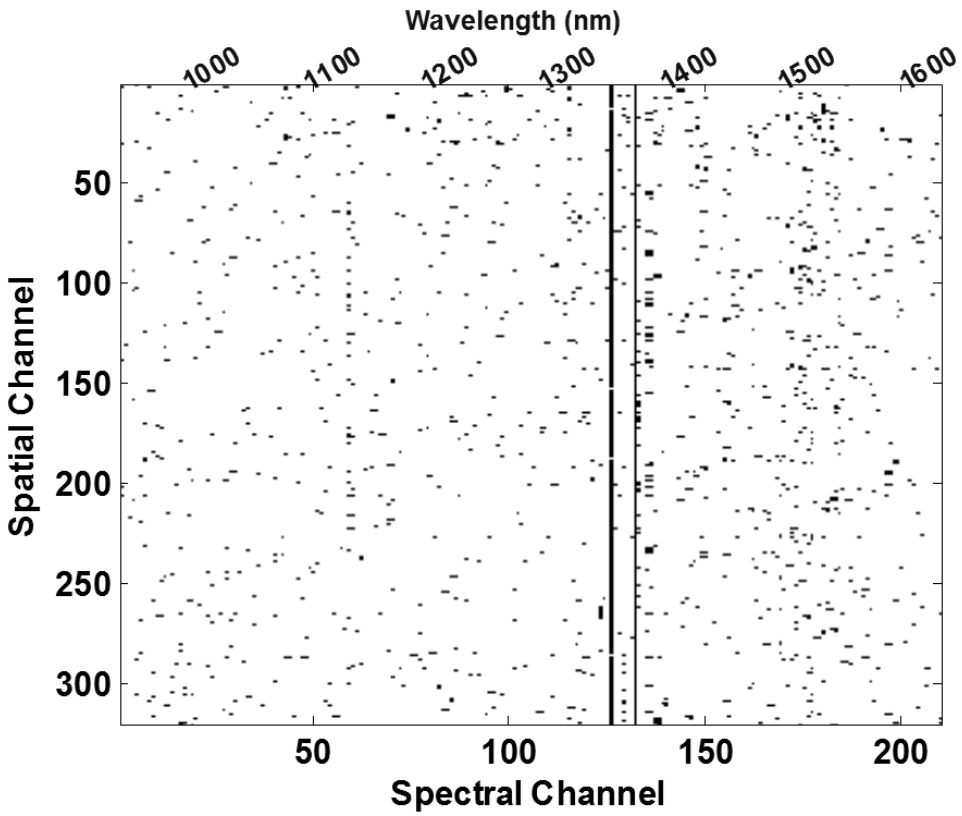

Figure 2-6: Location of the bad pixels on the imaged frame (number of bad cases = 2692, number of good cases = 67200).

After finding the wavelengths corresponding to extreme reflectance values, the corresponding reflectance values need to be recovered, i.e., replaced by the reflectance value of their neighbors' wavelengths. Before recovering the reflectance values of the bad pixels, we first transformed the wavelength channel number into true wavelength (in nm) using the conversion table of the camera manual. The corrected reflectance values were computed using a 5x1 median filter. Indeed, the median filter can work with non-linear data and considers the statistical data distribution (Richards and Jia, 2006). A median filter sorts the reflectance values within the bad pixel window in descending or ascending order, and the middle of the sorted data is selected as the filter output. The

output excludes the values which do not fit the statistical pattern of the local neighborhood. It should be noted that the median filter was not applied to the whole spectrum and only bad pixels were recovered, like it is shown in Figure 2-7.

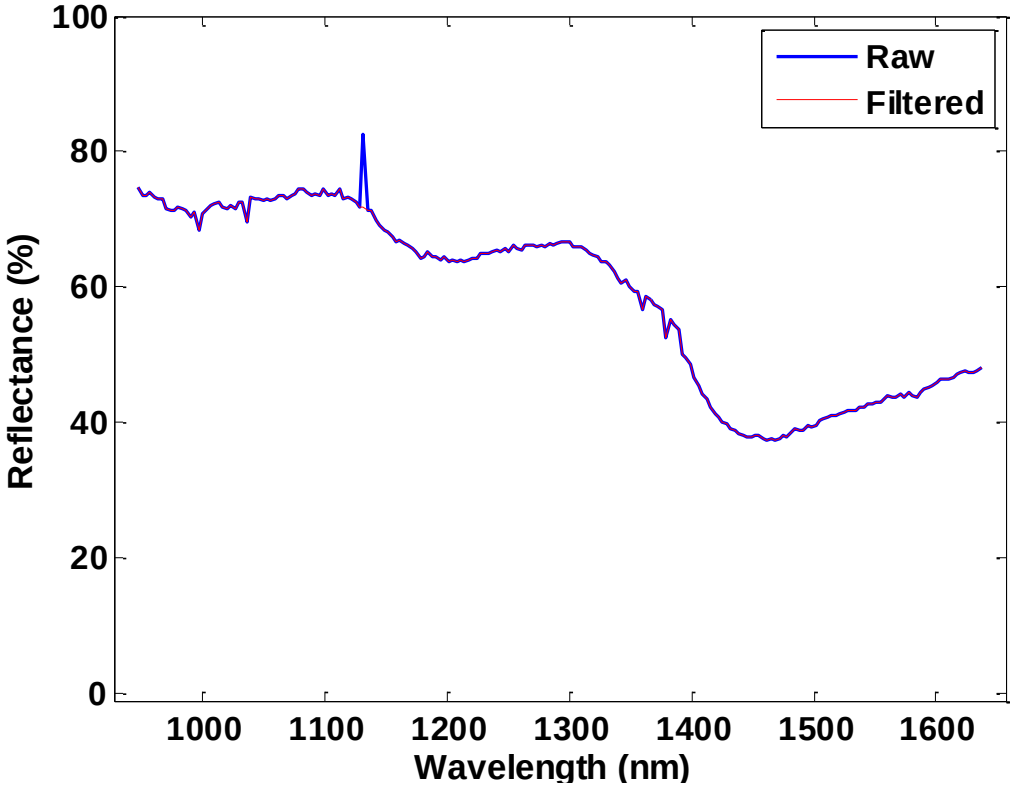

Figure 2-7: Raw and median-filtered spectra.

2.3.3.3. Finding small samples in each image

Each sample image has on average 1700 pixels that correspond to the 15 to 21 small samples that were imaged. It needs to be divided into one separate file for each sample for further processing. This operation was manually performed in *ENVI* using a rectangle having a size of 35 pixels by 50 pixels (or 3.5 by 3.5 cm). This step does not

need an automated operation as it was only done one time for the sample images and is not to be performed in real industrial settings where the whole boards will be imaged.

2.3.3.4. Abnormal spectra

Generally, images acquired with digital imaging sensor arrays have “dead” pixels which produce abnormal spectra (Burger and Geladi, 2005). In Figure 2-8, all the spectra are associated with the same wood sample, but some of them are distinctively different than the majority of the spectra. They correspond to the following cases: (1) the sensor is not measuring at the pixel location; (2) the sensor is producing an abnormal DN value at the pixel location; (3) there are barks, knots and other defects in the imaged wood at the pixel location.

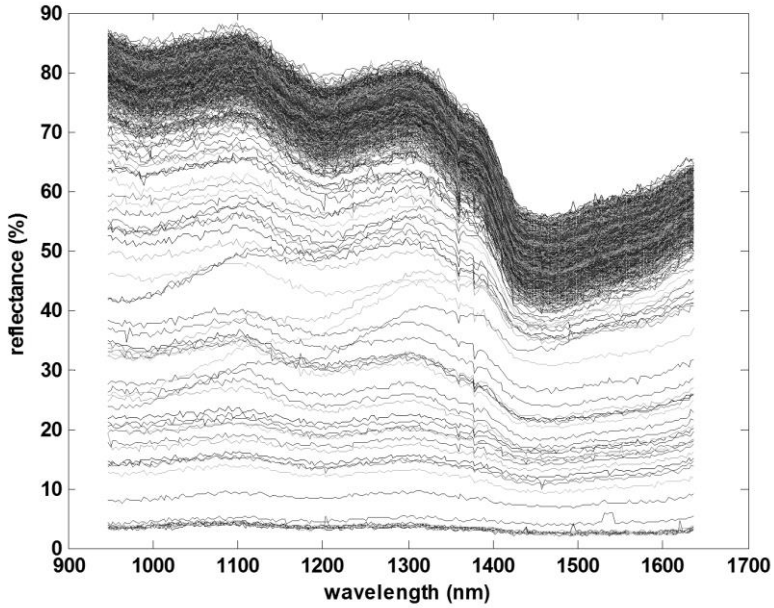

Figure 2-8: Reflectance spectra for a sample that include also the abnormal spectra.

Several methods have been proposed to identify these abnormal spectra. In a study using hyperspectral images over loblolly pine wood disks, Mora et al. (2011b) visually delineated them which are mainly included the bark region, but such method can be tedious. In our study, we used a combination of the principal component analysis (PCA) and the *boxplot* method of Laurikkala et al. (2000). First, the spectra are transformed using PCA into a new space that has uncorrelated axis. As shown in Figure 2-9, such PCA transformation allows easily identifying abnormal spectra as being the spectra that are located outside the cloud, which corresponds to the "good" spectra in the two-dimension plane made by the first and second principal components.

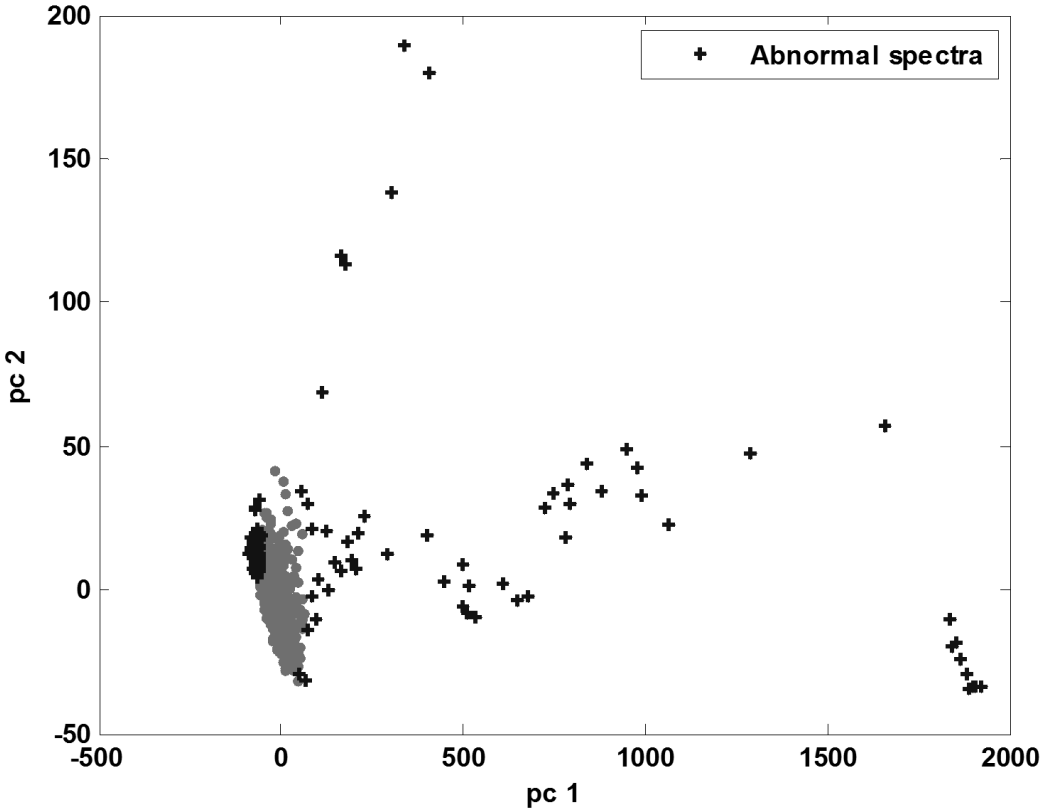

Figure 2-9: Location of the spectra in the PC1/PC2 plane allowing identification of abnormal spectra.

The Mahalanobis distance between the cloud point median and the individual spectra can then be calculated by (Richards and Jia, 2006):

$$D = (X - X_M)^T \Sigma^{-1} (X - X_M)$$

Equation 2.3

where D is the Mahalanobis distance of a spectrum from the cloud point median, **X** are the PC1 and PC2 vectors for an individual spectrum, $\mathbf{X_M}$ is the median PC1 and PC2 vectors for all spectra, Σ is the covariance matrix of PC1 and PC2. By contrast to the Euclidean distance, the Mahalanobis distance allows considering the weight of the PCs, PC1 having a higher weight in the distance calculation than PC2.

These distances are then used into the *boxplot* method of Laurikkala et al. (2000) as follows. First, the first and third quartiles of the distance distribution are computed by:

$$q_1 = 0.25 * (N - 1)$$
$$q_3 = 0.75 * (\mathrm{N} - 1)$$

Equation 2.4

where N is the number of data, q_1 and q_3 are the first and third quartiles of the distance distribution.

These quartiles represent the distance range that corresponds to 50% of the distances (Figure 2-10). These quartiles are then used to compute the maximum distance which is the acceptable distance for an individual spectrum not to be considered as an abnormal spectra by:

$$\mathrm{MAX} = q_3 + 1.5 * (q_3 - q_1)$$

Equation 2.5

where MAX is the maximum distance, which is the acceptable distance for an individual spectrum not to be considered as an abnormal spectrum. The abnormal spectra are spectra that have a distance higher than the maximum distance as shown in the box plot of Figure 2-10.

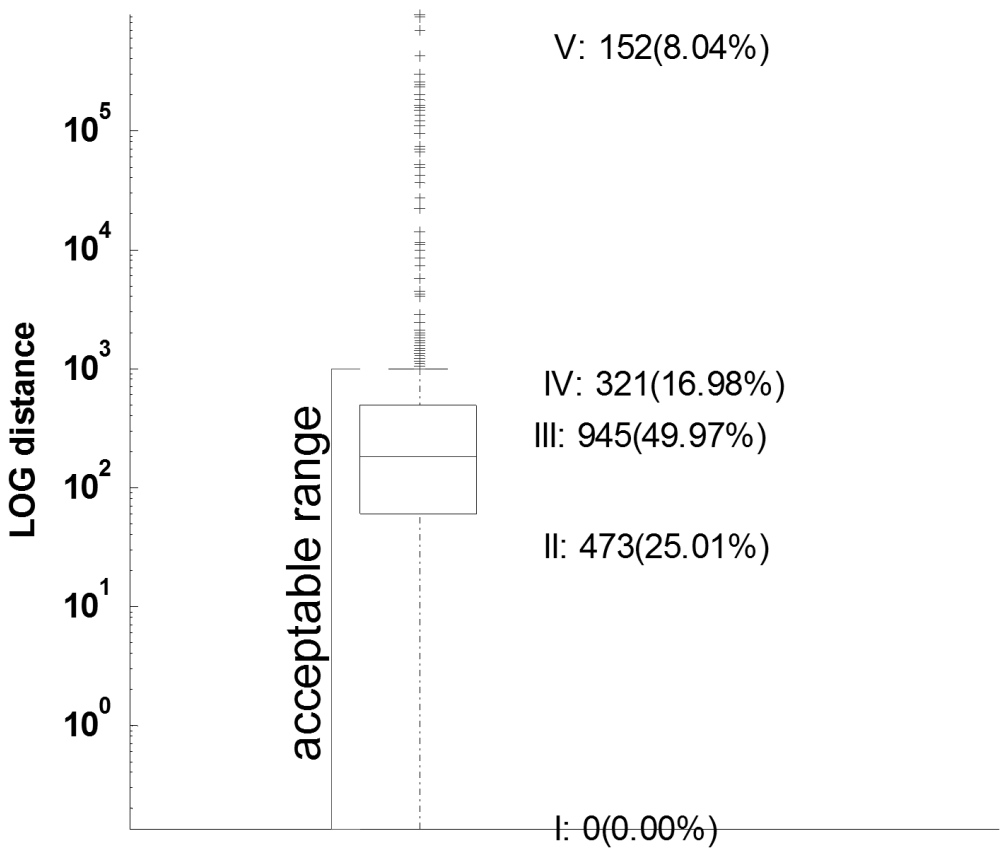

Figure 2-10: Distribution of the Mahalanobis distances. The gray crosses in the top of the box are the abnormal spectra. The number of data in each category (numbered with a Roman letter) and the corresponding percentage of the whole data set are also displayed.

Every time abnormal spectra are removed from the dataset, the median value of the cloud may change. Therefore, there is the need to apply the *boxplot* method iteratively, which can be time consuming. In fact, the median of the cloud would change very slightly and the number of iterations should not exceed two or three. In our case, we used one single iteration, because the cloud median did not change too much after the first iteration as the remaining spectra were very close together.

Because each spectrum is associated with a particular pixel of the image, the position of the abnormal pixels in the image can be found. Figure 2-11 is the sample reflectance image associated to the 1214 nm wavelength. This wavelength corresponds to a cellulose absorption band and the corresponding reflectance (as represented by the image gray level) is proportional to the cellulose content of the pixel and thus to the amount of wood. Figure 2-11 shows that most of the abnormal pixels were located on the borders of the image, probably because of the presence of bark or defects. They also correspond to the shadow from other samples.

Figure 2-11: Location of the abnormal spectra in the sample image. They are displayed as dark pixels.

Using the *PCA-boxplot* method, we found for each small sample image a maximum of 152 abnormal spectra over the 1700 spectra (i.e. about 8% of the spectra), which were excluded from further analysis.

Figure 2-12 shows the spectra before and after removal of the abnormal spectra. Both are compared with a spectrum collected on the same sample with a handheld NIR spectrometer (*Phazir*^{tm}*, Thermo Fisher Scientific, Wilmington, MA, USA*) that provides a reflectance spectrum between 939.5 nm and 1797 nm with a spectral resolution around 11 nm. This spectrum is within the range of spectra that was acquired by the NIR-HSI system.

(a) Spectra with abnormal spectra (b) Spectra without abnormal spectra

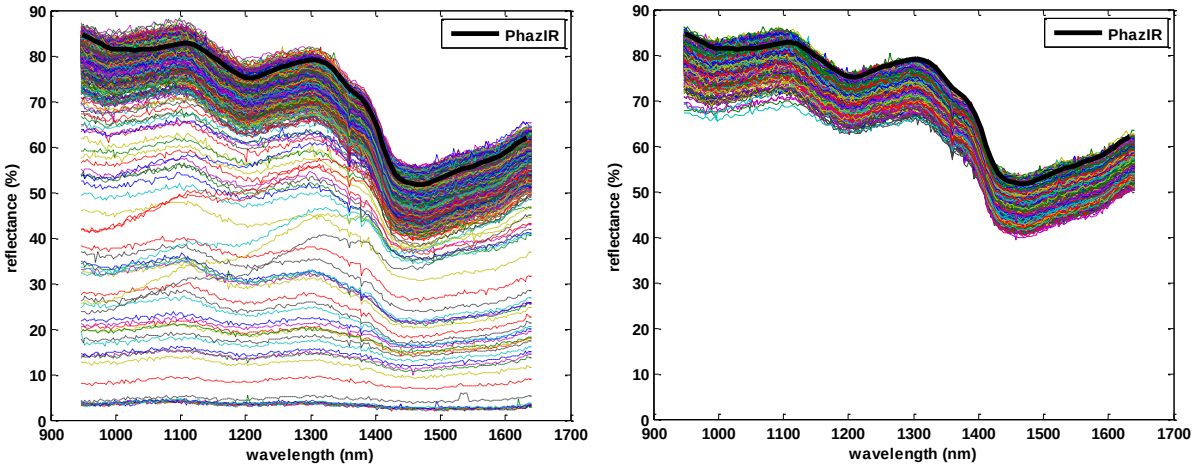

Figure 2-12: Comparison between the image-based absorbance spectra and a spectrum acquired with a handheld NIR spectrometer. (a) with the abnormal ones and. (b) without the abnormal ones.

The reflectance spectra were then converted into absorbance spectra by:

$$A = -log_{10}(R)$$

Equation 2.6

where $\boldsymbol{A}$ is the apparent absorbance (called here absorbance) vector.

In several studies, the raw absorbance spectra is subjected to spectral transformations, such as multiplicative scatter correction (Geladi et al., 1985), as well as first and second derivative (Demetriades-Shah et al., 1990) in order to remove multiplicative and additive scatter effects. Such transformations have also been tested here.

2.4. PLS modeling

Among all types of multivariate analysis methods, the partial least squares (PLS) regression is quick, accurate and suitable for data with many explanatory variables such as spectral data. It is especially useful when the data show a high level of multicollinearity, such as in our case, because the spectral reflectance values are not completely independent from each wavelength to another one. From two or more measured sets of variables, PLS transfers the input variables to uncorrelated variables called latent variables (LV). Since the first LVs have high information content and the last ones express noise and less important information content, the method only uses the first LVs to produce the regression method (Martens and Naes, 1989, Rosipal and Kramer, 2006).

Since there is one single MC value per sample, but more than 1000 spectra for each sample, the PLS models were established using two methods: 1) the median spectrum of each sample image and 2) 100 randomly selected spectra for each sample. Using median spectra instead of mean spectra has the advantage of not considering extreme values. In each case, the model was calibrated on a portion of the dataset and validated over another portion. Random selection of the samples for both datasets can be performed, but it causes dependency between both data sets because each sample was in various steps and thus the various levels of MCs are not independent, randomly choosing samples for calibration and validation data set. We therefore calibrated the PLS models on 70% of the boards and validated over the remained 30%. Before this step, 18 samples were removed from the whole data set because they exhibited too high

standardized residuals. The resulting data set has therefore only 838 samples. We also tested the influence of several spectral transformations on the PLS modeling, including multi scatter correction (MSC), as well as first and second derivative transformations.

In each case, the quality of each PLS model was assessed using the following statistics: 1) coefficient of determination (R^2) and its associated *p*-value or significance level, 2) the root mean square error (RMSE), and 3) ratio of performance to deviation (RPD). The RMSE from one-leave-out cross validation ($RMSE_{CV}$) was used to determine the optimal number of latent variables in the PLS models. The optimal number should be enough to model the complexity in the data (Haaland and Thomas, 1988), but a too high number of latent variables is not optimal as it just increases the noise and variance of the weights of the predictors which leads to over-fitting. If the number of latent variables is small, means that, although there is a huge number of information in the image, the most significant information is present in a limited number of latent variables, the remaining latent variables being mostly related to the signal noise (Salzer and Siesler, 2009). With the median spectra, we found that six was the number of latent variables that corresponds to the minimum RMSE (Figure 2-13). A model with six latent variables explained about 83% of the variation in MCs value. For the 100 spectra-based PLS model, we used 7 latent variables as this number corresponds to the minimum $RMSE_{CV}$.

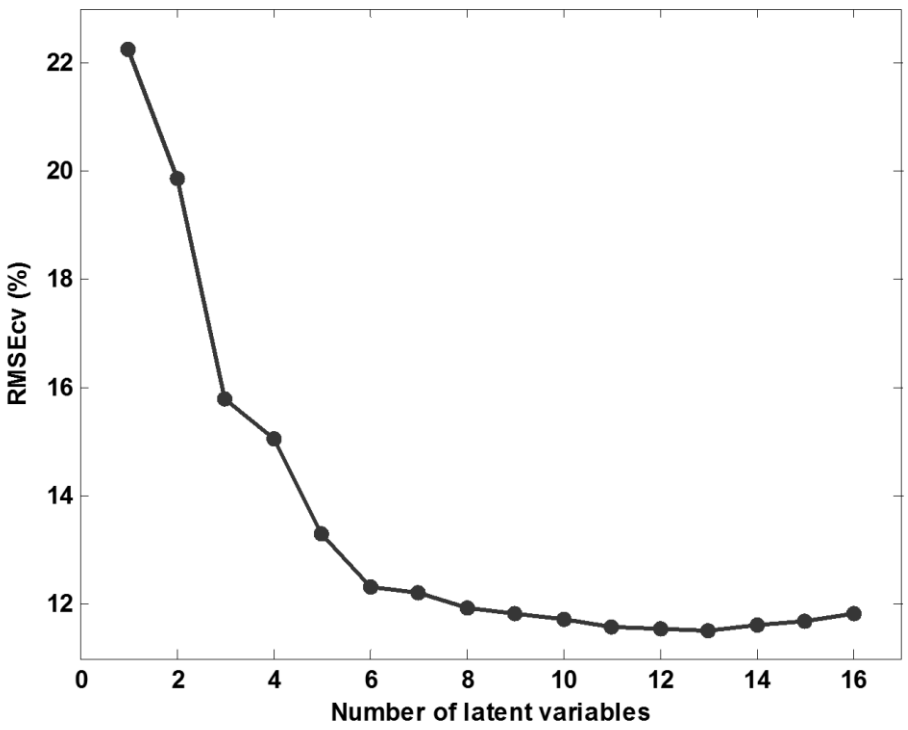

Figure 2-13: Determination of the optimal number of PLS latent variables as a function of the $RMSE_{CV}$ (in % dry weight). The optimal number of PLS latent variables (6) corresponds to the minimum $RMSE_{CV}$.

2.4.1. Results

As shown in Table 2-1, the applied spectral transformations did not give significant improvements in the PLS models. Therefore, only raw spectra will be considered further.

Table 2-1: Comparison of the PLS models [(*)] computed with the median spectra as a function of the transformation method

Transformation method	Number of LVs	Calibration (N: 562)			Validation (N: 276)		
		RMSE (%)	R^2	RPD	RMSE (%)	R^2	RPD
No transformation	6	12.63	0.81	2.30	10.85	0.85	2.62
MSC	5	12.02	0.83	2.41	11.99	0.82	2.37
1st derivative	4	12.63	0.81	2.30	11.04	0.85	2.58
2nd derivative	4	13.03	0.80	2.23	12.00	0.82	2.37

[(*)] *All the models are significant at p-value <0.001*

With the median spectra, the PLS model gives an R^2 of 0.81, RMSE of 12.63%, and RPD of 2.30, for the calibration data set, and an R^2 of 0.85, RMSE of 10.85%, and RPD of 2.62, for the validation data set (Figure 2-14 and Table 2-1). The scattering plots for both calibration and validation data set show a better correlation between NIR spectra-predicted and ASTM-measured MCs at low MC levels than at high levels of MC values (Figure 2-14). If only MC values of less than 50% are considered, the RMSE for the validation data set is reduced from 11% to 8.0%. A better model for low MC levels can be due to the fact that samples with high MC levels have more variables MCs.

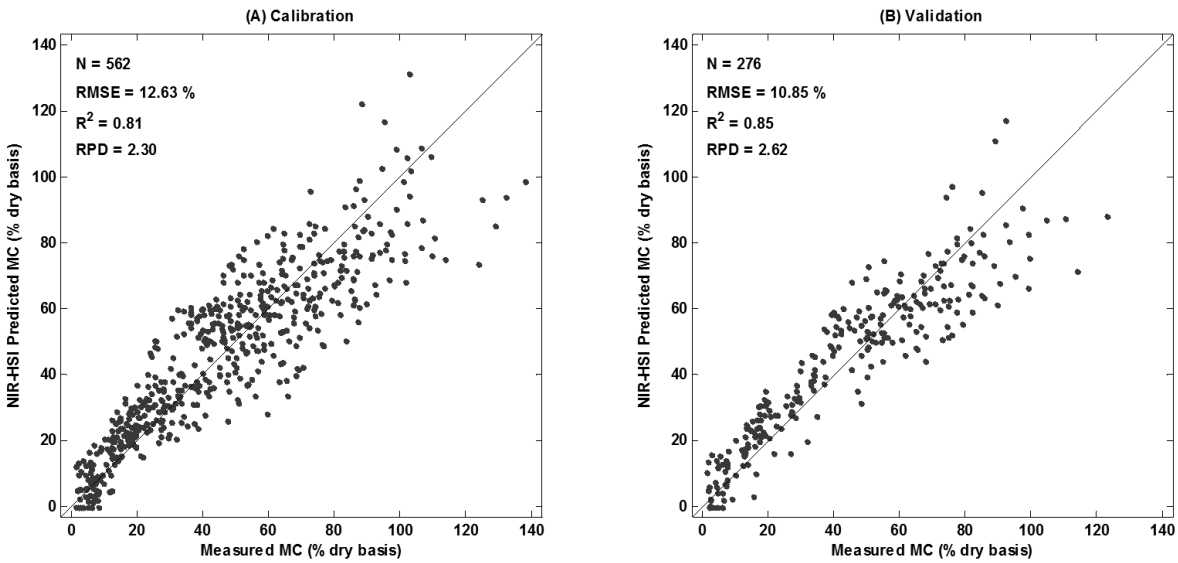

Figure 2-14: PLS model built with 6 latent variables using the median spectra of each sample for (A) the calibration data set and (B) validation data set.

With the 100 spectra, the resulting PLS model for calibration and validation data have an R^2 of 0.77 and 0.80, an RMSE of 13.85% and 12.76%, and an RPD of 2.09 and 2.23, respectively (Table 2-2). The results for this model are slightly less accurate than the models built with the median spectra. This is why the median spectrum-based model will be considered for further analysis.

Table 2-2: Comparison of the PLS models(*) computed with the raw spectra between a) median spectra and b) 100 spectra

Spectra type	Number of LVs	Calibration				Validation			
		RMSE (%)	R^2	RPD	N	RMSE (%)	R^2	RPD	N
Median	6	12.63	0.81	2.30	562	10.85	0.85	2.62	276
100 spectra	7	13.85	0.77	2.09	56200	12.76	0.80	2.23	27600

(*) *All the models are significant at p-value <0.001*

Figure 2-15 shows the MC images for the samples that were selected to represent the whole MC range. For each image, beside the measured MC value and the estimated mean MC value, the figure also presents the histogram of MC distribution showing the MC variation over the small sample. The histogram width gives some information about the precision of the PLS model (Burger and Geladi, 2006). As already shown in Figure 2-14, there is a good agreement between measured and estimated MC values, but the MC variation is greater for high MC values than for low MC values.

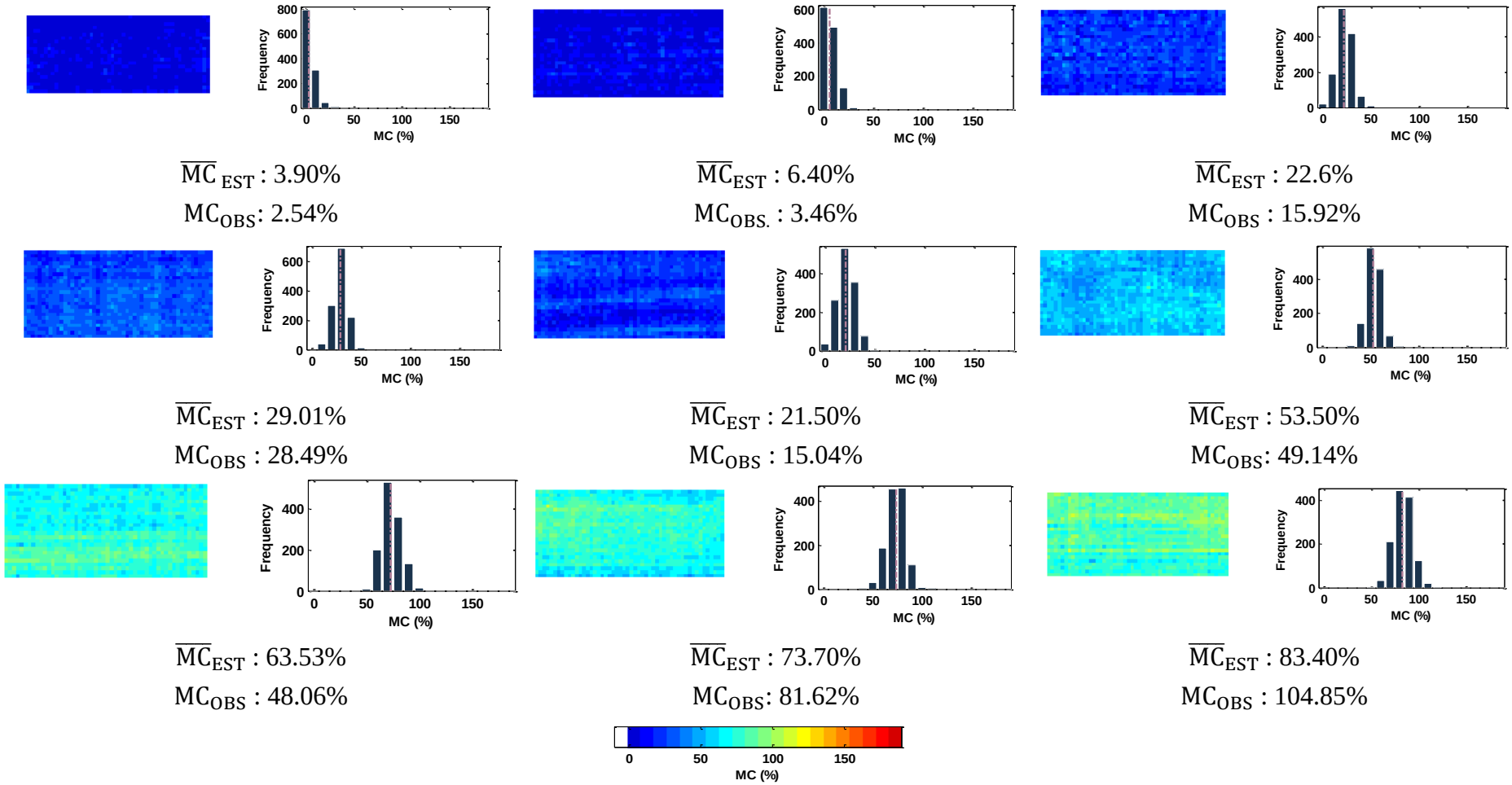

Figure 2-15: 2D images of moisture content for small samples and their corresponding MC histogram. The samples have been selected to represent the whole range of MC variations.

The PLS model was then used with the image acquired over the whole board to produce a 2D MC image that provides the MC value in each point of the board as well as its distribution across the board (Figure 2-16). This figure shows that the MC distribution is more variable at high mean MC. Beside the variation in MCs, the images also show the growth rings with the distinct earlywood and latewood and also some board defects, such as knots which have lower MC than the other parts of the board. Additionally, wet-pocket areas are visible in some parts of the first image of Figure 2-16.

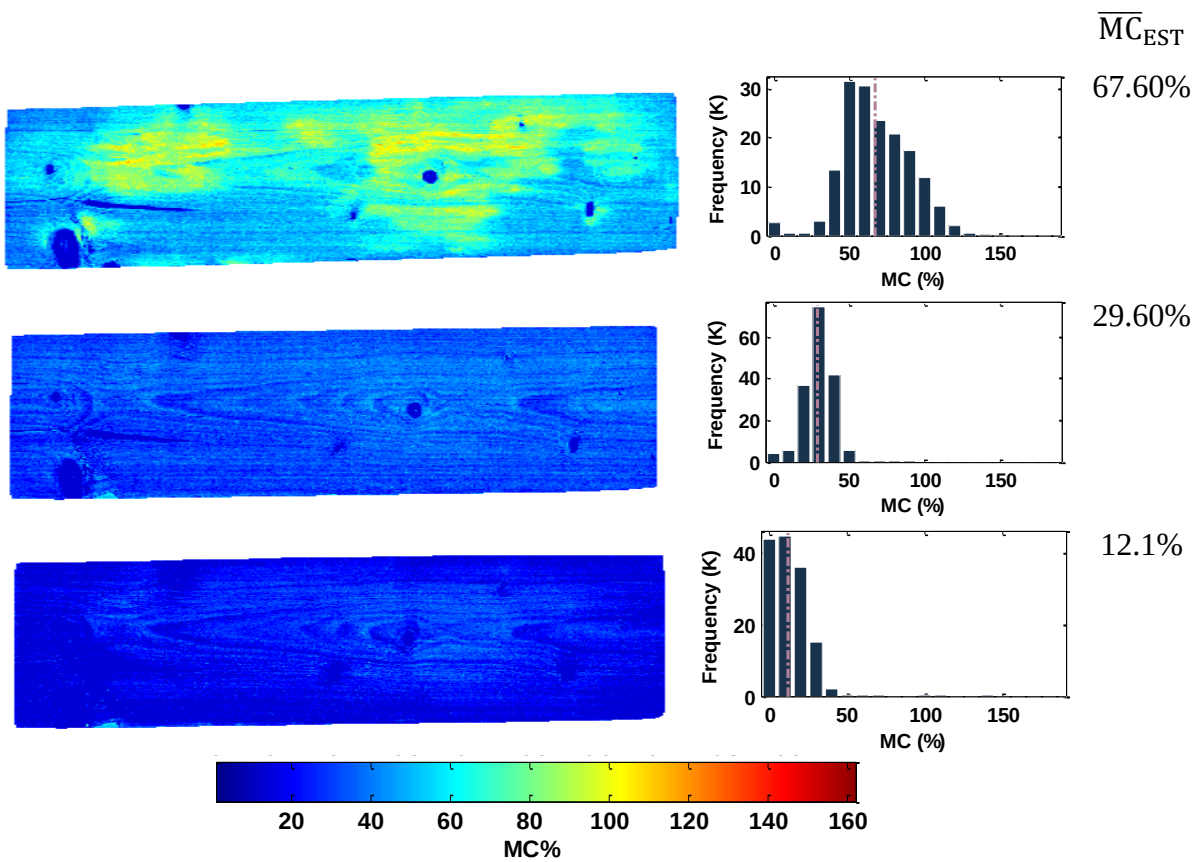

Figure 2-16: 2D image of moisture content for one whole board in different drying steps. The MC distribution and mean estimated value for each board is also presented.

2.4.2. Discussion

We found that the model based on raw spectra provide higher accuracy compare to the models based on MS-corrected, first and second derivative spectra (Table 2-1). Such observations were already made by Hans et al. (2013) with spot NIR spectra measured on black spruce frozen and thawed logs. The same is true for Kobori et al. (2013) that used NIR-HSI images to estimate MC of European beech and Scots pine. Several other studies, such as Mora et al. (2011b), did not even test any spectral transformations.

Our PLS models for MC were built with six latent variables. Kobori et al. (2013) found the model based on 6 numbers of latent variables and Mora et al. (2011b) used 8 latent variables. Our PLS models produced R^2 (0.85) and RMSE values that are on the same order as the ones obtained by Mora et al. (2011b) (R^2 of 0.81 and RMSE of 2.1%), despite the higher range of MCs in our case. Mora et al. (2011b) tested HSI images over loblolly pine disks having MC ranging from 45% to 65% (dry basis), whereas in our case, the range of variation for the MCs is 1% to 137%. However, RMSE from both Mora et al. (2011b) and this study are lower than those of Kobori et al. (2013) (R^2 of 0.99 and RMSE of 2.27%), who tested HSI images over European beach and Scot pine samples that have MC ranging from 20 to 121% (dry basis). Another reason of the better results of Kobori et al. (2013) is also the spectral range they used. Kobori et al. (2013) acquired images in the visible and near-infrared domains, whereas both Mora et al. (2011b) and this study used images acquired in the near-infrared domain.

Our PLS modeling results are especially good given that they were obtained with NIR measurements on radial sections. Transversal section measurements usually result in better PLS models than tangential or radial sections (Leblon et al., 2013). Indeed, tangential sections have lower absorbance than transverse sections because the radiation will first encounter the cell wall of the tangential sections, while for the transversal sections, the incident radiation directly interferes with the free water present in the lumina of the cell. The surface roughness of the sample increase as well since they were planned before image acquisition.

Figure 2-14 and 2-15 showed a more accurate MC estimation for low MC levels than for high MC values. In both cases, a higher variation can be due to differences between earlywood and latewood, because the cell wall of latewood is thicker compared to the cell wall of earlywood, while the lumina volume in earlywood is greater than latewood. For the bottom left sample of Figure 2-15, there is a high MC area in the bottom of the sample compare to the rest of the sample. This area corresponds to a wet-pocket which has a distinct dark color on the corresponding panchromatic image of Figure 2-17. Such color changes are due to a high content of extractives in the wet pocket (Ward and Pong, 1980).

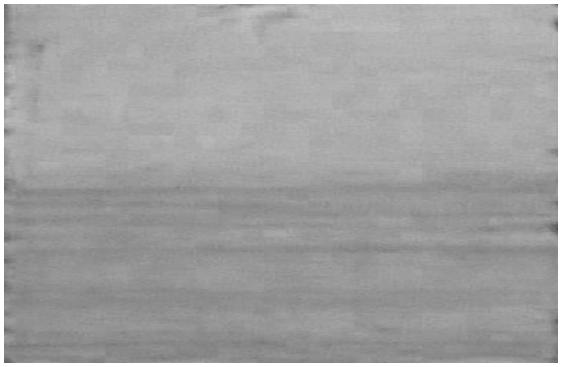

Figure 2-17: Panchromatic image of the surface of the bottom left sample of Figure 2-15.

As the whole board is drying, the distribution of the MCs becomes more homogeneous and the rate of water loss is decreasing (Figure 2-16 and Figure 2-15). Indeed water moves from the water zone to the drier region. Since more water is evaporated from the surface than the center of the board, so there is always more water in the center compare to the surface (Panshin and De Zeeuw, 1980). Figure 2-16 also shows a high variability in the MC for board having high MC. Such high variability can be caused first by the fact that the model predicts MC of the board with less accuracy when MC is relatively high. However, as shown in Figure 2-2, the board has also an inherent high MC variation as, the initial MC of board 14 has a 30% variation from the bottom to the top of the board.

2.5. Conclusions

Our study assessed the potential of NIR hyperspectral images to produce MC images of the subalpine fir board. The NIR hyperspectral images were subjected to the following image processing: image calibration in reflectance, recovering bad pixels

using a median filter, delineation of the small samples on each image, and removing abnormal spectra using a combination of the principal component analysis (PCA) and the *boxplot* method of Laurikkala et al. (2000). The remaining spectra were then used into PLS models.

Our study shows that the sampling method and the spectral transformations have very little impact on the resulting PLS models. The best PLS models were those established using the raw median spectra of each sample image that was randomly selected and an optimum number of LVs of six. The PLS model has an R^2 of 0.85 and an RMSE of 10.85%, when it is validated on a validation data set that includes the whole range of MC from 1% to 137%. The model is more accurate for low MC samples than for high MC samples. The RMSE is reduced to 8% when only low MC samples are used. The model was then applied to both the small wood samples and the whole board images in order to produce 2D images of MC.

The proposed method can be automated and provides not only MC distributions over board, but also other information about the board, such as the presence of knots and decay as well as the location of wet-pockets. This information will benefit to increase the efficiency of designing kiln-drying operations in sawmills.

The method is based on NIR radiation that has two major disadvantages. First, it has a limited penetration depth in solid wood, from 1 to 5 mm depending on surface roughness and the wavelength used (Tsuchikawa et al., 1996, Tsuchikawa et al., 2001, Sykes et al., 2005). More penetrating radiations, such as microwaves should be tested for estimating bulk MC of boards. Second, the spectral measurements highly rely on the

wood surface type and roughness, as already discussed in the *Results* section. Despite the low penetration of NIR systems, they have been becoming promising tools for finding wet pockets, as already shown in Watanabe et al. (2012). Another method is the computer tomography X-ray scanning, but this method has the disadvantages of being costly and related to higher safety issues (Alkan et al., 2007).

The setting used for acquiring the images was a camera with a field of view of 17.5° that was positioned at 48 cm height. A higher quality of spectra can be achieved using a camera with a wide field of view, because the environment interference on the spectra is reduced as the distance between the camera and the target decreases. It will be expected that the resulting PLS models will be more accurate.

In this study, we related NIR hyperspectral data to wood moisture content using a PLS model. Further work is needed to test a more deterministic approach that uses optical models like the one of the Tsuchikawa et al. (2001). Also, in this study, we derived board moisture content images from NIR hyperspectral images. Such method can also be applied to produce 2D images for other chemical components. This will be the subject of future work.

2.6. Acknowledgements

The authors thank G. Chow from FPInnovations as well as K. Phung (UNB) for their help during the experiments. The study was supported by an NSERC Strategic Grant awarded and a New Brunswick Foundation for Innovation grant to B. Leblon.

2.7. References

Alkan S., Zhang Y.L. & Lam F. (2007) Moisture distribution changes and wetwood behavior in subalpine fir wood during drying using high X-ray energy industrial CT scanner. *Drying Technology,* 25(1-3): 483-488. doi: 10.1080/07373930601184023

ASTM-D4442–07 (2009) *Standard test methods for direct moisture content measurement of wood and wood-base materials*, ASTM International, West Conshohocken, PA, doi: 10.1520/D4442-07, www.astm.org.

Bowyer J.L., Shmulsky R. & Haygreen J.G. (2007) *Forest products and wood science: An introduction.* Oxford, UK: John Wiley & Sons. 496 pages.

Burger J. (2009) Replacement of hyperspectral image bad pixels. *NIR news,* 20(7): 25-27. doi: 10.1255/nirn.11xx

Burger J. & Geladi P. (2005) Hyperspectral NIR image regression. Part 1: Calibration and correction. *Journal of Chemometrics,* 19(5-7): 355-363. doi: 10.1002/Cem.938

Burger J. & Geladi P. (2006) Hyperspectral NIR image regression. Part 2: Dataset preprocessing diagnostics. *Journal of Chemometrics,* 20(3-4): 106-119. doi: 10.1002/Cem.986

Chang C.I. (2007) *Hyperspectral data exploitation: Theory and applications.* New Jersey, USA: John Wiley & Sons. 465 pages.

Demetriades-Shah T.H., Steven M.D. & Clark J.A. (1990) High-resolution derivative spectra in remote-sensing. *Remote Sensing of Environment,* 33(1): 55-64. doi: 10.1016/0034-4257(90)90055-Q

Denig J., Wengert E.M. & Simpson W.T. (2000) Drying hardwood lumber, U.S. Department of Agriculture, Forest Service, Forest Products Laboratory, Tech. Rep. FPL–GTR–118, Madison, WI, USA, 138 pages.

Duncker P. & Spiecker H. (2009) Detection and classification of Norway spruce compression wood in reflected light by means of hyperspectral image analysis. *IAWA Journal,* 30(1): 59-70. doi: 10.1163/22941932-90000203

Forest Products Laboratory (2010) *Wood handbook: Wood as an engineering material.* Madison, WI, USA: U.S. Department of Agriculture, Forest Service, Forest Products Laboratory. 508 pages.

Geladi P., Burger J. & Lestander T. (2004) Hyperspectral imaging: Calibration problems and solutions. *Chemometrics and Intelligent Laboratory Systems,* 72(2): 209-217. doi: 10.1016/j.chemolab.2004.01.023

Geladi P., Macdougall D. & Martens H. (1985) Linearization and scatter-correction for near infrared reflectance spectra of meat. *Applied Spectroscopy,* 39(3): 491-500

Grahn H. & Geladi P. (2007) *Techniques and applications of hyperspectral image analysis.* Chichester, UK: John Wiley & Sons. 390 pages.

Haaland D.M. & Thomas E.V. (1988) Partial least-squares methods for spectral analyses .1. Relation to other quantitative calibration methods and the extraction of qualitative information. *Analytical Chemistry,* 60(11): 1193-1202. doi: 10.1021/Ac00162a020

Hans G., Leblon B., Stirling R., Nader J., LaRocque A. & Cooper P. (2013) Monitoring of moisture content and basic specific gravity in black spruce logs using a handheld MEMS-based near-infrared spectrometer. *The Forestry Chronicle,* 89(5): 605-618. doi: 10.5558/tfc2013-112

Isaksson T., Brischke C. & Thelandersson S. (2013) Development of decay performance models for outdoor timber structures. *Materials and Structures,* 46(7): 1209-1225. doi: 10.1617/s11527-012-9965-4

Kobori H., Gorretta N., Rabatel G., Bellon-Maurel V., Chaix G., Roger J.M. & Tsuchikawa S. (2013) Applicability of VIS-NIR hyperspectral imaging for monitoring wood moisture content (MC). *Holzforschung,* 67(3): 307-314. doi: 10.1515/Hf-2012-0054

Laurikkala J., Juhola M. & Kentala E. (2000) Informal identification of outliers in medical data, In *14th European Conference on Artificial Intelligence and 5th International Workshop on Intelligent Data Analysis in Medicine and Pharmacology IDAMAP-2000*, (Berlin, Germany), pp. 20-24

Leblon B., Adedipe O., Hans G., Haddadi A., Tsuchikawa S., Burger J., Stirling R., Pirouz Z., Groves K., Nader J. & LaRocque A. (2013) A review of near-infrared spectroscopy for monitoring moisture content and density of solid wood. *Forestry Chronicle,* 89(5): 595-606. doi: 10.5558/tfc2013-111

Martens H. & Naes T. (1989) *Multivariate calibration.* Chichester, UK: John Wiley & Sons. 438 pages.

Mora C.R., Schimleck L.R., Clark A. & Daniels R.F. (2011a) Determination of basic density and moisture content of merchantable loblolly pine logs by near infrared spectroscopy. *Journal of Near Infrared Spectroscopy,* 19(5): 391-399. doi: 10.1255/Jnirs.947

Mora C.R., Schimleck L.R. & Isik F. (2008) Near infrared calibration models for the estimation of wood density in *Pinus taeda* using repeated sample measurements. *Journal of Near Infrared Spectroscopy,* 16(6): 517-528. doi: 10.1255/Jnirs.816

Mora C.R., Schimleck L.R., Yoon S.C. & Thai C.N. (2011b) Determination of basic density and moisture content of loblolly pine wood disks using a near infrared hyperspectral imaging system. *Journal of Near Infrared Spectroscopy,* 19(5): 401-409. doi: 10.1255/Jnirs.948

Nystrom J. & Hagman O. (1999) Real-time spectral classification of compression wood in *Picea abies*. *Journal of Wood Science,* 45(1): 30-37. doi: 10.1007/Bf00579521

Olson J.R. & Arganbright D.G. (1977) Uniformity factor - proposed method for expressing variations in specific gravity. *Wood and Fiber,* 9(3): 202-210

Panshin A.J. & De Zeeuw C. (1980) *Textbook of wood technology: Structure, identification, uses, and properties of the commercial woods of the united states and Canada.* New York, USA: McGraw-Hill. 722 pages.

Richards J.A. & Jia X. (2006) *Remote sensing digital image analysis: An introduction.* Berlin, Germany: Springer. 420 pages.

Rosipal R. & Kramer N. (2006) Overview and recent advances in partial least squares. *Subspace, Latent Structure and Feature Selection,* 3940: 34-51

Salzer R. & Siesler H.W. (2009) *Infrared and Raman spectroscopic imaging.* Weinheim, Germany: John Wiley & Sons. 530 pages.

Skaar C. (1988) *Wood-water relations.* Berlin, Germany: Springer-Verlag. 283 pages.

Sykes R., Li B., Hodge G., Goldfarb B., Kadla J. & Chang H.-m. (2005) Prediction of loblolly pine wood properties using transmittance near-infrared spectroscopy. *Canadian Journal of Forest Research,* 35: 2423-2431. doi: 10.1139/X05-161

Thumm A., Riddell M., Nanayakkara B., Harrington J. & Meder R. (2010) Near infrared hyperspectral imaging applied to mapping chemical composition in wood samples. *Journal of Near Infrared Spectroscopy,* 18(6): 507-515. doi: 10.1255/Jnirs.909

Tsuchikawa S., Hayashi K. & Tsutsumi S. (1996) Nondestructive measurement of the subsurface structure of biological material having cellular structure by using near-infrared spectroscopy. *Applied Spectroscopy,* 50(9): 1117-1124. doi: 10.1366/0003702963905114

Tsuchikawa S., Torii M. & Tsutsumi S. (2001) Directional characteristics of near infrared light reflected from wood. *Holzforschung,* 55(5): 534-540. doi: 10.1515/HF.2001.086

Ward J.C. & Pong W.Y. (1980) Wetwood in trees: A timber resource problem, U.S. Department of Agriculture, Forest Service, Forest Products Laboratory, General Technical Report PNW- 112, Madison, WI, USA, 56 pages.

Watanabe K., Mansfield S.D. & Avramidis S. (2012) Wet-pocket classification in *Abies lasiocarpa* using spectroscopy in the visible and near infrared range. *European Journal of Wood and Wood Products,* 70: 61-67. doi: 10.1007/s00107-010-0490-2

Chapter 3. Using Near-Infrared Hyperspectral Images on Subalpine Fir Board – Part 2: Density and Basic Specific Gravity Estimation[2]

3.1. Abstract

Wood density (ρ_{MC}) and basic specific gravity (*BSG*) are important properties in several forest products manufacturing processes. In this study, near-infrared hyperspectral images were tested to produce two-dimensional (2D) ρ_{MC} and *BSG* images of subalpine fir (*Abies lasiocarpa* Hook) board. A total of 107 cubic samples with the size of 4 cm were prepared from 14 boards. All samples were dried to various moisture contents (MCs) during several steps until being completely dried. The resulting MCs ranged from 1% to 137% (dry basis). After the last drying step, the samples were soaked in water to determine BSG. Hyperspectral images and weight measurements were acquired over each sample at each drying step. ρ_{MC} was also estimated at each MC level. Partial least squares (PLS) models were developed for estimating both ρ_{MC} and *BSG* from the near-infrared hyperspectral imaging NIR-HSI (system) absorbance spectra acquired over all the samples during each drying step. The ρ_{MC} model provides a reasonable accuracy with the validation data-set (R^2= 0.81, RMSE= 39 kg/m^3, and RPD=2.3). For *BSG*, only models built with samples having MC of less than 12% are significant. The calibration data-set provides similar accuracy as the ρ_{MC} model

[2] This chapter was published in *Wood Material Science & Engineering* (Vol 10, issue 1, page 41-56, 2015) under the following authorship: Ataollah Haddadi, James Burger, Brigitte Leblon, Zarin Pirouz, Kevin Groves, and Joseph Nader. doi: 10.1080/17480272.2015.1011231. It is reproduced with the permission of the Taylor & Francis Group (see letter permission in Appendix D)

(RMSE= 0.004, R^2= 0.82, and RPD= 2.28), but the accuracy is lower with the validation data-set (RMSE= 0.007, R^2= 0.53, and RPD= 1.39). Our data-set has BSG values varying only from 0.326 to 0.374, and further work is needed to apply these methods to a data-set that includes a more extended range of *BSG* variations for improving estimation accuracy.

3.2. Introduction

Given that wood is a highly variable material and is used to manufacture a wide range of products, ability to measure its physical, mechanical, and chemical properties should allow more efficient allocation of this valuable resource to various end-products. Such properties can be highly variable between tree species, within one species, and even within a given tree. For example, the influence of factors such as climate, site, and age can lead to significant within-species variability (Garratt, 1931). Other factors governing the natural growth of trees can lead to different types of wood with varying properties within a tree, such as juvenile wood versus mature wood, or heartwood versus sapwood, compression wood, or other variations in grain, knottiness, or density. Wood properties can also vary from the bottom to the top of trees (Panshin and De Zeeuw, 1980, Schimleck et al., 2005a, Barnett and Jeronimidis, 2009). Measuring wood properties at various points in the production chain can help in controlling the variability of raw material used for manufacturing wood products either by sorting or improving breakdown optimization of logs and boards. Developing systems for wood property monitoring especially in real time, during various processing stages, can lead to higher product quality and lower manufacturing costs.

One of the important wood properties that needs to be monitored in the forest products industry is the wood density, which is related to product stiffness and strength (Garratt, 1931, Barnett and Jeronimidis, 2009). For example, knowledge of the density is required to estimate modulus of rupture (MOR) (Wang et al., 2000, Yin et al., 2010) and modulus of elasticity (MOE) (Barnett and Jeronimidis, 2009, Mora et al., 2009) from ultrasonic or acoustics measurements. Density monitoring can also be used for early detection of wood decay, because fungal activity makes decaying wood less dense (Stirling et al., 2007). Wood density can also help detect compression wood, which is denser than normal wood (Diaz-Vaz et al., 2009).

Wood density can be represented using three variables. The first one is the density (ρ_{MC}), which is the ratio between the mass and the volume of the sample at a given moisture content (MC) (Forest Products Laboratory, 2010, Williamson and Wiemann, 2010):

$$\rho_{MC} = \frac{W_{MC}}{V_{MC}}$$

Equation 3.1

Where:

- ρ_{MC} is the density of the sample at a given moisture content MC (kg/m^3)
- W_{MC} is the mass of the sample at a given MC (kg)
- V_{MC} is the volume of the sample at a given MC (m^3).

Equation (3-1) shows that ρ_{MC} strongly depends on the MC because wood is hydrophilic and absorbs or desorbs water. To express ρ_{MC}, MC needs therefore to be

specified. MC is usually expressed in % of dry basis by (Forest Products Laboratory, 2010, Williamson and Wiemann, 2010):

$$MC = (\frac{W_{MC} - W_{OD}}{W_{OD}}) * 100$$

Equation 3.2

Where:

- W_{OD} is the weight of oven-dry sample (kg)
- W_{MC} is weight of wood at a specific MC (kg).

Usually, ρ_{MC} is expressed either for air-dry, oven-dry, or green conditions. The oven-dry wood density is mainly related to cellulose, hemicellulose, lignin, and the proportion of void space in the wood.

Another variable to express the wood density is the BD which is defined as the ratio between the mass of an oven-dry sample to the volume of the same sample when it is green (Walker, 2006, Williamson and Wiemann, 2010, Watanabe et al., 2012):

$$BD = \frac{W_{OD}}{V_{Green}}$$

Equation 3.3

Where:

- W_{OD} is the weight of the oven-dry sample (kg)
- V_{Green} is the volume of the sample when it is green (m^3).

According to Williamson and Wiemann (2010), wood volume does not change above the fiber saturation point (FSP) (MC_{FSP} around 30%). V_{Green} can thus be

considered to be equivalent to the saturation volume that is measured following *Method B* of ASTM-D2395–07a (2009) after completely soaking the sample in water.

The third variable is the basic specific gravity (*BSG*), which is the ratio between the basic density (BD) and the water density (Forest Products Laboratory, 2010, Williamson and Wiemann, 2010).

$$BSG = \frac{BD}{\rho_{water}}$$

Equation 3.4

Where:

- BD = basic density of the sample (kg/m^3)
- ρ_{water} = water density (kg/m^3).

Because ρ_{water} is equal to 1000 kg/m^3 or to 1 g/cm^3 at 4°C and under normal atmospheric pressure, *BSG* is equal to BD when the unit of the BD is g/cm^3 (or one thousandth of BD when the unit of BD is kg/m^3). BD or *BSG* is the most useful description of wood density because W_{OD} does not depend on the sample MC and V_{Green} is constant. *BSG* was shown to be related to cell diameters, cell lengths, cell wall thickness, the proportion of the different cell types within the tree, and presence of extractives (Panshin and De Zeeuw, 1980).

Several sensors have been developed to measure wood density. X-ray densitometers have been developed to get the density variation in annual rings. This technique is laborious, needs time in sample preparation and measurement process and

is relatively expensive (Schweingruber, 1988). High frequency (10 MHz) densitometers were also used to measure the density, but similar to the X-ray densitometers, they only provide a linear profile of density throughout the sample without a two-dimensional (2D) image (Schinker et al., 2003).

Near-infrared (NIR) spectroscopy has been a popular tool in several industrial applications. It is based on spectra in the range of 700-2500 nm that are affected by molecular vibration and a combination of the fundamental overtones, such as OH, CH, and NH stretch (Schwanninger et al., 2011). NIR spectroscopy spot measurements were tested to predict the air-dry density (Table 3-1) and *BSG* (Table 3-2) of various wood sample types for various species.

Table 3-1: Literature review of PLS predicting models for air dry density (ρ_{MC}) estimation with spot NIR spectroscopy measurements.

Scanned section	Spectral range (nm)	Wood product	RMSE or SE (kg/m^3)	R^2	N	PLS latent variables	ρ_{MC} range (kg/m^3)	*MC* range (%)	Species	Authors
Radial	1100–2500	Strip (clear)	17.3	0.94	34	7	341–502	12	Loblolly pine *(Pinus taeda* L.*)*	Schimleck (2002)
	780–2500	Stick	20.0	0.75	80	5	494–767	7-16	Forest red gum *(Eucalyptus tereticornis* Sm.)	Kothiyal and Raturi (2011)
	1100–2500	Clear	20.0	0.49	59	3	330–480	12	Loblobby pine (*Pinus teada* L.)	Schimleck et al. (2005a)
	1100–2400	Dried clear	23.0	0.88	19	4	341–672	<8%	Balsam fir (*Abies balsamea* (L.) (Mill.) & black spruce (*Picea mariana* (Mill.) B.S.P.)	Xu et al. (2011)
	1100–2400	Green clear	25.0	0.87	19	6	341–672	green	Balsam fir (*Abies balsamea* (L.) (Mill.) & black spruce (*Picea mariana* (Mill.) B.S.P.)	Xu et al. (2011)
	1100–2500	Stick (clear)	26.4	0.91	34	5	440–990	12	Alpine ash (*Eucalyptus delegatensis* R.T. Baker)	Schimleck et al. (2001)
	1400–2200	Clear	30.0	0.84	20	3	400–710	13.1	Hybrid larch (*Larix gmelinii var. Japonica x Larix kaempferi*)	Fujimoto et al. (2007)
	1300–2300	Clear	30.0	0.73	70	8	390–660	13.1	Hybrid larch (*Larix gmelinii var. Japonica x Larix kaempferi*)	Fujimoto et al. (2008)
	1100–2500	Stick	30.6	0.92	34	5	440–990	12	Alpine ash (*Eucalyptus delegatensis* R.T. Baker)	Schimleck et al. (2001)
	1100–2500	Green strip	31.2	0.92	33	4	397–791	100-154	Loblobby pine (*Pinus teada* L.)	Schimleck et al. (2005c)
	1100–2500	Green strip	42.0	0.78	32	7	316–682	100-154	Loblobby pine (*Pinus teada* L.)	Mora and Schimleck (2009)

Table 3-1 (continued)

Scanned section	Spectral range (nm)	Wood product	RMSE or SE (kg/m^3)	R^2	N	PLS latent variables	ρ_{MC} range (kg/m^3)	*MC* range (%)	Species	Authors
Radial	1100–2498	Dried strip	42.2	0.85	101	4	327–810	8.0	Loblolly pine (*Pinus taeda* L.)	Mora and Schimleck (2010)
	1100–2500	Dried strip	45.8	0.82	225	5	337–833	7.0	Loblolly pine *(Pinus taeda* L.*)*	Jones et al. (2005)
	1100–2500	Green strips	57.6	0.74	32	3	394–853	100-154	Loblolly pine (*Pinus taeda* L.)	Schimleck et al. (2003)
	1000–2500	Dried strip	61.5	0.76	87	5	337–832	7.0	Loblolly pine *(Pinus taeda* L.*)*	Jones et al. (2007)
Tangential	1000–2500	Strip	19.0	0.91	45	8	660–940	Air dry	*Eucalyptus camaldulensis*	Inagaki et al. (2012)
	780–2500	Stick	21.0	0.58	80	6	494–767	6-21	Forest red gum *(Eucalyptus tereticornis* Sm.)	Kothiyal and Raturi (2011)
	1300–2300	Lumber	30.0	0.69	20	8	420–690	13.1	Hybrid larch (*Larix gmelinii var. Japonica x Larix kaempferi*)	Fujimoto et al. (2008)
	1300–2300	Clear	30.0	0.68	70	7	390–660	13.1	Hybrid larch (*Larix gmelinii var. Japonica x Larix kaempferi*)	Fujimoto et al. (2008)
	1300–2300	Lumber	32.2	0.57	34	3	382–721	10.6	Japanese larch *(Larix kaempferi)*	Fujimoto et al. (2010a)

Table 3-1 (continued)

Scanned section	Spectral range (nm)	Wood product	RMSE or SE (kg/m^3)	R^2	N	PLS latent variables	ρ_{MC} range (kg/m^3)	*MC* range (%)	Species	Authors
Transversal	715–2500	Stick	17.6	0.85	270	13	243–559	12-14 & 7.5	Sugi (*Cryptomeria Japonica* D. Don),	Watanabe et al. (2012)
	1200–2400	Clear	19.0	0.94	127	8	450–500	0–27	Norway spruce *(Picea abies (L.)* Karst.*)*	Hoffmeyer and Pedersen (1995)
	1100–2280	Disk	19.0	0.80	34	12	303–590	70–200	Loblolly pine (*Pinus taeda* L.)	Mora and Schimleck (2009)
	1100–2500	Clear	20.0	0.61	59	5	330–480	12.0	Loblobby pine (*Pinus teada* L.)	Schimleck et al. (2005a)
	1000–1961	Strip	29.0	0.95	84	6	241–639	Air dry	Larch (*Larix X eurolepis* Henry) & Maritime pine (*Pinus pinaster* Aiton)	Alves et al. (2012)
	1000–1961	Strip	31.0	0.92	89	5	270–650	Air dry	Larch (*Larix X eurolepis* Henry)	Alves et al. (2012)
	1100–2500	Green strip	42.0	0.83	33	3	398–791	100–154	Loblobby pine (*Pinus teada* L.)	Schimleck et al. (2005b)
	1100–2500	Dried strips	45.2	0.82	32	4	394–794	7.0	Loblolly pine (*Pinus taeda* L.)	Schimleck et al. (2003)
	1000–2500	Disk	50.7	0.76*	93	5	300–900	8.0±1.3	Longleaf pine (*Pinus palustris* Mill.)	Via et al. (2003)
	1100–2500	Green strips	60.1	0.74	32	3	394–794	100-154	Loblolly pine (*Pinus taeda* L.)	Schimleck et al. (2003)

(*) PCR regression.

Table 3-2: Literature review of PLS predicting models for *BSG* [(1)] with spot NIR spectroscopy measurements.

Scanned section	Spectral range (nm)	Wood product	RMSE or SE	R^2	N	latent variables	BSG range	*MC* range (%)	Species	Authors
Radial	640–1100[(2)]	Increment core	0.009	0.87	39	12	0.364–0.519	Saturation	*Eucalyptus nitens*	Galleguillos-Hart et al. (2010)
	1000–1960	Disk	0.011	0.92	45	4	0.432–0.649	Air dry	Blackwood *(Acacia melanoxylon* (R. Br.))	Santos et al. (2012)
	350–2500	Lumber	0.018	0.86	28	8	0.488–0.661	68–100	Red oak (*Quercus spp*.)	Defo et al. (2007)
	1000–1960	Clear	0.023	0.97	51	7	0.400–0.900	12.3±0.3	European larch (*Larix decidua* Mill.)	Gindl et al. (2001)
	800–2850	Clear	0.030	0.85	85	7	0.338-0.746	12	*Eucalyptus urophylla*	Hein et al. (2009c)
Tangential	350–2500	Lumber	0.017	0.55	28	8	0.488–0.661	68–100	Red oak (*Quercus spp*.)	Defo et al. (2007)
	800–2850	Clear	0.045	0.65	85	4	0.338-0.746	12	*Eucalyptus urophylla*	Hein et al. (2009c)

Table 3-2 (continued)

Scanned section	Spectral range (nm)	Wood product	RMSE or SE	R^2	N	latent variables	BSG range	*MC* range (%)	Species	Authors
Transversal	1200–2400	Disk	0.017	0.71	25	8	0.307–0.406	60–180	Norway spruce (*Picea abies* (L.) Karst.)	Thygesen (1994)
	900–1800	Disk	0.019	0.80	28	9	0.343–0.492	9.1–132	Black spruce (*Picea mariana* Mill.)	Hans et al. (2013)
	1005–1645	Disk	0.021	0.77	24	8	0.275–0.575	43-66	Loblolly pine *(Pinus taeda* L.*)*	Mora et al. (2011a)
	900–1800	Disk	0.022	0.60	90	9	0.295–0.447	14.1–139.2	Quaking aspen *(Populus tremuloides (Michx.))* & Balsam poplar *(Populus balsamifera* L.*)*	Hans et al. (2015)
	400–2500	Disk	0.023	0.80	36	9	0.275–0.575	59	Loblolly pine *(Pinus taeda* L.*)*	Mora et al. (2011a)
	800–2850	Lumber	0.024	0.85	40	5	0.407–0.708	14	*Eucalyptus urophylla* and *grandis*	Hein et al. (2009a)
	800–2850	Clear	0.033	0.83	85	7	0.338-0.746	12	*Eucalyptus urophylla*	Hein et al. (2009c)
	350–2500	Lumber	0.035	0.89	28	8	0.488–0.661	68–100	Red oak (*Quercus spp*.)	Defo et al. (2007)

(1) The results of the BD studies have been translated into BSG by dividing the RMSE or SE value by $\rho_{water;}$

(2) NIR transmittance

However, using spot measurements is more difficult to use for estimating density variations across the samples, especially for long boards or lumber. In contrast, a hyperspectral imaging (HSI) system records reflectance spectra for each pixel of the target surface over hundreds of wavelengths (Geladi et al., 2004, Salzer and Siesler, 2009). Depending on the viewing set-ups, they could be used to measure density variations over the sample at various resolutions, if appropriate models can be developed to estimate density from the spectral data. At the end, this technology could be operationally used to measure density variations within boards on a conveyor belt. The acquired spectra have a narrow spectral (hyperspectral) sampling, e.g., less than 10 nm, that allows derivative analysis, which is useful to resolve overlapping spectra to better separate components of the global spectrum (Demetriades-Shah et al., 1990).

HSI systems have been tested to identify compression wood in Norway spruce (*Picea abies* L.) and Scots pine (*Pinus sylvestris* L.) lumber (Hagman, 1997, Nystrom and Hagman, 1999) and in Norway spruce stem cross-sections (Duncker and Spiecker, 2009). More recently, they have been used to map the chemical composition (Thumm et al., 2010), as well as MC and BD of loblolly pine (*Pinus taeda* L) disks (Thumm et al., 2010, Mora et al., 2011b). They also served to estimate MC images of European beech (*Fagus sylvatica* L.) and Scots pine (*P. sylvestris* L.) disks (Kobori et al., 2013) and MC of subalpine fir (*Abies lasiocarpa* Hook) board (Haddadi et al., 2015a).

Our study presents a method to estimate ρ_{MC} and *BSG* from NIR-hyperspectral images that were acquired by an imaging spectrometer in the 947-1637 nm wavelength range over subalpine fir (*A. lasiocarpa* Hook) board samples and entire boards. As

shown in Tables 3-1 and 3-2, most of the previous studies on ρ_{MC} and *BSG* estimations used point-source NIR spectroscopy measurements. So far, only one study (Mora et al. 2011b) tested NIR-HSIs for estimating *BD* of loblolly pine. Our study differs from the one of Mora et al. (2011b) because it used a new image processing method that is based on median filtering for finding and replacing bad pixels and a modified version of the *boxplot* method for finding abnormal spectra. It also considered samples that have a larger MC range (1 –137% dry basis) than Mora et al. (2011b) who used logs having MC ranging from 45% to 65% dry basis. Finally, Mora et al. (2011b) estimated *BD* (which is similar as BSG), while our study was also able to estimate ρ_{MC}. This is significant as considering samples both above and below fiber saturation requires that the effect of shrinkage be taken into consideration, and this is achieved by estimating ρ_{MC} as well as *BSG*. A model for ρ_{MC} is based on the mass (wood and water) and green volume of a given piece of wood (V_{MC}) at the time of measurement and is more likely to be correlated to the spectra collected on green wood. On the other hand, any attempt to estimate *BSG* (a property defined for dry wood) based on spectra measurements on a green (pre-shrinkage) piece of wood must implicitly predict shrinkage. However, prediction of dry mass based on the green spectra is challenging, especially if the model was made based on spectra collected on dry wood. This is due to the fact that the area/volume of wood in the field of view of the spectrometer is fixed, but depending on green or dry state (due to shrinkage), spectra from the same area will be reflected from different wood mass (less in green state). While in the industry, ρ_{MC} is used less frequently than *BD* or BSG*;* its estimation can be of interest. Indeed, during various processing stages of solid wood products, ρ_{MC} gives a more accurate representation of

the actual state of the work piece. According to Williamson and Wiemann (2010), ρ_{MC} "*is a measure of the wood mass per unit volume and is a measure of a wood's mass for practical purposes such as shipping or estimation of load*". Also it measurement is required to estimate MOR and MOE from ultrasonic or acoustics measurements) (Wang et al. 2000, Yin et al. 2010).

3.3. Materials and Methods

3.3.1. Sampling and ρ_{MC} /BSG determination

In this study, we used the same one hundred and seven 4×4×4 cm samples as in the MC study of Haddadi et al. (2015). They were extracted from 14 subalpine fir boards, which were dried in eight drying steps. Hyperspectral images and weight measurements were acquired over each sample at each drying step. A total of 856 images were obtained but 18 of them were considered as outlier images (Haddadi et al., 2015). As a result, the ρ_{MC} and BSG models were calibrated and validated over 838 images. However, we also estimated a BSG model using only 88 images that were acquired over the dry samples (having an MC of less than 12% dry basis).

In order to determine the sample density at each MC level (ρ_{MC}), first the weight of the samples at each drying step was measured (W_{MC}). The dry weight of each sample was determined at the end of the drying process in order to be able to determine a posteriori MC at each step using Equation (2) following Method A of ASTM-D4442–07 (2009). To get the corresponding volume, the following modeling was done. For samples with MC superior to MC_{FSP} (around 30%), there is no sample volumetric

shrinkage, so the percentage of volumetric shrinkage $(S_{MC_{FSP}-MC})$ is equal to 0 and V_{MC} is equal to the volume at MC=FSP ($V_{MC_{FSP}}$). For MC below FSP, there is a volumetric shrinkage occurring when the sample MC is changing from MC_{FSP} to a lower MC, so the V_{MC} is lower than the fiber saturation volume ($V_{MC_{FSP}}$) and the percentage of volumetric shrinkage is defined by (Forest products Laboratory 2010):

$$S_{MC_{FSP}-MC} = \frac{V_{MC_{FSP}} - V_{MC}}{V_{MC_{FSP}}} * 100$$

Equation 3.5

For subalpine fir, the percentage of volumetric shrinkage was shown to be not correlated to the BSG (Knudson et al., 2008), but, as shown by Equation (3-5), it varies with the MC level reached by the sample during drying (Forest Products Laboratory 2010).

$S_{MC_{FSP}-MC}$ can be expressed by a linear interpolation between MC levels, as a function of the percentage of volumetric shrinkage $(S_{MC_{Green}-MC_{OD}})$ between the FSP and the oven-dry MC conditions (Forest Products Laboratory, 2010):

$$S_{MC_{FSP}-MC} = \frac{(MC_{FSP} - MC)}{MC_{FSP}} (S_{MC_{FSP}-MC_{OD}})$$

(for $0 \leq MC \leq MC_{FSP}$)

Equation 3.6

where

- MC_{FSP} is the moisture content (%dry basis) at FSP. For subalpine fir, MC_{FSP} is equal 30% (Forest Products Laboratory, 2010)
- $s_{MC_{FSP}-MC_{OD}}$ is the volumetric shrinkage percentage from FSP to oven-dry conditions. Values of $s_{MC_{FSP}-MC_{OD}}$ ranging from 9.0% to 9.8% were reported in the literature (Wangaard 1950, Gonzales 1990, Simpson 1991, Forest Product Laboratory 2010). The corresponding mean and standard deviation values are 9.4% and 0.4%. We will use here this mean value similarly as in Bowyer et al. (2007) and Rowell (2013).

Combining Equations (3-5) and (3-6) allows deriving V_{MC} from $V_{MC_{FSP}}$ as follows:

$$V_{MC} = V_{MC_{FSP}}.(1-\frac{S_{MC_{FSP}-MC}}{100}) = V_{MC_{FSP}}.(1-(1-MC/MC_{FSP}).(\frac{S_{MC_{FSP}-MC_{OD}}}{100}))$$

Equation 3.7

with $s_{MC_{FSP}-MC} = 0$ if MC>MC_{FSP}

Combining Equations (3-1) and (3-7) leads to the following expression for ρ_{MC}:

$$\rho_{MC} = \frac{W_{MC}}{V_{MC_{FSP}}.\{1-(1-MC/MC_{FSP}).S_{MC_{FSP}-MC_{OD}}\}}.100$$

Equation 3.8

Equation (3-8) requires knowing $V_{MC_{FSP}}$. It was estimated by:

$$V_{MC_{FSP}} = \frac{V_{Dry}}{(1 - \frac{S_{MC_{FSP}-MC_{OD}}}{100})}$$

Equation 3.9

Where V_{Dry} is the volume corresponding to the oven-dry MC (m^3) which was determined as follows. Samples were soaked in water during 4 s and the weight of the displaced water volume was measured. Samples immerged in water may swell, but swelling can be considered as negligible with such a short soaking duration.

Because for MC higher than FSP, there is no shrinkage and v_{Green} is equal to $V_{MC_{FSP}}$, the determination of $V_{MC_{FSP}}$ by Equation 9 allows estimation of the sample BSG using Equations (3-3) and (3-4), W_{OD} being the oven-dry sample weight at the last drying step of the MC study.

3.3.2. Image Processing and PLS Modeling

The NIR-HSI images were subjected to the image processing detailed in (Haddadi et al., 2015) study that includes the following steps: (1) image calibration in reflectance, (2) recovering bad pixels that produce extreme reflectance values at some wavelengths with a median filter, (3) delineation of the small samples on each image, 4) removing outlier spectra using a combination of the principal component analysis (PCA) and the *boxplot* method of Laurikkala et al. (2000), and (5) conversion of the remaining reflectance spectra into absorbance spectra. The whole image processing was performed in *MATLAB 7.12.0 (Torrance, CA, USA)* and *ENVI-IDL* image processing software (*Exelis Visual Information solution, Boulder, Colorado, CO, USA*).

Among all types of multivariate linear analysis methods, the partial least squares (PLS) regression is quick, accurate, and suitable for data with many variables such as spectral data. It is especially useful when the data show a high level of multicollinearity, such as in our case, because the reflectance values are not completely independent from each wavelength to another one. PLS yields informative, reliable information by projecting the spectra into a fewer variables, which have less noise and unwanted over-fitting (Rosipal and Kramer 2006). Distinct PLS models were constructed for estimating ρ_{MC} and *BSG*. In each case, the models were built using the median spectra of each sample image as explanatory variables. Indeed, in our MC study, we showed that the median spectra provide a better accuracy for the PLS models compared to 100 randomly selected spectra (Haddadi et al. 2015). Also the median spectra have the advantage over the average spectra of not considering extreme spectra values.

For ρ_{MC}, the whole data-set was considered, whereas for *BSG*, two cases were considered: one with the whole data-set and one with only spectra corresponding to samples that have an MC of less than 12%. Indeed, *BSG* is associated to oven-dry weight and as such should not be related to samples having high MC. The 12% threshold is comparable to the ones used in other density studies. Samples were considered as dry when their MC was around 8% in Via et al.'s (2003), less than 12% in Hans et al.'s (2013) and in Hein's (2010) studies. For both ρ_{MC} and *BSG* modeling, the data-set was split into a calibration data-set that was used to build the PLS model and a validation data-set that was used for validating the model. For each variable, the calibration and validation data-sets were created by randomly dividing in two halves in a way that covers the whole variable range. However, for the BSG models, we also tested

the method over part of the whole dataset that corresponds to samples of low MC (MC of less than 12 %). The performance of each model was assessed using the coefficient of determination (R^2), the root mean square error (RMSE) and the ratio of performance to deviation (RPD) of the models. For each model, the number of latent variables corresponds to the minimum RMSE of the leave-one out cross-validation.

3.4. Results

The distribution histogram of all the sample spectra is shown in Figure 3-1a, for ρ_{MC} and in Figure 3-1b, for *BSG*. ρ_{MC} ranges between 365 and 862 kg/m^3, with a mean value of 515 kg/m^3 and a standard deviation of 94 kg/m^3. *BSG* ranges from 0.325 to 0.375, with a mean value of 0.350 and a standard deviation of 0.011.

(a)

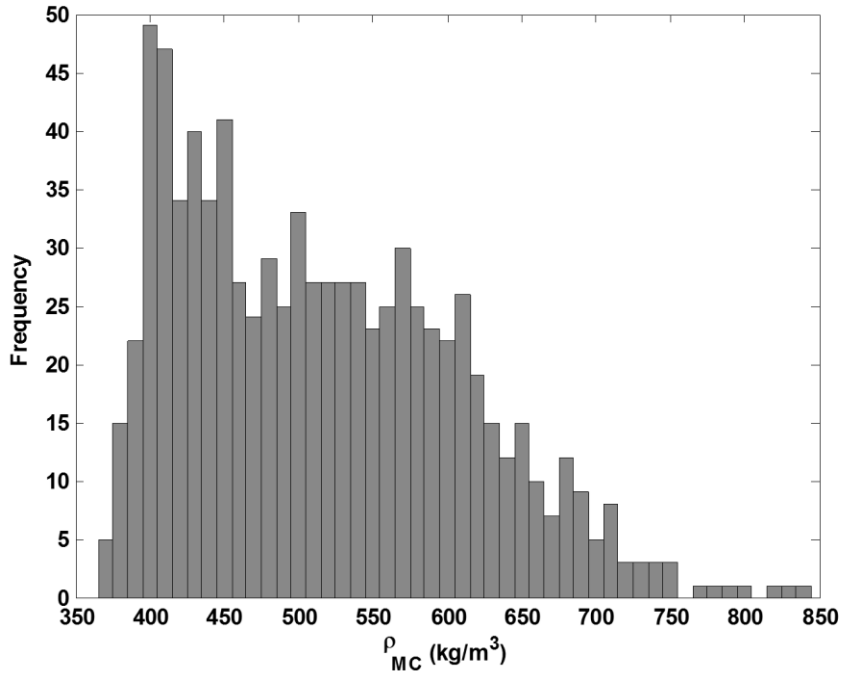

(b)

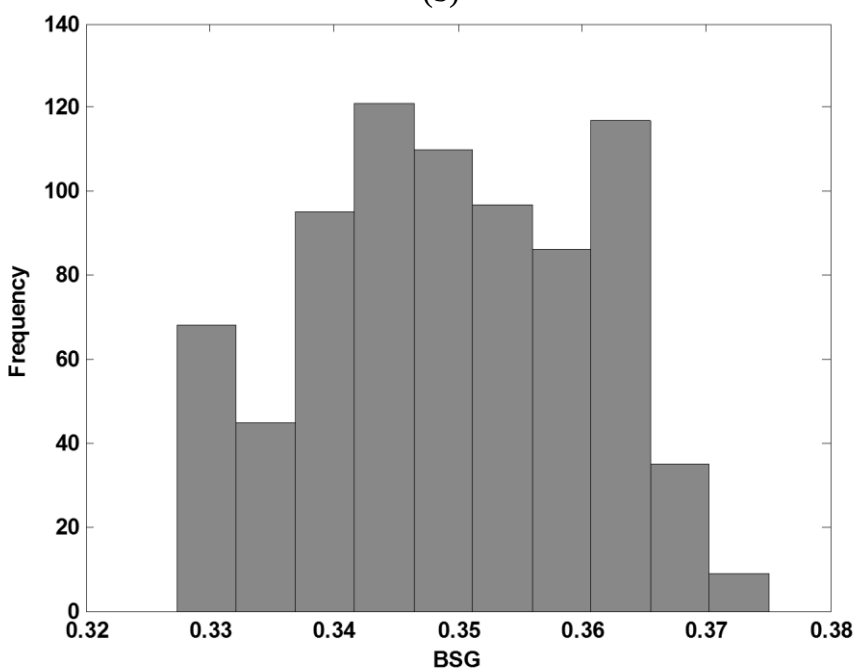

Figure 3-1: Distribution histogram for (a) ρ_{MC} (kg/m^3) and (b) BSG of all the samples.

Figure 3-2 shows median NIR absorbance spectra of a sample as a function of ρ_{MC} and MC for a constant *BSG* value of 0.355. When ρ_{MC} increases, the whole spectrum shifts upward. The MC has also a strong influence. When MC increases, the whole spectrum shifts upward. In the water absorption bands, e.g., 1200 nm and 1420 nm, the rate of increase is much higher than in the other parts of the spectrum. The rate of increase after removing the effects of surface roughness by applying MSC is approximately 1.4% in the neighborhood of 1200 nm and between 3.1% and 4.5% in the neighborhood of 1420 nm.

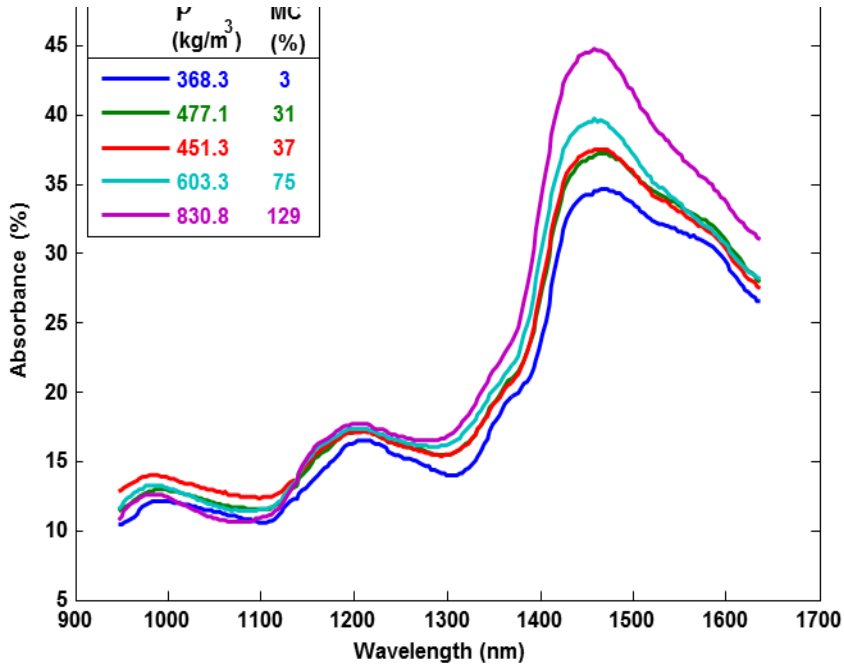

Figure 3-2: Absorbance spectra of a sample having increasing ρ_{MC} (kg/m^3) as moisture content increases. The sample has a BSG of 0.355.

NIR absorbance spectra are shown as a function of *BSG* in Figure 3-3a, for the whole range of MC and in Figure 3-3b, for samples with low MC (less than 12%), because of the possible effect of MC on the spectra. In Figure 3-3a, a distinct pattern

cannot be seen because of the MC influence. By contrast, in Figure 3-3b, when *BSG* increases, the entire spectrum shifts upward. This shift is more apparent in the spectral domain around 1500 nm than in the other part of the spectrum. This spectral region corresponds to the first overtone of OH-bound that is linked to cellulose (Schwanninger et al., 2011).

(a)

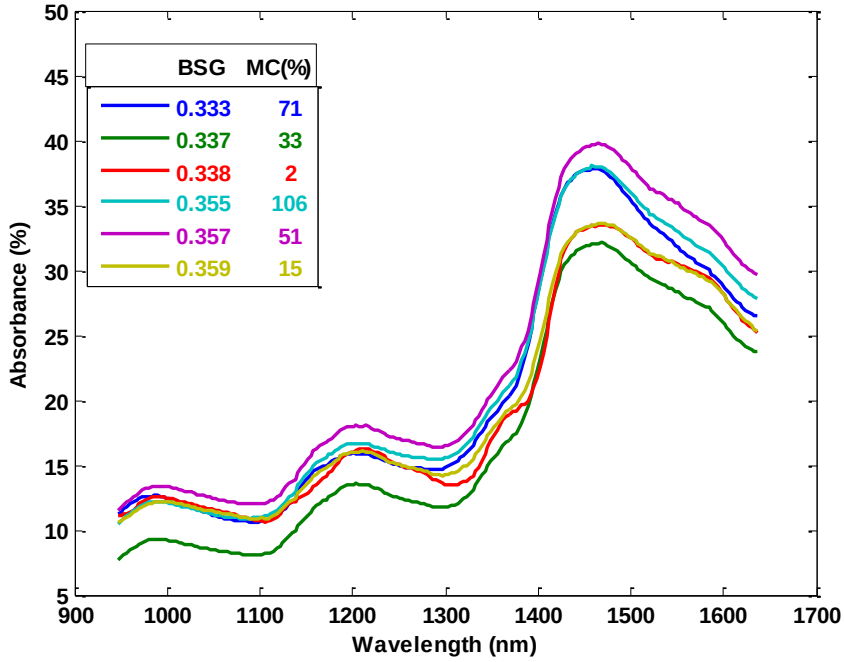

(b)

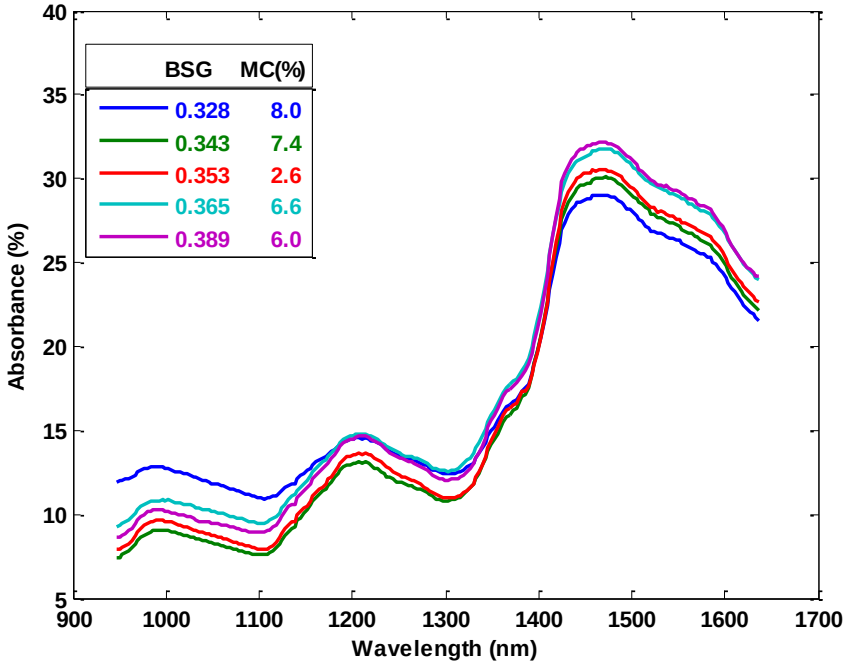

Figure 3-3: Absorbance spectra as a function of BSG for (a) selected samples covering the whole MC range (b) samples with low MC (<12%).

PLS models for ρ_{MC} with eight latent variables provided the best accuracy. The model has an R^2 of 0.81 and an RMSE of 41 kg/m^3 for the calibration data-set and an R^2 of 0.81 and an RMSE of 40 kg/m^3 for the validation data-set (Table 3-3). The model is better for low ρ_{MC} values (less 700 kg/m^3) (Figure 3-4).

These models were obtained without any transformation of the density data. Indeed, because the distribution of the density data was not Gaussian (Figure 3-1a), we applied various mathematical transformations on the density data, such as logarithm and histogram stretching before employing the PLS regression analysis, but these transformations did not improve the model accuracy.

Table 3-3: Statistics of the PLS calibration and validation data-set for ρ_{MC} and *BSG*.

Statistics	**ρ_{MC} (kg/m^3)**		***BSG***			
			All sample spectra		**Sample spectra with *MC*<12%**	
	Calibration	**Validation**	**Calibration**	**Validation**	**Calibration**	**Validation**
Number of LVs	8		12		9	
N	419	419	419	419	62	26
RMSE	40.67	39.48	0.01	0.01	0.004	0.007
R^2	0.82	0.81	0.45	0.29	0.82	0.53
RPD	2.33	2.29	1.31	1.19	2.28	1.39
p-value	< 0.001	< 0.001	0.50	0.50	0.036	<0.001

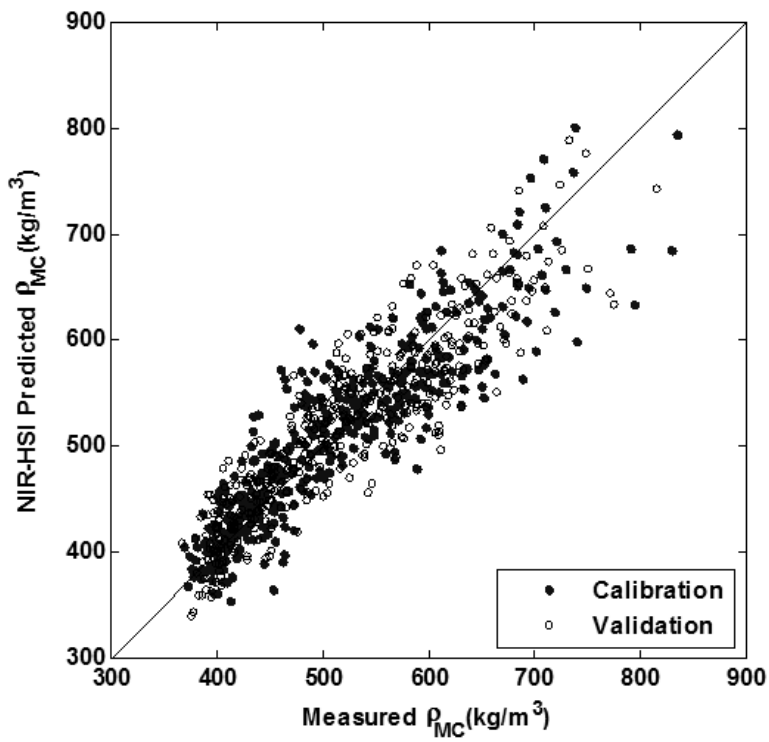

Figure 3-4: Calibration and validation PLS models for ρ_{MC} (kg/m^3) built with 8 latent variables. The statistics associated with each model are given in Table 3-1.

For the *BSG* modeling, when the whole data-set is considered, both the calibration and validation data-sets are not significant (*p*-value of 0.5) despite the high number of latent variables used (12) (Table 3-3). One reason of this lack of significance is that the model tries to estimate a relationship between two sets of variables, but one of them (*BSG*) does not vary significantly as the samples were extracted from boards having lower *BSG* variation. Also the whole dataset includes spectra acquired over both green and dry wood, whereas *BSG* is related to oven-dry weight and green volume. The PLS model does not take shrinkage between green wood and dry wood into account. Above 12% MC, the actual density is lower and the model ignores that and tries to correlate it to the spectra for dry wood. As a result, *BSG* is not correlated to the first PC

of the PCA (Figure 3-5). Also, only the first X-loading is different than zero (Figure 3-6) and thus contributes the most in finding the regression coefficient for the response variable, i.e., *BSG*. The first X-loading is mostly correlated to the absorption bands of cellulose and water. Even when 20 latent variables are used in the PLS model, the model only explains 60% of the variance observed in *BSG* (Figure 3-7).

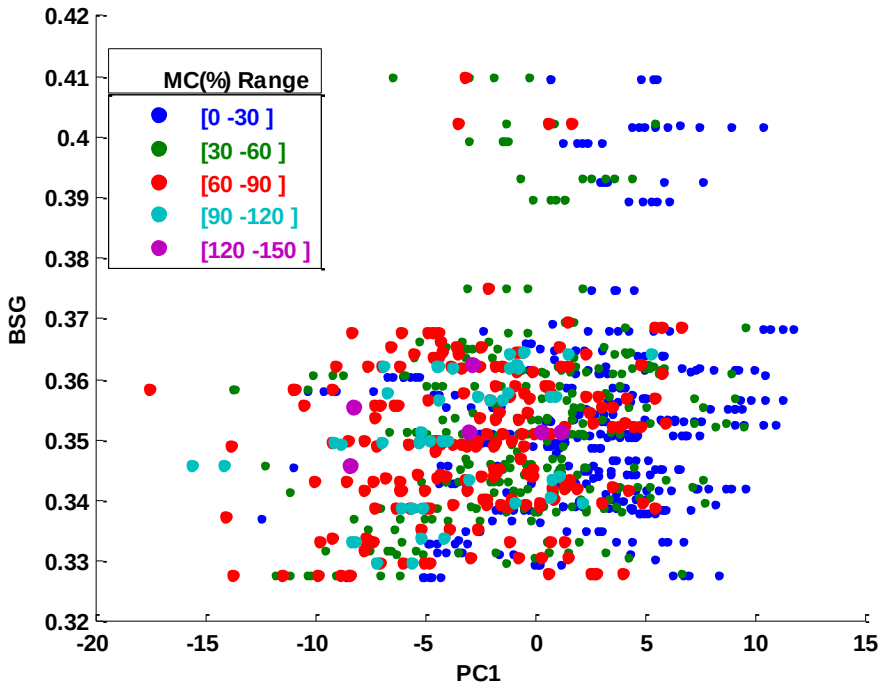

Figure 3-5: Relationship between the first PC of PCA and BSG for different levels of MC.

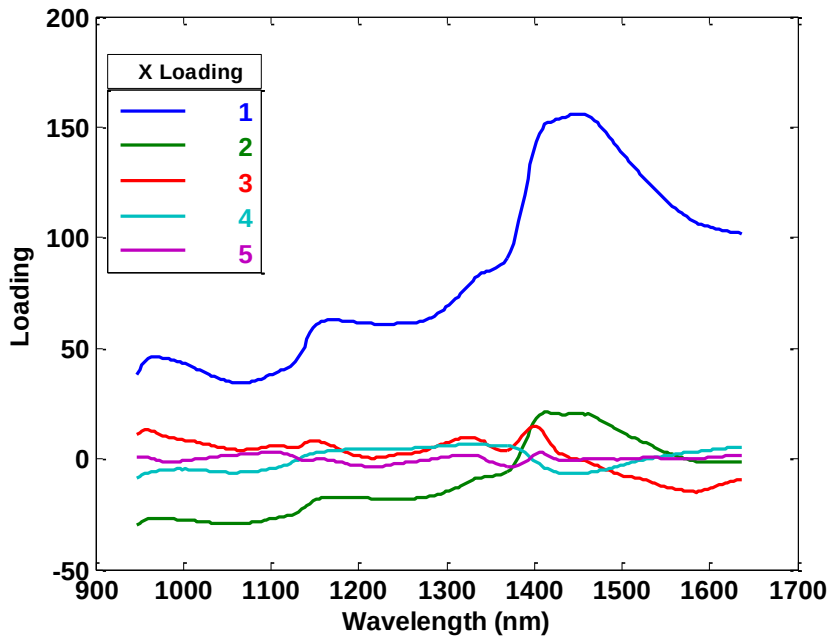

Figure 3-6: First five X-loadings of the PLS models for BSG with the whole data-set.

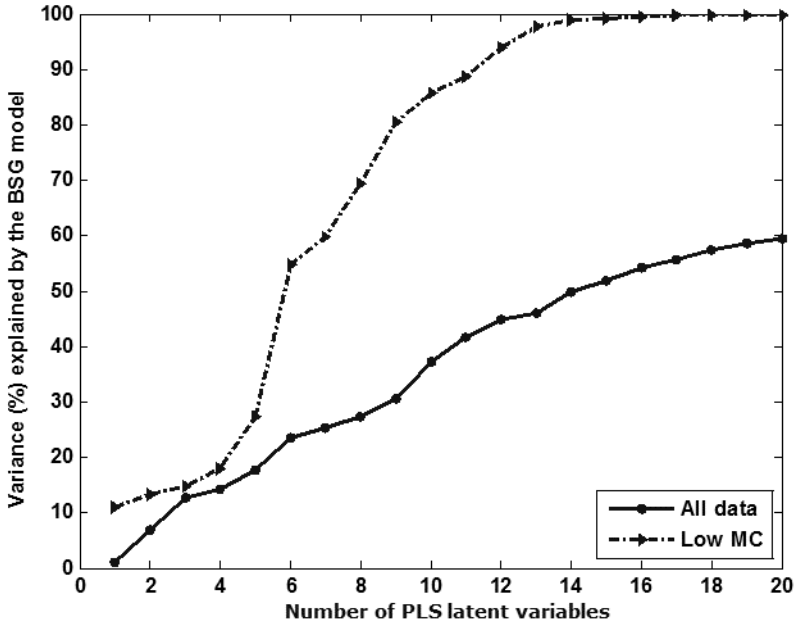

Figure 3-7: Comparison of the variation explained by the BSG model fitted with the whole data set and with low MC samples.

When only low MC sample (MC<12%) spectra are used, the model needs nine latent variables to be built and both the calibration and the validation data-sets are significant (p-value< 0.05; Table 3-3). The R^2 of the calibration data-set increases to 0.82 and the one of the validation data-set increases to 0.53. The RMSE decreases to 0.004 for the calibration data-set and to 0.007 for the validation data-set (Table 3-3). Such differences between the calibration and the validation data-sets are also visible in Figure 3-8, where the validation data are more spread.

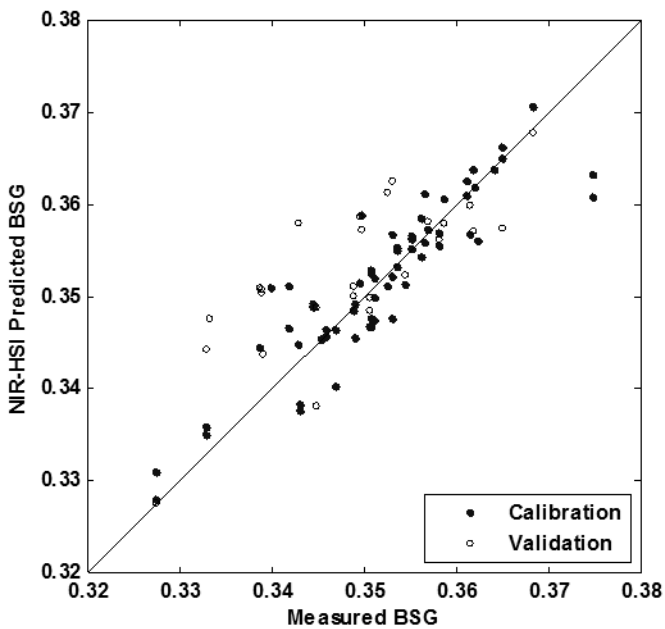

Figure 3-8: Calibration and validation PLS models for BSG built with 9 latent variables for low MC (<12%) samples. The statistics associated with each model are given in Table 3-3.

The good PLS modeling obtained for ρ_{MC} allows applying the model to the whole sample images. Figure 3-9 presents 2D images of ρ_{MC} for samples that were selected to represent an increasing ρ_{MC}. For each sample, the mean and standard deviation of the estimated ρ_{MC} were also determined and the mean estimated value is

compared to the measured bulk ρ_{MC}. The model was also applied to the whole board for producing a 2D ρ_{MC} image of the board (Figure 3-10). Figure 3-10 shows that the knots in the boards have a higher ρ_{MC} because of anatomical changes. Knots are the result of a deformation of cellular structure that produces a high number of cells with a low number of empty spaces between the cells.

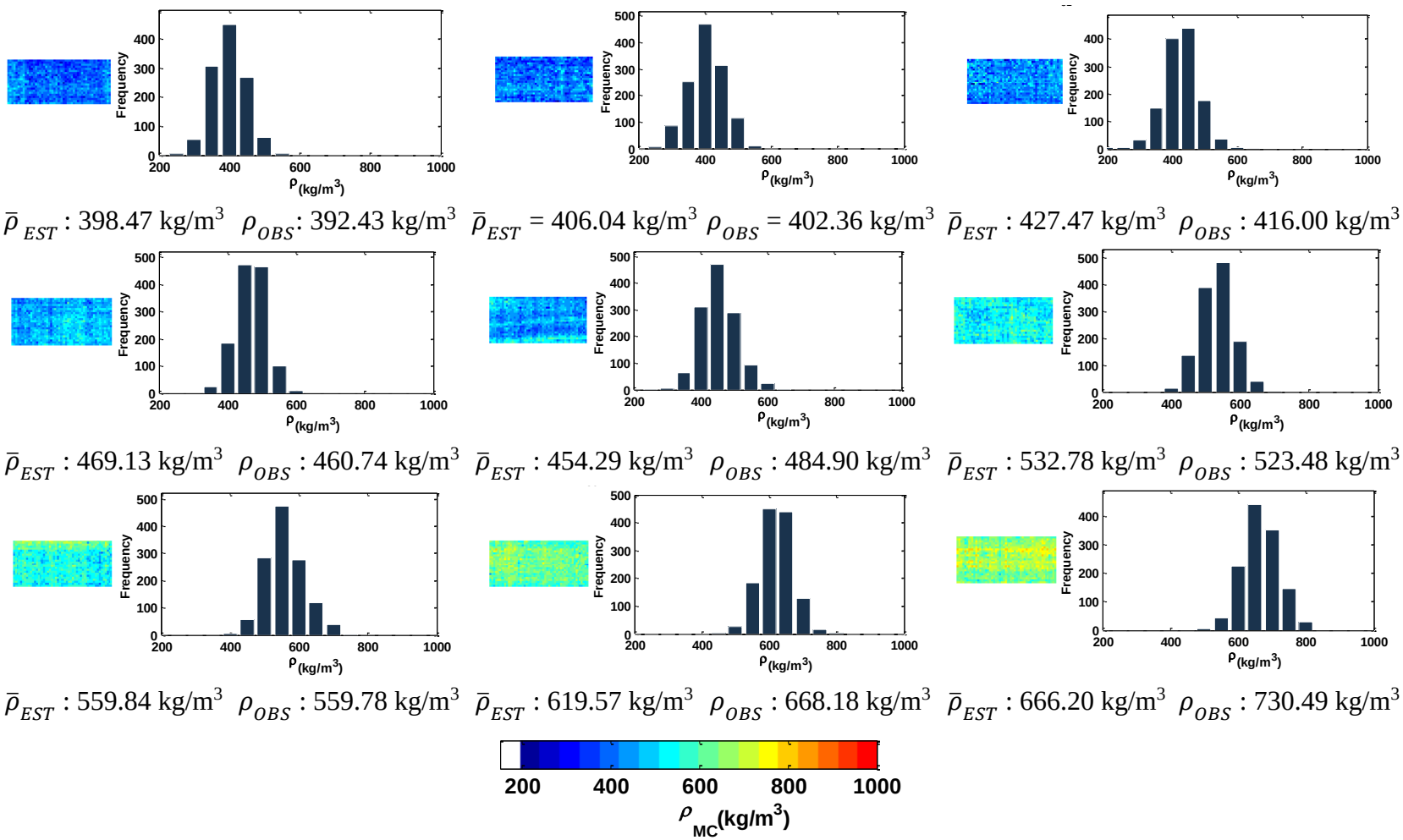

Figure 3-9: 2D ρ_{MC} images for the small samples that were selected to have an increasing ρ_{MC} and their corresponding ρ_{MC} distribution histogram.

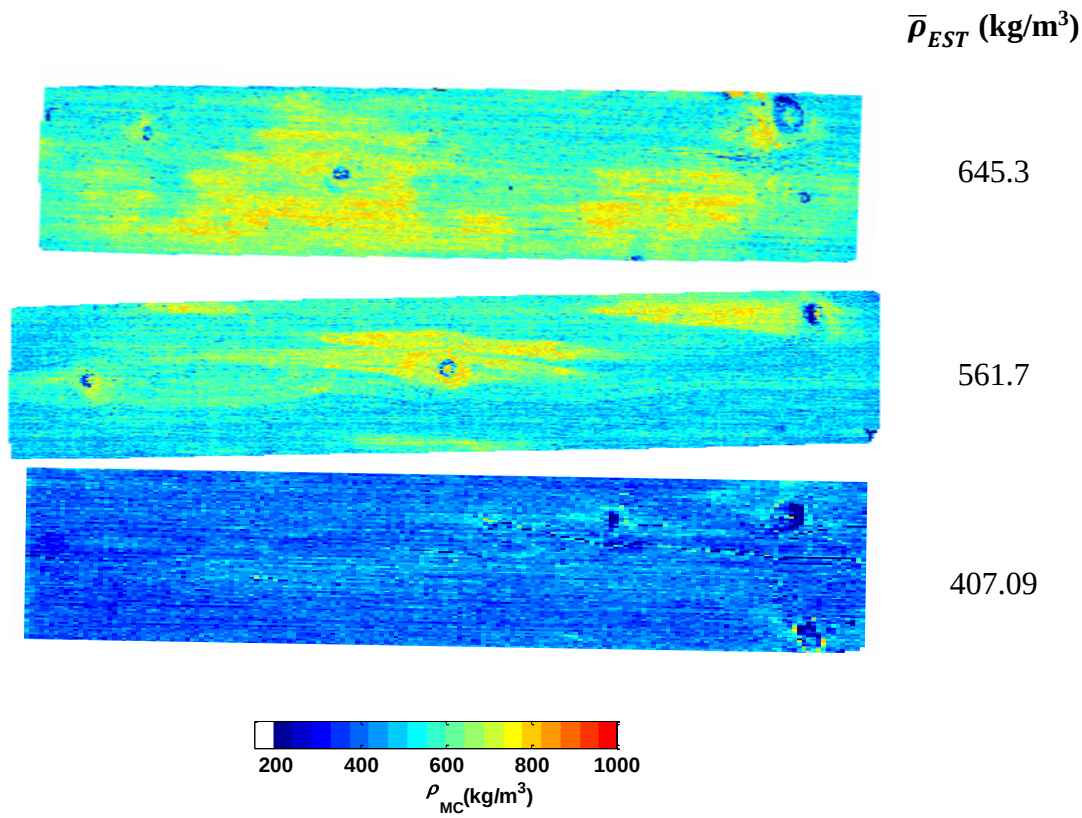

Figure 3-10: 2D ρ_{MC} images of a whole board of decreasing ρ_{MC}.

The model of *BSG* based on sample spectra with MC <12% was applied to the whole board for producing a 2D *BSG* image of the board (Figure 3-11). The mean estimated *BSG* for each board is also presented.

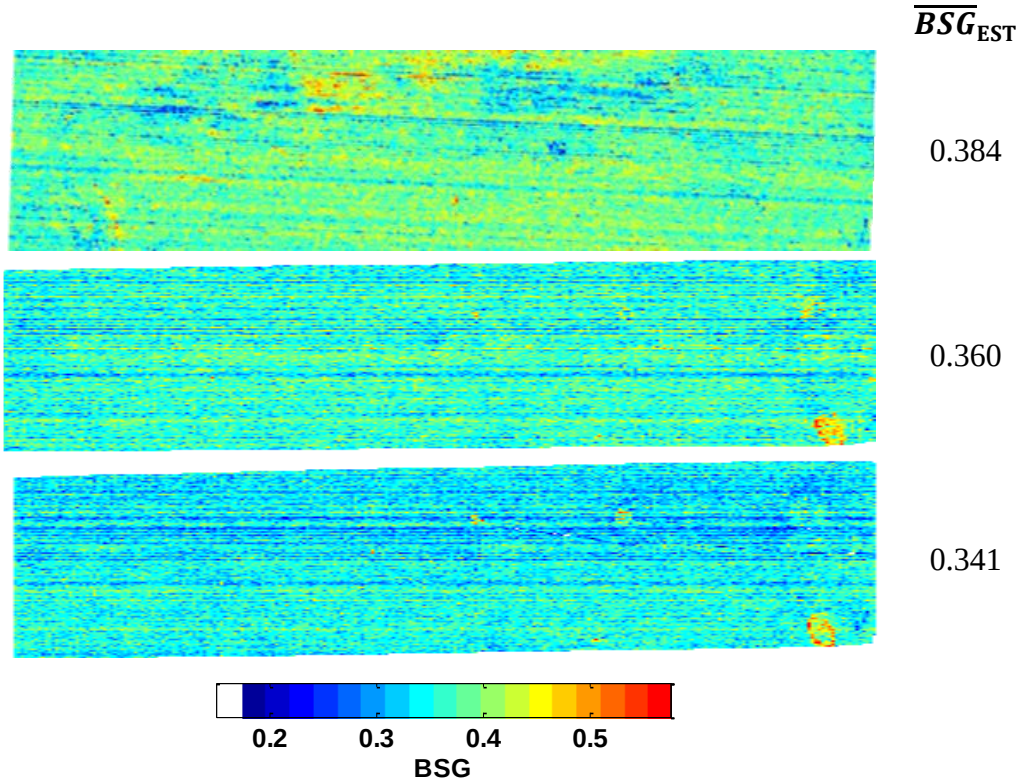

Figure 3-11: 2D BSG images of a whole board of decreasing BSG.

3.5. Discussion

PLS models between ρ_{MC} and NIR absorbance spectra extracted from NIR-hyperspetcral images were established. The PLS model has eight latent variables for both the calibration and validation data-sets. The same number of latent variables was used in the PLS models of the companion MC study (Haddadi et al. 2015), as well as in several other air-dry density studies (Hoffmeyer and Pedersen 1995, Fujimoto et al. 2008, Inagaki et al. 2012), but it is higher than those of Jones et al.'s (2007) study, which uses hyperspectral imaging data and those of several other studies using spot NIRS measurements (Schimleck et al. 2001, Schimleck 2002, Schimleck et al. 2003,

Via et al. 2003, Jones et al. 2005, Schimleck et al. 2005a, 2005b, Fujimoto et al. 2007, Jones et al. 2007, Fujimoto et al. 2010, Mora and Schimleck 2010, Kothiyal and Raturi 2011, Xu et al. 2011, Santos et al. 2012). The only PLS model, which has more than eight latent variables was the one established for oven-drying density of sugi (*Cryptomeria Japonica* D. Don) from NIRS spot measurements (Watanabe et al. 2012).

Our models were significant at p-value < 0.001. It gave an R^2 of 0.81 with both the calibration and the validation data-sets. This R^2 is a little higher than the one obtained for the PLS of the companion MC study (R^2= 0.76; Haddadi et al. 2015). Our models produced an RMSE of 41 kg/m^3 and an RPD of 2.33, with the calibration data-set, and an RMSE of 40 kg/m^3 and an RPD of 2.29, with the validation data-set. Such standard error of the estimates is higher than those obtained by several other studies (Hoffmeyer and Pedersen 1995, Schimleck et al. 2001, Schimleck 2002, Schimleck et al. 2003, Schimleck et al. 2005a, 2005b, Fujimoto et al. 2007, 2008, 2010, Kothiyal and Raturi 2011, Xu et al. 2011, Alves et al. 2012, Inagaki et al. 2012, Watanabe et al. 2012), but these studies used spot NIR spectroscopy measurements that are made with contact to the wood sample. Our RMSE is better than the RMSE obtained by some studies using spot NIRS measurements (Schimleck et al. 2003, Jones et al. 2007, Mora and Schimleck 2010) and highly better that the one obtained with hyperspectral imaging data (RMSE = 97 kg/m3; Jones et al. 2007).

For the *BSG* estimation, despite the high number of latent variables (12) compared to the ρ_{MC} model, both the calibration and validation data-sets were not significant when the whole data-set was used. One of the reasons is that the variation of

BSG was not large enough to produce statistically significant models. Another reason is related to the fact that the whole dataset includes spectra acquired over both green and dry wood, whereas *BSG* is related to oven-dry weight and green volume. The PLS model does not take shrinkage between green wood and dry wood into account. Above 12% MC, the actual density is lower and the model ignores that and tries to correlate it to the spectra for dry wood. For the models fitted with low MC sample spectra, the PLS models have nine latent variables. A same number of latent variables was used to derive PLS models for BSG or BD estimation of low MC samples and using NIRS spot measurements in the case of lodgepole pine (Mora et al. 2011a), black spruce (*Picea mariana* Mill.) (Hans et al. 2013), as well as quaking aspen (*Populus tremuloides* Michx.) and balsam poplar (*Populus balsamifera* L.) (Hans et al. 2015). However, fewer latent variables were used for the PLS models established with hyperspectral imaging data (Mora et al. 2011b), as well as for those established with spot NIRS measurements in several studies of Table II (Thygesen 1994, Gindl et al. 2001, Defo et al. 2007, Hein et al. 2009a, 2009b, Mora and Schimleck 2009, Mora et al. 2011b, Santos et al. 2012) A higher number of latent variables were used to establish PLS models in two studies of Table II (Mora and Schimleck 2009, Galleguillos-Hart et al. 2010).

With the calibration data-set, the *BSG* model based on low MC samples has an R^2 of 0.82, which is similar to the one for the MC (R^2= 0.83) and ρ_{MC} (R^2= 0.81) models, but for the validation data-set, R^2 is 0.53 and thus is lower than the one for the MC model (R^2= 0.76) and the ρ_{MC} model (R^2= 0.81). The corresponding RMSE is 0.004 and 0.007 for the calibration and validation data-sets, respectively. The corresponding RPD with the calibration data-set is 2.28, but the RPD with the validation data-set is low

(1.39). Both RMSEs are lower than those obtained by the other studies on *BSG* estimation using NIR spot measurements (Table 3-2), as well as by Mora et al. (2011b) who used hyperspectral imaging data.

3.6. Conclusions

Our study assessed the potential of NIR hyperspectral images to produce ρ_{MC} and *BSG* images of subalpine fir boards. The models were calibrated and validated using the median spectra of each sample image. For ρ_{MC}, both the calibration and validation data-sets produced significant models at *p*-value < 0.001. The validation data-set produced a model having an R^2 of 0.81, an RMSE of 40 kg/m^3, and an RPD of 2.29. It was applied to both the small sample images and the whole board image in order to produce 2D images of ρ_{MC}. For *BSG*, only models built with low MC samples were significant, despite the higher number of latent variables used with the whole data-set. Indeed, the variation of *BSG* was not large enough to produce statistically significant models. Also the whole dataset includes spectra acquired over both green and dry wood, whereas *BSG* is related to oven-dry weight and green volume. The PLS model does not take shrinkage between green wood and dry wood into account. Above 12% MC, the actual density is lower and the model ignores that and tries to correlate it to the spectra for dry wood. The R^2 of the *BSG* model with low MC samples for the calibration and validation data-set was 0.82 and 0.53, respectively, and the corresponding RMSE was 0.004 and 0.007, respectively. Further work is needed to test the method over a data-set having a higher *BSG* variation.

All the spectra used in the models were extracted from images that were acquired with a camera having a field of view of 17.5° and being positioned at 48 cm height. A higher quality of spectra can be achieved using a camera with a wider field of view, which allows a reduced distance between the camera and the target and thus lower environmental interference. This would be expected to lead to a more accurate estimation of ρ_{MC} or *BSG*.

The method presented here is based on NIR radiations that have two major disadvantages. First, they have a limited penetration depth in solid wood, from 1 to 5 mm depending on surface roughness and the wavelength used (Tsuchikawa et al. 1996, Tsuchikawa et al. 2001, Sykes et al. 2005). More penetrating radiations, such as microwaves, should be tested for estimating ρ_{MC} or *BSG* of boards. Second, the spectral measurements are highly influenced by the wood surface type and roughness and further work is needed to test the influence of these factors on the estimation. Finally, the method used PLS models to relate NIR hyperspectral imaging spectra to ρ_{MC} and *BSG*. Further work is needed to test a more deterministic approach that uses optical models, such as the one of Tsuchikawa et al. (2001). Indeed, the model of Tsuchikawa et al. (2001) allows the computation of the scattering S and absorption K coefficients using the Kubelka-Munk theory from the reflectance spectra. These coefficients (in particular K) can then be related to the concentration of cellulose and hemicellulose, which are the main components of the wood density. Such a study is currently underway.

3.7. Acknowledgements

The authors thank G. Chow from FPInnovations as well as K. Phung (UNB) for their help during the experiments. Special thanks to Guillaume Hans for helping with Tables 3-1 and 3-2. The study was supported by an NSERC Strategic Grant awarded and a New Brunswick Foundation for Innovation grant to Prof. B. Leblon. This paper was written in memoriam of Dr. James Burger, who suddenly died on 6 September 2014.

3.8. References

Alves A., Santos A., Rozenberg P., Paques L.E., Charpentier J.P., Schwanninger M. & Rodrigues J. (2012) A common near infrared-based partial least squares regression model for the prediction of wood density of *Pinus pinaster* and *Larix x eurolepis*. *Wood Science and Technology*, 46(1-3): 157-175. doi: 10.1007/s00226-010-0383-x

ASTM-D2395–07a (2009) *Standard test methods for specific gravity of wood and wood-based materials*, ASTM International, West Conshohocken, PA, doi: 10.1520/D2395-07A, www.astm.org.

ASTM-D4442–07 (2009) *Standard test methods for direct moisture content measurement of wood and wood-base materials*, ASTM International, West Conshohocken, PA, doi: 10.1520/D4442-07, www.astm.org.

Barnett J. & Jeronimidis G. (2009) *Wood quality and its biological basis.* Wiley. 226 pages.

Bowyer J.L., Shmulsky R. & Haygreen J.G. (2007) *Forest products and wood science: An introduction.* Oxford, UK: John Wiley & Sons. 496 pages.

Defo M., Taylor A.M. & Bond B. (2007) Determination of moisture content and density of fresh-sawn red oak lumber by near infrared spectroscopy. *Forest Products Journal*, 57(5): 68-72

Demetriades-Shah T.H., Steven M.D. & Clark J.A. (1990) High-resolution derivative spectra in remote-sensing. *Remote Sensing of Environment*, 33(1): 55-64. doi: 10.1016/0034-4257(90)90055-Q

Diaz-Vaz J.E., Ananías R.A., Rodríguez S., Torres M., Fernández A. & Poblete H. (2009) Compression wood in *Pinus radiata* ii: Density and chemical composition. *Ciencia y tecnología*, 11(2): 139-151. doi: 10.4067/S0718-221X2009000200005

Duncker P. & Spiecker H. (2009) Detection and classification of Norway spruce compression wood in reflected light by means of hyperspectral image analysis. *IAWA Journal*, 30(1): 59-70. doi: 10.1163/22941932-90000203

Forest Products Laboratory (2010) *Wood handbook: Wood as an engineering material.* Madison, WI, USA: U.S. Department of Agriculture, Forest Service, Forest Products Laboratory. 508 pages.

Fujimoto T., Kurata Y., Matsumoto K. & Tsuchikawa S. (2008) Application of near infrared spectroscopy for estimating wood mechanical properties of small clear and full length lumber specimens. *Journal of Near Infrared Spectroscopy*, 16(6): 529-537. doi: 10.1255/Jnirs.813

Fujimoto T., Kurata Y., Matsumoto K. & Tsuchikawa S. (2010a) Feasibility of near-infrared spectroscopy for on-line grading of sawn lumber. *Applied Spectroscopy*, 64(1): 92-99

Fujimoto T., Kurata Y., Matsumoto K. & Tsuchikawa S. (2010b) Feasibility of near-infrared spectroscopy for online multiple trait assessment of sawn lumber. *Journal of Wood Science*, 56(6): 452-459

Fujimoto T., Yamamoto H. & Tsuchikawa S. (2007) Estimation of wood stiffness and strength properties of hybrid larch by near-infrared spectroscopy. *Applied Spectroscopy*, 61(8): 882-888. doi: 10.1366/000370207781540150

Galleguillos-Hart C., Fernandez M.P. & Guesalaga A. (2010) A portable method to estimate wood basic density from increment cores using spectroscopic techniques. *Journal of Near Infrared Spectroscopy,* 18(6): 465-472

Garratt G.A. (1931) The mechanical properties of wood: Including a discussion of the factors affecting the mechanical properties, working stresses for structural timber, and methods of timber, and methods of timber testing. New York, USA: John Wiley & Sons. 276 pages.

Geladi P., Burger J. & Lestander T. (2004) Hyperspectral imaging: Calibration problems and solutions. *Chemometrics and Intelligent Laboratory Systems,* 72(2): 209-217. doi: 10.1016/j.chemolab.2004.01.023

Gindl W., Teischinger A., Schwanninger M. & Hinterstoisser B. (2001) The relationship between near infrared spectra of radial wood surfaces and wood mechanical properties. *Journal of Near Infrared Spectroscopy,* 9(4): 255-261. doi: 10.1255/jnirs.311

Haddadi A., Burger J., Leblon B., Pirouz Z., Groves K. & Nader J. (2015) Using near infrared hyperspectral images on subalpine fir board - part 1: Moisture content estimation. *Wood Material Science & Engineering,* 10(1): 27-40. doi: 10.1080/17480272.2014.965743

Hagman O. (1997) Multivariate prediction of wood surface features using an imaging spectrograph. *Holz als Roh- und Werkstoff,* 55(6): 377-382. doi: 10.1007/s001070050250

Hans G., Leblon B., Cooper P., LaRocque A., Nader J. & Stirling R. (2015) Determination of moisture content and basic specific gravity of *Populus tremuloides* (Michx.) and *Populus balsamifera* (l.) logs using a portable near-infrared spectrometer. *Wood Material Science & Engineering,* 10(1): 3-16. doi: 10.1080/17480272.2014.916349

Hans G., Leblon B., Stirling R., Nader J., LaRocque A. & Cooper P. (2013) Monitoring of moisture content and basic specific gravity in black spruce logs using a handheld MEMS-based near-infrared spectrometer. *The Forestry Chronicle,* 89(5): 605-618. doi: 10.5558/tfc2013-112

Hein P.R.G. (2010) Multivariate regression methods for estimating basic density in *eucalyptus* wood from near infrared spectroscopic data. *Cerne Lavras,* 16: 90-96

Hein P.R.G., Campos A.C.M., Trugilho P.F., Lima J.T. & Chaix G. (2009a) Near infrared spectroscopy for estimating wood basic density in *eucalyptus urophylla* and *eucalyptus grandis*. *Cerne,* 15(2): 133-141. doi: abr./jun. 2009

Hein P.R.G., de Sa V.A., Bufalino L. & Mendes L.M. (2009b) Calibrations based on near infrared spectroscopic data to estimate wood-cement panel properties. *Bioresources,* 4(4): 1620-1634

Hein P.R.G., Lima J.T. & Chaix G. (2009c) Robustness of models based on near infrared spectra to predict the basic density in *eucalyptus urophylla* wood. *Journal of Near Infrared Spectroscopy,* 17(3): 141-150

Hoffmeyer P. & Pedersen J.G. (1995) Evaluation of density and strength of Norway spruce wood by near infrared reflectance spectroscopy. *Holz als Roh- und Werkstoff,* 53(3): 165-170. doi: 10.1007/BF02716418

Inagaki T., Schwanninger M., Kato R., Kurata Y., Thanapase W., Puthson P. & Tsuchikawa S. (2012) *Eucalyptus camaldulensis* density and fiber length estimated

by near-infrared spectroscopy. *Wood Science and Technology,* 46(1-3): 143-155. doi: 10.1007/s00226-010-0379-6

Jones P.D., Schimleck L.R., Peter G.F., Daniels R.F. & Clark A. (2005) Nondestructive estimation of *Pinus taeda* l. Wood properties for samples from a wide range of sites in Georgia. *Canadian Journal of Forest Research,* 35(1): 85-92. doi: 10.1139/x04-160

Jones P.D., Schimleck L.R., So C.L., Clark A. & Daniels R.F. (2007) High resolution scanning of radial strips cut from increment cores by near infrared spectroscopy. *IAWA Journal,* 28(4): 473-484. doi: 10.1163/22941932-90001657

Kobori H., Gorretta N., Rabatel G., Bellon-Maurel V., Chaix G., Roger J.M. & Tsuchikawa S. (2013) Applicability of VIS-NIR hyperspectral imaging for monitoring wood moisture content (mc). *Holzforschung,* 67(3): 307-314. doi: 10.1515/Hf-2012-0054

Kothiyal V. & Raturi A. (2011) Estimating mechanical properties and specific gravity for five-year-old *eucalyptus tereticornis* having broad moisture content range by NIR spectroscopy. *Holzforschung,* 65(5): 757-762. doi: 10.1515/HF.2011.055

Laurikkala J., Juhola M. & Kentala E. (2000) Informal identification of outliers in medical data, In 14th European Conference on Artificial Intelligence and 5th International Workshop on Intelligent Data Analysis in Medicine and Pharmacology IDAMAP-2000, (Berlin, Germany), pp. 20-24

Mora C.R. & Schimleck L.R. (2009) Determination of specific gravity of green *Pinus taeda* samples by near infrared spectroscopy: Comparison of pre-processing methods using multivariate figures of merit. *Wood Science and Technology,* 43(5-6): 441-456. doi: 10.1007/s00226-008-0235-0

Mora C.R. & Schimleck L.R. (2010) Kernel regression methods for the prediction of wood properties of *Pinus taeda* using near infrared spectroscopy. *Wood Science and Technology,* 44(4): 561-578. doi: 10.1007/s00226-009-0299-5

Mora C.R., Schimleck L.R., Clark A. & Daniels R.F. (2011a) Determination of basic density and moisture content of merchantable loblolly pine logs by near infrared spectroscopy. *Journal of Near Infrared Spectroscopy,* 19(5): 391-399. doi: 10.1255/Jnirs.947

Mora C.R., Schimleck L.R., Isik F., Mahon J.M., Clark A. & Daniels R.F. (2009) Relationships between acoustic variables and different measures of stiffness in standing *Pinus taeda* trees. *Canadian Journal of Forest Research,* 39(8): 1421-1429. doi: 10.1139/X09-062

Mora C.R., Schimleck L.R., Yoon S.C. & Thai C.N. (2011b) Determination of basic density and moisture content of loblolly pine wood disks using a near infrared hyperspectral imaging system. *Journal of Near Infrared Spectroscopy,* 19(5): 401-409. doi: 10.1255/Jnirs.948

Nystrom J. & Hagman O. (1999) Real-time spectral classification of compression wood in *Picea abies*. *Journal of Wood Science,* 45(1): 30-37. doi: 10.1007/Bf00579521

Panshin A.J. & De Zeeuw C. (1980) Textbook of wood technology: Structure, identification, uses, and properties of the commercial woods of the united states and Canada. New York, USA: McGraw-Hill. 722 pages.

Rosipal R. & Kramer N. (2006) Overview and recent advances in partial least squares. *Subspace, Latent Structure and Feature Selection,* 3940: 34-51

Rowell R.M. (2013) *Handbook of wood chemistry and wood composites.* Boca Raton, USA: CRC Press. 687 pages.

Salzer R. & Siesler H.W. (2009) *Infrared and Raman spectroscopic imaging.* Weinheim, Germany: John Wiley & Sons. 530 pages.

Santos A.J.A., Alves A.M.M., Simoes R.M.S., Pereira H., Rodrigues J. & Schwanninger M. (2012) Estimation of wood basic density of *acacia melanoxylon* (r. Br.) by near infrared spectroscopy. *Journal of Near Infrared Spectroscopy,* 20(2): 267-274. doi: 10.1255/Jnirs.386

Schimleck L.R. (2002) Estimation of wood properties of increment cores by near infrared spectroscopy. *Abstracts of Papers of the American Chemical Society,* 223: U139-U140

Schimleck L.R. & Evans R. (2003) Estimation of air-dry density of increment cores by near infrared spectroscopy. *Appita Journal,* 56(4): 312-317

Schimleck L.R., Evans R. & Ilic J. (2001) Estimation of *eucalyptus* delegatensis wood properties by near infrared spectroscopy. *Canadian Journal of Forest Research,* 31(10): 1671-1675. doi: 10.1139/cjfr-31-10-1671

Schimleck L.R., Evans R. & Matheson A.C. (2002) Estimation of *Pinus radiata* d. Don clear wood properties by near-infrared spectroscopy. *Journal of Wood Science,* 48(2): 132-137. doi: 10.1007/Bf00767290

Schimleck L.R., Jones P.D., Clark A., Daniels R.F. & Peter G.F. (2005a) Near infrared spectroscopy for the nondestructive estimation of clear wood properties of *Pinus taeda* l. From the southern united states. *Forest Products Journal,* 55(12): 21-28

Schimleck L.R., Jones P.D., Peter G.F., Daniels R.F. & Clark A. (2005b) Success in using near infrared spectroscopy to estimate wood properties of *Pinus taeda* radial strips not due to autocorrelation. *Journal of Near Infrared Spectroscopy,* 13(1): 47-51

Schimleck L.R., Michell A.J., Raymond C.A. & Muneri A. (1999) Estimation of basic density of *eucalyptus globulus* using near-infrared spectroscopy. *Canadian Journal of Forest Research,* 29: 194-201. doi: 10.1139/x98-204

Schimleck L.R., Mora C. & Daniels R.F. (2003) Estimation of the physical wood properties of green *Pinus taeda* radial samples by near infrared spectroscopy. *Canadian Journal of Forest Research,* 33(12): 2297-2305. doi: 10.1139/X03-173

Schimleck L.R., Rezende G.D.S.R., Demuner B.J. & Downes G.M. (2006) Estimation of whole-tree wood quality traits using near infrared spectra from increment cores. *Appita Journal,* 59(3): 231-236

Schimleck L.R., Sturzenbecher R., Mora C., Jones P.D. & Daniels R.F. (2005c) Comparison of *Pinus taeda* l. Wood property calibrations based on NIR spectra from the radial-longitudinal and radial-transverse faces of wooden strips. *Holzforschung,* 59(2): 214-218

Schinker M.G., Hansen N. & Spiecker H. (2003) High-frequency densitometry - a new method for the rapic evaluation of-wood density variations. *IAWA Journal,* 24(3): 231-239

Schwanninger M., Rodrigues J.C. & Fackler K. (2011) A review of band assignments in near infrared spectra of wood and wood components. *Journal of Near Infrared Spectroscopy,* 19(5): 287-308. doi: 10.1255/Jnirs.955

Schweingruber F.H. (1988) Tree rings: Basics and applications of dendrochronology. Springer. 276 pages.

Stirling R., Trung T., Breuil C. & Bicho P. (2007) Predicting wood decay and density using NIR spectroscopy. *Wood and Fiber Science,* 39(3): 414-423

Sykes R., Li B., Hodge G., Goldfarb B., Kadla J. & Chang H.-m. (2005) Prediction of loblolly pine wood properties using transmittance near-infrared spectroscopy. *Canadian Journal of Forest Research,* 35: 2423-2431. doi: 10.1139/X05-161

Thumm A., Riddell M., Nanayakkara B., Harrington J. & Meder R. (2010) Near infrared hyperspectral imaging applied to mapping chemical composition in wood samples. *Journal of Near Infrared Spectroscopy,* 18(6): 507-515. doi: 10.1255/Jnirs.909

Thygesen L.G. (1994) Determination of dry matter content and basic density of Norway spruce by near infrared reflectance and transmittance spectroscopy. *Journal of Near Infrared Spectroscopy,* 2: 127–135. doi: 10.1255/jnirs.39

Tsuchikawa S., Hayashi K. & Tsutsumi S. (1996) Nondestructive measurement of the subsurface structure of biological material having cellular structure by using near-infrared spectroscopy. *Applied Spectroscopy,* 50(9): 1117-1124. doi: 10.1366/0003702963905114

Tsuchikawa S., Torii M. & Tsutsumi S. (2001) Directional characteristics of near infrared light reflected from wood. *Holzforschung,* 55(5): 534-540. doi: 10.1515/HF.2001.086

Via B.K., Shupe T.F., Groom L.H., Stine M. & So C.L. (2003) Multivariate modelling of density, strength and stiffness from near infrared spectra for mature, juvenile and pith wood of Longleaf pine (*Pinus palustris*). *Journal of Near Infrared Spectroscopy,* 11(5): 365-378

Walker J.C.F. (2006) *Primary wood processing: Principles and practice.* Dordrecht, The Netherlands: Springer. 596 pages.

Wang X., Ross R.J., Erickson J.R., Forsman J.W., McGinnis G.D. & Groot R.C.D. (2000) Nondestructive methods of evaluating quality of wood in preservative-treated piles, U.S. Department of Agriculture, Forest Service, Forest Products Laboratory, F. Service, Research Note FPL-RN-0274, Madison, WI, USA, 11 pages.

Watanabe K., Kobayashi I., Kuroda N., Harada M. & Noshiro S. (2012) Predicting oven-dry density of sugi (*Cryptomeria Japonica*) using near infrared (NIR) spectroscopy and its effect on performance of wood moisture meter. *Journal of Wood Science,* 58(5): 383-390. doi: 10.1007/s10086-012-1268-4

Williamson G.B. & Wiemann M.C. (2010) Measuring wood specific gravity ... Correctly. *American Journal of Botany,* 97(3): 519-524. doi: 10.3732/Ajb.0900243

Xu Q.H., Qin M.H., Ni Y.H., Defo M., Dalpke B. & Sherson G. (2011) Predictions of wood density and module of elasticity of balsam fir (*Abies balsamea*) and black spruce (*Picea mariana*) from near infrared spectral analyses. *Canadian Journal of Forest Research,* 41(2): 352-358. doi: 10.1139/X10-215

Yin Y., Nagao H., Liu X. & Nakai T. (2010) Mechanical properties assessment of *cunninghamia lanceolata* plantation wood with three acoustic-based nondestructive methods. *Journal of Wood Science,* 56(1): 33-40. doi: 10.1007/s10086-009-1067-8

Chapter 4. Prediction of Wood Properties for Thawed and Frozen Logs of Quaking Aspen, Balsam Poplar, and Black Spruce from Near-infrared Hyperspectral Images[3]

4.1. Abstract

This study tested the use of near-infrared hyperspectral images to estimate moisture content (MC) and basic specific gravity (BSG) of thawed and frozen logs of three species: quaking aspen, balsam poplar, and black spruce. For each species, more than 90 small 4 cm cubic samples were prepared and subjected to drying steps in both frozen and thawed conditions. At each step, hypercube images and sample weights were recorded to determine MC and BSG of each sample. Partial least squares (PLS) models were calibrated by considering two factors: log state (thawed and frozen conditions) and species, and their combination. With respect to the species, the PLS model accuracy depends on the range of variation of the input data. The model accuracy was the best for black spruce samples that have the lowest range of variation for both MC and BSG, whereas the model accuracy was the lowest for balsam poplar samples that have the highest range of variation for both MC and BSG. With all the data, the accuracy of the MC model worsened, but the accuracy of the BSG model reached a maximum ($R^2_{Validation}$=0.88). The best PLS model was then employed to produce 2D MC and BSG images over the whole log disks. PLS discriminant analysis was also applied to

[3] This chapter was published in *Wood Science and Technology* (October 2015) under the following authorship: Ataollah Haddadi, Brigitte Leblon, Zarin Pirouz, Joseph Nader, and Kevin Groves. doi: 10.1007/s00226-015-0767-z. It is reproduced with the permission of the Springer (see letter permission in Appendix D)

sort the samples according to three MC or BSG classes, the species, and the log state (frozen and thawed). The overall accuracy was higher than 72% for both the MC and BSG sorting, 86% for the species sorting, and 97% for the log state sorting.

4.2. Introduction

Given that wood is a highly variable material and is used to manufacture a wide range of products; ability to measure at-line its physical, mechanical, and chemical properties allows more efficient allocation of this valuable resource to various end-products. For example, logs need to be sorted according to their moisture content (MC) in the oriented strand board industry, because dry logs will produce a high number of dusts and wet logs will require a drying step, which is one of the most expensive and time-consuming step in wood product manufacturing (Denig et al., 2000). Wood basic specific gravity (BSG), which is defined as the ratio between oven-dry weight and green volume divided by the water density (Bowyer et al., 2007, Williamson and Wiemann, 2010), needs to be determined when measuring mechanical properties (module of elasticity (MOE) and module of rupture (MOR)) using acoustic methods (Barnett and Jeronimidis, 2009). Also some manufacturing industries, such as the pulp and paper industry, requires the ability to sort the logs as a function of the species. Finally, in countries such as Canada having lengthy winters with freezing conditions, there is the need to consider the log state (frozen or thawed) when determining wood MC, BSG, or species. It is important to know whether the wood is frozen or not, because frozen wood requires more time and energy to dry than thawed wood and frozen logs require

increased cutting speed than thawed wood and produce lower chip thickness (Krilek et al., 2014).

Several sensors have been developed for non-destructive measurement of wood properties. NIR spectroscopy has been used widely for estimation of several wood properties, including MC and BSG (Thygesen, 1994, Hoffmeyer and Pedersen, 1995, Thygesen and Lundqvist, 2000b, Schimleck et al., 2001b, 2001a, Schimleck et al., 2002b, Schimleck and Evans, 2003, Schimleck et al., 2003b, Via et al., 2003, Jones et al., 2005, Schimleck et al., 2005a, Via et al., 2005, Schimleck et al., 2006, Defo et al., 2007, Fujimoto et al., 2008, Hein et al., 2009, Cooper et al., 2011, Mora et al., 2011a, Schwanninger et al., 2011, Watanabe et al., 2011, Alves et al., 2012, Inagaki et al., 2012, Hans et al., 2013, Leblon et al., 2013, Haddadi et al., 2015a, 2015b, Hans et al., 2015), chemical properties (So et al., 2004, Meder et al., 2010), stiffness and strength (Fujimoto et al., 2007), mechanical properties (MOE and MOR) (Gindl et al., 2001, Fujimoto et al., 2008, Xu et al., 2011), fiber length (Inagaki et al., 2012), shrinkage (Hein, 2012), microfibril angle (Schimleck et al., 2001a, 2001b, Meder et al., 2010, Hein, 2012), compression strength (Hoffmeyer and Pedersen, 1995), and species identification (Tsuchikawa et al., 2003, Adedipe et al., 2008, Haartveit and Flæte, 2008, Russ et al., 2009, Cooper et al., 2011, Hans et al., 2015).

However, most of these studies used spot NIR spectroscopy measurements that do not measure the distribution of wood properties. Biological materials like wood are heterogeneous, and its properties are susceptible to seasonal effect, climate change, and silvicultural treatment. Thus, only one measurement or even some measurements in

different locations are not sufficient to show the distribution of wood properties across the product. Near-infrared hyperspectral imaging (NIR-HSI) systems can provide such distribution of wood properties at a fine resolution by capturing thousands of spectra within a two-dimensional space in a short period of time. Hyperspectral images have already been tested to identify compression wood in Norway spruce (*Picea abies* L.) and in Scot pine (*Pinus sylvestris* L.) lumber (Nystrom and Hagman, 1999, Duncker and Spiecker, 2009), as well as in radiata pine (*P. radiata* D. Don) timber (Meder and Meglen, 2012), to map the chemical composition of wood disks (Thumm et al., 2010), bulk MC and density of loblolly pine (*Pinus taeda* L.) log disks (Mora et al., 2011b), and of subalpine fir (*Abies lasiocarpa* Hook) boards (Haddadi et al., 2015a, 2015b), as well as MC of European beech (*Fagus sylvatica* L.) and Scots pine (*Pinus sylvestris* L.) disks (Kobori et al., 2013). It also has been used for measuring intra-ring density profile of stone pine (*Pinus pinea* L.) samples (Fernandes et al., 2013a, 2013b).

Our study presents a method to estimate MC and BSG images from NIR-HSI images that were acquired by an imaging spectrometer in the 947-1637 nm range over thawed and frozen samples and the entire disks from quaking aspen (*Populus tremuloides* Michx), balsam poplar (*Populus balsamifera* L.), and black spruce (*Picea mariana* Mill.) logs. Most of the previous studies on log MC and BSG estimation used point-source NIR spectroscopy measurements. So far, only Mora et al. (2011b), Fernandes et al. (2013a), (2013b), and Kobori et al. (2013) tested NIR-HSI for estimating MC and/or density of logs, but none of these studies considered the effect of freezing conditions, which could be important for countries such as Canada, which experiences lengthy winters. Also, our study uses an image processing method that is

different than the ones used in Mora et al. (2011b), Fernandes et al. (2013a), (2013b), and Kobori et al. (2013). It consists of a median filtering for finding and replacing bad pixels and a modified version of the *boxplot* method of (Laurikkala et al., 2000) to automatically find abnormal spectra (Haddadi et al., 2015a). This study also considers samples that have a larger MC range (0.1−181.3% dry basis) than Mora et al. (2011b) (46−65% dry basis), (Fernandes et al. (2013a), 2013b)) (12% dry basis), and Kobori et al. (2013) (28−122% dry basis). In this study, we finally tested the use of these images for sorting the samples as a function of MC and BSG classes, species, or log state (frozen and thawed) using a partial least squares discriminant analysis (PLS-DA) method.

4.3. Materials and methods

4.3.1. Sample origin

Disks of quaking aspen (also called trembling aspen) (*Populus tremuloides* Michx), balsam poplar (also called black poplar) (*Populus balsamifera* L.), and black spruce (*Picea mariana* Mill.) were cut in July 2012 from the base of each log in the mill yard of an oriented strand board (OSB) mill located in Meadow Lake, Saskatchewan, Canada. The logs were visually inspected to avoid sampling decayed and abnormal logs. From each log, one 4 cm thick disk was cut with a chain saw from about one meter of the large log end. The disks were sealed in plastic bags in order to not lose their MC and shipped to FPInnovations in Vancouver, BC, Canada, for further analysis. In total, 17

logs of quaking aspen, 21 logs of balsam poplar, and 19 logs of black spruce were sampled.

4.3.2. Sample preparation and wood property measurements

After removing the disks from the plastic bag, 6−8 cube samples were cut with a handheld circular saw at different positions of a 4 × 4 cm^2 grid (Figure 4-1). For each species, five disks were randomly chosen and kept uncut (sample B) in order to acquire images over the whole disk for producing MC and BSG 2D images. They were also used to measure reference bulk MC or BSG, which were compared with the mean MC or BSG estimated from the hyperspectral images.

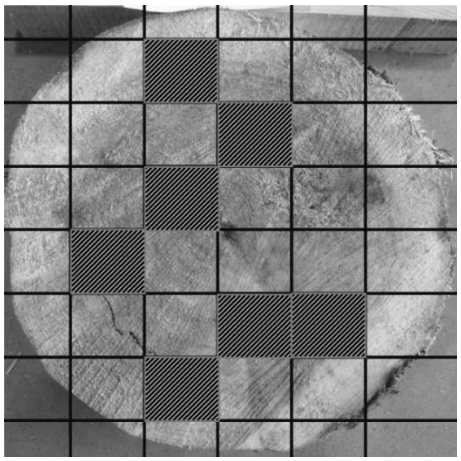

Figure 4-1: Designed grid for selecting the small samples.

In order to get all ranges of MCs, the frozen and thawed samples were dried at various MC levels. As detailed in Haddadi et al. (2015a), the reference MC at each drying step was determined by the gravimetric method following Method A of ASTM-D4442–07 (2009) as follows:

$$MC(\%\ dry\ basis) = \frac{M_{wet} - M_{dry}}{M_{dry}} * 100$$

Equation 4.1

where M_{wet} is the wet weight (kg) of the sample at the drying/freezing step and M_{dry} is the oven-dry weight (kg) of the sample at the last drying step.

As detailed in Haddadi et al. (2015b), the reference BSG was determined as the ratio between the oven-dry sample weight and the green volume that is considered to be equivalent to the saturation volume measured following Method B of ASTM-D2395–07a (2009). Both reference MC and BSG were compared to the mean MC and BSG estimated from the hyperspectral images.

Image acquisition was carried out on the sample transversal section. It was followed by measuring the samples' fresh weight using an electronic scale with 0.01 g sensitivity. The samples were kept in a dry location (for the thawed samples) and in a freezer at a temperature of -15 °C (for the frozen samples) during measurements to avoid abrupt changes in moisture and change in log state conditions. At the last drying step, the oven-dry weight of each sample was measured and MC and BSG of each sample were determined following *Method A* of ASTM-D4442–07 (2009) and *Method B* of ASTM-D2395–07a (2009), respectively.

4.3.3. NIR-HSI image acquisition

Hypercubes of the diffuse reflectance were acquired on both the small samples and the whole disks using the same camera and setting as in (Haddadi et al., 2015a, 2015b). The camera is a combination of a *N17E ImSpector* imaging spectrograph and a temperature-stabilized *InGaAs* camera *(Spectral Imaging Ltd., FIN–90571 Oulu, Finland)*. It was positioned at 48 cm above the surface sample, and recorded 256-band reflectances of 320 pixel lines. The samples were on a conveyer whose speed was adjusted to provide an image with a resolution of around 1 mm. The major difference with (Haddadi et al., 2015a, 2015b) is that the images were acquired over the cross section of the samples instead of the radial section. Also the images were acquired over disks that were cut with a chain saw and were not subjected to any planing treatment for decreasing the surface roughness, whereas in (Haddadi et al., 2015a, 2015b), the samples and boards were planed before the image acquisition step. The images were processed using the method described in (Haddadi et al., 2015a, 2015b) that includes the following steps: (1) image calibration in reflectance, (2) recovering bad pixels using a median filter, (3) removing abnormal spectra using a combination of PCA and *boxplot* method of (Laurikkala et al., 2000), (4) delineating the small samples, and (5) converting the reflectance spectra to the absorbance spectra.

4.3.4. Multivariate analysis

PLS is one of the most widespread statistical methods in qualitative and quantitative analyses. It is robust and easy to use. Although it provides a linear regression model, PLS is capable of modeling nonlinear relationships, such as in our

case, since MC measured in an oven-dry basis is not linearly related to NIR absorbance, it was already shown on soil samples (Lobell and Asner, 2002).

Specific PLS models of MC and BSG were designed for each species and log state condition, separately. General models were also computed whatever the species and the log state. Haddadi et al. (2015b) have already showed that the BSG models were not statistically significant when both wet and dry samples are used together because of the dominant effect of MC on the spectra. Thereby, in this study, the BSG models were developed using spectra acquired over samples with low MC (<12%) and over samples with high MC (almost green MC), separately. For each model, the data set was randomly divided into a calibration and a validation data set in order that both sets cover the entire range of response variables (MC or BSG). For the modeling of MC, the whole data set was divided equally, but for the BSG modeling, 65% of the data were used for calibration and 35% for validation, because the number of usable data decreases under the MC constraint. For each model, both the raw spectra and spectra transformed by a multiplicative scatter correction (MSC), a first derivative, or a second derivative transformation were used. In the case of MSC spectra, the MSC coefficients used for the validation data set were the same as those for the mean spectrum of the calibration data set, because the spectra were recorded on each sample without changing the position of the camera or the illumination unit. Only the models giving the highest accuracy are presented.

The model performance was evaluated using the following statistics: the coefficient of determination (R^2), as fitness measurements between the measured and

predicted values and the root mean square error (RMSE), as an average measure of uncertainty between the measured and predicted values. We did not use RPD for assessing the model performance, as RPD can provide redundant information with R^2, because it is directly related to R^2 as follows (Minasny and McBratney, 2013):

$$RPD = \frac{1}{\sqrt{(1 - R^2)}}$$

Equation 4.2

To obtain robust models, a minimum, but sufficient, number of latent variables (LV) should be inputted to the models. The optimal number of LV for each model was selected based on the first local minimum of the RMSE of a leave-one-out cross-validation method.

In the second part of the paper, PLS-DA (Barker and Rayens, 2003) models were developed for sorting the scanned samples according to their MC, BSG, species, or log state. For these PLS-DA models, we employed the same spectra as those used to estimate MC and BSG of the samples. Compare to the PLS modeling, the type of response variable in PLS-DA is categorical, because it represents a class index. The confusion matrix and the corresponding sensitivities, specificities, and overall accuracies were calculated to evaluate the performance of each PLS-DA model. The class limits for MC and BSG were the same as in Hans et al. (2015).

4.4. Results

4.4.1. Wood properties

The statistics for MC and BSG measurements are given in Table 4-1 as a function of the species. The MC of the balsam poplar samples is higher than the one of the black spruce and quaking aspen samples, because the balsam poplar logs were freshly cut. The BSG values are in the 0.35−0.58 range for quaking aspen samples and in the 0.24−0.58 range for balsam poplar samples, but are higher for black spruce samples (0.38−0.69).

Table 4-1: Statistics for basic specific gravity and moisture content measurements in the case of quaking aspen (*Populus tremuloides* Michx.), balsam poplar (*Populus balsamifera* L.), and black spruce (*Picea mariana* Mill.) samples

Species	**Statistics**	**MC (% dry basis)**	**BSG**
Black spruce	N	770	
	Mean	17.5	0.448
	Standard deviation	8.9	0.048
	Minimum	0.2	0.370
	Maximum	49.4	0.614
Quaking aspen	N	910	
	Mean	28.4	0.399
	Standard deviation	17.1	0.030
	Minimum	0.4	0.314
	Maximum	88.4	0.516
Balsam poplar	N	1100	
	Mean	56.4	0.359
	Standard deviation	32.2	0.057
	Minimum	0.1	0.220
	Maximum	181.3	0.512

4.4.2. NIR spectra by hyperspectral imaging

We found that the absorbance spectrum of the radial and tangential sections has lower values and presents less variation than the absorbance spectrum of the transversal section. The same pattern was observed with the other species and with the thawed samples. Only cross (or transversal)-sectional measurements will be considered further because the transversal section gives the highest signal and because the images over the whole disk can only be acquired over the transversal section.

Figure 4-2 shows the effect of log state on mean second derivative MS-corrected spectra acquired over the transversal section of the same black spruce sample in frozen and thawed conditions. The sample has an MC of 18.1% and a BSG of 0.422. The spectrum collected over frozen wood presents a slight shift toward high wavelengths (right) and an upward shift around 1351, 1441, and 1522 nm. The shift between both spectra in these wavelengths is 7.3, 3.7, and 5.2 nm, respectively. Also, there is a sharp peak in 1445 nm, because of the frost over the surface of the frozen sample, although most of the frost was removed with a steel wire brush before image acquisition.

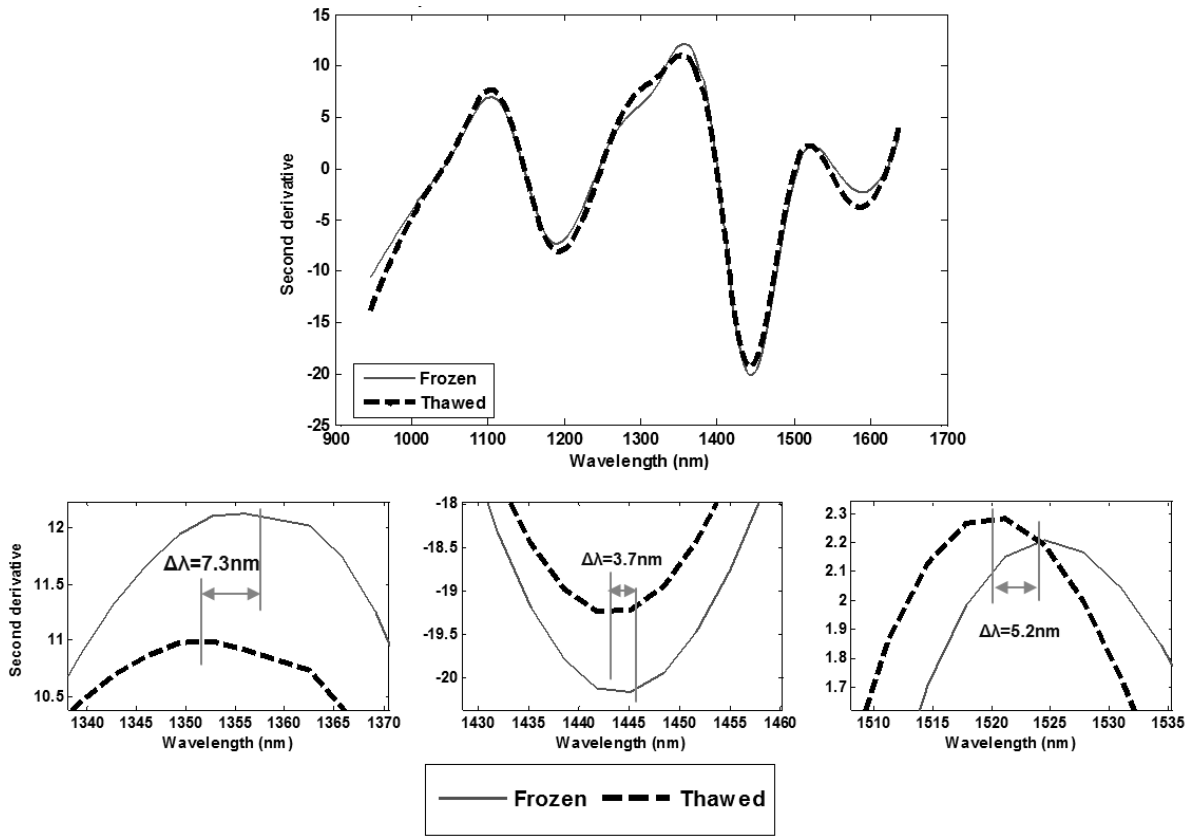

Figure 4-2: Second derivative of MS-corrected spectra for a frozen and thawed black spruce sample (MC= 18.1%, BSG= 0.422) and detailed snapshots of the spectra showing the spectral shift due to change in log state. The spectra have been acquired on transversal sections.

Figure 4-3 shows the influence of the species on the mean MS-corrected spectra over cross sections acquired over thawed samples having an MC between 8 and 12%. The mean BSG is 0.44 for quaking aspen, 0.43 for balsam poplar, and 0.46 for black spruce. In comparison with black spruce and quaking aspen, the balsam poplar spectrum show higher and lower absorbance below and above 1130 nm, respectively. The same pattern was observed with the frozen samples (results not shown).

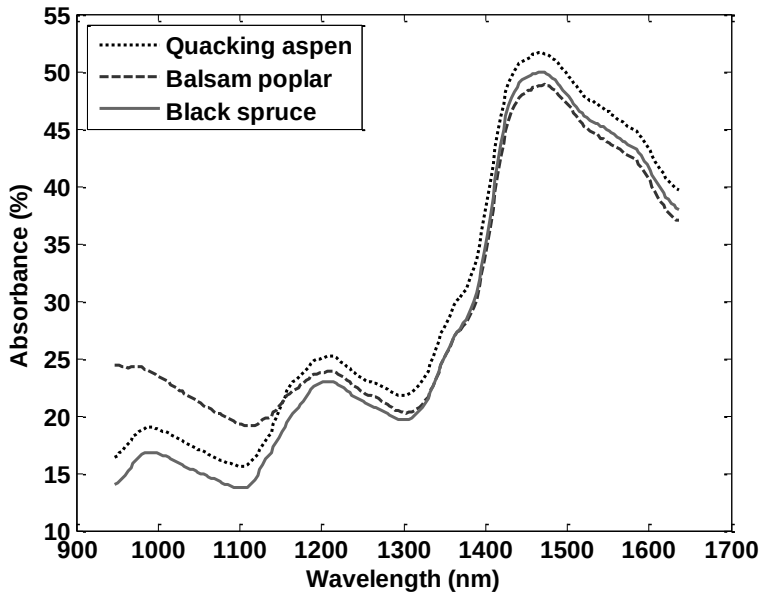

Figure 4-3: Influence of the species on the MS-corrected spectra acquired over the transversal section of thawed samples. All the samples have an MC of 12% and have similar BSG (BSG_{aspen}= 0.44, BSG_{poplar}= 0.43, BSG_{spruce}= 0.46).

4.4.3. MC modeling

We found that with the MSC spectra, the result for each MC model was slightly better by 2−3% and the number of latent variables decreased; thus, the MC models will be based on MSC spectra. The model statistics for each species, log state (frozen/thawed), and their combinations are presented in Table 4-2. The model accuracy for the thawed samples was slightly better than that for the frozen samples. The balsam poplar samples produced the model with the lowest accuracy (R_V^2=0.69 and RMSEv=15.49%) and the black spruce samples produced the model with highest accuracy (R_V^2=0.82 and RMSEv=2.94%). A reasonable performance was obtained for the general model using all the data (R_V^2=0.75 and RMSEv=13.27%) as well as with the model combining both hardwood species (R_V^2=0.73 and RMSEv=14.17%). It seems

therefore that there is a species effect on the MC model. It is why MC models were presented in Figure 4-4 as a function of the species. In particular, the accuracy of the model for balsam poplar samples is lower than for the other species, because this species has samples with high MC that cannot be well estimated. However, except for balsam poplar, Figure 4-4 shows that there is not a strong clumping of the data according to the log state, which means that such technology can be used for both thawed and frozen logs.

Table 4-2: PLS models for moisture content (MC % oven-dry basis) prediction according to the species and log state using multi scatter corrected (MSC) spectra.

Species	**Log state**	**LV**	**Calibration**			**Validation**		
			$RMSE_C$ (%)	**R^2_C(*)**	**N**	**$RMSE_V$ (%)**	**R^2_V(*)**	**N**
Black spruce	Thawed	4	3.17	0.84	134	2.30	0.90	134
	Frozen	7	3.25	0.79	192	2.63	0.83	192
	Both	8	3.20	0.82	326	2.94	0.82	326
Quaking Aspen	Thawed	8	6.72	0.81	183	6.13	0.83	182
	Frozen	8	7.50	0.79	227	6.70	0.80	226
	Both	6	7.88	0.72	409	7.99	0.75	409
Balsam Poplar	Thawed	5	15.19	0.77	248	11.95	0.80	248
	Frozen	4	17.73	0.67	274	16.13	0.66	274
	Both	4	19.48	0.63	522	15.49	0.69	522
Balsam poplar and quaking aspen	Thawed	4	15.86	0.73	501	13.95	0.74	500
	Frozen	8	12.26	0.79	431	11.32	0.81	430
	Both	6	14.86	0.73	931	14.17	0.73	931
All species	Thawed	4	15.09	0.74	693	12.21	0.78	692
	Frozen	8	12.29	0.79	565	10.88	0.82	564
	Both	6	13.96	0.75	1257	13.27	0.75	1257

(*) *p-value* < 0.001 for the all the models

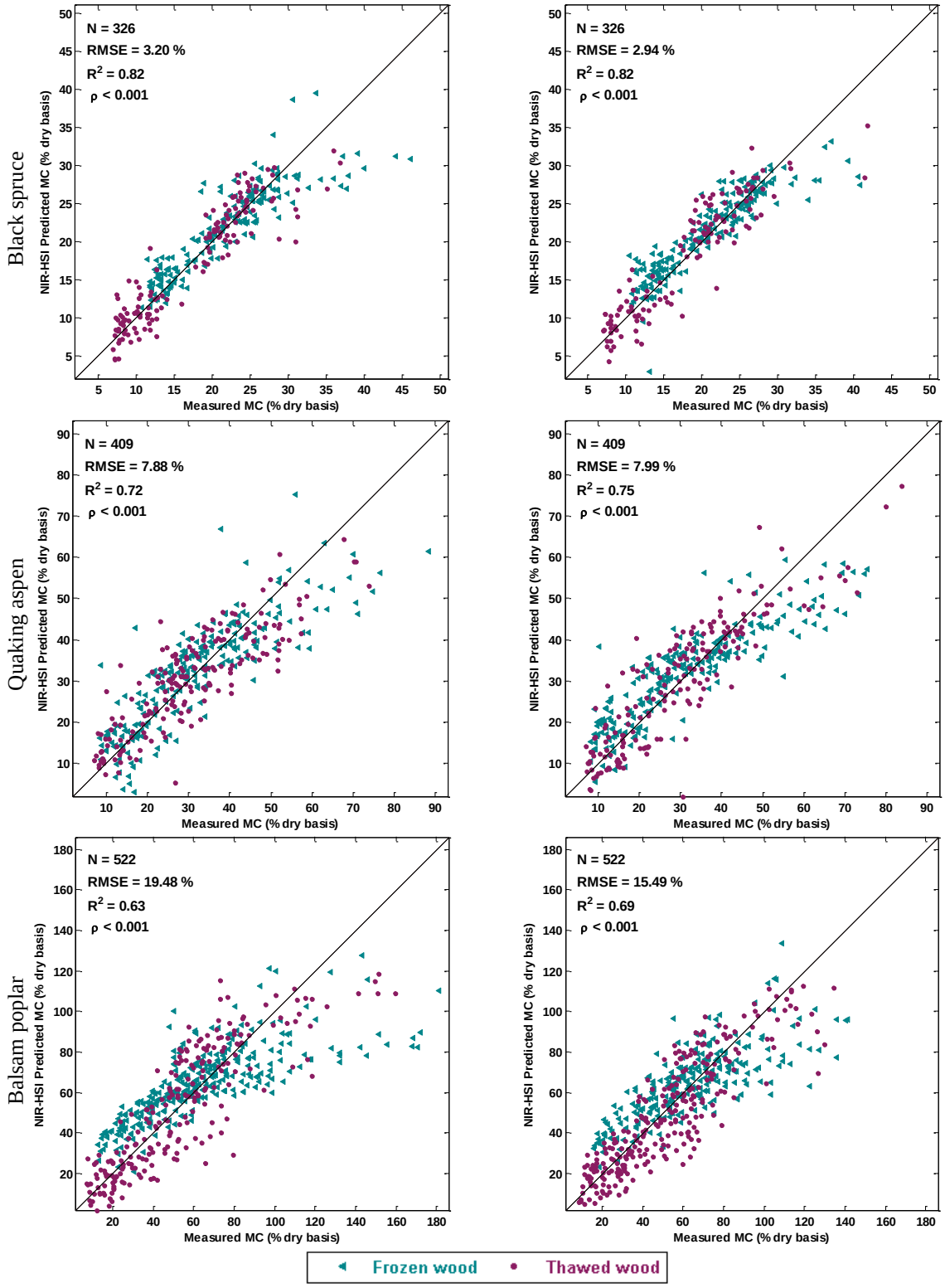

Figure 4-4: Specific PLS models for both frozen and thawed wood for MC estimation using MS-corrected spectra as a function of the species. The models have 8, 6, and 5 LVs, respectively.

The specific model for each species and log state was then employed over the images acquired over the whole disks of similar bulk MC to derive a 2D MC image (Figure 4-5). Measured bulk MC and estimated mean MC for each disk are also provided in Figure 4-5. For all the disks, there are some discrepancies between both MCs, indicating that the bulk MC is maybe not representative of the disk MC. In all of the disks, the estimated MC is lower than the bulk MC, except for the balsam poplar frozen disk. It is also for this disk that there is more variation in the MC across the disk. Figure 4-5 also gives the corresponding MC histogram distribution. For most samples, the MC histogram follows a Gaussian distribution function.

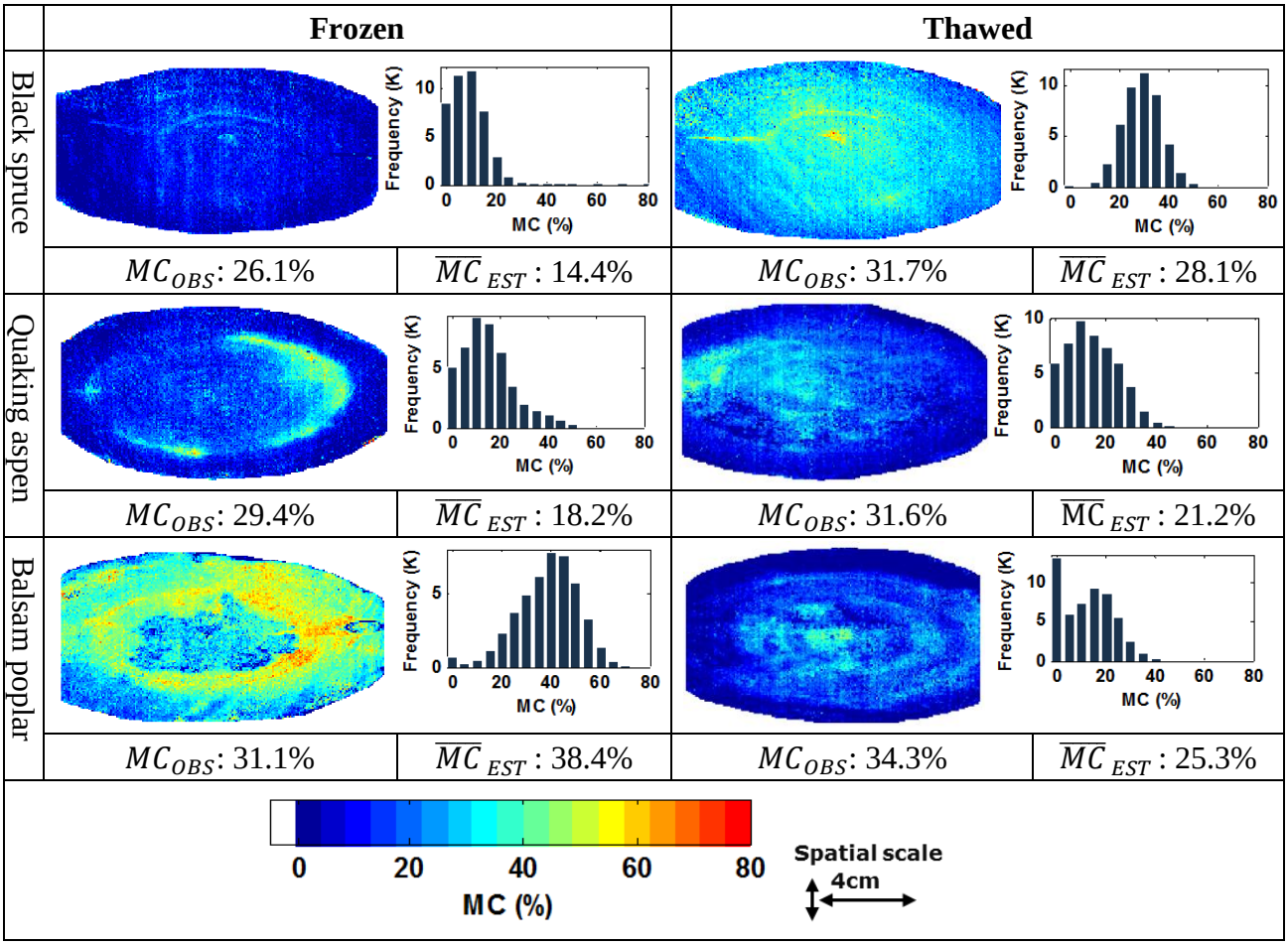

Figure 4-5: 2D MC images of frozen and thawed logs from different species.

4.4.4. BSG modeling

Similar to MC, PLS models were built for each species, log state (frozen/thawed), and their combinations. Different models were built for spectra acquired over low-MC (<12%) samples (Table 4-3) and over green samples (MC>40% for quaking aspen, MC>80% for balsam poplar, and MC>25% for black spruce) (Table 4-4).

Table 4-3: PLS models for basic specific gravity (BSG) prediction according to the species and log state using raw spectra acquired over samples with high-MC (MC > 40% for quaking aspen, 80% for balsam poplar and 25% for black spruce)

Species	**Log state**	**LV**	**Calibration**			**Validation**		
			$RMSE_C$	**R^2_C(*)**	**N**	**$RMSE_V$**	**R^2_V(*)**	**N**
Black spruce	Thawed	5	0.025	0.49	21	0.035	0.47	20
	Frozen	6	0.029	0.53	26	0.039	0.49	22
	Both	6	0.019	0.79	26	0.028	0.67	21
Quaking Aspen	Thawed	7	0.009	0.84	27	0.014	0.69	20
	Frozen	6	0.019	0.49	22	0.021	0.58	22
	Both	4	0.026	0.27	32	0.022	0.51	25
Balsam Poplar	Thawed	6	0.051	0.46	38	0.043	0.64	27
	Frozen	10	0.025	0.87	38	0.042	0.69	21
	Both	11	0.023	0.92	45	0.040	0.74	32
Balsam poplar and quaking aspen	Thawed	6	0.044	0.67	42	0.045	0.66	28
	Frozen	7	0.041	0.69	42	0.040	0.72	28
	Both	8	0.050	0.57	42	0.038	0.73	21
All species	Thawed	10	0.026	0.88	42	0.042	0.72	28
	Frozen	6	0.052	0.52	42	0.039	0.74	21
	Both	10	0.022	0.92	42	0.035	0.78	21

(*) *p*-value < 0.001 for all the models

Table 4-4: PLS models for basic specific gravity (BSG) prediction according to the species and log state using the raw spectra acquired over samples with MC < 12% (dry basis)

Species	**Log state**	**LV**	**Calibration**			**Validation**		
			$RMSE_C$	**R^2_C(*)**	**N**	**$RMSE_V$**	**R^2_V(*)**	**N**
Black spruce	Thawed	6	0.043	0.49	44	0.036	0.67	31
	Frozen	7	0.030	0.64	40	0.036	0.69	29
	Both	6	0.041	0.51	38	0.035	0.72	23
Quaking Aspen	Thawed	9	0.010	0.91	31	0.021	0.70	23
	Frozen	6	0.019	0.63	32	0.021	0.65	24
	Both	6	0.024	0.58	38	0.022	0.66	26
Balsam Poplar	Thawed	6	0.037	0.49	28	0.049	0.48	29
	Frozen	7	0.018	0.84	19	0.033	0.74	21
	Both	7	0.035	0.65	41	0.048	0.57	33
Balsam poplar and quaking aspen	Thawed	9	0.017	0.89	39	0.032	0.70	30
	Frozen	10	0.017	0.89	38	0.052	0.47	31
	Both	7	0.036	0.70	51	0.044	0.67	35
All species	Thawed	10	0.009	0.99	39	0.041	0.84	26
	Frozen	10	0.029	0.91	46	0.048	0.74	33
	Both	11	0.021	0.95	47	0.036	0.88	28

(*) *p*-value < 0.001 for all the models.

For both the low- and high-MC samples, we found that the raw spectra produced a better accuracy for BSG estimation than using MSC, first or second derivative spectra. Also, the best model accuracy was obtained with the general model (all data) when all the species and log states were considered because it includes a larger BSG variation than the specific models. Figure 4-6 displays the scatter plots for the general calibration and validation BSG model for the low-MC samples as a function of the species (A and B) and the log state (C and D). The figure shows a distinct BSG range for each species leading to data clustering, but there is some overlapping between BSG ranges of the two hardwood species, i.e., quaking aspen and balsam poplar. However, there is no data

clustering as a function of the log state. This general model can therefore be applied on both frozen and thawed logs.

The general model was then used to derive a 2D BSG image of the whole disk for the different species and different log states (Figure 4-7). For each disk, the BSG histogram is also presented. It follows a Gaussian distribution function as in the case of the MC images. The difference between the measured bulk BSG and the estimated mean BSG for each disk varies between 0.006 (in the case of frozen black spruce) and 0.033 (in the case of thawed balsam poplar).

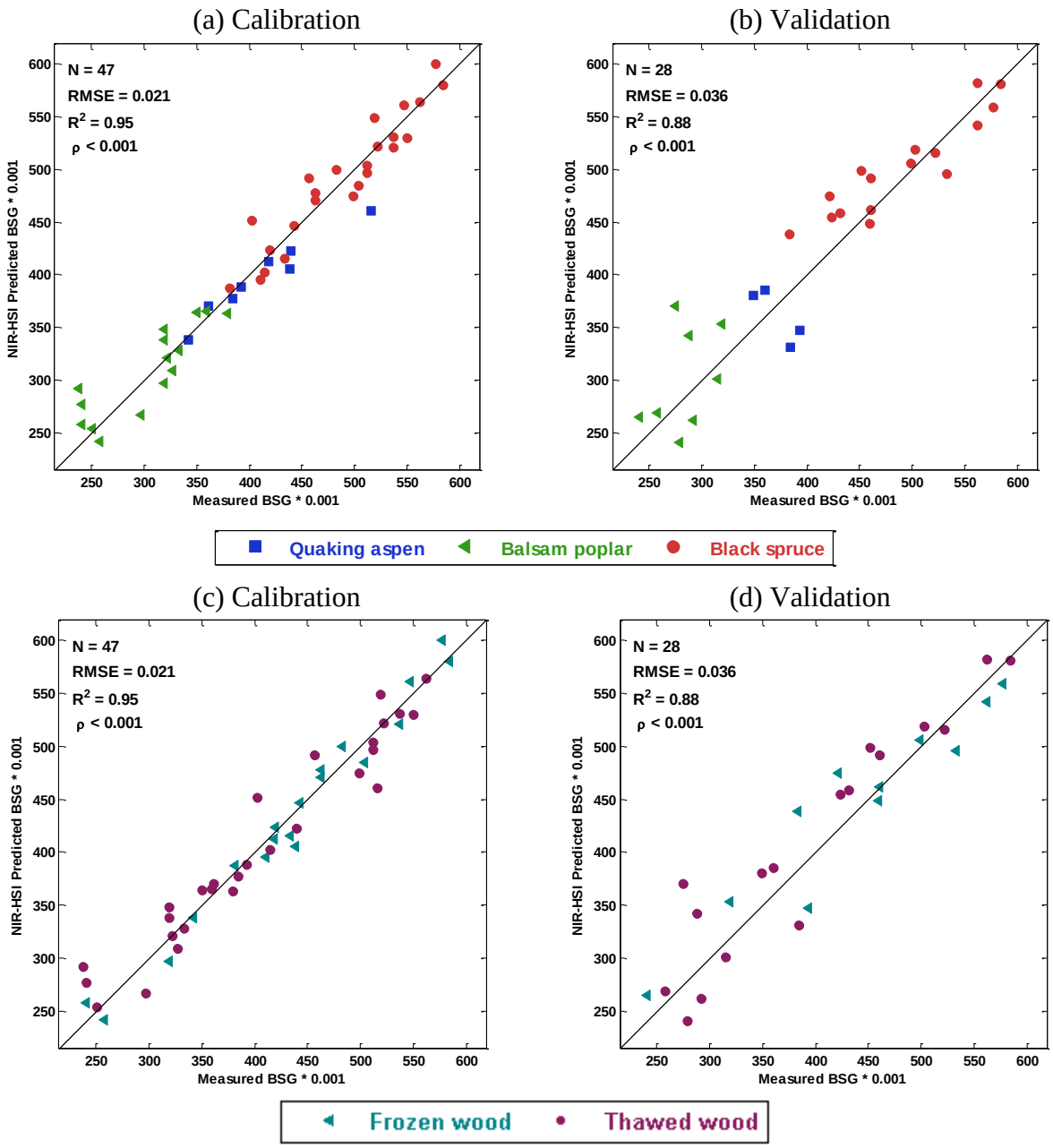

Figure 4-6: General PLS model for BSG estimation of low MC samples with 11 latent variables using raw spectra. The scatter plots of the calibration and validation data sets are colored as a function of the species (a, b) and of the log state (c, d).

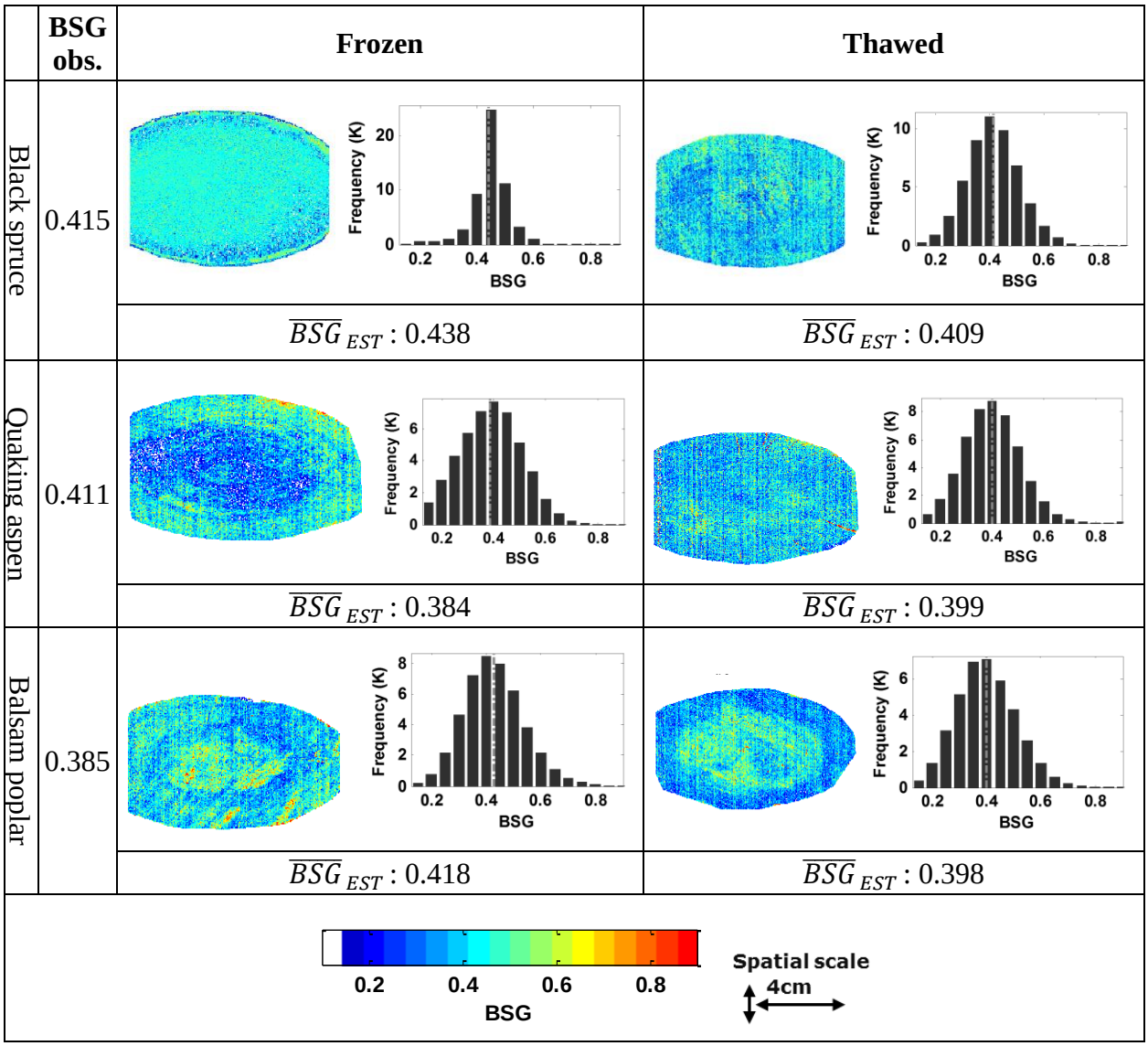

Figure 4-7: 2D BSG images of the different species in frozen and thawed conditions.

4.4.5. PLS Discriminant Analysis (DA)

PLS-DA models were developed to sort the samples as a function of their MC, BSG, species, and log state (frozen and thawed). The confusion matrix, sensitivity, specificity, and overall accuracy for each model are presented in Table 4-5. The model overall accuracy for both MC and BSG sorting were similar (72 vs. 75%). For both MC

and BSG, the medium classes had a lower sensitivity (less than 62%) than the two other classes (more than 83%). The model overall accuracy for species sorting was 86%. The sensitivity and specificity of the model for species sorting were higher than 89% for all species, except balsam poplar, for which the sensitivity was 75%. We also used a PLS-DA model to discriminate the samples in terms of frozen and thawed conditions. This model had the highest overall accuracy (97%), with sensitivity and specificity higher than 94%.

Table 4-5: PLS-DA models (*) for log sorting according to their moisture content (MC), basic specific gravity (BSG), species, or log state.

Factor	Class	*N*		Confusion matrix			Sensitivity (%)	Specificity (%)	Overall accuracy (%)
				L	M	H			
MC	Low (≤ 45%)	40	L	29	5	1	83	87	76
	Medium (45% < MC ≤ 90%)	40	M	10	34	11	62	91	
	High (> 90%)	40	H	1	1	28	93	87	
				L	M	H			
BSG	Low (≤ 0.350)	43	L	28	2	1	90	85	72
	Medium (0.350 < BSG ≤ 0.400)	43	M	14	36	13	57	89	
	High (> 0.400)	43	H	1	5	29	83	85	
				QA	BP	BS			
Species	Quaking aspen	45	QA	34	2	1	92	89	86
	Balsam poplar	45	BP	10	42	4	75	96	
	Black spruce	45	BS	1	1	40	95	95	
				FR	TH				
Log state	Frozen	45	FR	42	0		100	94	97
	Thawed	45	TH	3	45		94	100	

(*) The number of latent variables for each model is 9.

4.5. Discussion

4.5.1. Wood property measurements

MC data range between 0.4 and 88.4% for quaking aspen, and between 0.1 and 181.3% for balsam poplar. Our maximum values of MC for quacking aspen and balsam poplar are the same as the maximum MC reported in Hans et al. (2015) (88% for

quaking aspen and 181% for balsam poplar) who used the same trees from Saskatchewan harvested in the same time of the year (June), but our minimum MC values are lower because we used small samples that were dried longer than the disks used by Hans et al. (2015) who reported a minimum MC of 14% for both species. The maximum values reported in Hans et al. (2015) and in this study are below to the one reported in Forest Products Laboratory (2010) (113%) for trees growing in the USA and harvested in various seasons. Kroll et al. (1992) reported a maximum value of 140% for balsam poplar trees growing in Minnesota, USA and harvested in late September- early October. Such as for Hans et al. (2015), some high-MC samples can also be due to the presence of wet pockets (Kroll et al., 1992). In the case of black spruce samples, which were extracted from Saskatchewan trees harvested in June, both the minimum and maximum MCs (0.2 and 49.2%, respectively) were lower than in Hans et al. (2013) who used trees from Newfoundland, which were sampled in May (9 and 140%, respectively).

The mean BSG value is 0.399 for quaking aspen and 0.359 for balsam poplar, which are similar as the values of Hans et al. (2015), who reported a value of 0.405 and 0.352, respectively for logs collected on the same trees. These values are similar to those reported by Kroll et al. (1992) (BSG = 0.36) for balsam poplar trees sampled in Minnesota, USA, but are a little higher than the values published by Kennedy (1965) (BSG=0.342) who used balsam poplar trees from different sites in Canada. Our values for quaking aspen are also a little higher than those observed by Kennedy (1965) (BSG = 0.374) measured on trees from different sites in Canada. Similarly to Hans et al. (2015), the BSG variation in balsam poplar is twice the one of quaking aspen. For black spruce, the mean BSG value (0.448) is higher than the mean BSG of quaking aspen and

balsam poplar. It is also higher than the value reported by Hans et al. (2013) (0.430) who measured BSG over trees from Newfoundland, Canada. Our value is also lower than the one reported by Kennedy (1965)'s (BSG=0.406) who studied trees from different sites in Canada.

4.5.2. NIR spectra

We observed that the absorbance spectrum of the radial and tangential sections is lower than the one of the transversal section, whatever the species and the log state. Such pattern was already observed over NIR spectra acquired over thawed Sitka spruce (*Picea sitchensis*) samples (Tsuchikawa et al., 1996), over green red oak (*Quercus rubra*) lumber (Defo et al., 2007), and over black spruce disks (Hans et al. 2013). These authors explained that the transversal section is rougher than both the radial or tangential sections because of fiber orientation. When the sample surface becomes rough, the scattering from the surface becomes uneven and influences the reflectance measurements.

The comparison between the spectra of the frozen and thawed black spruce sample (Figure 4-2) shows a peak shift toward high wavelengths as the temperature decrease. It has been shown that when the temperature decreases, the number of H bonds increases and leads to a shift in the OH absorption bands toward longer wavelengths (Libnau et al., 1994, Pang, 2013). In addition, when the temperature drops below 0 ^{o}C, the change in the water state from liquid to solid can also lead to an increase in the number of H bonds from 1.5 to 4 (Pang, 2013).

The maximum shift (7.3 nm) occurs at 1350 nm while shifts of 5.2 and 3.2 nm are observed at 1525 and 1440 nm, respectively. The shift around 1450 nm is lower than those reported over spectra acquired over sapwood and heartwood of black spruce (17.2 and 8.6 nm, respectively) (Hans et al. 2013) and of Norway spruce (*Picea abies* (L.) H. Karst (25 and 5 nm, respectively) (Thygesen and Lundqvist, 2000a). Such differences with our study can be explained by the low sensitivity of our hyperspectral imaging system, which was distant of 48 cm from the wood surface, while the other studies used handheld spectroscopy systems that are in contact with the wood surface. Also, MC can influence the magnitude of the shift (Thygesen and Lundqvist, 2000a). Figure 4-2 also shows a sharp peak in 1445 nm, because of frost over the surface of the frozen samples, despite its removal using a steel wire brush. Hans et al. (2013) also observed such sharp peak and explained it by the presence of ice that produces scattering.

Figure 4-3 compares spectra acquired over thawed samples from the three species having a similar MC and BSG. Although the chemical composition of quaking aspen, balsam poplar, and black spruce wood is different (Bakuzis and Hansen, 1965, Micko, 1987), the spectral difference between species is mainly due to light scattering and surface roughness, even though we decrease the effect of scattering by applying MSC transformation. We did not measure the surface roughness; however, visually we observed that balsam poplar surface roughness was different than the other two species, which results in different spectra. This finding is in agreement with Hans et al. (2013, 2015) who collected spectra from the same species with a handheld spectrometer (*PhazIR*).

4.5.3. MC modeling

The best models were obtained using MSC spectra that were collected on the transversal section. Indeed, the MS correction allows removing some of the scattering effects due to surface roughness of the transversal section and frost on the sample surface. This result is different than Hans et al. (2013, 2015) and Haddadi et al. (2015a) who found that the raw spectra give the best results. Hans et al. (2013, 2015) used a handheld NIR spectrometer that is in contact with the wood surface, whereas Haddadi et al. (2015a) tested NIR-HSI images acquired over planned thawed samples.

The MC models based on frozen and thawed samples have a reasonable accuracy regardless of the species and log state ($R^2_V > 0.75$). Thawed sample models were slightly better than the frozen sample ones because frozen wood produces more spectral variation due to frost and ice over the sample surface. This is in agreement with Thygesen and Lundqvist (2000b) and Hans et al. (2013, 2015) who also reported better results with thawed samples. When both the frozen and thawed samples are combined together (Figure 4-4), the best model is achieved with the black spruce samples and the worse model is achieved with the balsam poplar samples. Balsam poplar samples have high MC that cannot be well estimated. This is perhaps because the surfaces of the disks have the same moisture content for all whole-sample average moisture contents for these high MC or because the spectral information is not able to detect high MC, as if the camera is saturating.

Black spruce samples have a low MC range and low MC variation (Table 4-1) leading to a better RMSE. For this species, the number of latent variable (8) is similar as

in Mora et al. (2011b) (8) and in Kobori et al. (2013) (6) who used imaging systems for MC modeling over loblolly pine (*Pinus taeda* L.), European beech (*Fagus sylvatica* L.), and Scots pine (*Pinus sylvestris* L.) thawed logs. The combination of quaking aspen and balsam poplar does not improve significantly the accuracy of MC models (R^2_V =0.73). With this combination, the number of latent variables (6) also does not change significantly, while Hans et al. (2015) found a better accuracy (R^2_V =0.83) for such species combination by using a model with nine latent variables. For balsam poplar there is a curvilinear trend at higher MC that may be related to some signal saturations of the camera we used. Despite this problem, the overall linear regression model gives acceptable estimation accuracies.

When all the data are used whatever the species and the log state, the general model gives an acceptable accuracy ($RMSE_V$ = 13.27% and R^2_V = 0.75), but it is still lower than the specific models (Table 4-2). It is therefore recommended to use specific models, if the log state and/or the species of the sample are known. When specific models were applied over whole disk images as a function of the different species or log state, there was some difference between the mean MC estimated from the resulting 2D MC images and the measured bulk MC, indicating that the bulk MC is not representative of the whole disk (Figure 4-5). The images also show a higher MC variation for the balsam poplar samples, which can be explained by the fact that logs were fresher than logs of the two other species. Also, this can be due to the presence of wet pockets for this species as already reported by Kroll et al. (1992).

4.5.4. BSG modeling

The best BSG models were obtained using raw spectra. When the spectra were transformed, the accuracy of the models did not improve (in term of R^2 and RMSE) but, the number of latent variables decreased. Such result was already obtained by Hans et al. (2013, 2015) and in (Haddadi et al., 2015b). Several studies who showed that second derivative spectra provide a better BSG model (Schimleck et al., 1999, Schimleck et al., 2003b, Schimleck et al., 2005a, Schimleck et al., 2005b, Schimleck et al., 2006, Jones et al., 2007, Fujimoto et al., 2008, Zhu et al., 2009, Alves et al., 2012). MSC and other transformations decrease the impact of particle size and surface roughness (Isaksson and Naes, 1988); in this method, it is assumed that the scattering is constant in the entire wavelength range and the ideal coefficient is the average of all of all sample. Moreover, with this transformation, some of the relevant information may be removed from the spectra (Burger et al., 1997).

In the BSG modeling, we also considered the effect of MC. Different models were built for low MC samples (Table 4-3) and high-MC samples (Table 4-4). Except for the balsam poplar models, models built with low-MC samples are better than those built with high-MC samples. Such result is in agreement with models obtained on Norway spruce logs (Thygesen, 1994), on loblolly pine logs (Schimleck et al., 2003b), and on balsam poplar and quaking aspen logs (Hans et al., 2015).

The best model was obtained when all species were combined together, leading to an R^2_V of 0.92 for the frozen samples, an R^2_V of 0.95 for the thawed samples, and an R^2_V of 0.91 for both types of samples (Figure 4-6). Hans et al. (2015) already reported a

high accuracy when data from quaking aspen and balsam poplar are combined together. They explained this by the fact that the BSG of the whole data set has a high variation, such as in the case of our data (Table 4-1). Similarly, BSG models built with data from 54 different species were shown to be more robust than species-specific models (Schimleck et al., 2001a, Schimleck et al., 2002a, Schimleck et al., 2003a). Indeed, BSG is a species-dependent characteristic and varies between species as well as between trees of the same species (Barnett and Jeronimidis, 2009), although the variation within trees is less than between species according to Smith et al. (2003).

The whole disk 2D BSG images are presented as a function of the species and log states in Figure 4-7. They show higher variation in BSG across the disks in the case of quaking aspen and balsam poplar than in the case of black spruce. It has been already shown that the density gradually decreases from the pith to the bark in several softwood species, but the opposite is true with ring-porous hardwood species (Barnett and Jeronimidis, 2009). However, we did not observe a correlation between the growth rings and the BSG.

Such as in Mora et al. (2011b) and such for MC, the estimation of BSG with the NIR-HSI camera was lower than the one obtained on similar samples with a spectrometer by Hans et al. (2015), because the spectrometer measurements were performed with contact to the samples, while NIR-HSI measurements were done at a certain distance (48cm) from the sample, leading to environmental spectral interferences.

4.5.5. PLS-DA

We achieved a sorting accuracy of 76% among the MC classes, which is 10% lower than Hans et al. (2015)'s results, but our sorting accuracy of 72% among the BSG classes was almost 10% higher than the one of Hans et al. (2015)'s results. Such difference can be explained by the low MC ranges and the large BSG ranges in our data set compare to Hans et al. (2015). With respect to the species sorting, our overall accuracy of 86% was lower than those of Hans et al. (2015) (98%), who just considered two species: quaking aspen and balsam poplar. Haartveit and Flæte (2008) also obtained a better overall accuracy (94%) when distinguishing of Norway spruce (*Picea abies* (L.) H. Karst), Sitka spruce (*Picea sitchensis* (Bong.) Carr.), and Lutz spruce (*Picea x lutzii* Little) logs. Our accuracy for the log state sorting (97%) was high and but cannot compare with the aforementioned studies, which did not sort logs according to their state (frozen/thawed).

4.6. Conclusion

Our study assessed the potential of NIR hyperspectral images to produce MC and BSG images of frozen and thawed log disks of quaking aspen, balsam poplar, and black spruce. The NIR hyperspectral images were subjected to the following image processing: image calibration in reflectance, recovering bad pixels using a median filter, delineation of the small samples on each image, and removing abnormal spectra using a combination of the principal component analysis (PCA) and the *boxplot* method of Laurikkala et al. (2000). The resulting spectra were then used into PLS models to estimate MC or BSG.

For MC, the best PLS models were those established using the MSC-corrected spectra and a LV number ranging between 5 and 8. For both the black spruce and quaking aspen, the models gave reasonable accuracies, but for the balsam poplar samples, high-MC samples cannot be well estimated. For BSG, the best PLS models were those established with the raw spectra and by considering the whole data set. The LV number ranges between 6 and 10. For both MC and BSG models, the log state does not overall produce significant differences in model accuracies. BSG model performances depend on the species as BSG variations are species dependent.

The best MC models were based on MSC spectra. The MSC coefficients used for the validation data set were the same as those for the mean spectrum of the calibration data set. Further work is needed to assess whether using different MSC coefficients for both the calibration and validation data sets will improve the models. The setting used for acquiring the images was a camera with a field of view of 17.5° that was positioned at 48 cm height. A higher quality with high spatial resolution of spectra can be achieved using a camera with a wider field of view, because the environment interference on the spectra is reduced as the distance between the camera and the target decreases. It will be expected that the resulting PLS models will be more accurate and the distribution of latewood and earlywood can be estimated.

The method presented is based on NIR radiation that has two major disadvantages. First, it has a limited penetration depth in solid wood, from 1 to 5 mm depending on surface roughness and the wavelength used (Tsuchikawa et al., 1996, Tsuchikawa et al., 2001, Sykes et al., 2005). More penetrating radiations, such as

microwaves, should be tested for estimating bulk MC and BSG of logs. Second, the spectral measurements are highly affected by the wood surface type and roughness. Also, this study related NIR hyperspectral data to the wood moisture content and basic specific gravity using a PLS model. Further work is needed to test a more deterministic approach that uses optical models like the one based on the Kubelka-Munk theory (Tsuchikawa et al. 2001). Finally, in this study, we derived moisture content and basic specific gravity images of logs from NIR hyperspectral images. Such method can also be applied to produce 2D images for other chemical components. This will be the subject of future work.

4.7. Acknowledgements

The authors thank G. Chow from FPInnovations, as well as G. Hans (UNB) and K. Phung (UNB) for their help during the experiments. The study was supported by an NSERC Strategic grant and a New Brunswick Innovation Foundation grant awarded to B. Leblon. This paper was written in memoriam of Dr. James Burger, who suddenly died on September 6, 2014.

4.8. References

Adedipe O.E., Dawson-Andoh B., Slahor J. & Osborn L. (2008) Classification of red oak (*Quercus rubra*) and white oak (*Quercus alba*) wood using a near infrared spectrometer and soft independent modelling of class analogies. *Journal of Near Infrared Spectroscopy*, 16(1): 49-57. doi: 10.1255/Jnirs.760

Alves A., Santos A., Rozenberg P., Paques L.E., Charpentier J.P., Schwanninger M. & Rodrigues J. (2012) A common near infrared-based partial least squares regression model for the prediction of wood density of *Pinus pinaster* and *Larix x eurolepis*. *Wood Science and Technology*, 46(1-3): 157-175. doi: 10.1007/s00226-010-0383-x

ASTM-D2395–07a (2009) *Standard test methods for specific gravity of wood and wood-based materials*, ASTM International, West Conshohocken, PA, doi: 10.1520/D2395-07A, www.astm.org.

ASTM-D4442–07 (2009) *Standard test methods for direct moisture content measurement of wood and wood-base materials*, ASTM International, West Conshohocken, PA, doi: 10.1520/D4442-07, www.astm.org.

Bakuzis E.V. & Hansen H.L. (1965) *Balsam fir: A monographic review.* University of Minnesota Press. 445 pages.

Adedipe O.E., Dawson-Andoh B., Slahor J. & Osborn L. (2008) Classification of red oak (*Quercus rubra*) and white oak (*Quercus alba*) wood using a near infrared spectrometer and soft independent modelling of class analogies. *Journal of Near Infrared Spectroscopy*, 16(1): 49-57. doi: 10.1255/Jnirs.760

Alves A., Santos A., Rozenberg P., Paques L.E., Charpentier J.P., Schwanninger M. & Rodrigues J. (2012) A common near infrared-based partial least squares regression model for the prediction of wood density of *Pinus pinaster* and *Larix x eurolepis*. *Wood Science and Technology*, 46(1-3): 157-175. doi: 10.1007/s00226-010-0383-x

ASTM-D2395–07a (2009) *Standard test methods for specific gravity of wood and wood-based materials*, ASTM International, West Conshohocken, PA, doi: 10.1520/D2395-07A, www.astm.org.

ASTM-D4442–07 (2009) *Standard test methods for direct moisture content measurement of wood and wood-base materials*, ASTM International, West Conshohocken, PA, doi: 10.1520/D4442-07, www.astm.org.

Bakuzis E.V. & Hansen H.L. (1965) *Balsam fir: A monographic review.* University of Minnesota Press. 445 pages.

Barker M. & Rayens W. (2003) Partial least squares for discrimination. *Journal of Chemometrics*, 17(3): 166-173

Barnett J. & Jeronimidis G. (2009) *Wood quality and its biological basis.* John Wiley & Sons. 226 pages.

Bowyer J.L., Shmulsky R. & Haygreen J.G. (2007) *Forest products and wood science: An introduction.* Oxford, UK: John Wiley & Sons. 496 pages.

Burger T., Kuhn J., Caps R. & Fricke J. (1997) Quantitative determination of the scattering and absorption coefficients from diffuse reflectance and transmittance

measurements: Application to pharmaceutical powders. *Applied Spectroscopy,* 51(3): 309-317. doi: 10.1366/0003702971940404

Cooper P.A., Jeremic D., Radivojevic S., Ung Y.T. & Leblon B. (2011) Potential of near-infrared spectroscopy to characterize wood products. *Canadian Journal of Forest Research,* 41(11): 2150-2157. doi: 10.1139/X11-088

Defo M., Taylor A.M. & Bond B. (2007) Determination of moisture content and density of fresh-sawn red oak lumber by near infrared spectroscopy. *Forest Products Journal,* 57(5): 68-72

Denig J., Wengert E.M. & Simpson W.T. (2000) Drying hardwood lumber, U.S. Department of Agriculture, Forest Service, Forest Products Laboratory, Tech. Rep. FPL–GTR–118, Madison, WI, USA, 138 pages.

Duncker P. & Spiecker H. (2009) Detection and classification of Norway spruce compression wood in reflected light by means of hyperspectral image analysis. *IAWA Journal,* 30(1): 59-70. doi: 10.1163/22941932-90000203

Fernandes A., Lousada J., Morais J., Xavier J., Pereira J. & Melo-Pinto P. (2013a) Comparison between neural networks and partial least squares for intra-growth ring wood density measurement with hyperspectral imaging. *Computers and Electronics in Agriculture,* 94: 71-81. doi: 10.1016/j.compag.2013.03.010

Fernandes A., Lousada J., Morais J., Xavier J., Pereira J. & Melo-Pinto P. (2013b) Measurement of intra-ring wood density by means of imaging VIS/NIR spectroscopy (hyperspectral imaging). *Holzforschung,* 67(1): 59-65. doi: 10.1515/Hf-2011-0258

Forest Products Laboratory (2010) *Wood handbook: Wood as an engineering material.* Madison, WI, USA: U.S. Department of Agriculture, Forest Service, Forest Products Laboratory. 508 pages.

Fujimoto T., Kurata Y., Matsumoto K. & Tsuchikawa S. (2008) Application of near infrared spectroscopy for estimating wood mechanical properties of small clear and full length lumber specimens. *Journal of Near Infrared Spectroscopy,* 16(6): 529-537. doi: 10.1255/Jnirs.813

Fujimoto T., Yamamoto H. & Tsuchikawa S. (2007) Estimation of wood stiffness and strength properties of hybrid larch by near-infrared spectroscopy. *Applied Spectroscopy,* 61(8): 882-888. doi: 10.1366/000370207781540150

Gindl W., Teischinger A., Schwanninger M. & Hinterstoisser B. (2001) The relationship between near infrared spectra of radial wood surfaces and wood mechanical properties. *Journal of Near Infrared Spectroscopy,* 9(4): 255-261. doi: 10.1255/jnirs.311

Haartveit E.Y. & Flæte P.O. (2008) Near infrared spectroscopy (nirs) as a tool for effective classification of wood In *51st International Convention of Society of Wood Science and Technology,* (Concepción, CHILE), pp. 1-9

Haddadi A., Burger J., Leblon B., Pirouz Z., Groves K. & Nader J. (2015a) Using near infrared hyperspectral images on subalpine fir board - part 1: Moisture content estimation. *Wood Material Science & Engineering,* 10(1): 27-40. doi: 10.1080/17480272.2014.965743

Haddadi A., Burger J., Leblon B., Pirouz Z., Groves K. & Nader J. (2015b) Using near infrared hyperspectral images on subalpine fir board - part 2: Density and basic

specific gravity estimation. *Wood Material Science & Engineering,* 10(1): 41-56. doi: 10.1080/17480272.2015.1011231

Hans G., Leblon B., Cooper P., LaRocque A., Nader J. & Stirling R. (2015) Determination of moisture content and basic specific gravity of *Populus tremuloides* (Michx.) and *Populus balsamifera* (l.) logs using a portable near-infrared spectrometer. *Wood Material Science & Engineering,* 10(1): 3-16. doi: 10.1080/17480272.2014.916349

Hans G., Leblon B., Stirling R., Nader J., LaRocque A. & Cooper P. (2013) Monitoring of moisture content and basic specific gravity in black spruce logs using a handheld MEMS-based near-infrared spectrometer. *The Forestry Chronicle,* 89(5): 605-618. doi: 10.5558/tfc2013-112

Hein P.R.G. (2012) Estimating shrinkage, microfibril angle and density of *eucalyptus* wood using near infrared spectroscopy. *Journal of Near Infrared Spectroscopy,* 20(4): 427-436. doi: 10.1255/jnirs. 1005

Hein P.R.G., Campos A.C.M., Trugilho P.F., Lima J.T. & Chaix G. (2009) Near infrared spectroscopy for estimating wood basic density in *eucalyptus urophylla* and *eucalyptus grandis*. *Cerne,* 15(2): 133-141. doi: abr./jun. 2009

Hoffmeyer P. & Pedersen J.G. (1995) Evaluation of density and strength of Norway spruce wood by near infrared reflectance spectroscopy. *Holz als Roh- und Werkstoff,* 53(3): 165-170. doi: 10.1007/BF02716418

Inagaki T., Schwanninger M., Kato R., Kurata Y., Thanapase W., Puthson P. & Tsuchikawa S. (2012) *Eucalyptus camaldulensis* density and fiber length estimated by near-infrared spectroscopy. *Wood Science and Technology,* 46(1-3): 143-155. doi: 10.1007/s00226-010-0379-6

Isaksson T. & Naes T. (1988) The effect of multiplicative scatter correction (msc) and linearity improvement in NIR spectroscopy. *Applied Spectroscopy,* 42(7): 1273-1284

Jones P.D., Schimleck L.R., Peter G.F., Daniels R.F. & Clark A. (2005) Nondestructive estimation of *Pinus taeda* l. Wood properties for samples from a wide range of sites in Georgia. *Canadian Journal of Forest Research,* 35(1): 85-92. doi: 10.1139/x04-160

Jones P.D., Schimleck L.R., So C.L., Clark A. & Daniels R.F. (2007) High resolution scanning of radial strips cut from increment cores by near infrared spectroscopy. *IAWA Journal,* 28(4): 473-484. doi: 10.1163/22941932-90001657

Kennedy E.I. (1965) Strength and related properties of woods grown in Canada, Cat. No. Fo 57-1104, Working Paper 2006-16, Department of Forestry and Urban Development, Forestry Branch, Ottawa, Ontario, Canada, 51 pages.

Kobori H., Gorretta N., Rabatel G., Bellon-Maurel V., Chaix G., Roger J.M. & Tsuchikawa S. (2013) Applicability of VIS-NIR hyperspectral imaging for monitoring wood moisture content (MC). *Holzforschung,* 67(3): 307-314. doi: 10.1515/Hf-2012-0054

Krilek J., Kováč J. & Kučera M. (2014) Wood crosscutting process analysis for circular saws. *Crosscutting analysis BioResources,* 9(1): 417-1429

Kroll R.E., Ritter D.C., Gertjejansen R.O. & Au K.C. (1992) Anatomical and physical-properties of balsam poplar (*Populus-balsamifera* l) in minnesota. *Wood and Fiber Science,* 24(1): 13-24

Laurikkala J., Juhola M. & Kentala E. (2000) Informal identification of outliers in medical data, In *14th European Conference on Artificial Intelligence and 5th International Workshop on Intelligent Data Analysis in Medicine and Pharmacology IDAMAP-2000*, (Berlin, Germany), pp. 20-24

Leblon B., Adedipe O., Hans G., Haddadi A., Tsuchikawa S., Burger J., Stirling R., Pirouz Z., Groves K., Nader J. & LaRocque A. (2013) A review of near-infrared spectroscopy for monitoring moisture content and density of solid wood. *Forestry Chronicle,* 89(5): 595-606. doi: 10.5558/tfc2013-111

Libnau F.O., Toft J., Christy A.A. & Kvalheim O.M. (1994) Structure of liquid water determined from infrared temperature profiling and evolutionary curve resolution. *Journal of the American Chemical Society,* 116(18): 8311-8316. doi: 10.1021/ja00097a043

Lobell D.B. & Asner G.P. (2002) Moisture effects on soil reflectance. *Soil Science Society of America Journal,* 66(3): 722-727

Meder R., Marston D., Ebdon N. & Evans R. (2010) Spatially-resolved radial scanning of tree increment cores for near infrared prediction of microfibril angle and chemical composition. *Journal of Near Infrared Spectroscopy,* 18(6): 499-505. doi: 10.1255/Jnirs.903

Meder R. & Meglen R.R. (2012) Near infrared spectroscopic and hyperspectral imaging of compression wood in *Pinus radiata* d. Don. *Journal of Near Infrared Spectroscopy,* 20(5): 583-589. doi: 10.1255/Jnirs.1001

Micko M.M. (1987) Alberta aspen vs. Black poplar wood quality differences, M. o. f. S. a. S. Canada, Fo 42-91/28 - 1988E, Canadian Forestry Service, Edmonton, Alberta, 38 pages.

Minasny B. & McBratney A. (2013) Why you don't need to use RPD. *Pedometron,* 33: 14-15

Mora C.R., Schimleck L.R., Clark A. & Daniels R.F. (2011a) Determination of basic density and moisture content of merchantable loblolly pine logs by near infrared spectroscopy. *Journal of Near Infrared Spectroscopy,* 19(5): 391-399. doi: 10.1255/Jnirs.947

Mora C.R., Schimleck L.R., Yoon S.C. & Thai C.N. (2011b) Determination of basic density and moisture content of loblolly pine wood disks using a near infrared hyperspectral imaging system. *Journal of Near Infrared Spectroscopy,* 19(5): 401-409. doi: 10.1255/Jnirs.948

Nystrom J. & Hagman O. (1999) Real-time spectral classification of compression wood in *Picea abies*. *Journal of Wood Science,* 45(1): 30-37. doi: 10.1007/Bf00579521

Pang X.-F. (2013) *Water : Molecular structure and properties.* Hackensack, New Jersey: World Scientific Publishing Company. 472 pages.

Russ A., Fiserova M. & Gigac J. (2009) Preliminary study of wood species identification by NIR spectroscopy. *Wood Research,* 54(4): 23-32

Schimleck L.R. & Evans R. (2003) Estimation of air-dry density of increment cores by near infrared spectroscopy. *Appita Journal,* 56(4): 312-317

Schimleck L.R., Evans R. & Ilic J. (2001a) Application of near infrared spectroscopy to a diverse range of species demonstrating wide density and stiffness variation. *IAWA Journal,* 22(4): 415-429. doi: 10.1163/22941932-90000386

Schimleck L.R., Evans R. & Ilic J. (2001b) Estimation of *eucalyptus* delegatensis wood properties by near infrared spectroscopy. *Canadian Journal of Forest Research,* 31(10): 1671-1675. doi: 10.1139/cjfr-31-10-1671

Schimleck L.R., Evans R. & Ilic J. (2003a) Application of near infrared spectroscopy to the extracted wood of a diverse range of species. *IAWA Journal,* 24(4): 429-438

Schimleck L.R., Evans R., Ilic J. & Matheson A.C. (2002a) Estimation of wood stiffness of increment cores by near-infrared spectroscopy. *Canadian Journal of Forest Research,* 32(1): 129-135. doi: 10.1139/X01-176

Schimleck L.R., Evans R. & Matheson A.C. (2002b) Estimation of *Pinus radiata* d. Don clear wood properties by near-infrared spectroscopy. *Journal of Wood Science,* 48(2): 132-137. doi: 10.1007/Bf00767290

Schimleck L.R., Jones P.D., Clark A., Daniels R.F. & Peter G.F. (2005a) Near infrared spectroscopy for the nondestructive estimation of clear wood properties of *Pinus taeda* l. From the southern united states. *Forest Products Journal,* 55(12): 21-28

Schimleck L.R., Michell A.J., Raymond C.A. & Muneri A. (1999) Estimation of basic density of *eucalyptus globulus* using near-infrared spectroscopy. *Canadian Journal of Forest Research,* 29: 194-201. doi: 10.1139/x98-204

Schimleck L.R., Mora C. & Daniels R.F. (2003b) Estimation of the physical wood properties of green *Pinus taeda* radial samples by near infrared spectroscopy. *Canadian Journal of Forest Research,* 33(12): 2297-2305. doi: 10.1139/X03-173

Schimleck L.R., Rezende G.D.S.R., Demuner B.J. & Downes G.M. (2006) Estimation of whole-tree wood quality traits using near infrared spectra from increment cores. *Appita Journal,* 59(3): 231-236

Schimleck L.R., Sturzenbecher R., Mora C., Jones P.D. & Daniels R.F. (2005b) Comparison of *Pinus taeda* l. Wood property calibrations based on NIR spectra from the radial-longitudinal and radial-transverse faces of wooden strips. *Holzforschung,* 59(2): 214-218

Schwanninger M., Rodrigues J.C. & Fackler K. (2011) A review of band assignments in near infrared spectra of wood and wood components. *Journal of Near Infrared Spectroscopy,* 19(5): 287-308. doi: 10.1255/Jnirs.955

Smith I., Landis E. & Gong M. (2003) *Fracture and fatigue in wood.* Chichester, England: John Wiley & Sons 234 pages.

So C.L., Via B.K., Groom L.H., Schimleck L.R., Shupe T.F., Kelley S.S. & Rials T.G. (2004) Near infrared spectroscopy in the forest products industry. *Forest Products Journal,* 54(3): 6-16

Sykes R., Li B., Hodge G., Goldfarb B., Kadla J. & Chang H.-m. (2005) Prediction of loblolly pine wood properties using transmittance near-infrared spectroscopy. *Canadian Journal of Forest Research,* 35: 2423-2431. doi: 10.1139/X05-161

Thumm A., Riddell M., Nanayakkara B., Harrington J. & Meder R. (2010) Near infrared hyperspectral imaging applied to mapping chemical composition in wood samples. *Journal of Near Infrared Spectroscopy,* 18(6): 507-515. doi: 10.1255/Jnirs.909

Thygesen L.G. (1994) Determination of dry matter content and basic density of Norway spruce by near infrared reflectance and transmittance spectroscopy. *Journal of Near Infrared Spectroscopy,* 2: 127–135. doi: 10.1255/jnirs.39

Thygesen L.G. & Lundqvist S.O. (2000a) Nir measurement of moisture content in wood under unstable temperature conditions. Part 1. Thermal effects in near infrared spectra of wood. *Journal of Near Infrared Spectroscopy,* 8(3): 183-189. doi: 10.1255/jnirs.277

Thygesen L.G. & Lundqvist S.O. (2000b) Nir measurement of moisture content in wood under unstable temperature conditions. Part 2. Handling temperature fluctuations. *Journal of Near Infrared Spectroscopy,* 8(3): 191-199. doi: 10.1255/jnirs.278

Tsuchikawa S., Hayashi K. & Tsutsumi S. (1996) Nondestructive measurement of the subsurface structure of biological material having cellular structure by using near-infrared spectroscopy. *Applied Spectroscopy,* 50(9): 1117-1124. doi: 10.1366/0003702963905114

Tsuchikawa S., Inoue K., Noma J. & Hayashi K. (2003) Application of near-infrared spectroscopy to wood discrimination. *Journal of Wood Science,* 49(1): 29-35. doi: 10.1007/s100860300005

Tsuchikawa S., Torii M. & Tsutsumi S. (2001) Directional characteristics of near infrared light reflected from wood. *Holzforschung,* 55(5): 534-540. doi: 10.1515/HF.2001.086

Via B.K., Shupe T.F., Groom L.H., Stine M. & So C.L. (2003) Multivariate modelling of density, strength and stiffness from near infrared spectra for mature, juvenile and pith wood of Longleaf pine (*Pinus palustris*). *Journal of Near Infrared Spectroscopy,* 11(5): 365-378

Via B.K., So C.L., Shupe T.F., Stine M. & Groom L.H. (2005) Ability of near infrared spectroscopy to monitor air-dry density distribution and variation of wood. *Wood and Fiber Science,* 37(3): 394-402

Watanabe K., Mansfield S.D. & Avramidis S. (2011) Application of near-infrared spectroscopy for moisture-based sorting of green hem-fir timber. *Journal of Wood Science,* 57(4): 288-294. doi: DOI 10.1007/s10086-011-1181-2

Williamson G.B. & Wiemann M.C. (2010) Measuring wood specific gravity ... Correctly. *American Journal of Botany,* 97(3): 519-524. doi: 10.3732/Ajb.0900243

Xu Q.H., Qin M.H., Ni Y.H., Defo M., Dalpke B. & Sherson G. (2011) Predictions of wood density and module of elasticity of balsam fir (*Abies balsamea*) and black spruce (*Picea mariana*) from near infrared spectral analyses. *Canadian Journal of Forest Research,* 41(2): 352-358. doi: 10.1139/X10-215

Zhu X.R., Shan Y., Li G.Y., Huang A.M. & Zhang Z.Y. (2009) Prediction of wood property in chinese fir based on visible/near-infrared spectroscopy and least square-support vector machine. *Spectrochimica Acta Part a-Molecular and Biomolecular Spectroscopy,* 74(2): 344-348. doi: 10.1016/j.saa.2009.06.008

Barnett J. & Jeronimidis G. (2009) *Wood quality and its biological basis.* John Wiley & Sons. 226 pages.

Bowyer J.L., Shmulsky R. & Haygreen J.G. (2007) *Forest products and wood science: An introduction.* Oxford, UK: John Wiley & Sons. 496 pages.

Burger T., Kuhn J., Caps R. & Fricke J. (1997) Quantitative determination of the scattering and absorption coefficients from diffuse reflectance and transmittance

measurements: Application to pharmaceutical powders. *Applied Spectroscopy,* 51(3): 309-317. doi: 10.1366/0003702971940404

Cooper P.A., Jeremic D., Radivojevic S., Ung Y.T. & Leblon B. (2011) Potential of near-infrared spectroscopy to characterize wood products. *Canadian Journal of Forest Research,* 41(11): 2150-2157. doi: 10.1139/X11-088

Defo M., Taylor A.M. & Bond B. (2007) Determination of moisture content and density of fresh-sawn red oak lumber by near infrared spectroscopy. *Forest Products Journal,* 57(5): 68-72

Denig J., Wengert E.M. & Simpson W.T. (2000) Drying hardwood lumber, U.S. Department of Agriculture, Forest Service, Forest Products Laboratory, Tech. Rep. FPL–GTR–118, Madison, WI, USA, 138 pages.

Duncker P. & Spiecker H. (2009) Detection and classification of Norway spruce compression wood in reflected light by means of hyperspectral image analysis. *IAWA Journal,* 30(1): 59-70. doi: 10.1163/22941932-90000203

Fernandes A., Lousada J., Morais J., Xavier J., Pereira J. & Melo-Pinto P. (2013a) Comparison between neural networks and partial least squares for intra-growth ring wood density measurement with hyperspectral imaging. *Computers and Electronics in Agriculture,* 94: 71-81. doi: 10.1016/j.compag.2013.03.010

Fernandes A., Lousada J., Morais J., Xavier J., Pereira J. & Melo-Pinto P. (2013b) Measurement of intra-ring wood density by means of imaging VIS/NIR spectroscopy (hyperspectral imaging). *Holzforschung,* 67(1): 59-65. doi: 10.1515/Hf-2011-0258

Forest Products Laboratory (2010) *Wood handbook: Wood as an engineering material.* Madison, WI, USA: U.S. Department of Agriculture, Forest Service, Forest Products Laboratory. 508 pages.

Fujimoto T., Yamamoto H. & Tsuchikawa S. (2007) Estimation of wood stiffness and strength properties of hybrid larch by near-infrared spectroscopy. *Applied Spectroscopy,* 61(8): 882-888. doi: 10.1366/000370207781540150

Fujimoto T., Kurata Y., Matsumoto K. & Tsuchikawa S. (2008) Application of near infrared spectroscopy for estimating wood mechanical properties of small clear and full length lumber specimens. *Journal of Near Infrared Spectroscopy,* 16(6): 529-537. doi: 10.1255/Jnirs.813

Gindl W., Teischinger A., Schwanninger M. & Hinterstoisser B. (2001) The relationship between near infrared spectra of radial wood surfaces and wood mechanical properties. *Journal of Near Infrared Spectroscopy,* 9(4): 255-261. doi: 10.1255/jnirs.311

Haartveit E.Y. & Flæte P.O. (2008) Near infrared spectroscopy (NIRS) as a tool for effective classification of wood In *51st International Convention of Society of Wood Science and Technology,* (Concepción, Chile), pp. 1-9

Haddadi A., Burger J., Leblon B., Pirouz Z., Groves K. & Nader J. (2015a) Using near infrared hyperspectral images on subalpine fir board - part 1: Moisture content estimation. *Wood Material Science & Engineering,* 10(1): 27-40. doi: 10.1080/17480272.2014.965743

Haddadi A., Burger J., Leblon B., Pirouz Z., Groves K. & Nader J. (2015b) Using near infrared hyperspectral images on subalpine fir board - part 2: Density and basic

specific gravity estimation. *Wood Material Science & Engineering,* 10(1): 41-56. doi: 10.1080/17480272.2015.1011231

Hans G., Leblon B., Stirling R., Nader J., LaRocque A. & Cooper P. (2013) Monitoring of moisture content and basic specific gravity in black spruce logs using a handheld MEMS-based near-infrared spectrometer. *The Forestry Chronicle,* 89(5): 605-618. doi: 10.5558/tfc2013-112

Hans G., Leblon B., Cooper P., LaRocque A., Nader J. & Stirling R. (2015) Determination of moisture content and basic specific gravity of *Populus tremuloides* (Michx.) and *Populus balsamifera* (l.) logs using a portable near-infrared spectrometer. *Wood Material Science & Engineering,* 10(1): 3-16. doi: 10.1080/17480272.2014.916349

Hein P.R.G., Campos A.C.M., Trugilho P.F., Lima J.T. & Chaix G. (2009) Near infrared spectroscopy for estimating wood basic density in *eucalyptus urophylla* and *eucalyptus grandis*. *Cerne,* 15(2): 133-141. doi: abr./jun. 2009

Hein P.R.G. (2012) Estimating shrinkage, microfibril angle and density of *eucalyptus* wood using near infrared spectroscopy. *Journal of Near Infrared Spectroscopy,* 20(4): 427-436. doi: 10.1255/jnirs. 1005

Hoffmeyer P. & Pedersen J.G. (1995) Evaluation of density and strength of Norway spruce wood by near infrared reflectance spectroscopy. *Holz als Roh- und Werkstoff,* 53(3): 165-170. doi: 10.1007/BF02716418

Inagaki T., Schwanninger M., Kato R., Kurata Y., Thanapase W., Puthson P. & Tsuchikawa S. (2012) *Eucalyptus camaldulensis* density and fiber length estimated by near-infrared spectroscopy. *Wood Science and Technology,* 46(1-3): 143-155. doi: 10.1007/s00226-010-0379-6

Isaksson T. & Naes T. (1988) The effect of multiplicative scatter correction (msc) and linearity improvement in NIR spectroscopy. *Applied Spectroscopy,* 42(7): 1273-1284

Jones P.D., Schimleck L.R., Peter G.F., Daniels R.F. & Clark A. (2005) Nondestructive estimation of *Pinus taeda* l. Wood properties for samples from a wide range of sites in Georgia. *Canadian Journal of Forest Research,* 35(1): 85-92. doi: 10.1139/x04-160

Jones P.D., Schimleck L.R., So C.L., Clark A. & Daniels R.F. (2007) High resolution scanning of radial strips cut from increment cores by near infrared spectroscopy. *IAWA Journal,* 28(4): 473-484. doi: 10.1163/22941932-90001657

Kennedy E.I. (1965) Strength and related properties of woods grown in Canada, Cat. No. Fo 57-1104, Working Paper 2006-16, Department of Forestry and Urban Development, Forestry Branch, Ottawa, Ontario, Canada, 51 pages.

Kobori H., Gorretta N., Rabatel G., Bellon-Maurel V., Chaix G., Roger J.M. & Tsuchikawa S. (2013) Applicability of VIS-NIR hyperspectral imaging for monitoring wood moisture content (MC). *Holzforschung,* 67(3): 307-314. doi: 10.1515/Hf-2012-0054

Krilek J., Kováč J. & Kučera M. (2014) Wood crosscutting process analysis for circular saws. *Crosscutting analysis BioResources,* 9(1): 417-1429

Kroll R.E., Ritter D.C., Gertjejansen R.O. & Au K.C. (1992) Anatomical and physical-properties of balsam poplar (*Populus-balsamifera* l) in minnesota. *Wood and Fiber Science,* 24(1): 13-24

Laurikkala J., Juhola M. & Kentala E. (2000) Informal identification of outliers in medical data, In *14th European Conference on Artificial Intelligence and 5th International Workshop on Intelligent Data Analysis in Medicine and Pharmacology IDAMAP-2000*, (Berlin, Germany), pp. 20-24

Leblon B., Adedipe O., Hans G., Haddadi A., Tsuchikawa S., Burger J., Stirling R., Pirouz Z., Groves K., Nader J. & LaRocque A. (2013) A review of near-infrared spectroscopy for monitoring moisture content and density of solid wood. *Forestry Chronicle,* 89(5): 595-606. doi: 10.5558/tfc2013-111

Libnau F.O., Toft J., Christy A.A. & Kvalheim O.M. (1994) Structure of liquid water determined from infrared temperature profiling and evolutionary curve resolution. *Journal of the American Chemical Society,* 116(18): 8311-8316. doi: 10.1021/ja00097a043

Lobell D.B. & Asner G.P. (2002) Moisture effects on soil reflectance. *Soil Science Society of America Journal,* 66(3): 722-727

Meder R., Marston D., Ebdon N. & Evans R. (2010) Spatially-resolved radial scanning of tree increment cores for near infrared prediction of microfibril angle and chemical composition. *Journal of Near Infrared Spectroscopy,* 18(6): 499-505. doi: 10.1255/Jnirs.903

Meder R. & Meglen R.R. (2012) Near infrared spectroscopic and hyperspectral imaging of compression wood in *Pinus radiata* d. Don. *Journal of Near Infrared Spectroscopy,* 20(5): 583-589. doi: 10.1255/Jnirs.1001

Micko M.M. (1987) Alberta aspen vs. Black poplar wood quality differences, M. o. f. S. a. S. Canada, Fo 42-91/28 - 1988E, Canadian Forestry Service, Edmonton, Alberta, 38 pages.

Minasny B. & McBratney A. (2013) Why you don't need to use RPD. *Pedometron,* 33: 14-15

Mora C.R., Schimleck L.R., Yoon S.C. & Thai C.N. (2011a) Determination of basic density and moisture content of loblolly pine wood disks using a near infrared hyperspectral imaging system. *Journal of Near Infrared Spectroscopy,* 19(5): 401-409. doi: 10.1255/Jnirs.948

Mora C.R., Schimleck L.R., Clark A. & Daniels R.F. (2011b) Determination of basic density and moisture content of merchantable loblolly pine logs by near infrared spectroscopy. *Journal of Near Infrared Spectroscopy,* 19(5): 391-399. doi: 10.1255/Jnirs.947

Nystrom J. & Hagman O. (1999) Real-time spectral classification of compression wood in *Picea abies*. *Journal of Wood Science,* 45(1): 30-37. doi: 10.1007/Bf00579521

Pang X.-F. (2013) *Water : Molecular structure and properties.* Hackensack, New Jersey: World Scientific Publishing Company. 472 pages.

Russ A., Fiserova M. & Gigac J. (2009) Preliminary study of wood species identification by NIR spectroscopy. *Wood Research,* 54(4): 23-32

Schimleck L.R., Michell A.J., Raymond C.A. & Muneri A. (1999) Estimation of basic density of *eucalyptus globulus* using near-infrared spectroscopy. *Canadian Journal of Forest Research,* 29: 194-201. doi: 10.1139/x98-204

Schimleck L.R., Evans R. & Ilic J. (2001a) Application of near infrared spectroscopy to a diverse range of species demonstrating wide density and stiffness variation. *IAWA Journal,* 22(4): 415-429. doi: 10.1163/22941932-90000386

Schimleck L.R., Evans R. & Ilic J. (2001b) Estimation of *eucalyptus* delegatensis wood properties by near infrared spectroscopy. *Canadian Journal of Forest Research,* 31(10): 1671-1675. doi: 10.1139/cjfr-31-10-1671

Schimleck L.R., Evans R. & Matheson A.C. (2002a) Estimation of *Pinus radiata* d. Don clear wood properties by near-infrared spectroscopy. *Journal of Wood Science,* 48(2): 132-137. doi: 10.1007/Bf00767290

Schimleck L.R., Evans R., Ilic J. & Matheson A.C. (2002b) Estimation of wood stiffness of increment cores by near-infrared spectroscopy. *Canadian Journal of Forest Research,* 32(1): 129-135. doi: 10.1139/X01-176

Schimleck L.R. & Evans R. (2003) Estimation of air-dry density of increment cores by near infrared spectroscopy. *Appita Journal,* 56(4): 312-317

Schimleck L.R., Evans R. & Ilic J. (2003a) Application of near infrared spectroscopy to the extracted wood of a diverse range of species. *IAWA Journal,* 24(4): 429-438

Schimleck L.R., Mora C. & Daniels R.F. (2003b) Estimation of the physical wood properties of green *Pinus taeda* radial samples by near infrared spectroscopy. *Canadian Journal of Forest Research,* 33(12): 2297-2305. doi: 10.1139/X03-173

Schimleck L.R., Sturzenbecher R., Mora C., Jones P.D. & Daniels R.F. (2005a) Comparison of *Pinus taeda* l. Wood property calibrations based on NIR spectra from the radial-longitudinal and radial-transverse faces of wooden strips. *Holzforschung,* 59(2): 214-218

Schimleck L.R., Jones P.D., Clark A., Daniels R.F. & Peter G.F. (2005b) Near infrared spectroscopy for the nondestructive estimation of clear wood properties of *Pinus taeda* l. From the southern united states. *Forest Products Journal,* 55(12): 21-28

Schimleck L.R., Rezende G.D.S.R., Demuner B.J. & Downes G.M. (2006) Estimation of whole-tree wood quality traits using near infrared spectra from increment cores. *Appita Journal,* 59(3): 231-236

Schwanninger M., Rodrigues J.C. & Fackler K. (2011) A review of band assignments in near infrared spectra of wood and wood components. *Journal of Near Infrared Spectroscopy,* 19(5): 287-308. doi: 10.1255/Jnirs.955

Smith I., Landis E. & Gong M. (2003) *Fracture and fatigue in wood.* Chichester, England: John Wiley & Sons 234 pages.

So C.L., Via B.K., Groom L.H., Schimleck L.R., Shupe T.F., Kelley S.S. & Rials T.G. (2004) Near infrared spectroscopy in the forest products industry. *Forest Products Journal,* 54(3): 6-16

Sykes R., Li B., Hodge G., Goldfarb B., Kadla J. & Chang H.-m. (2005) Prediction of loblolly pine wood properties using transmittance near-infrared spectroscopy. *Canadian Journal of Forest Research,* 35: 2423-2431. doi: 10.1139/X05-161

Thumm A., Riddell M., Nanayakkara B., Harrington J. & Meder R. (2010) Near infrared hyperspectral imaging applied to mapping chemical composition in wood samples. *Journal of Near Infrared Spectroscopy,* 18(6): 507-515. doi: 10.1255/Jnirs.909

Thygesen L.G. (1994) Determination of dry matter content and basic density of Norway spruce by near infrared reflectance and transmittance spectroscopy. *Journal of Near Infrared Spectroscopy,* 2: 127–135. doi: 10.1255/jnirs.39

Thygesen L.G. & Lundqvist S.O. (2000a) Nir measurement of moisture content in wood under unstable temperature conditions. Part 1. Thermal effects in near infrared spectra of wood. *Journal of Near Infrared Spectroscopy,* 8(3): 183-189. doi: 10.1255/jnirs.277

Thygesen L.G. & Lundqvist S.O. (2000b) Nir measurement of moisture content in wood under unstable temperature conditions. Part 2. Handling temperature fluctuations. *Journal of Near Infrared Spectroscopy,* 8(3): 191-199. doi: 10.1255/jnirs.278

Tsuchikawa S., Hayashi K. & Tsutsumi S. (1996) Nondestructive measurement of the subsurface structure of biological material having cellular structure by using near-infrared spectroscopy. *Applied Spectroscopy,* 50(9): 1117-1124. doi: 10.1366/0003702963905114

Tsuchikawa S., Torii M. & Tsutsumi S. (2001) Directional characteristics of near infrared light reflected from wood. *Holzforschung,* 55(5): 534-540. doi: 10.1515/HF.2001.086

Tsuchikawa S., Inoue K., Noma J. & Hayashi K. (2003) Application of near-infrared spectroscopy to wood discrimination. *Journal of Wood Science,* 49(1): 29-35. doi: 10.1007/s100860300005

Via B.K., Shupe T.F., Groom L.H., Stine M. & So C.L. (2003) Multivariate modelling of density, strength and stiffness from near infrared spectra for mature, juvenile and pith wood of Longleaf pine (*Pinus palustris*). *Journal of Near Infrared Spectroscopy,* 11(5): 365-378

Via B.K., So C.L., Shupe T.F., Stine M. & Groom L.H. (2005) Ability of near infrared spectroscopy to monitor air-dry density distribution and variation of wood. *Wood and Fiber Science,* 37(3): 394-402

Watanabe K., Mansfield S.D. & Avramidis S. (2011) Application of near-infrared spectroscopy for moisture-based sorting of green hem-fir timber. *Journal of Wood Science,* 57(4): 288-294. doi: DOI 10.1007/s10086-011-1181-2

Williamson G.B. & Wiemann M.C. (2010) Measuring wood specific gravity ... Correctly. *American Journal of Botany,* 97(3): 519-524. doi: 10.3732/Ajb.0900243

Xu Q.H., Qin M.H., Ni Y.H., Defo M., Dalpke B. & Sherson G. (2011) Predictions of wood density and module of elasticity of balsam fir (*Abies balsamea*) and black spruce (*Picea mariana*) from near infrared spectral analyses. *Canadian Journal of Forest Research,* 41(2): 352-358. doi: 10.1139/X10-215

Zhu X.R., Shan Y., Li G.Y., Huang A.M. & Zhang Z.Y. (2009) Prediction of wood property in chinese fir based on visible/near-infrared spectroscopy and least square-support vector machine. *Spectrochimica Acta Part a-Molecular and Biomolecular Spectroscopy,* 74(2): 344-348. doi: 10.1016/j.saa.2009.06.008

Chapter 5. Determination of optical parameters and moisture content of wood with visible-NIR spectroscopy[4]

5.1. Abstract

We used the Kubelka–Munk theory equations for calculating the absorption coefficient (K_λ), the scattering coefficient (S_λ), the transport absorption ($\sigma_{\lambda a}$), the reduced scattering coefficient [$\sigma_{\lambda s}$ (1 − g)] and the penetration depth (δ_λ) from visible–near infrared reflectance spectra acquired over thin samples of quaking aspen and black spruce conditioned at three different moisture levels. The computed absorption and scattering coefficients varied from 0.1 mm^{-1} to 4.0 mm^{-1} and from 5.5 mm^{-1} to 10.0 mm^{-1}, respectively. The absorption coefficients varied according to the absorption band, but the scattering coefficients decreased slowly towards high wavelengths. The sample moisture content was then estimated using the partial least squares (PLS) regression method from the K_λ and/or S_λ spectra, and the resulting PLS models were compared to those obtained with raw and transformed (multiplicative scatter corrected (MSC), first and second derivative) absorption spectra. The best PLS models for black spruce, quaking aspen and both species were obtained when only the 800–1800 nm range was used with the raw or MSC spectra. They led to a root mean square error of cross validation ($RMSE_{CV}$) of 1.40%, 1.09% and 1.23%, respectively, and to a coefficient of determination (R^2_{CV}) higher than 0.94. We also found that the K_λ spectra between 800

[4] This chapter was published in *Journal of Near Infrared Spectroscopy* (November, 2015) under the following authorship: Ataollah Haddadi, Guillaume Hans, Brigitte Leblon, Zarin Pirouz, Satoru Tsuchikawa, Joseph Nader, and Kevin Groves. doi: 10.1255/jnirs.1174
It is reproduced with the permission of the Springer (see letter permission in Appendix D)

nm and 1800 nm can provide PLS models having an acceptable accuracy for moisture content estimation (R^2_{CV} = 0.83 and $RMSE_{CV}$ = 2.32%), regardless of the species.

5.2. Introduction

Spectroscopy systems have opened a new horizon for the analysis of chemical composition and physical properties of materials, such as wood. These systems record reflected or transmitted radiation between 400 and 2500 nm that can be related to scattering and absorption properties of the material. These properties can provide, in turn, information about the physical or chemical properties of the material. In wood science, visible-near-infrared (VIS-NIR) spectroscopy sensors and hyperspectral imaging systems have been tested as a non-destructive technique for the estimation of several wood properties, including pulp yield and pulping chemistry (Birkett and Gambino, 1989, Wallbacks et al., 1991, Meder et al., 1994, Michell, 1995, Michell and Schimleck, 1998), moisture content (MC) and density (Thygesen, 1994, Thygesen and Lundqvist, 2000, Schimleck et al., 2001, Schimleck et al., 2002b, Schimleck and Evans, 2003, Via et al., 2003, Schimleck et al., 2005, Schimleck et al., 2006, Fujimoto et al., 2008, Mora et al., 2011a, Mora et al., 2011b, Schwanninger et al., 2011, Watanabe et al., 2011, Inagaki et al., 2012, Hans et al., 2013, Leblon et al., 2013, Haddadi et al., 2015a, 2015b, Haddadi et al., 2015c, Hans et al., 2015), chemical properties (Schimleck et al., 2002a, Kelley et al., 2004, So et al., 2004, Meder et al., 2010), mechanical properties (MOE, MOR and stiffness) (Gindl et al., 2001, Fujimoto et al., 2007, Fujimoto et al., 2008, Xu et al., 2011), fiber length (Inagaki et al., 2012), shrinkage (Hein, 2012), microfibril angle (Meder et al., 2010, Hein, 2012), compression strength (Hoffmeyer

and Pedersen, 1995), species identification (Tsuchikawa et al., 2003, Adedipe et al., 2008, Haartveit and Flæte, 2008, Russ et al., 2009, Cooper et al., 2011, Haddadi et al., 2015c, Hans et al., 2015), and early detection of wood decay (Stirling et al., 2007, Green et al., 2010).

All the aforementioned studies used statistical analysis to relate the wood properties to the NIR measurements. An alternate approach would be to use a more deterministic approach based on the physical principles of electromagnetic waves. Tsuchikawa et al. (1996) developed an optical model, which explicitly describes the interaction between wood properties and NIR spectra. Wood is modeled as an aggregate of semi-infinite inclined square tubes representing the tracheids with a membrane having a certain thickness. The model also assumes that the incident radiation is made of parallel beams. For each wavelength (λ), it computes the radiation absorbance $A_\lambda(d)$ from the diffuse reflectance $R_\lambda(d)$ for a sample of thickness d by:

$$A_\lambda(d) = \log(1/R_\lambda(d))$$

Equation 5.1

For each wavelength λ, the diffuse reflectance $R_\lambda(d)$ and transmittance $T_\lambda(d)$ are computed by the equations of the Kubelka-Munk (K-M) theory (Kubelka, 1948, 1954). In the K-M theory, the propagation of radiation in a medium that absorbs, emits, and scatters is described using a two-flux approach (Kortum, 1969). The theory has the following assumptions (Olinger and Griffiths, 1988, Cheong et al., 1990): (i) the light propagates in the sample through two fluxes, which are opposite to each other; (ii) the illumination over the sample is monochromatic, (iii) the scattered radiation distribution

is isotropic or is specular; (iv) the sample is made of particles that are randomly distributed in the different sample layers and that have a size much smaller than the layer thickness and the wavelengths of the incident radiation; and (v) the surface of the sample is much greater than its thickness. According to this theory, when the thickness of a sample (*d*) increases, its reflectance increases. Thereby, for each wavelength λ, $R_\lambda(d)$ *and* $T_\lambda(d)$ are expressed as a function of the sample thickness *d*, the scattering coefficient S_λ, and the absorption coefficient K_λ by the following equations (Kubelka, 1948, Kortum, 1969, Tsuchikawa et al., 1996):

$$T_\lambda(d) = \frac{\beta}{\alpha \sinh X + \beta \cosh X}$$

$$R_\lambda(d) = \frac{\sinh X}{\alpha \sinh X + \beta \cosh X}$$

Equation 5.2

where

$$X = \beta . S_\lambda . d$$

$$\alpha = \frac{K_\lambda}{S_\lambda} + 1$$

$$\beta = \sqrt{\alpha^2 - 1}$$

Equation 5.3

where *d* is the sample thickness (mm), $T_\lambda(d)$ is the transmittance of the sample having a thickness d, $R_\lambda(d)$ is the reflectance of the sample having a thickness d, K_λ is the absorption coefficient (mm^{-1}), and S_λ is the scattering coefficient (mm^{-1}). $T_\lambda(d)$, $R_\lambda(d)$, K_λ, and S_λ depend on the wavelength λ.

In order to estimate both S_λ and K_λ from $R_\lambda(d)$ using Equations (5-1−5-3), there is the need to have at least two reflectance measurements from a sample in two different thicknesses ($R_\lambda(d_1)$ *and* $R_\lambda(d_2)$). It is important to understand that S_λ and K_λ of the K-M theory are only approximation of the true scattering coefficient (μ_s) and absorption (μ_k) coefficients. μ_s and μ_k represent the probability of absorption and scattering per unit path length (Shi and Anderson, 2009) and they are about half of K_λ and S_λ, respectively (Olinger and Griffiths, 1988, Hapke, 1993). However, when the sample acts like a diffuse medium, K_λ and S_λ allow deriving other optical parameters of the scanned samples, such as the transport absorption coefficient ($\sigma_{\lambda a}$) and the reduced scattering coefficient ($\sigma_{\lambda s}(1-g)$) as follows (van Gemert and Star, 1987, Sterenborg et al., 1989, Shi and Anderson, 2010, Roy et al., 2012):

$$K_\lambda = \frac{2\sigma_{\lambda a}}{1+\sigma_{\lambda a}/\left(2\left[\sigma_{\lambda a}+\sigma_{\lambda s}(1-g)\right]\right)}$$

Equation 5.4

$$S_\lambda = \frac{\frac{3}{4}\sigma_{\lambda s}(1-g)}{1+19\sigma_{\lambda a}/\left(30\left[\sigma_{\lambda a}+\sigma_{\lambda s}(1-g)\right]\right)}$$

Equation 5.5

where $\sigma_{\lambda a}$ is the transport absorption coefficient (mm^{-1}), $\sigma_{\lambda s}(1-g)$ is the reduced scattering coefficient (mm^{-1}), g is the anisotropy factor (dimensionless) which is computed as the mean cosine scattering angle. In the case of isotropic scattering, g equals to zero. The absorption and reduced scattering coefficients can also be derived using time-of-flight (TOF) near-infrared spectroscopy measurements. Both coefficients

were computed from TOF measurements in the 700 to 1100 nm wavelength range in the case of European silver fir (*Abies alba* Mill.) and sweet chestnut (*Castanea sativa* Mill.) (D'Andrea et al., 2008, D'Andrea et al., 2009). This technique was also used to calculate the absorption and reduced scattering coefficients at 846 nm and to relate these coefficients to wood air-dry density of seven different species (Hans et al., 2014).

Both $\sigma_{\lambda a}$ and $\sigma_{\lambda s}(1\text{-}g)$ allow defining another optical parameter, which is the penetration depth (δ_λ) by (Sterenborg et al., 1989, Leonardi and Burns, 1999):

$$\delta_\lambda = \left(3\sigma_{\lambda a}\left[\sigma_{\lambda a} + \sigma_{\lambda s}(1-g)\right]\right)^{-0.5}$$

Equation 5.6

δ_λ is a good indicator of the radiation penetration in the sample, but it is not the effective penetration depth, which is the depth where the amount of radiation energy or intensity is reduced to 37% (Welch and van Gemert, 2011). Note that Equations (5-7) are only valid when the scattering dominates the absorption.

In this paper, we derived the scattering (S_λ) and absorption (K_λ) coefficients at each wavelength λ by applying the Kubelka-Munk theory equations (Equations (2) and (3)) to hemispherical diffuse reflectance spectra recorded between 400 and 2500 nm on thin wood samples extracted from log disks of a hardwood species (quaking aspen (*Populus tremuloides* Michx.)) and a softwood species (black spruce (*Picea mariana* Mill.)). The samples were produced with five thickness levels and were conditioned at three MC levels. A model to estimate the sample MC from the K_λ or S_λ spectra was established using the partial least squares (PLS) regression method and compared to the

one estimated by applying PLS regression analysis to raw and multiplicative scatter correction (MSC), 1st, or 2nd derivative absorbance spectra (Rinnan et al., 2009). For each MC model, the influence of the species and of the wavelength range was considered. Finally, we analyzed the effect of MC on the calculated values of the transport absorption coefficient, the reduced scattering coefficient, and the penetration depth. Our study uses the same method as in Tsuchikawa et al. (1996) to estimate the K_λ and S_λ spectra, but it is the first time that this method is applied to black spruce and quaking aspen samples. Also, in contrast to Tsuchikawa et al. (1996), our study proposed a model to estimate MC from the K_λ or S_λ spectra and compared it to the MC model built with raw, MSC, 1st, or 2nd derivative absorbance spectra. In addition, we computed the transport absorption coefficient ($\sigma_{\lambda a}$), the reduced scattering coefficient ($\sigma_{\lambda s}(1-g)$), and the penetration depth (δ_λ.) of our samples and analyzed the effect of MC on these optical parameters.

5.3. Materials and methods

5.3.1. Sample preparation

For this study, a total of 120 thin layer samples were prepared. Two species were considered: quaking aspen (*Populus tremuloides* Michx.), as a hardwood species and black spruce (*Picea mariana* Mill.), as a softwood species. For each species, two disks were prepared and from each disk, we cut two blocks of 25x25x45 mm in the tangential (T), longitudinal (L), and radial (R) directions, respectively (Figure 5-1). From each

block, three sets of five thin samples were cut with a microtome in the following thicknesses: 100 µm, 200 µm, 400 µm, 600 µm, and 1000 µm.

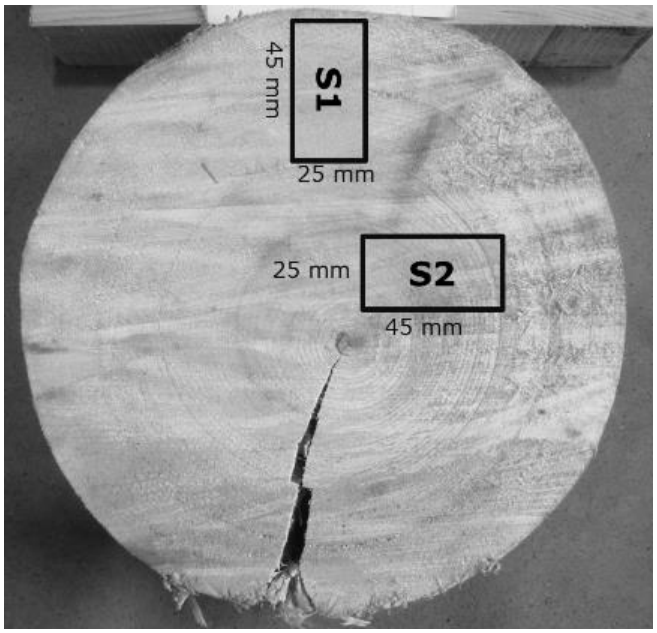

Figure 5-1: Relative location of the samples taken from a disk.

The thin samples were positioned on numbered aluminum dishes that were placed in three desiccators. Each desiccator contained a different salt solution that allowed conditioning samples at three MC levels. According to Lide (2004), 3% and 7% equilibrium MC (EMC) can be reached by placing samples in a desiccator containing saturated salt solutions of ammonium sulfate $(NH_4)_2SO_4$) and sodium iodide (NaI) respectively, which achieve relative humidities of 81% and 37% at room temperature. Similarly, 16% EMC can be reached by placing samples in desiccators containing dry silica gel (SiO_2) that correspond to a relative humidity of 9% at room temperature (Gautam and Henderson, 2011). The samples were kept in the desiccators for more than two days to ensure that they reached the desired EMC in equilibrium with the relative

humidity within the desiccator. In addition, the sample EMC for each desiccator was controlled using three dummy samples. These three samples were oven-dried and their reference MCs (% dry basis) were computed using the gravimetric method (*Method A* of ASTM-D4442–07 (2009)). Due to the low weight of the thin samples, a high precision (0.01 mg) analytical balance was used (Mettler Toledo XS 105 (Mettler Toledo, Mississauga, Canada)). The measured MC was 1.6% higher than the theoretical MC than that which should have been reached within the 3% and 7% desiccators and 0.6% lower than the theoretical MC than that which should have been reached within the 16% desiccator. Given these low errors, we can assume that the measured sample MCs were almost equal to the desiccator's MCs.

5.3.2. Spectral measurements

Hemispherical diffuse reflectance spectra were acquired in the 350-2500 nm wavelength range with a 1 nm resolution using a portable ASD FieldSpec Pro FR spectroradiometer (Analytical Spectral Devices, Inc., Boulder, CO, USA) equipped with an 1800-12 LI-COR (LI-COR Inc., Lincoln, NE, USA) attached to an external integrating sphere illuminated with a 3100K halogen light source. The integrating sphere had an internal diameter of ca. 10 cm and was internally coated with barium sulfate ($BaSO_4$) to act as a uniform diffuse reflector. To obtain reflectance spectra, the spectroradiometer was calibrated by covering the sample port of the integrating sphere with a barium sulfate plug (white reference). We averaged 30 spectra for each thin sample in order to improve the signal to noise ratio.

In the raw spectra, some wavelength regions were noisy because of the high sensitivity of the detectors (Figure 5-2). For this reason, reflectance spectra were smoothed using an adaptive mean filtering method, which was found to be better than the median filter or Savitzky–Golay filtering method (Orfanidis, 1996). In our method, the window size of the mean filter is variable. It was set at 9 for the spectral region between 430 nm and 1950 nm and at 21, for the spectral regions below 430 nm and above 1950 nm. Using a filter with a constant window size may not remove the noise completely or removes the noise for only some wavelengths. Figure 5-2 shows the effect of the filtering on a spectrum acquired from a black spruce sample having a thickness of 200 µm and an MC of 7%. It shows that most of the spectral fluctuations below 2200 nm are suppressed and the best curve is fitted to the spectrum above 2200 nm. The filtered reflectance spectra were then used to derive the absorbance spectra using Equation 5.1 and the K_λ and S_λ spectra using Equation 5.2 and 5.3. The raw absorbance spectra were also transformed into multiplicative scatter corrected (MSC) and 1st and 2nd derivative absorbance spectra.

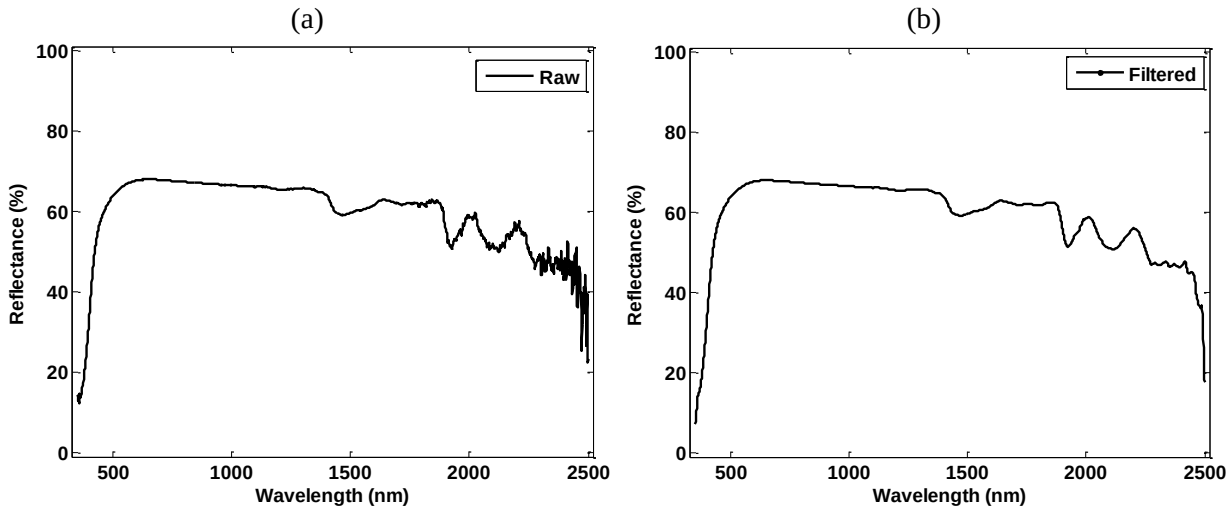

Figure 5-2: (a) raw and (b) filtered spectra with an adaptive mean filtering in the case of black spruce sample (thickness=200 μm, MC=7%).

To calculate K_λ and S_λ spectra in each wavelength (λ) a least squares method was applied to minimizes the difference between the filtered reflectance spectra estimated using Equation 5.2 and Equation 5.3 and those measured over the five thickness samples. The derived K_λ and S_λ spectra were further smoothed using the Savitzky-Golay method (Orfanidis, 1996) with a window size of 41 and a three-degree polynomial. However, even after applying this method, the spectra were still too noisy for the wavelengths below 430 nm and above 2380 nm. Thereby, only the 430-2380 nm spectra were used in further analysis. The K_λ and S_λ spectra as well as the raw and transformed absorbance spectra were then compared to the sample MCs using multivariate data analysis to derive MC estimation models.

5.3.3. Multivariate analysis

NIR spectroscopy protocols are based on the Lambert-Beer's law that describes a linear relationship between the absorbance of the NIR radiation (*A*) and the concentration of a substance (*c*) (Burger, 2006):

$$A = c * \varepsilon * \delta$$

Equation 5.7

where δ represents the path length of the radiation through the sample, and ε is the molar absorptivity. Because both ε and δ of a chemical component are constant, we can simplify Equation 5.8 by:

$$c = A * b$$

Equation 5.8

where $b = (\varepsilon\delta)^{-1}$.

Equation 5.9 can be generalized using a simple linear regression as follows:

$$y = x * b + e$$

Equation 5.9

where *y* is the response variable (here the concentration *c)*, *x* is the explanatory variable (here, the absorbance *A)*, *b* is the regression coefficient, which contains the information about the molar absorptivity and path length of the radiation, and *e* represents the error.

The partial least squares (PLS) regression allows finding the best estimate of *b* by maximizing the covariance derived from *x* and *y*, which minimizes *e* at the same time. The PLS method is also suitable for analyzing correlated (collinear) data, especially when the number of explanatory variables (*x*) is high. For this study, PLS models to estimate MC were first built for each species separately and then a model that combines data from both species was built. In both cases, they were derived using first the K_λ and S_λ spectra. The MC models were then compared to those derived using PLS regression applied directly to (1) raw absorbance spectra; (2) multiplicative scatter corrected (MSC) absorbance spectra; (3) 1st derivative absorbance spectra, and (4) 2nd derivative absorbance spectra. We did not consider the standard normal variate (SNV) transformation over raw absorbance spectra, because SNV-transformed spectra have a linear relationship with MSC spectra, which results in a similar MC model for both transformations (Dhanoa et al., 1994). All the PLS models based on raw and transformed absorbance spectra were derived from the data acquired over the thickest samples (1000 µm) in order to be representative of MC estimation from reflectance spectra acquired over classical wood products.

For each MC model, we considered two wavelength ranges: 1) the whole spectral range between 430 and 2380 nm and 2) a reduced wavelength range between 800 and 1800 nm that corresponds to less noisy spectra and still includes the water absorption bands at 970, 1190, and 1450 nm (Burns and Ciurczak, 2007). We calibrated the PLS models using all the samples and the model performance was evaluated using the root mean square error of leave-one-out cross validation ($RMSE_{CV}$) and the corresponding coefficient of determination (R^2) between observed and estimated MC

values. The optimal number of latent variables in the PLS models was determined as the one which minimizes $RMSE_{CV}$.

5.4. Results

5.4.1. Visible and NIR reflectance and absorbance

The reflectance MS-corrected spectra of black spruce and quaking aspen samples having a thickness of 400 μm and an MC of 7% are compared in Figure 5-3. Visually, both samples have a similar color and are very difficult to discriminate. However, the black spruce sample has a slightly lower blue (450-475 nm), green (495-570 nm), and red (620-750 nm) reflectance (Figure 5-3). Similarly, between 750 and 1420 nm, the reflectance difference is only about 3%, but beyond 1420 nm the reflectance difference increases to 7%.

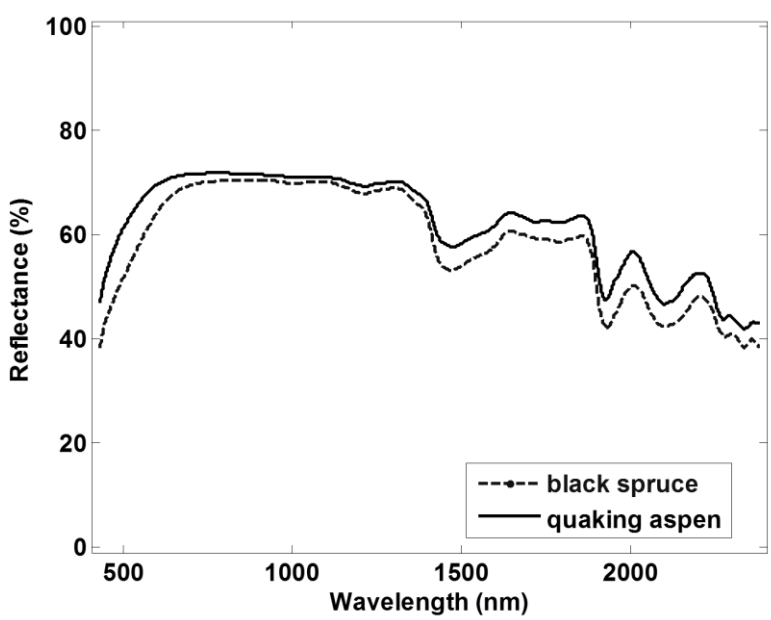

Figure 5-3: Reflectance MS-corrected spectra of 400 μm thick quaking aspen and black spruce samples having an MC of 7%.

Reflectances of quaking aspen samples increase with the sample thickness (*d*) (Figure 5-4), because of an increasing optical path length. All the samples were conditioned at the same MC level (7%) and have the same chemical properties, since they were all cut in the same locations of the same disk. Figure 5-4 also shows that the difference between spectra as a function of the sample thickness is stronger for the wavelengths between 500 and 1450 nm. Below 500 nm, there is no significant difference between the spectra. Beyond 1450 nm, only the 100 and 200 µm samples have a distinct spectrum. Such effect of the sample thickness is also apparent when plotting the absorbance versus the sample thickness for three specific wavelengths (1100, 1680, 2230 nm) (Figure 5-5). In the three selected wavelengths, the absorbance decreases with increasing sample thickness *d* until it reaches a saturation level. The corresponding thickness (d_o) decreases with increasing wavelengths. d_o is higher than 1000 µm for the 1100 nm case, but is around 400 µm for the 1680 nm case, and 200 µm for the 2230 nm case. All these results are also valid for our black spruce samples (results not shown).

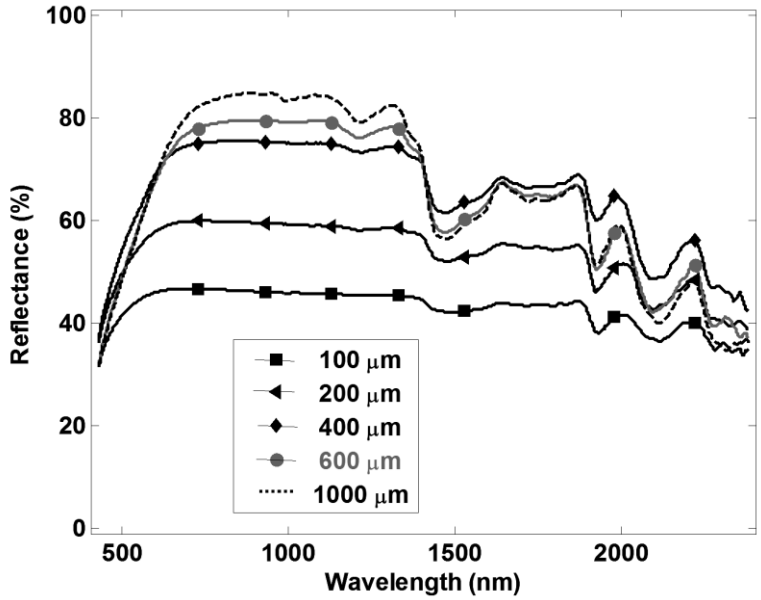

Figure 5-4: Reflectance spectra collected over the quaking aspen samples having an MC of 7% as a function of the sample thickness.

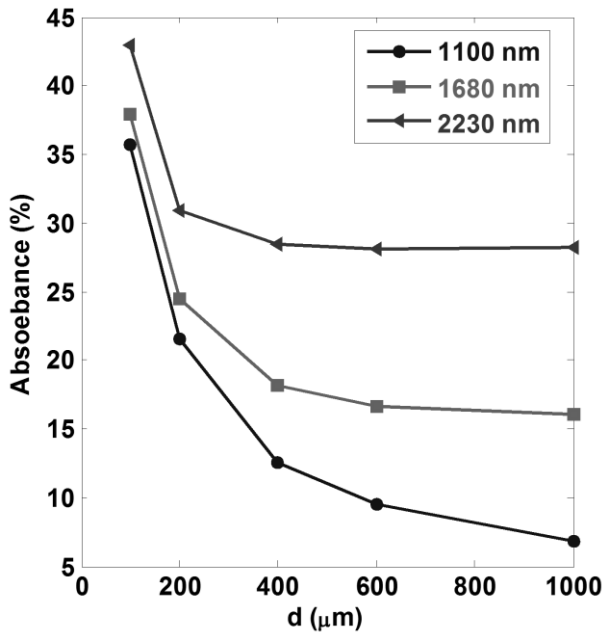

Figure 5-5: Absorbances in the 1100, 1680, and 2230 nm wavelength as a function of the sample thickness for quaking aspen samples having an MC of 7%.

5.4.2. K and S spectra

Figure 5-6 compares the averaged, calculated K_λ and S_λ spectra for both black spruce and quaking aspen samples having an MC of 7%. The black dashed line corresponds to K_λ and S_λ spectra determined by Tsuchikawa et al. (1996) from Sitka spruce samples having an MC of about 7%. Whatever the species, the pattern of K_λ as a function of the wavelength is similar. K_λ increases in OH absorption bands (1400, 1940, 2110 nm) and CH absorption bands (2270 and 2320 nm) (Schwanninger et al., 2011). In addition, there is no difference in the K_λ spectra between both black spruce and Sitka spruce samples, but the K_λ spectrum of quaking aspen sample presents lower absorbances beyond 1900 nm.

S_λ spectra for quaking aspen and black spruce samples have similar patterns. The difference between both spectra gradually decreases by 0.3 mm^{-1} until 1470 nm and then increases by 1 mm^{-1}. Compared to the K_λ spectra, the S_λ spectra are noisier, especially for the wavelengths above 1900 nm. The S_λ coefficients for quaking aspen and black spruce have higher values than for Sitka spruce.

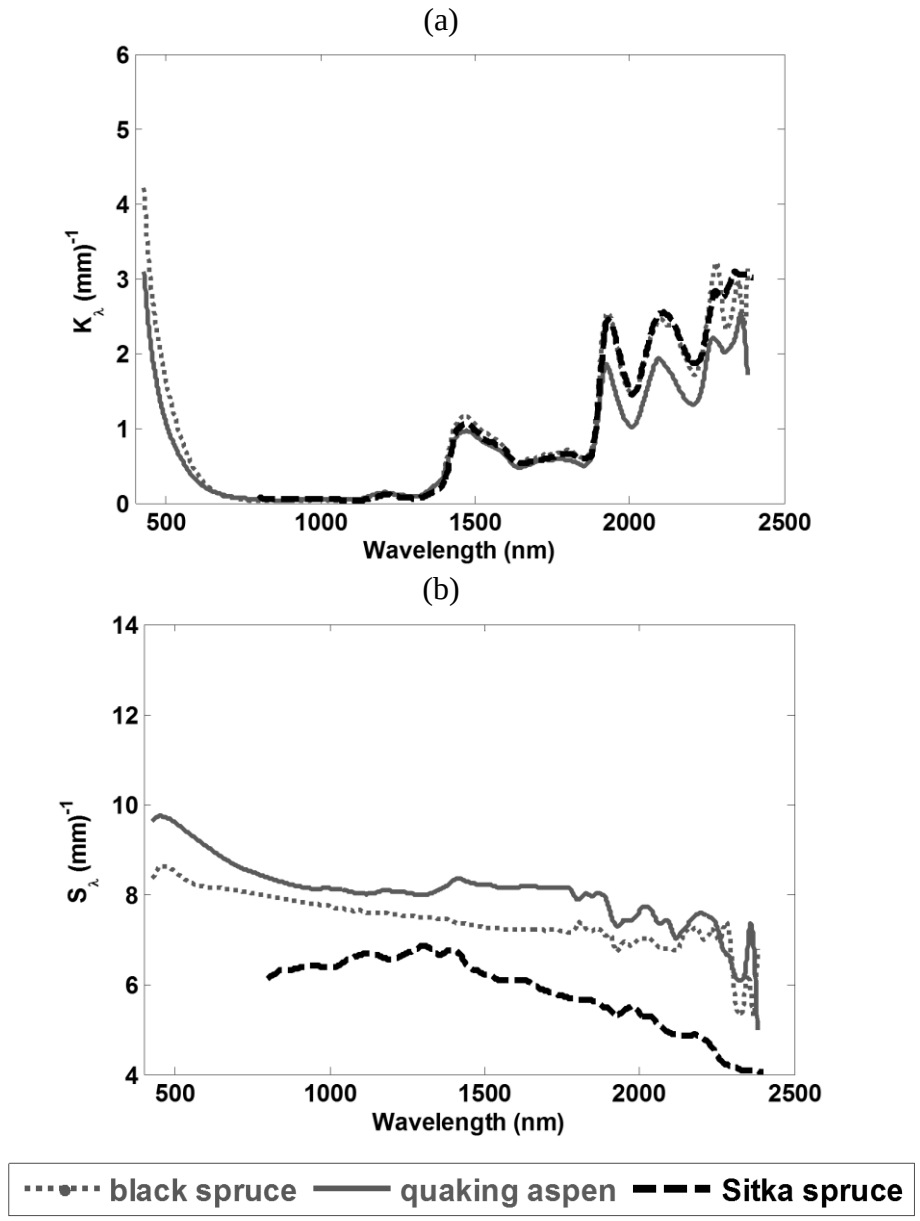

Figure 5-6: (a) K_λ and (b) S_λ spectra computed from the absorbance spectra of black spruce and quaking aspen samples having different thicknesses and an MC of 7%. The black dashed line corresponds to (a) K_λ and (b) S_λ spectra determined from Sitka spruce samples having an MC of 7% (Tsuchikawa et al. 1996).

Because one objective of the study is to estimate MC from the K_λ and S_λ spectra, we also analyzed the influence of MC on the derived K_λ and S_λ spectra for each species (Figure 5-7). For both species, K_λ increases when MC increases for all of the wavelengths between 1450 nm and 2350 nm. The highest increase is observed for the OH absorption bands (1450 and 1950 nm). Values for S_λ appear to increase with MC, but the trend is less obvious above 1450 nm, where a decrease in S_λ for the sample at 3% MC in the region of the 1950 nm absorption band even occurs.

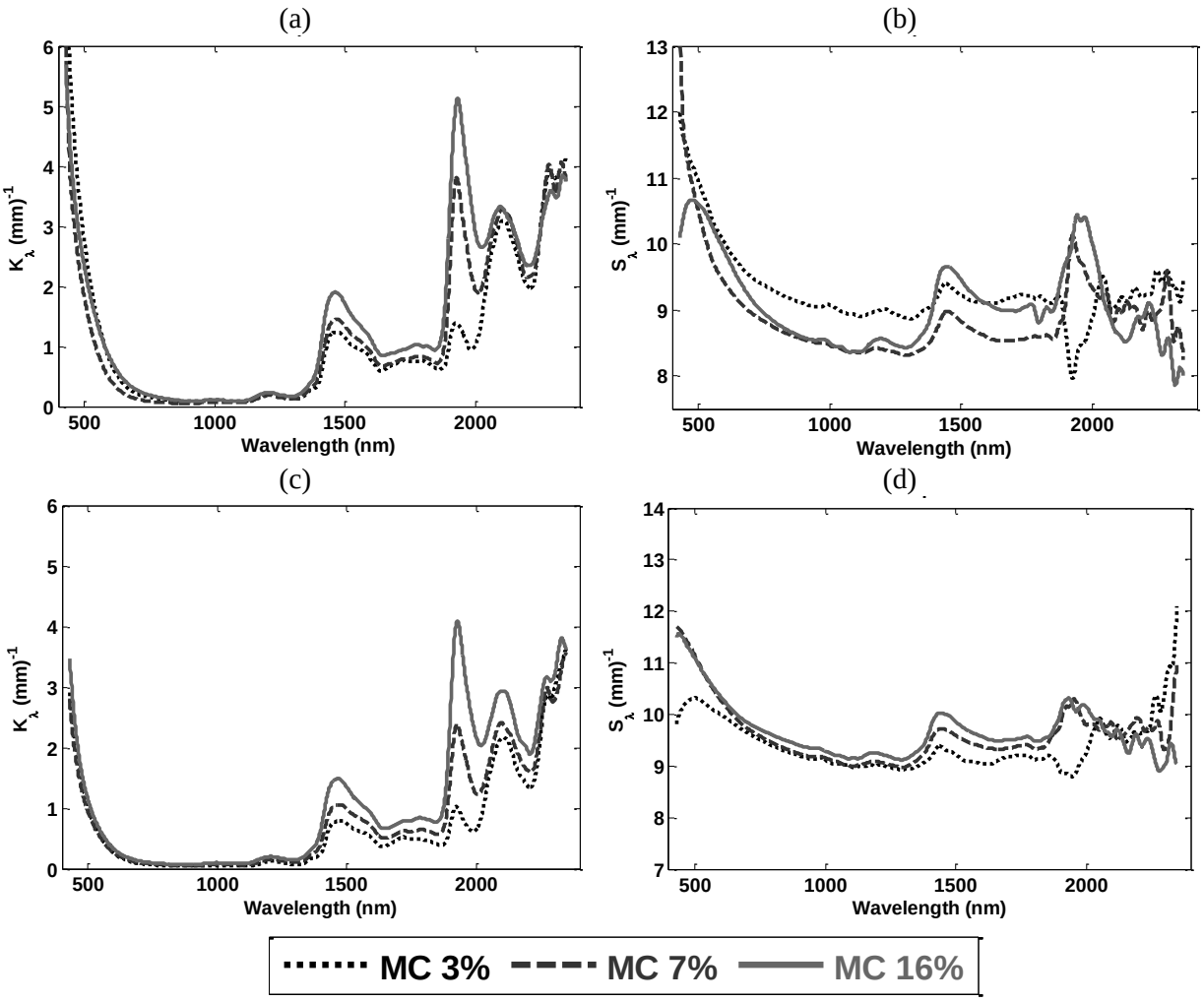

Figure 5-7: Influence of the sample moisture content on the Kλ and Sλ spectra for (a) and (b) black spruce samples and (c) and (d) quaking aspen samples.

5.4.3. MC modeling

Table 5-1 compares the calibration and cross validation PLS models for estimating MC that were built with $K\lambda$ and/or $S\lambda$ spectra as an explanatory variable to those that were built with the raw, MSC, 1st and 2nd derivative absorbance spectra. Generally, better MC models were obtained using data acquired in the truncated wavelength range (800-1800 nm), whatever the type of input spectra.

As expected, the accuracy of the models based on K_λ spectra was much better than those based on S_λ spectra. For the full wavelength range (430-2380 nm), the best MC models were obtained using the K_λ spectra for both black spruce ($RMSE_{CV}$=2.10% and R^2=0.85) and quaking aspen samples ($RMSE_{CV}$=2.55% and R^2=0.80). However, the model built with MSC spectra was the best when both species are considered together with $RMSE_{CV}$ =2.20% and R^2=0.83, while the worst models were based on S_λ spectra, except for black spruce samples, which had an R^2 of 0.75 and an $RMSE_{CV}$ of 2.44%. For the truncated wavelength range (800-1800 nm), the best MC models were obtained with the raw spectra for black spruce ($RMSE_{CV}$=1.40% and R^2=0.94) and both species ($RMSE_{CV}$=1.23% and R^2=0.95) and MSC spectra for quaking aspen ($RMSE_{CV}$=1.09% and R^2=0.97).

Table 5-1: PLS models for moisture content (MC in % dry basis) prediction according to the species using K_λ and/or S_λ, raw absorbance, MSC, 1st and 2nd derivative spectra, in two different ranges of wavelengths (N = number of samples used in the model; LV = latent variables).

Species	Wavelength (nm)	Spectra	LV	Calibration		Cross Validation	
				$RMSE_C$ (%)	R^2_C	$RMSE_{CV}$ (%)	R^2_{CV}
Black spruce (N = 12)	430-2380	K	4	0.81	0.98	2.10	0.85
		S	5	0.65	0.99	2.44	0.75
		K& S	5	0.70	0.98	2.58	0.81
		Raw	2	1.75	0.90	2.67	0.72
		MSC	2	1.86	0.88	2.67	0.75
		1st derivative	2	1.77	0.89	2.64	0.71
		2nd derivative	4	0.72	0.98	3.30	0.33
	800-1800	K	3	1.44	0.93	3.61	0.72
		S	6	0.76	0.98	6.02	0.06
		K& S	7	0.47	0.99	4.95	0.59
		Raw	5	0.41	0.99	1.40	0.94
		MSC	3	1.11	0.96	1.97	0.87
		1st derivative	3	0.73	0.98	1.76	0.89
		2nd derivative	5	0.15	1.00	2.05	0.85
Quaking aspen (N = 12)	430-2380	K	4	1.23	0.95	2.55	0.80
		S	2	4.46	0.33	5.47	0.21
		K& S	6	0.58	0.99	3.32	0.74
		Raw	3	1.76	0.90	2.80	0.73
		MSC	2	2.06	0.86	2.66	0.73
		1st derivative	1	2.57	0.79	3.42	0.29
		2nd derivative	3	1.94	0.88	4.70	0.19
	800-1800	K	4	0.69	0.98	1.96	0.88
		S	3	3.64	0.55	5.73	0.16
		K& S	3	0.86	0.98	2.09	0.82
		Raw	3	1.30	0.95	2.25	0.83
		MSC	7	0.17	1.00	1.09	0.97
		1st derivative	5	0.26	1.00	1.51	0.92
		2nd derivative	3	0.89	0.97	1.98	0.85
Both species (N = 24)	430-2380	K	4	1.69	0.90	2.66	0.75
		S	4	3.15	0.66	4.44	0.20
		K& S	4	1.69	0.90	2.66	0.75
		Raw	3	1.92	0.88	2.43	0.78
		MSC	4	1.45	0.93	2.20	0.83
		1st derivative	2	2.20	0.84	2.70	0.69
		2nd derivative	2	2.43	0.81	3.12	0.51
	800-1800	K	3	1.51	0.92	2.32	0.83
		S	8	0.98	0.97	3.21	0.62
		K& S	9	0.63	0.99	2.43	0.84
		Raw	5	0.79	0.98	1.23	0.95
		MSC	3	1.28	0.95	1.67	0.90
		1st derivative	5	0.50	0.99	1.45	0.93
		2nd derivative	3	1.35	0.94	2.13	0.84

5.4.4. Other optical parameters

Several other optical parameters, such as the mean transport absorption coefficient, the reduced scattering coefficient, and the penetration depth, can be calculated from K_λ and S_λ, when the scattering is more dominant than the absorption. Such assumption is valid in our case since wood is considered as a turbid medium (Martelli, 2012) and since the amount of scattering observed in this study was 5 to 10 times greater than the amount of absorption (Figure 5-6). As shown in Figure 5-8, the transport absorption coefficient is lower and the two other parameters are higher for quaking aspen than black spruce. For both species, the penetration depth reaches its maximum (around 1 mm) between 800 and 1300 nm and decreases beyond 1300 nm to reach 0.2 mm after 1450 nm.

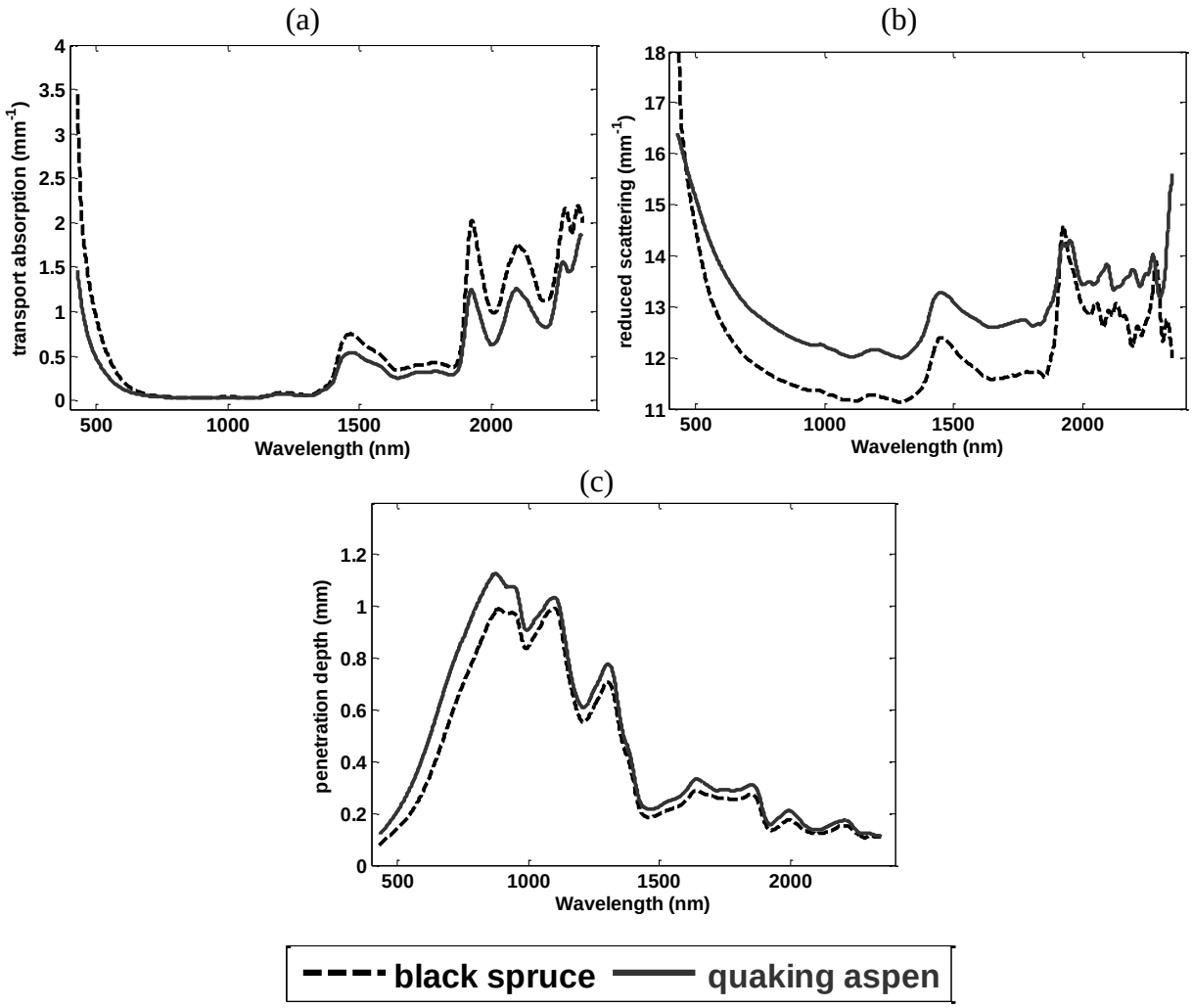

Figure 5-8: Effect of the species on the (a) transport absorption, (b) reduced scattering, and (c) penetration depth spectra derived from mean K_λ and S_λ spectra for black spruce and quaking aspen samples.

Similar to K_λ and S_λ, MC has an influence on the transport absorption coefficient (Figure 5-9), the reduced scattering coefficient (Figure 5-10), and the penetration depth (Figure 5-11). The transport absorption coefficient and the reduced scattering coefficient follow the same pattern as K_λ and S_λ, respectively (Figure 5-7). Both coefficients increase with the MC, but the reduced scattering coefficient has a highly more variable pattern beyond 1900 nm, with even a decrease with increasing MC. The penetration

depth decreases with increasing MC for quaking aspen samples, but for black spruce samples, the penetration depth is higher at 7% MC than at 3% and 16% MC, which both give similar values.

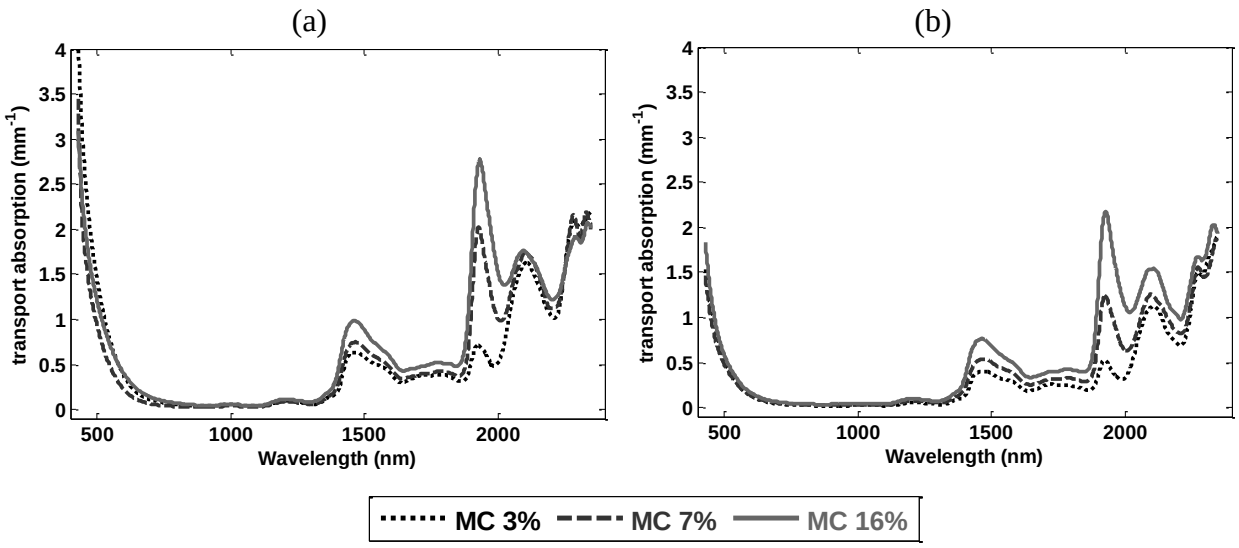

Figure 5-9: Effect of MC on the transport absorption spectra derived from mean K_λ and S_λ spectra for (a) black spruce and (b) quaking aspen samples.

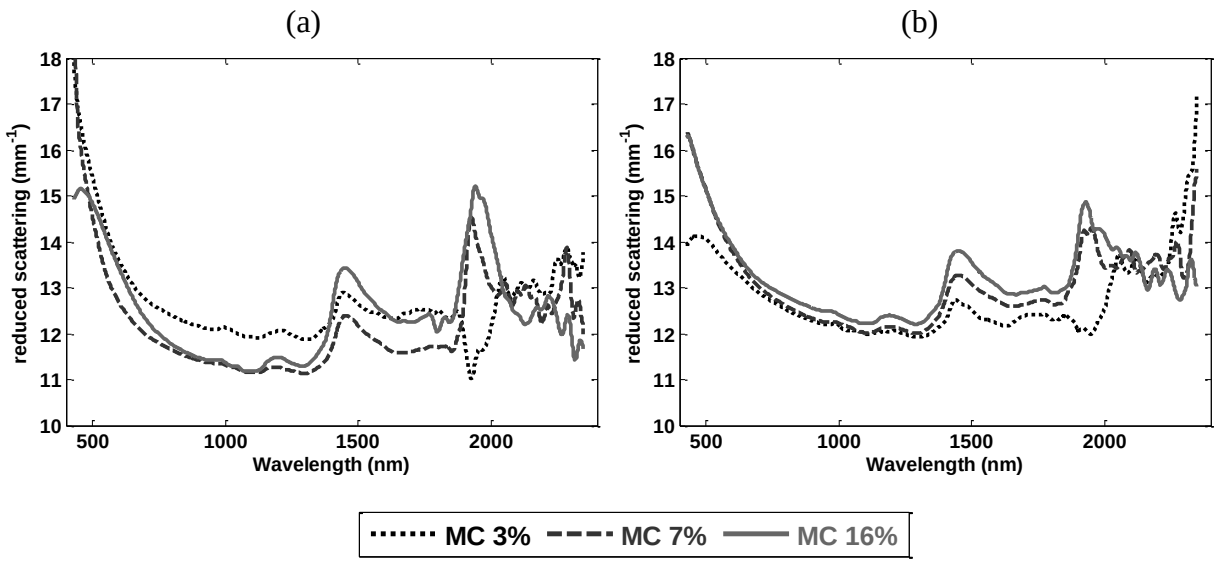

Figure 5-10: Effect of the MC on the reduced scattering spectra derived from mean K_λ and S_λ spectra for (a) black spruce and (b) quaking aspen samples.

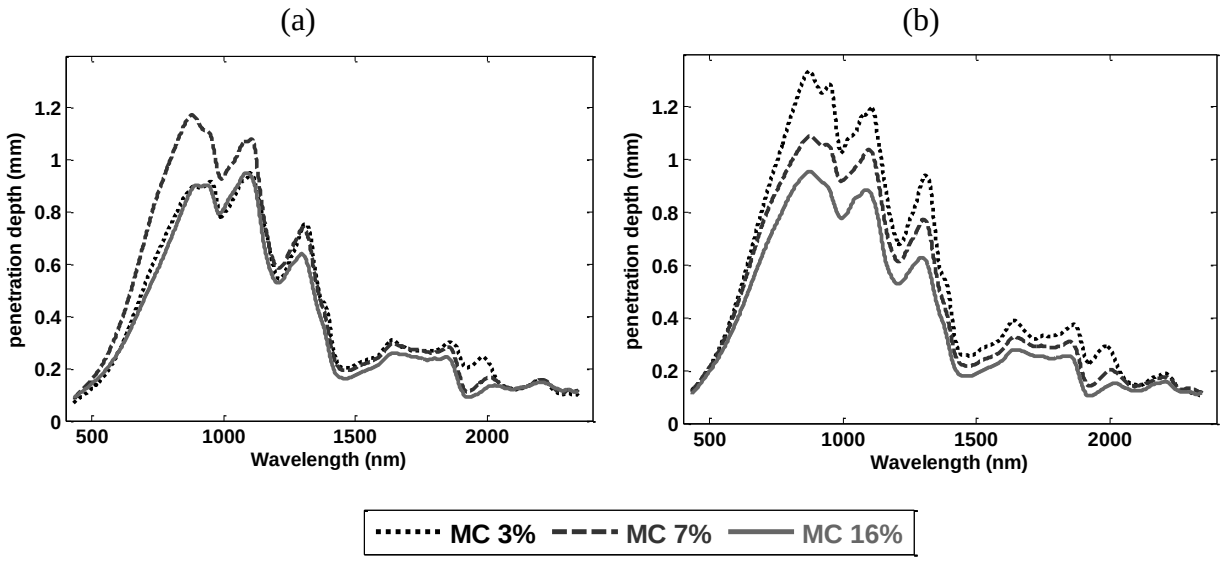

Figure 5-11: Effect of the MC of the penetration depth spectra derived from mean K_λ and S_λ spectra for (a) black spruce and (b) quaking aspen samples.

5.5. Discussion

5.5.1. VIS-NIR spectra

The comparison between black spruce and quaking aspen reflectance spectra in the visible spectral domain shows that the black spruce sample is a bit darker than the quaking aspen sample which can be due to the annual rings. Indeed, the transition from earlywood to latewood was more distinct in black spruce than in quaking aspen because the latewood in black spruce is denser and contains more lignin (Rowell, 2013). In the near-infrared spectral domain (from 750 to 1420 nm), the spectral difference between species is low, but increases to 7% above 1420 nm. In a previous study on the test of an NIR hyperspectral imaging system for estimating MC and basic specific gravity of frozen and thawed logs of the same species, Haddadi et al. (2015c) found small

difference between the absorbance spectra of both species in the region between 947 and 1637 nm.

Whatever the species, the reflectance increases with the sample thickness *d*, which leads to a decrease of the corresponding absorbance with the sample thickness, until a plateau occurs at a certain thickness. Similar absorbance trends were observed with thin samples of Sitka spruce having an MC of 6.7% (Tsuchikawa et al., 1996), but the range of absorbance variation in the black spruce and quaking aspen samples used in this study is almost half that observed in the Sitka spruce samples. One reason for this difference is that Tsuchikawa et al. (1996) collected diffuse reflectance spectra of the samples that were at a distance of 9 mm from the integrating sphere, while in this study, the spectra were collected without any offset from the integrating sphere. Additionally, Tsuchikawa et al. (1996) considered the effect of surface roughness on the resulting K_λ and S_λ spectra, while we did not consider this factor, because the surface roughness of our samples was considered to be constant as the samples were prepared using a microtome.

5.5.2. K and S spectra

Whatever the species, K_λ increases in the water absorption bands (997, 1438, and 1929 nm), in the cellulose and hemicellulose absorption bands (1212, 1471, 2112, 2291, and 2328 nm) and in the lignin absorption band (2267 nm) (Schwanninger et al., 2011). The K_λ spectra obtained from Sitka spruce samples by Tsuchikawa et al. (1996) were very similar to the ones obtained in this study with the black spruce samples. As mentioned earlier, the K_λ values for quaking aspen samples are very similar to the ones

of spruce samples below 1900 nm, but are systematically lower above 1900 nm (Figure 5-6). Such difference can be due to the difference in cell types between softwood (spruce) and hardwood (aspen) species (Panshin and De Zeeuw, 1980, Bowyer et al., 2007). Similarities between spruce samples and dissimilarities with the aspen samples show the power of K_λ spectra for differentiating anatomical differences between spruce and aspen wood.

The differences between S_λ spectra of our samples and those of Tsuchikawa et al. (1996) can be explained by the scattering phenomenon. In turbid media, the scattering of NIR radiation originates from two major different sources: the heterogeneity of the refractive index inside the medium and the effect of the particles dispersed inside the medium (Martelli, 2012). Indeed, scattering is due to a refractive index difference between the cell wall substances on one hand, and the water present in lumens and cells walls on the other hand. The scattering is also due to the air present in both the lumen as our samples have an MC lower than MC at FSP. Scattering depends also on the microphysical properties (size, shape and refractive index) of the particles composing the medium. Mie scattering occurs when the size of the particles is equal to, or greater than, the wavelength of the radiation (Jacques, 2013). This is the case for wood tracheids that have a diameter of 25-45 µm and a cell wall thickness of 2-8 µm, which are larger than the visible and NIR wavelengths. Higher S_λ for quaking aspen samples can be related to the high penetration depth of the radiation (Figure 5-8) leading to more scattering from the wood sample.

For both species, K_λ increases when MC increases for all the wavelengths between 1450 and 2350 nm. The highest increases are observed for the OH absorption bands (1450 and 1950 nm). According to the Lambert-Beer law, the absorption coefficient increases when the concentration increases (Equation 8). For non-scattering samples, the absorption coefficient has a linear relationship with the concentration and absorbing intensity (Dahm and Dahm, 1999). S_λ also increases with the MC, but the relationship is considerably variable beyond 1900 nm. In this range, a reduction of S_λ with MC was even observed, which could be due to changes in the refractive index. The pattern of S_λ at various MC levels can also be due to variations in density, which leads to a higher variation of S_λ in spruce than in aspen. Indeed, the density variation in black spruce is much higher than in quaking aspen because black spruce has a lower growth rate than quaking aspen (Barnett and Jeronimidis, 2003).

Our results show that the scattering is a function of wavelength. Burger et al. (1997) also found the dependency of scattering spectra to the wavelength. The absorption and scattering spectra were derived from diffuse reflectance and transmittance measurements acquired over pharmaceutical powders by applying a three-flux approximation of the radiative transfer equation for wavelengths between 1.4 and 3.0 µm. Thus, the scattering effects in spectra cannot be removed by a simple transformation e.g. MSC, because such transformation assumes that the scattering remains constant in all wavelengths.

5.5.3. MC modeling

The better performance of models based on K_λ and MSC absorbance spectra can be explained by the lack of interference with the scattering component. Indeed, the K_λ based models do not contain scattering information, while the MSC removes scattering from the spectra. Several other studies on the use of hyperspectral data for wood MC estimation already concluded that transformed spectra gave better MC models than raw spectra (Cooper et al., 2011, Mora et al., 2011a, Haddadi et al., 2015c). For both wavelength ranges and whatever the species, less accurate models were obtained with S_λ spectra, showing the poor relationship between scattering and MC. Moreover, when a combination of S_λ and K_λ spectra was used in the models, the accuracy increased mainly due to K_λ spectra. This can be explained by the fact that absorption bands in K_λ spectra contain chemical information about the sample, while S_λ spectra only explain light scattering.

5.5.4. Other optical parameters

The transport absorption spectra and the reduced scattering spectra have similar patterns to the K_λ and S_λ spectra, respectively. In particular, the reduced scattering coefficient does not vary with the wavelength below 1000 nm. D'Andrea et al. (2008) already showed on silver fir and sweet chestnut samples that the reduced scattering coefficient, derived from time-resolved techniques, does not vary with wavelengths in the 700-1040 nm range.

A more informative optical parameter is the penetration depth. We found that for our samples, the penetration depth of the visible and NIR radiation varies between 0.2 and 1.3 mm depending on the wavelength. In our case, the penetration depth gradually increases with the wavelength up to about 1000 nm. This is why the absorbance variation with sample thickness reaches a constant value at a higher thickness for short wavelengths than for long wavelengths (Figure 5-5). The penetration depth reaches its maximum of about 1.3 mm at 880 nm. Such penetration depth is lower than those computed for Sitka spruce (around 4 mm) (Tsuchikawa et al., 1996, Tsuchikawa et al., 2001). The local minimums in the penetration depth spectra correspond to the OH and CH absorption bands that occur at 990, 1200, 1450, 1925, and 2100 nm. A higher penetration depth in quaking aspen than in black spruce was observed and can be explained by the difference in wood density and anatomy. Indeed, density is higher for black spruce than for quaking aspen, therefore a higher concentration of compounds in black spruce increase the absorbance and decreases the penetration depth. Moreover, in contrast to quacking aspen, which is a hardwood species, black spruce is a softwood species, which does not contain any vessels that can favor deep radiation penetration (Panshin and De Zeeuw, 1980, Bowyer et al., 2007).

Different patterns of spruce penetration depth at different MC levels compare to the ones of aspen and can be related to the high variation of spruce density. In a growth ring, the density of earlywood and latewood in black spruce is 390 and 640 kg/m^3, respectively (Koubaa et al., 2002), while the range of density for aspen is between 300 and 400 kg.m^{-3} (Hogg et al., 2002).

5.6. Conclusions

Diffuse reflectance spectra measured with an integrating sphere in the 430-2380 nm region for thin samples of quaking aspen and black spruce were used to calculate K_λ and S_λ spectra using the Kubelka-Munk equations. The samples were conditioned at three MC levels (3%, 7%, and 16%). The K_λ and S_λ coefficients are influenced by the species and the MC of the samples and they both are wavelength-dependent.

K_λ and S_λ spectra were then used in a PLS modeling approach for estimating MC. The models were compared to those obtained by using raw and transformed spectra. Generally, better MC models were obtained using data acquired in the full wavelength range (430-2380 nm) with K_λ spectra, but for raw and transformed spectra, truncated spectra in the wavelength range 800-1800 nm was optimal. For the full wavelength range (430-2380 nm), the best MC model was obtained using the K_λ spectra for black spruce ($RMSE_{CV}$=2.10%, R^2=0.85) and quaking aspen ($RMSE_{CV}$ =2.55%, R^2=0.80), and with the MSC spectra for both species ($RMSE_{CV}$ =2.20%, R^2=0.83). For the truncated wavelength range (800-1800 nm), the best MC model was obtained with the raw absorbance spectra for black spruce ($RMSE_{CV}$ =1.40%, R^2=0.94) and both species ($RMSE_{CV}$ =1.23%, R^2=0.95) and MSC spectra for quaking aspen ($RMSE_{CV}$ =1.09%, R^2=0.97). The S_λ based models were poor, which can be explained by the fact that the S_λ spectra do not contain information about wood MC.

Whatever the species, the scattering coefficients S_λ were higher than the absorption coefficients K_λ. This allows the use of K_λ and S_λ to compute several other

optical parameters, such as the mean transport absorption coefficient, the reduced scattering coefficient, and the penetration depth. Black spruce samples have higher transport absorption coefficients, but lower reduced scattering coefficient than quaking aspen samples. For both species, the penetration depth reaches its maximum (around 1.3 mm) between 800 and 1300 nm, but beyond 1300 nm, it decreases and reaches 0.2 mm above 1450 nm. Therefore, extracting K_λ and S_λ from absorbance spectra is a powerful tool to derive other optical parameters that allow a better understanding of the behavior of visible and NIR radiation in wood.

While encouraging, these results are based on thin samples and more work is needed to develop a modeling approach that allows deriving these optical parameters from thick samples. Such a modeling approach should use the ratio between K_λ and S_λ as derived using the K-M theory equations, because this ratio can be used to derive the reflectance of an infinitely thick sample (Kortum, 1969, Geladi et al., 1985). The MC models were based on a limited number of samples. More reliable results can be expected if a higher number of samples are used. These models used the MC of the desiccators as reference MC values, but changes in the relative humidity of the room during the spectral measurements can have an effect on the MC of thin samples. Such influence should be taken into account in further experiments.

5.7. Acknowledgements

The authors thank D. McCarthy (UNB) for his help during the experiment. The study was supported by an NSERC Strategic grant and a New Brunswick Innovation

Foundation grant awarded to B. Leblon. This paper was written in memoriam of Dr. James Burger, who suddenly died on September 6th, 2014. We also thank the anonymous reviewers for their useful comments.

5.8. References

Adedipe O.E., Dawson-Andoh B., Slahor J. & Osborn L. (2008) Classification of red oak (*Quercus rubra*) and white oak (*Quercus alba*) wood using a near infrared spectrometer and soft independent modelling of class analogies. *Journal of Near Infrared Spectroscopy*, 16(1): 49-57. doi: 10.1255/Jnirs.760

ASTM-D4442–07 (2009) *Standard test methods for direct moisture content measurement of wood and wood-base materials*, ASTM International, West Conshohocken, PA, doi: 10.1520/D4442-07, www.astm.org.

Barnett J.R. & Jeronimidis G. (Eds) (2003) *Wood quality and its biological basis.* Oxford; Boca Raton, FL: CRC Press, 226 pages.

Birkett M.D. & Gambino M.J.T. (1989) Estimation of pulp kappa number with near-infrared spectroscopy. *Tappi Journal*, 72(9): 193-197

Bowyer J.L., Shmulsky R. & Haygreen J.G. (2007) *Forest products and wood science: An introduction.* Oxford, UK: John Wiley & Sons. 496 pages.

Burger J.E. (2006) *Hyperspectral NIR image analysis, data exploration, correction, and regression*. Doctoral Thesis, Swedish University of Agricultural Sciences, Arkitektkopia, Umeå, Sweden, 131 pages.

Burger T., Kuhn J., Caps R. & Fricke J. (1997) Quantitative determination of the scattering and absorption coefficients from diffuse reflectance and transmittance measurements: Application to pharmaceutical powders. *Applied Spectroscopy*, 51(3): 309-317. doi: 10.1366/0003702971940404

Burns D.A. & Ciurczak E.W. (Eds) (2007) *Handbook of near-infrared analysis.* Boca Raton, FL, USA: CRC Press, 808 pages.

Cheong W.F., Prahl S.A. & Welch A.J. (1990) A review of the optical-properties of biological tissues. *IEEE Journal of Quantum Electronics*, 26(12): 2166-2185. doi: 10.1109/3.64354

Cooper P.A., Jeremic D., Radivojevic S., Ung Y.T. & Leblon B. (2011) Potential of near-infrared spectroscopy to characterize wood products. *Canadian Journal of Forest Research*, 41(11): 2150-2157. doi: 10.1139/X11-088

D'Andrea C., Farina A., Comelli D., Pifferi A., Taroni P., Valentini G., Cubeddu R., Zoia L., Orlandi M. & Kienle A. (2008) Time-resolved optical spectroscopy of wood. *Applied Spectroscopy*, 62(5): 569-574

D'Andrea C., Nevin A., Farina A., Bassi A. & Cubeddu R. (2009) Assessment of variations in moisture content of wood using time-resolved diffuse optical spectroscopy. *Applied Optics*, 48(4): B87-B93

Dahm D.J. & Dahm K.D. (1999) Spectrographic analysis instrument and method based on discontinuum theory. In *googl.patent*,US5912730 A, Foss NIRSytems, Inc., Silver Spring, Md. USA

Dhanoa M., Lister S., Sanderson R. & Barnes R. (1994) The link between multiplicative scatter correction (msc) and standard normal variate (snv) transformations of NIR spectra. *Journal of Near Infrared Spectroscopy*, 2(1): 43-47. doi: 10.1255/jnirs.30

Fujimoto T., Kurata Y., Matsumoto K. & Tsuchikawa S. (2008) Application of near infrared spectroscopy for estimating wood mechanical properties of small clear

and full length lumber specimens. *Journal of Near Infrared Spectroscopy,* 16(6): 529-537. doi: 10.1255/Jnirs.813

Fujimoto T., Yamamoto H. & Tsuchikawa S. (2007) Estimation of wood stiffness and strength properties of hybrid larch by near-infrared spectroscopy. *Applied Spectroscopy,* 61(8): 882-888. doi: 10.1366/000370207781540150

Gautam B.K. & Henderson G. (2011) Relative humidity preference and survival of starved formosan subterranean termites (isoptera: Rhinotermitidae) at various temperature and relative humidity conditions. *Environmental Entomology,* 40(5): 1232-1238

Geladi P., Macdougall D. & Martens H. (1985) Linearization and scatter-correction for near infrared reflectance spectra of meat. *Applied Spectroscopy,* 39(3): 491-500

Gindl W., Teischinger A., Schwanninger M. & Hinterstoisser B. (2001) The relationship between near infrared spectra of radial wood surfaces and wood mechanical properties. *Journal of Near Infrared Spectroscopy,* 9(4): 255-261. doi: 10.1255/jnirs.311

Green B., Jones P.D., Schimleck L.R., Nicholas D.D. & Shmulsky R. (2010) Rapid assessment of southern pine decayed by g. Trabeum by near infrared spectra collected from the radial surface. *Wood and Fiber Science,* 42(4): 450-459

Haartveit E.Y. & Flæte P.O. (2008) Near infrared spectroscopy (NIRS) as a tool for effective classification of wood In *51st International Convention of Society of Wood Science and Technology,* (Concepción, Chile), pp. 1-9

Haddadi A., Burger J., Leblon B., Pirouz Z., Groves K. & Nader J. (2015a) Using near infrared hyperspectral images on subalpine fir board - part 1: Moisture content estimation. *Wood Material Science & Engineering,* 10(1): 27-40. doi: 10.1080/17480272.2014.965743

Haddadi A., Burger J., Leblon B., Pirouz Z., Groves K. & Nader J. (2015b) Using near infrared hyperspectral images on subalpine fir board - part 2: Density and basic specific gravity estimation. *Wood Material Science & Engineering,* 10(1): 41-56. doi: 10.1080/17480272.2015.1011231

Haddadi A., Leblon B., Nader J., Pirouz Z. & Groves K. (2015c) Prediction of wood properties for thawed and frozen logs of quaking aspen, balsam poplar, and black spruce from near-infrared hyperspectral images. *Wood Science and Technology,* doi: 10.1007/s00226-015-0767-z

Hans G., Kitamura R., Inagaki T., Leblon B. & Tsuchikawa S. (2014) Assessment of variations in air-dry wood density using time-of-flight near-infrared spectroscopy. *Wood Material Science & Engineering,* 10(1): 57-68. doi: 10.1080/17480272.2014.923937

Hans G., Leblon B., Cooper P., LaRocque A., Nader J. & Stirling R. (2015) Determination of moisture content and basic specific gravity of *Populus tremuloides* (Michx.) and *Populus balsamifera* (l.) logs using a portable near-infrared spectrometer. *Wood Material Science & Engineering,* 10(1): 3-16. doi: 10.1080/17480272.2014.916349

Hans G., Leblon B., Stirling R., Nader J., LaRocque A. & Cooper P. (2013) Monitoring of moisture content and basic specific gravity in black spruce logs using a handheld MEMS-based near-infrared spectrometer. *The Forestry Chronicle,* 89(5): 605-618. doi: 10.5558/tfc2013-112

Hapke B. (1993) *Theory of reflectance and emittance spectroscopy.* Cambridge, England; New York, USA: Cambridge University Press. 455 pp.

Hein P.R.G. (2012) Estimating shrinkage, microfibril angle and density of *eucalyptus* wood using near infrared spectroscopy. *Journal of Near Infrared Spectroscopy,* 20(4): 427-436. doi: 10.1255/jnirs. 1005

Hoffmeyer P. & Pedersen J.G. (1995) Evaluation of density and strength of Norway spruce wood by near infrared reflectance spectroscopy. *Holz als Roh- und Werkstoff,* 53(3): 165-170. doi: 10.1007/BF02716418

Hogg E.H., Hart M. & Lieffers V.J. (2002) White tree rings formed in trembling aspen saplings following experimental defoliation. *Canadian Journal of Forest Research-Revue Canadienne De Recherche Forestiere,* 32(11): 1929-1934

Inagaki T., Schwanninger M., Kato R., Kurata Y., Thanapase W., Puthson P. & Tsuchikawa S. (2012) *Eucalyptus camaldulensis* density and fiber length estimated by near-infrared spectroscopy. *Wood Science and Technology,* 46(1-3): 143-155. doi: 10.1007/s00226-010-0379-6

Jacques S.L. (2013) Optical properties of biological tissues: A review. *Physics in Medicine and Biology,* 58(11): R37-R61

Kelley S.S., Rials T.G., Snell R., Groom L.H. & Sluiter A. (2004) Use of near infrared spectroscopy to measure the chemical and mechanical properties of solid wood. *Wood Science and Technology,* 38(4): 257-276. doi: 10.1007/s00226-003-0213-5

Kortum G. (1969) *Reflectance spectroscopy principles, methods, applications.* Berlin-Heidelberg, Germany: Springer-Verlag. 366 pages.

Koubaa A., Zhang S.Y.T. & Makni S. (2002) Defining the transition from earlywood to latewood in black spruce based on intra-ring wood density profiles from X-ray densitometry. *Annals of Forest Science,* 59(5-6): 511-518. doi: 10.1051/forest:2002035

Kubelka P. (1948) New contributions to the optics of intensely light-scattering materials. Part i. *JOURNAL OF THE OPTICAL SOCIETY OF AMERICA,* 38(5): 448-457. doi: 10.1364/JOSA.38.000448

Kubelka P. (1954) New contributions to the optics of intensely light-scattering materials. Part ii: Nonhomogeneous layers. *JOURNAL OF THE OPTICAL SOCIETY OF AMERICA,* 44(4): 330-335. doi: 10.1364/JOSA.44.000330

Leblon B., Adedipe O., Hans G., Haddadi A., Tsuchikawa S., Burger J., Stirling R., Pirouz Z., Groves K., Nader J. & LaRocque A. (2013) A review of near-infrared spectroscopy for monitoring moisture content and density of solid wood. *Forestry Chronicle,* 89(5): 595-606. doi: 10.5558/tfc2013-111

Leonardi L. & Burns D.H. (1999) Quantitative measurements in scattering media: Photon time-of-flight analysis with analytical descriptors. *Applied Spectroscopy,* 53(6): 628-636

Lide D.R. (2004) *Crc handbook of chemistry and physics.* Taylor & Francis. 2712 pages.

Martelli F. (2012) An abc of near infrared photon migration in tissues: The diffusive regime of propagation. *Journal of Near Infrared Spectroscopy,* 20(1): 29-42

Meder R., Gallagher S., Kimberley M., Uprichard M. & Mackie K. (1994) Prediction of wood chip and pulp and paper properties via multivariate analysis of spectral

data, In *48th Appita Annual General Conference*, (Melbourne, Australia), pp. 479-484

Meder R., Marston D., Ebdon N. & Evans R. (2010) Spatially-resolved radial scanning of tree increment cores for near infrared prediction of microfibril angle and chemical composition. *Journal of Near Infrared Spectroscopy,* 18(6): 499-505. doi: 10.1255/Jnirs.903

Michell A.J. (1995) Pulpwood quality estimation by near-infrared spectroscopic measurements on eucalypt woods. *Appita Journal,* 48(6): 425-428

Michell A.J. & Schimleck L.R. (1998) Developing a method for the rapid assessment of pulp yield of plantation eucalypt trees beyond the year 2000. *Appita Journal,* 51(6): 428-432

Mora C.R., Schimleck L.R., Clark A. & Daniels R.F. (2011a) Determination of basic density and moisture content of merchantable loblolly pine logs by near infrared spectroscopy. *Journal of Near Infrared Spectroscopy,* 19(5): 391-399. doi: 10.1255/Jnirs.947

Mora C.R., Schimleck L.R., Yoon S.C. & Thai C.N. (2011b) Determination of basic density and moisture content of loblolly pine wood disks using a near infrared hyperspectral imaging system. *Journal of Near Infrared Spectroscopy,* 19(5): 401-409. doi: 10.1255/Jnirs.948

Olinger J.M. & Griffiths P.R. (1988) Quantitative effects of an absorbing matrix on near-infrared diffuse reflectance spectra. *Analytical Chemistry,* 60(21): 2427-2435

Orfanidis S.J. (1996) *Introduction to signal processing.* Prentice Hall. p.

Panshin A.J. & De Zeeuw C. (1980) *Textbook of wood technology: Structure, identification, uses, and properties of the commercial woods of the united states and Canada.* New York, USA: McGraw-Hill. 722 pages.

Rinnan A., van den Berg F. & Engelsen S.B. (2009) Review of the most common pre-processing techniques for near-infrared spectra. *Trac-Trends in Analytical Chemistry,* 28(10): 1201-1222

Rowell R.M. (2013) *Handbook of wood chemistry and wood composites.* Boca Raton, USA: CRC Press. 687 pages.

Roy A., Ramasubramaniam R. & Gaonkar H.A. (2012) Empirical relationship between kubelka–munk and radiative transfer coefficients for extracting optical parameters of tissues in diffusive and nondiffusive regimes. *Journal of Biomedical Optics,* 17(11): 115006-115006. doi: 10.1117/1.JBO.17.11.115006

Russ A., Fiserova M. & Gigac J. (2009) Preliminary study of wood species identification by NIR spectroscopy. *Wood Research,* 54(4): 23-32

Schimleck L.R. & Evans R. (2003) Estimation of air-dry density of increment cores by near infrared spectroscopy. *Appita Journal,* 56(4): 312-317

Schimleck L.R., Evans R. & Ilic J. (2001) Estimation of *eucalyptus* delegatensis wood properties by near infrared spectroscopy. *Canadian Journal of Forest Research,* 31(10): 1671-1675. doi: 10.1139/cjfr-31-10-1671

Schimleck L.R., Evans R., Ilic J. & Matheson A.C. (2002a) Estimation of wood stiffness of increment cores by near-infrared spectroscopy. *Canadian Journal of Forest Research,* 32(1): 129-135. doi: 10.1139/X01-176

Schimleck L.R., Evans R. & Matheson A.C. (2002b) Estimation of *Pinus radiata* d. Don clear wood properties by near-infrared spectroscopy. *Journal of Wood Science,* 48(2): 132-137. doi: 10.1007/Bf00767290

Schimleck L.R., Jones P.D., Clark A., Daniels R.F. & Peter G.F. (2005) Near infrared spectroscopy for the nondestructive estimation of clear wood properties of *Pinus taeda* l. From the southern united states. *Forest Products Journal,* 55(12): 21-28

Schimleck L.R., Rezende G.D.S.R., Demuner B.J. & Downes G.M. (2006) Estimation of whole-tree wood quality traits using near infrared spectra from increment cores. *Appita Journal,* 59(3): 231-236

Schwanninger M., Rodrigues J.C. & Fackler K. (2011) A review of band assignments in near infrared spectra of wood and wood components. *Journal of Near Infrared Spectroscopy,* 19(5): 287-308. doi: 10.1255/Jnirs.955

Shi Z.Q. & Anderson C.A. (2009) Scattering orthogonalization of near-infrared spectra for analysis of pharmaceutical tablets. *Analytical Chemistry,* 81(4): 1389-1396. doi: 10.1021/ac802105v

Shi Z.Q. & Anderson C.A. (2010) Pharmaceutical applications of separation of absorption and scattering in near-infrared spectroscopy (NIRS). *Journal of Pharmaceutical Sciences,* 99(12): 4766-4783. doi: 10.1002/Jps.22228

So C.L., Via B.K., Groom L.H., Schimleck L.R., Shupe T.F., Kelley S.S. & Rials T.G. (2004) Near infrared spectroscopy in the forest products industry. *Forest Products Journal,* 54(3): 6-16

Sterenborg H.J.C.M., van Gemert M.J.C., Kamphorst W., Wolbers J.G. & Hogervorst W. (1989) The spectral dependence of the optical properties of human brain. *Lasers in Medical Science,* 4(4): 221-227. doi: 10.1007/BF02032451

Stirling R., Trung T., Breuil C. & Bicho P. (2007) Predicting wood decay and density using NIR spectroscopy. *Wood and Fiber Science,* 39(3): 414-423

Thygesen L.G. (1994) Determination of dry matter content and basic density of Norway spruce by near infrared reflectance and transmittance spectroscopy. *Journal of Near Infrared Spectroscopy,* 2: 127–135. doi: 10.1255/jnirs.39

Thygesen L.G. & Lundqvist S.O. (2000) Nir measurement of moisture content in wood under unstable temperature conditions. Part 2. Handling temperature fluctuations. *Journal of Near Infrared Spectroscopy,* 8(3): 191-199. doi: 10.1255/jnirs.278

Tsuchikawa S., Hayashi K. & Tsutsumi S. (1996) Nondestructive measurement of the subsurface structure of biological material having cellular structure by using near-infrared spectroscopy. *Applied Spectroscopy,* 50(9): 1117-1124. doi: 10.1366/0003702963905114

Tsuchikawa S., Inoue K., Noma J. & Hayashi K. (2003) Application of near-infrared spectroscopy to wood discrimination. *Journal of Wood Science,* 49(1): 29-35. doi: 10.1007/s100860300005

Tsuchikawa S., Torii M. & Tsutsumi S. (2001) Directional characteristics of near infrared light reflected from wood. *Holzforschung,* 55(5): 534-540. doi: 10.1515/HF.2001.086

van Gemert M.J.C. & Star W.M. (1987) Relations between the Kubelka-Munk and the transport equation models for anisotropic scattering. *Laser Life Sci,* 1: 287-298

Via B.K., Shupe T.F., Groom L.H., Stine M. & So C.L. (2003) Multivariate modelling of density, strength and stiffness from near infrared spectra for mature, juvenile and pith wood of Longleaf pine (*Pinus palustris*). *Journal of Near Infrared Spectroscopy,* 11(5): 365-378

Wallbacks A., Edlund U., Norden B., Iversen T. & Mohlin U.B. (1991) Multivariate characterization of pulp part 2. Interpretation and prediction of beating processes. *Nordic Pulp and Paper Research Journal,* 3(6): 104-109

Watanabe K., Mansfield S.D. & Avramidis S. (2011) Application of near-infrared spectroscopy for moisture-based sorting of green hem-fir timber. *Journal of Wood Science,* 57(4): 288-294. doi: DOI 10.1007/s10086-011-1181-2

Welch A.J. & van Gemert M.J.C. (2011) *Optical-thermal response of laser-irradiated tissue.* Dordrecht, Heidelberg, Germany; London, UK; New York, USA: Springer. 972 pages.

Xu Q.H., Qin M.H., Ni Y.H., Defo M., Dalpke B. & Sherson G. (2011) Predictions of wood density and module of elasticity of balsam fir (*Abies balsamea*) and black spruce (*Picea mariana*) from near infrared spectral analyses. *Canadian Journal of Forest Research,* 41(2): 352-358. doi: 10.1139/X10-215

Chapter 6. Conclusions

Moisture content (MC) and basic specific gravity (BSG) are two major wood properties that should be monitored on the production chain for to maximize product quality. This work presented an assessment of an NIR hyperspectral imaging system, *Specim* (*Spectral Imaging Ltd., FIN–90571 Oulu, Finland*) for estimating MC and BSG of subalpine fir boards and of frozen and thawed logs of three species (balsam poplar, quaking aspen and black spruce). Wood optical properties were also determined based on NIR spectra collected with a portable *ASD FieldSpec Pro FR* spectroradiometer (*Analytical Spectral Devices, Inc., Boulder, CO 80301 USA*) equipped with an integrating sphere *1800-12 LI-COR (LI-COR Inc., Lincoln, NE, USA)*. The technical details of both the spectroradiometer and the integrating sphere are presented in appendix A.

Board samples were subjected to several drying steps, until completely dried. Hyperspectral images and weight measurements were acquired over each sample at each drying step. The images were taken over the radial section of the samples as well as over the whole board. Log samples were subjected to several freezing steps as well as several drying steps until samples were completely dried. Hyperspectral images and weight measurements were recorded at each drying and freezing step. The images were taken over the transversal section on both the thawed and frozen log samples as well as over the whole disks. For both the logs and the boards. MC of each sample was estimated at each drying step and BSG was estimated at the end of the experiment.

Because the NIR hyperspectral spectra extracted from the images were not as clean as the spectra collected by an NIR spectroradiometer, they needed to pass through an image processing method that included the following main steps: image calibration by converting the image digital numbers into reflectances, recovering bad pixels, and removing abnormal spectra.

In other studies these image processing steps were limited to the image calibration and finding the regions of interest which have no abnormal pixels. Such findings are done using a threshold (Thumm et al., 2010) or manually (Mora et al., 2011). In our case, the bad pixels were recovered automatically using a median filter. Additionally, we developed a novel approach that combines a PCA algorithm with a boxplot method of Laurrikala et al. (2000) to remove abnormal spectra from the whole datasets.

The corrected spectra were then used as explanatory variables in PLS models. The raw spectra were subjected to several additional spectral transformations, such as the multiplicative scatter correction (MSC), the 1st, or the 2nd derivative. Hyperspectral images are able to provide one spectrum per pixel for each sample. Two different methods to select the most representative spectrum for each sample were tested: 1) median spectra, 2) 100 spectra for each image. The results showed that the sampling method based on the median spectra provided slightly a better accuracy and it is why this method was used in the PLS modeling. Table 6-1 summarizes the best model for each property (MC or BSG) as a function of the species, the type of wood sample, and the transformation applied to the spectra.

From Table 6-1, we can see that the models predict wood MC with an error that varies between 2.94% in the case of black spruce logs to 15.49% in the case of balsam poplar logs. The BSG estimation is better when several species are used together. The model has an R^2 of 0.88 and an RMSE of 0.036.

PLS-DA models were also developed to sort log samples according to their MC, BSG, species, or log state (frozen/thawed). The model overall accuracy for both MC and BSG sorting were above 72%. Species and log state sorting has an overall accuracy of 86% and 97%, respectively.

Table 6-1: Best PLS models obtained in this thesis.

Property	**Wood type**	**Species**	**Transformation**	**Number of LVs**	**RMSE**	**R^2**	**N**
MC	Board	Subalpine fir	None	6	10.85%	0.85	276
	Log*	Black spruce	MSC	8	2.94%	0.82	326
		Quaking aspen	MSC	6	7.99%	0.75	409
		Balsam poplar	MSC	4	15.49%	0.69	522
BSG	Board	Subalpine fir	None	9	0.007	0.53	26
	Log*	Black spruce	None	6	0.035	0.72	23
		Quaking aspen	None	6	0.022	0.66	26
		Balsam poplar	None	7	0.048	0.57	33
		General model**	None	11	0.036	0.88	28

** Frozen and thawed samples; ** including the three species: black spruce, balsam poplar, and quaking aspen*

Our study showed that it is possible to use hyperspectral NIR images to estimate MC, BSG, and/or sort wood as a function of MC, BSG, species, or log state using a fast image processing method. Such method can be applied at-line to estimate MC and BSG distributions over boards and logs and sorting them. Such information is critical for increasing the efficiency kiln-drying operations in sawmills, cutting process, and

improving board and log grading. Further studies are needed to test such images in other at-line applications, such as detecting the location of knots, decays, wet-pockets, and other defects.

The images were acquired by a camera with a field of view of 17.5° that was positioned at 48 cm height. A higher quality of spectra at a fine spatial resolution should be achieved using a camera with a wide field of view, because the environment interference on the spectra is reduced as the distance between the camera and the target decreases. It will be expected that the resulting PLS model accuracy will increase.

Our study tested the use of NIR hyperspectral images over log disks at normal (21ºC) and frozen (-15ºC) temperatures, but there is the need to investigate further the temperature effect on NIR spectra and thus on MC and BSG estimation, particularly with spectra acquired around 0°C which is a critical temperature, where the structure of water molecules changes.

Furthermore, there are some fundamental issues that need to be solved before the use of NIR-HSI sensors can be operational. Image acquisitions of the samples are the main challenge, because the speed of the production chain is much faster than the image acquisition. Another issue is related to spectral influences of the environment, for example, those related to the incoming radiation, on the illumination and viewing geometries. Also, our results showed that the estimation accuracy is suitable for some species (black spruce), but needs improvements for species with high MC, such as balsam poplar.

Such as in most of previous studies on MC and BSG estimation using NIR hyperspectral images, our study used mainly PLS modeling, which is empirical. In an attempt to develop a more physical based method that is less empirical, we used the Kubelka-Munk theory equations for calculating the absorption and scattering coefficient spectra from reflectance spectra acquired over thin samples from quaking aspen and black spruce and then related these coefficient spectra to MC using a PLS modeling approach. The models were compared to those obtained by applying PLS models to raw and transformed absorbance spectra. The best MC models were obtained using the absorption coefficient spectra in the full wavelength range (430-2380 nm), but using raw and MSC spectra the best model achieved in the NIR wavelength range (800-1800 nm). Better models were obtained with the NIR wavelength range (800-1800 nm) than with the full wavelength range and for quaking aspen ($RMSE_{CV}$=1.09%, R^2=0.97) than for black spruce ($RMSE_{CV}$=1.40%, R^2=0.94). As expected, the worst models were based on the scattering coefficient spectra, as these spectra are not related to water absorption bands.

The scattering coefficients were much higher than the absorption coefficients, which means the scattering is dominant for wood in the NIR range. This allows the computing of several other optical properties, such as the mean transport absorption coefficient, the reduced scattering coefficient, and the penetration depth, in order to better characterize the path of visible and NIR radiation in wood. For both species, the penetration depth reaches its maximum (of about 1 mm) between 800 and 1300 nm, but beyond 1300 nm, it decreases dramatically and reaches 0.2 mm after 1450 nm. Our results obtained with the Kubelka-Munk theory equations were in agreement with other

similar studies (Tsuchikawa et al. 1996), but the study was based on a limited number of samples. More reliable results can be expected if a higher number of samples is used. Our results were also collected over thin samples, and further studies are needed to develop such method over thick samples, in order that it can be applied for MC estimation at-line.

Appendix A. Technical details of the sensors

Spectral camera (Specim)

Optical characteristics	
Spectrograph	ImSpector N17E
Spectral range	900 - 1700 nm ±10nm
Spectral resolution	5 nm (30 µm slit)
Spectral sampling / pixel	4nm
Spatial resolution	rms spot radius < 15 µm
Aberrations	Insignificant astigmatism Smile < 5µm (0.066%) Keystone < 5µm (0.035%)
Numerical aperture	F/2.0
Slit width options	30 µm (18, 50, 80 µm optional)
Slit length	14.3 mm
Effective slit length	9.6 nm
Total efficiency (typical)	> 50%, independent of polarization
Stray light	< 0.5 % (halogen lamp, 1400 nm notch filter)
Optical Input	Telecentric

Electrical characteristics	
Sensor	TE-cooled InGaAs photodiode array
Pixels in image frame	320 x 256
Active pixels	320 (spatial) x 240 (spectral)
Pixel size	30 x 30 µm
Cooling	Forced convection cooling
Camera output	12-bit, CameraLink
Frame rate	50 fps
Exposure time range	1 µs – 500 ms
Power consumption	< 30 W
Input voltage	12 V

Mechanical characteristics	
Size (W x H x L)	60 x 60 x 220 mm
Weight	1500 g
Lens Mount	Standard C-mount
Camera Mount	Standard C-mount or U-mount
User Adjustments	Image axis rotation relative to detector rows, back focal length adjustable ±1 mm

Environmental characteristics	
Storage	-20 ... +85°C
Operating	+5 … +40°C, non-condensing

FieldSpectroPro ASD

Optical characteristics	
Detectors	**VNIR**: 512 element silicon photo-diode array for the spectral region 350 to 1000 nm. **SWIR 1**: graded index, TE-cooled, extended range, InGaAs, photo-diode for the spectral region 1001 nm to 1800 nm. **SWIR 2**: graded index, TE-cooled, extended range, InGaAs, photo-diode for the spectral region 1801 nm to 2500 nm.
Spectral range	350-2500 nm
Spectral resolution	**VNIR:** 3 nm **SWIR 1:** 10 nm **SWIR 2:** 12 nm
Spectral sampling	1.4 nm for the spectral region 350-1000 nm. 2.0 nm for the spectral region 1001-2500 nm.
Radiometric resolution	16-bit
Time acquisition of a spectrum	VNIR: 8.5 ms SWIR1/2: 200 ms
FOV	25º

Electrical characteristics	
Battery	Type NiMH (Nickel-Metal Hydride) Rating 12 V 9 amp hour Life Over four hours using a contact probe in an ambient environment.
Power input	AC input 90-240 VAC, 50/60 Hz DC input +12 VDC, 60 W

Mechanical characteristics	
Size (W x H x L)	368 x 127 x 292 mm
Weight	5.44 kg

Environmental characteristics	
Storage	-15 ... +45°C
Operating	0 … +40°C, non-condensing

Appendix B. MATLAB codes

Defining bad pixels

```
% find the bad value in NIR spectra
% B_raw: black raw
% B_ref: black reflectance
% W_ref: white reflectance
% W_raw: white raw
%
%
% written by: Ataollah Haddadi-G.
% 01/2013
%
function badP = detect_badP_V1(B_raw, B_ref, W_raw, W_ref)
[s1 s2 s3] = size(B_raw);

%% raw b
Mb = squeeze(median(B_raw, 1));
Sb = squeeze(std(B_raw, 1));
Mmb = mean(Mb); Mmb2 = mean(Mb,2);

SDb = abs((Mb./repmat(Mmb2,1,s3)) - 1);
ind1 = (SDb>1);

Mw = squeeze(median(W_raw, 1));
Sw = squeeze(std(W_raw, 1));

%% reflectance B
Mb_r = squeeze(median(B_ref, 1));
Sb_r = squeeze(std(B_ref, 1));  % std

P0 = zeros(size(Mb_r));
dw = abs(P0-Mb_r);
ind2 = (abs(dw)>3);

%% raw white
% finding zero value W
ind0 = zeros(s2,s3);
ind4095=ind0;
for i=1:s1
    w_l = squeeze(W_raw(i,:,:));

    ind0    = ind0 + (w_l==0);
    ind4095 = ind4095 + (w_l==4095);
end
ind0    = (ind0>0);
ind4095 = (ind4095>0);

%% reflectance W
Mw_r = squeeze(median(W_ref, 1)); % medians
Sw_r = squeeze(std(W_ref, 1));  % std

P100 = ones(size(Mw_r))*100;
```

```
dw = P100./Mw_r;
dw = abs(dw-1);
ind3 = (abs(dw)>0.03);

IND = ind0+ ind1+ind2+ind3+ind4095;
badP = IND>0;

th4S = 3;
% all line of white image
for i=1:s1
    Mw_r = squeeze(W_ref(i,:,:));
    dw = abs(P100-Mw_r); % calculate differences
    dw = abs(dw - repmat(median(dw),s2,1));
    indl = (dw > (th4S*Sw_r));  % ind= dw>nS
    IND = IND + indl;
end
badP = IND>0;

% all line of black image
for i=1:s1
    Mb_r = squeeze(B_ref(i,:,:));
    dw = abs(P0-Mb_r);
    dw = abs(dw - repmat(median(dw),s2,1));
    indl = (dw > (th4S*Sb_r));
    IND = IND + indl;
end
badP = IND>0;
```

Recovering bad pixels

```
% using median for recovering the bad pixels
function Icr = recoverBadPix(I, badP)

[s1 s2 s3] = size(I);
badp = reshape(badP',1,s2*s3);
load('Wavelengths.mat')
for i=1:s1
    I0 = squeeze(I(i,:,:));
    %I0 = I0';

    % I1 = reshape(I0, 1, s2*s3); % the data

    m2 = medfilt2(I0,[3 3], 'symmetric');
    I2 = I0;
    % I2(badp) = m2(badp);% corected data
    I2(badP) = m2(badP);% corected data

    m2 = medfilt2(I2,[1 3], 'symmetric');
    % I2 = I0;
    I2(badP) = m2(badP);% corected data
    I3=I2;

    Icr(i,:,:)=I3;

end
```

Detection of abnormal spectra

```
% remove abnormal spectra based on Box_plot
% M is a 2D matrix (band - observation)

function [M outall]= Remove_outliers_ataV1(M)

n = size(M,2);
[COEFF V L] = princomp(M');

MV = mean(V(:,[1 2]) );
IDX = knnsearch(V(:, [1 2]), MV, 'k',10);
X = mahal(V(:, [1 2]), V(IDX, [1 2])); % Mahalanobis

firstind = 1;
xSorted1group = sort(X);

i25 = firstind+ .30*(n-firstind);
i50 = firstind+ .50*(n-firstind);
i75 = firstind+ .70*(n-firstind);

p25Ratio = i25-floor(i25);
if p25Ratio==0
    p25 = xSorted1group(i25);
else
    p25 = xSorted1group(floor(i25))*(1-p25Ratio) ...
        +xSorted1group(ceil(i25))*p25Ratio;
end

p50Ratio = i50-floor(i50);
if p50Ratio==0
    p50 = xSorted1group(i50);
else
    p50 = xSorted1group(floor(i50))*(1-p50Ratio) ...
        +xSorted1group(ceil(i50))*p50Ratio;
end

p75Ratio = i75-floor(i75);
if p75Ratio==0
    p75 = xSorted1group(i75);
else
    p75 = xSorted1group(floor(i75))*(1-p75Ratio) ...
        +xSorted1group(ceil(i75))*p75Ratio;
end

whisker=1.2;
% Calculate whisker endpoints.
maxw = p75+whisker*(p75-p25);
minw = p25-whisker*(p75-p25);

whi = find(xSorted1group<=maxw,1,'last');
wlo = find(xSorted1group>=minw,1,'first');
% wlo = min(wlo,p25);

wlo = xSorted1group(wlo);
whi=xSorted1group(whi);
```

```
q1 = p25;
q2= p50;
q3= p75;

outall = (X>whi);
M = M(:,outall==0);
```

PLS

```
% X: explanatory variable  n*p
% Y: responce variabkle    n*1
% LV: number of latent variable
%
% Xl/p: X block factor loadings
% Yl/q: Y block factor loadings
% Xs/t: X block factor weights
% Ys/u: Y block factor weights
% R: X block factor weights
% B: regression coefficients
%
function [Xl,Yl,Xs, Ys, R, B, h, varX, varY] =
simpls_Jong(X,Y, LV)

[n, nw] = size(X);

mX = mean(X);
mY = mean(Y);
X0 = X - repmat(mX, n, 1);
Y0 = Y - mY;         % center Y
V = zeros(nw, LV);
S = X0'*Y0;           % cross-product
for i = 1:LV
    [q, ~] = svd(S);   % Singular value decomposition
    r = q(:,1);      % X block factor weights
    t = X0*r;        % X block factor scores

    normt = norm(t);
    t = t./normt;
    Xl(:,i) = X0'*t;     % X block factor loadings

    q = Y0'*t;           % Y block factor loadings
    Yl(:,i) = q;

    Xs(:,i) = t;
    Ys(:,i) = Y0*Y0'*t;
    R(:,i) = r./normt;

    v = Xl(:,i);
    v = v - V*(V'*v);
    v = v./norm(v);
    V(:,i) = v;  % update V

    S = S - V*(V'*S);   % update S
end
```

```
B = R*Yl';
B = [mY - mX*B; B]; % coefficients

h = diag(Xs*Xs') + 1/n;
varX = diag(Xl'*Xl)/(n-1);     % variance explained for X
variables
varY = diag(Yl'*Yl)/(n-1);     % variance explained for Y
variables
```

Appendix C. Letter of permission from the journals

Wood Material Science & Engineering

from: Academic Journals SWOO Production <swoo-production@tandf.co.uk>
to: Ata Haddadi Goyaghaj <ata.haddadi@unb.ca>
date: Fri, Sep 25, 2015 at 6:08 AM
subject: RE: Permission letters for my published papers

Dear Haddadi,

Thank you for checking this with me.
There is no need to specifically ask for permission to use own articles in thesis or dissertations, this is already covered for in the Journal Author Publishing Agreements that you have signed with us. Please see sentence below which is included in the agreement under "Rights retained by you as the author":
"The right to include the article in a thesis or dissertation that is not to be published commercially, provided that acknowledgement to prior publication in the Journal is given."
Please do let me know if you have any further queries.

Best wishes,
Gayatri

Wood Science and Technology

from: ata haddadi <ata.haddadi@unb.ca>
to: Springer <springeralerts@springeronline.com>
date: Tue, Nov 3, 2015 at 12:35 AM
subject: Permission letters for my published paper

To whom it may concern,

I am a PhD student in the University of New Brunswick and I would like to deliver my PhD thesis in paper based format.

I am writing to get the permission of my published paper in the journal of "Wood Science and Technology".

I appreciate if you send me a letter for my following published paper in this journal:

http://link.springer.com/article/10.1007/s00226-015-0767-z

Thank you very much for your attention.

Regards,

Ata Haddadi

Journal of Near Infrared Spectroscopy

from: ata haddadi <ata.haddadi@unb.ca>
to: Sara Green <sara@impublications.com>
date: Tue, Nov 3, 2015 at 12:45 AM
subject: Permission letters for my published paper

Dear Sara Green,
I am a PhD student in the University of New Brunswick and I would like to deliver my PhD thesis in paper based format.

I am writing to get the permission of my published paper in the journal of "Journal of Near Infrared Spectroscopy".

I appreciate if you send me a letter for my following published paper in this journal:

Haddadi A, Hans G, Leblon B, Pirouz Z, Tsuchikawa S, Nader J, and Groves K. 2015. Determination of optical parameters and moisture content of wood with visible-NIR spectroscopy. doi: 10.1255/jnirs.1174

Thank you very much for your attention.

Regards,

Ata Haddadi

Appendix D. Curriculum Vitae

PROFESSIONAL PROFILE

- Proficient in Near Infrared Spectroscopy and Hyperspectral Imaging.
- Proficient in geospatial data analysis.
- Proficient in Chemometrics statistical analysis including: PCA, PLS, PLS-DA, Genetic algorithm, and ANN.
- Proficient in ArcGIS, ENVI, eCognition, ERDAS, and PCI Geomatics software.
- Proficient in programming Languages of MATLAB, and familiar with C# and IDL.
- Proficient in Autodesk Land Desktop, and Civil 3D surveying software.
- Proficient in Photoshop CS, Microsoft word, Excel, PowerPoint, Publisher, and Access.

EDUCATION

PhD in Forestry and Environmental Management, University of New Brunswick, Canada. **Feb 2012 – Jan 2016**

Diploma in University Teaching, University of New Brunswick. **Jun 2014 – Sept 2014**

MSc in Remote Sensing Engineering, Faculty of Geodesy & Geomatics Engineering, K.N. Toosi University of Technology, Tehran, Iran. **Sept 2006 – Dec 2009**

BSc in Geomatics & Surveying Engineering, Faculty of Engineering, Isfahan University, Iran. **Sept 2002 – Aug 2006**

\WORK & RESEARCH EXPERIENCE

Research Assistant, University of New Brunswick **Feb 2012 – May 2015**

- In this post I have employed a near-infrared hyperspectral imaging system and a near-infrared spectroscopy on wood products. This was to quantify moisture content and density of wood samples, as well as species identification.

Remote Sensing and GIS Technician, MahanGostar Co, Shiraz, Iran **Dec 2009 – Jan 2012**

- In this post I collected and analyzed geospatial data for urban development in different scales such as detailed plans and regional plans of *Hamadan* and *Kermanshah* Provinces in Iran.

Research Assistant, K.N.Toosi University of Technology, Tehran, Iran **Feb 2007 – Sept 2009**

- In this post I was involved with spatial data infrastructure (SDI) projects for the urban development in Iran. The aim of this project was to define a well suited standard for representing geospatial data. I was mainly responsible for all features of *national maps*, and *all maps of Zagros region*. Each map was described and its cartography was well defined.

Geomatics Engineer, MahanGostar Co, Shiraz, Iran **Aug 2006 – Jan 2007**

- In this post I used total station and level instruments to collect the position of the features such as parcels, man-made or natural boundaries. I was also responsible for production and cartography of the maps.

Additional Research Assistant in:

Remote Sensing and GIS Expert for Research, Development and Technology Affairs of K.N. Toosi University of Technology, **GIS study plan and database implementation of urban planning project** **2008 – 2009**

Remote Sensing and GIS Expert for Research, Remote sensing and GIS center of Tehran University, **Domestic and Regional Dust Storm Sources Identification and Offering the Ways for Restraining and Controlling project** **2009**

Remote Sensing Expert for Research, Development and Technology Affairs of K. N. Toosi University of Technology, **Radiometric Calibration of SAR images project** and **Selection of the Best Parameter of SAR Sensor Designing Appropriated for Iran project** **2007**

RESEARCH INTERESTS

- Remote sensing and image processing
- Geospatial data analysis
- Classification and quantification analysis

PEER-REVIEWED PUBLICATIONS

Haddadi A., Burger J., Leblon B., Pirouz Z., Groves K. & Nader J. (2015a) Using near infrared hyperspectral images on subalpine fir board. Part 1: Moisture content estimation. *Wood Material Science & Engineering*. doi: 10.1080/17480272.2014.965743.

Haddadi A., Burger J., Leblon B., Pirouz Z., Groves K. & Nader J. (2015b) Using near infrared hyperspectral images on subalpine fir board. Part 2: Density and Basic Specific Gravity Estimation *Wood Material Science & Engineering*. doi: 10.1080/17480272.2015.1011231.

Haddadi A., Leblon B., Nader J., Pirouz Z. & Groves K. (2015c) Prediction of Wood Properties for Thawed and Frozen Logs of Quaking Aspen, Balsam Poplar, and Black Spruce from Near-infrared Hyperspectral Images. *Wood Science and Technology*, doi: 10.1007/s00226-015-0767-z.

Haddadi A., Leblon B., Nader J., Pirouz Z. & Groves K. (2015d) Optical properties of wood and their relationship to moisture content. *Journal of Near Infrared Spectroscopy*, doi: 10.1255/jnirs.1174.

Leblon B., Adedipe O., Hans G., Haddadi A., Tsuchikawa S., Burger J., Stirling R., Pirouz Z., Groves K., Nader J. & LaRocque A. (2013) A review of near-infrared spectroscopy for monitoring moisture content and density of solid wood. *Forestry Chronicle*, 89(5): 595-606. doi: 10.5558/tfc2013-111.

Shahsavarhaghighi S., Sahebi M.R., Valdanzoej M.J. & Haddadi A. (2013) A Comparison of IEM and SPM Model for Oil Spill Detection Using Inversion Technique and Radar Data. *Journal of the Indian Society of Remote Sensing,* 41(2): 425-431. doi: 10.1007/s12524-012-0217-4.

Haddadi A., Sahebi M.R. & Mansourian A. (2011) Polarimetric SAR feature selection using a genetic algorithm. *Canadian Journal of Remote Sensing,* 37(1): 27-36. doi: 10.5589/m11-013.

Haddadi A., Sahebi M.R., Mokhtarzade M. & Fattahi H. (2009) Classification of Remote Sensing Data Using Combination of Supervised and Unsupervised Neural Network. *Journal of REMOTE SENSING & GIS,* 3(1): 23-50.

PUBLICATIONS IN PROFESSIONAL CONFERENCES

Haddadi A., Burger J., Leblon B., Pirouz Z., Groves K. & Nader J. (2014) Use of Near Infrared Hyperspectral Images for Estimating Moisture Content and Basic Specific Gravity of Subalpine Fir Board. In *68th International Forest Product Society (FPS) 2014 ConventionForest Product Society*. Quebec, Canada.

Haddadi A., Burger J., Leblon B., Pirouz Z., Groves K. & Nader J. (2013) Moisture content image of subalpine fir board from near infrared hyperspectral images. In *18th International Nondestructive Testing and Evaluation of Wood SymposiumForest Products Laboratory*. Madison, Wisconsin, USA.

Haddadi A. & Sahebi M. (2011) POLSAR data classification using Self-Organizing Map. In *Geomatics 89, National Conference & Exhibition of NCC*. Tehran, Iran.

ShahsavarHaghighi S., Valadanzoej M.J., Sahebi M. & Haddadi A. (2011) Oil Spill Pollution Survey Using Radar Systems and Its Parameters Influence Regarding Backscattering Models. In *International Symposium on Sustainable Systems and the Environment, ISSE11*. American University of Sharjah, Sharjah, UAE.

Haddadi A., Sahebi M., Valadanzoej M.J. & Mohammadzadeh A. (2008) Image Segmentation Using Wavelet and watershed transform. In *Geomatics 87, National Conference & Exhibition of NCC*. Tehran, Iran.

TEACHING EXPERIENCES

- Co-supervising MSc Thesis of S. ShahsavarHaghighi entitled: Oil Spill Detection by Using SAR Data, K.N. Toosi University of Technology, Tehran, Iran, 2009-2011
- Supervising of Basic Surveying, final project of Interns, in *University of Zabol*, Zabol, Iran, 2011.
- Supervising of Remote Sensing, final project of Interns in *Estahban Azad University*, Estahban, Iran, 2010.
- Lecturer of Survey of Roads, Basic Survey and Electronic Distance Measurement in *Sirjan University of Technology*, 2009-2010.

- Lecturer of Survey of Roads, Basic Survey, Programming Language and Practical Cartography in *Darolfonoon University*, Ghazvin, Iran, 2009-2010.
- Lecturer of Digital Image Processing, Basic Survey and Survey of Road in *Estahban Azad University*, Estahban, Iran, 2009.

AWARDS AND HONORS

- Wood preservation fund student scholarship, forest product society, 2014.
- Graduate Student Scholarship, Department of Forestry and Environmental Management, University of New Brunswick, 2012-2015.
- International Differential Scholarship, University of New Brunswick, 2012-2015.
- Best student award in MSc. K.N. Toosi University of Technology, Tehran, Iran, 2009.
- Best student award in BSc. Isfahan University, Iran, 2007

TRAINING AND WORKSHOPS ATTENDED

- The workshops of Mitacs Inc
    - *Business Etiquette*
    - *Networking*
    - *Skills of Communication*
    - *Foundations of Project Management*
- The workshop on *Multivariate Classification and analysis of hyperspectral images, 2012*, by BurgerMetrics. http://www.iasim.net/